UNIVERSITY OF SOUTHAMPTON
Optoelectronics Research Centre

Applications of Light Propagation in Novel Photonic Devices

Anna Claire Peacock

A thesis submitted for the degree of
Doctor of Philosophy

August 2004

University
of Southampton

UNIVERSITY OF SOUTHAMPTON

ABSTRACT

OPTOELECTRONICS RESEARCH CENTRE

Doctor of Philosophy

APPLICATIONS OF LIGHT PROPAGATION IN NOVEL PHOTONIC DEVICES

by Anna Claire Peacock

In this thesis, the propagation of light in novel photonic devices has been studied theoretically, numerically and experimentally. In particular, self-similar solutions to the nonlinear Schrödinger equation have been investigated as a means of avoiding distortions associated with high power pulse propagation in optical fibres. The results show that it is the interplay between the nonlinear and dispersive effects that leads to stable formation of the self-similar solutions. By considering generalised nonlinear Schrödinger equations we have extended the previous investigations of linearly chirped parabolic pulse solutions, which exist in the normal dispersion regime, and have found a new broader class of self-similar solutions, which exist when the fibre parameters are allowed to vary longitudinally. Numerical simulations of these systems confirm the analytic predictions. Experimental confirmation of parabolic pulse generation in high gain cascaded amplifier systems and in highly nonlinear microstructured fibres is also reported.

In addition, the propagation of light in modulated crystal structures has been investigated. By modifying the linear and nonlinear properties of the crystals it has been shown that it is possible to manipulate the speed and the wavelength of the propagating light. In particular, negative refractive index materials have been shown to support fast and / or slow propagating light, whilst two dimensional nonlinear photonic crystals have been used to demonstrate multiple harmonic generation over a wide range of phase matching angles. The influence of waveguiding geometries has also been considered to determine the optimum design for the efficiency of the devices.

Contents

DECLARATION OF AUTHORSHIP

I, Anna Claire Peacock, declare that the thesis entitled:

APPLICATIONS OF LIGHT PROPAGATION IN NOVEL PHOTONIC DEVICES

and the work presented in it are my own. I confirm that:

- this work was done wholly or mainly while in candidature for a research degree at this university;
- where any part of this thesis has previously been submitted for a degree or any other qualification at this university or any other institution, this has been clearly stated;
- where I have consulted the published work of others, this is always clearly attributed;
- where I have quoted from the work of others, the source is always given. With the exception of such quotations, this thesis is entirely my own work;
- I have acknowledged all main sources of help;
- where the thesis is based on work done by myself jointly with others, I have made clear exactly what was done by others and what I have contributed myself;
- parts of this work have been published as:

  1. A. C. Peacock and N. G. R. Broderick, Opt. Express, 11(20):2502, 2003.
  2. V. I. Kruglov, A. C. Peacock, and J. D. Harvey, Phys. Rev. Lett., 90(11):113902, 2003.
  3. A. C. Peacock, N. G. R. Broderick, and T. M. Monro, 218:167, 2003.
  4. K. Gallo, R. T. Bratfalean, A. C. Peacock, N. G. R. Broderick, C. B. E. Gawith, L. Ming, P. G. R. Smith, and D. J. Richardson, Electron. Lett., 39(1):75, 2002.

Signed:

Date: 5 August 2004

Acknowledgments

I have been particularly fortunate to work with a number of exceptional people over the course of this thesis and it gives me great pleasure to take this opportunity to thank them.

Firstly, I must thank my supervisor Neil Broderick who has not only provided much support and guidance, but has also been a great source of coffee. His extensive knowledge of both theoretical and experimental optics has played a crucial role in the development of this thesis.

Great thanks must also be extended to David Richardson and John Harvey, whose broad experiences in the field of optics have provided invaluable guidance throughout my research. John in particular, for his extended discussions and e-mails which have provided some much needed relief in times of stress.

Thanks also to my collegues Radu Bratfalean and Katia Gallo, to whom I am greatly indebted. Without your help, time and patience, both in and out of the lab, many of the investigations presented in this thesis would simply not have been possible. On this note, much thanks to Jonathan Price, Andy Malinowski and Jerry Prawiharjo for allowing me to “borrow” much laboratory equipment.

Many thanks must go to Benn Thomsen and Martin O’Connor, who have been a great source of help in the lab, and also to Vladimir Kruglov and Tanya Monro, who have provided invaluable mathematical and numerical support in certain aspects of this work.

I am especially grateful to Eleanor, Corin, Stu and Beckett, whose helpful and constructive comments have played an important role in the final shaping of this thesis.

Of course there are my fellow students, office companions and house mates who have been the source of many hours of entertainment and distractions. Special thanks must go to Laurie, Paddy and Iain for their support and companionship both at work and in the Crown; and to Pete for the endless cups of tea.

Finally, I would like to thank my family and friends for providing the essential balance to keep me in touch with reality. Your support and words of encouragement have been invaluable.

Abbreviations

AOM	Accousto-Optic Modulator
ASE	Amplified Spontaneous Emission
CW	Continuous Wave
FROG	Frequency-Resolved Optical Gating
FWHM	Full Width Half Maximum
GVD	Group Velocity Dispersion
HeXLN	Hexagonally Poled Lithium Niobate
LMA	Large Mode Area
NLSE	Nonlinear Schrödinger Equation
OPO	Optical Parametric Oscillator
OSA	Optical Spectrum Analyser
PC	Polarisation Controller
PPLN	Periodically Poled Lithium Niobate
QPM	Quasi-Phase Matching
RMS	Root-Mean-Square
SESAM	Semiconductor Saturable Absorber Mirror
SHG	Second Harmonic Generation
SMF	Single Mode Fibre
SPM	Self-Phase Modulation
SRS	Stimulated Raman Scattering
TBP	Time-Bandwidth Product
XPM	Cross-Phase Modulation

List of Figures

Chapter 1

Introduction

The concept of controlling and manipulating the propagation of light to our advantage is by no means a new one. In fact, optical technologies have been a part of our lives for thousands of years in the form of devices such as glasses and mirrors [1]. It is thus not surprising that optical devices have not only had a major influence on our lifestyles of today, but they have also made important contributions towards our understanding of the natural world.[1] Paradoxically, this influence is often "invisible" as the use of optical technologies in everyday devices such as compact disk (CD) players and infrared remote controls is frequently taken for granted.

As our understanding of optical systems advances, the importance of light in our lives will continue to increase. In particular, fundamental studies in optics are essential for the advancement of a wide range of technologies in fields including telecommunications, medicine, micromachining and information storage. In such fields, understanding both the linear and nonlinear processes which occur in the optical components, whether they be optical fibres or bulk crystals, is vital for the optimisation of the system. What establishes an "understanding" of a system can either be a theoretical description or an experimental observation. However, ideally the most complete description will come from a combination of the two. Indeed, sometimes there is a need for experimental confirmation of a theoretical result whilst in others it is the experimental observation of a process that sparks a theoretical analysis of a

[1] For example Galileo Galilei's use of a telescope for astronomical observations.

system. In particular, it was the latter case that lead to the discovery of solitons after John Scott Russell observed a “great solitary wave” propagating in the Edinburgh-Glasgow canal [2]. Significantly, subsequent studies of wave propagation in the presence of nonlinear and dispersive effects have not only lead to the establishment of solitons as one of the most important components in physical systems today, but they have also proved to be invaluable for describing a much wider range of dynamical physical phenomena [3, 4].

The results of the investigations presented in this thesis essentially cover two main areas of research involving both linear and nonlinear phenomena. In Part 1 of this thesis I will investigate distortion free self-similar pulse propagation in nonlinear optical fibres to generate high power short pulses. Significantly, it will be shown that it is the interplay between the nonlinear and dispersive effects in the fibres that leads to the stable formation of these pulses. Then, in Part 2, I will consider the control and manipulation of light in novel crystal structures. In particular I will focus on modulated crystals which are often referred to as metamaterials and can be used to manipulate the speed or wavelength of the propagating light. In both cases the mathematical formalism necessary to describe the physical processes will be introduced in the respective parts. Although these two areas are of great fundamental and practical interest on their own, improved understanding of the individual processes can be combined to aid with the design of more efficient devices and this will be the focus of the third and final part of the thesis.

Part I

Self-Similar Pulse Propagation in Optical Fibres

Chapter 2

Introduction

With rapid advancements in the technology of optical fibre amplifiers to generate high power pulses, the main technical challenge restricting the use of higher peak powers in optical systems are the pulse distortions resulting from the interplay between nonlinear and dispersive effects. In the anomalous dispersion regime these distortions are often associated with the pulse breaking up into a series of sub-pulses [5], and in the normal dispersion regime they can lead to the phenomenon of optical wave breaking [6]. As a result, numerous investigations have been conducted to establish conditions for avoiding these deleterious effects in nonlinear systems [7, 8, 9]. To date, the greatest successes have been associated with the discovery of solitary wave solutions which can propagate distortion free over large distances while maintaining their functional form.

Like any physical investigation, the study of nonlinear systems is based on the search for explicit solutions of the differential equations which describe them. In some cases the underlying propagation equations are mathematically integrable and the solutions can be found directly. This is the case for the nonlinear Schrödinger equation (NLSE) describing pulse propagation in optical fibres. In this instance, the use of a mathematical technique known as the inverse scattering method allows soliton solutions [10]. However, for situations where the propagation equation is more complicated the solutions are often found via less systematic techniques such as the method of trial and error. Indeed, it was this method that led to the discovery of the amplifier soliton solutions of the Ginzburg-Landau equation, which describes short pulse propagation in

optical fibre amplifiers [4].

More recently there has been increased interest in the mathematical technique known as “symmetry reduction.” Importantly, this technique can be used to find solutions of non-integrable equations; solutions which, although not necessarily “solitary,” do obey relatively simple scaling laws in such a way that their propagation can be described as self-similar [11]. The key to using symmetry reduction relies on identifying an invariance in the form of the solution so that it can be mapped from one point in its evolution to another via simple scaling laws. In particular, techniques based on symmetry reduction have recently led to the discovery of an important class of pulses which can propagate in a highly nonlinear, normal dispersion fibre amplifier such that they avoid the effects of wavebreaking. These solutions, which have been described as “similaritons,” were found to have an intensity profile which is parabolic and a frequency chirp which is strictly linear, and will propagate in an amplifier subject to the self-similar scaling of their intensity and temporal width [12, 13]. In addition to these solutions being of fundamental interest (since they represent a new class of solution to the NLSE with gain) they are also of considerable practical interest as they offer a viable solution to overcoming the challenge of increasing the peak powers in optical systems.

In this part of the thesis I will investigate self-similar solutions for high intensity pulses propagating in optical fibres and optical fibre amplifiers. Owing to the importance of the parabolic pulse solutions discussed above, the earlier analysis of their propagation in rare-earth doped fibre amplifiers has been extended to consider novel, more flexible, approaches to parabolic pulse generation. In addition, a new broader class of self-similar solutions found for systems which can be modelled by the NLSE with distributed parameters will also be presented. In all instances, it is expected that the self-similar solutions will find wide application in many areas of optical technology in both the laboratory and in industry.

2.1 Outline for Part 1

Chapter 3 introduces the basic theory describing optical pulses and their propagation in single mode optical fibres and optical fibre amplifiers. In particular, the NLSE and the various techniques used to find its solutions will be described.

Because of the key role that self-similarity plays in this part of the thesis, Chapter 4 introduces this concept in more detail, outlining in particular the associated mathematical formalism. After discussing the previous research that motivated the theoretical analysis of the parabolic pulse solutions, a brief description of the results of these calculations will be presented. The experiments which provided the first confirmation of the parabolic pulse solutions will also be discussed.

In Chapter 5, experiments to investigate the generation of parabolic pulses in a cascaded fibre amplifier chain, where the characteristics of each of the amplifiers differ, will be described. The experimental results are analysed via numerical simulations to establish the limitations and assist with the optimisation of the system.

Chapter 6 considers parabolic pulse generation using an undoped microstructured fibre Raman amplifier. After a discussion of the Raman amplifier system, numerical simulations are used to analyse the parabolic pulse propagation. Preliminary experimental results provide confirmation of parabolic pulse generation in a highly nonlinear, normally dispersive microstructured fibre.

In Chapter 7 a new class of solutions which exist for a generalised form of the NLSE with distributed coefficients is investigated. After a brief discussion of the previous research which motivated our theoretical analysis, the results of calculations which use self-similarity methods to analyse the solutions are presented. Numerical simulations are used to confirm the theoretical results before being extended to investigate the stability of the results.

Finally, in Chapter 8 I will present the conclusions to Part 1 of this thesis.

Chapter 3

Pulse Propagation in Single Mode Fibres

3.1 Introduction

As discussed in the previous chapter, in the first part of this thesis self-similar pulse propagation in optical fibres and fibre amplifiers will be investigated. In order to understand physically how such solutions can arise, this chapter introduces some of the basic linear and nonlinear effects that a pulse can experience as it propagates in an optical fibre.

The discussion begins with a simple qualitative description of single mode optical fibres and then the mathematical formalism necessary to describe the electric field of an optical pulse guided in such a fibre is established. The linear and nonlinear effects which influence the evolution of a propagating pulse are discussed before the description is extended to include optical fibre amplifiers. To quantify the discussion, the propagation equation referred to as the nonlinear Schrödinger equation (NLSE) will be introduced. The important analytic solutions which exist under special conditions will be discussed, with particular reference to soliton and solitary wave solutions. Following which consideration will be paid to how it can be solved numerically in regimes where no analytic solutions have yet been found. Finally, generalised forms of the NLSE will be presented to describe propagation when the spectral width of the pulse becomes large.

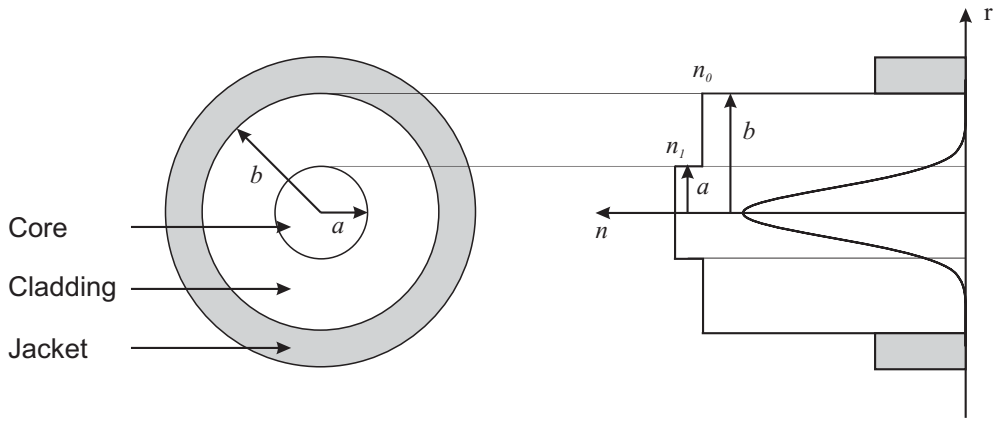

Figure 3.1: Refractive index profile of a standard step-index fibre. The right hand side of the figure shows the fundamental mode profile in the fibre.

3.2 Single Mode Optical Fibres

The simplest form of a single mode optical fibre has a step-index geometry which consists of a thin central core, where the light is confined, surrounded by a cladding layer. As illustrated in Fig. 3.1, for a standard single mode fibre (SMF) the refractive index of the core n_1 is slightly higher than the refractive index of the cladding n_0 where

$$n = \sqrt{\varepsilon/\varepsilon_0}, \tag{3.1}$$

and ε_0 is the dielectric permittivity in a vacuum.[1] The two parameters which characterise a step-index fibre are the relative core-cladding index difference,

$$\Delta = \frac{n_1^2 - n_0^2}{2n_1^2}, \tag{3.2}$$

and the normalised frequency

$$V = k_0 a \left(n_1^2 - n_0^2\right)^{1/2}, \tag{3.3}$$

where $k_0 = 2\pi/\lambda_0$, a is the core radius and λ_0 is the wavelength of the transmitted wave [14]. In a geometrical optics picture, this difference in refractive index gives rise to total internal reflection at the core-cladding interface, which will confine certain light rays to the core. It is useful to note that the maximum light acceptance angle of the fibre is known as the numerical aperture (NA)

[1] This assumes that the magnetic permeability of the fibre is equal to the vacuum value so that $\mu = \mu_0$.

and, for a small index difference, this can be related to Δ via:

$$\mathrm{NA} \simeq n_1\sqrt{2\Delta}. \tag{3.4}$$

In a more rigorous analysis, Maxwell's equations predict a finite set of guided transverse modes with their energy concentrated mostly in the core. The number of modes supported by a particular fibre depends both on the wavelength of the incident light and on the fibre parameters. It can be shown that for a fixed wavelength, reducing the core radius until $V < 2.405$ ensures that only one transverse mode is guided [14]. It is this regime of SMF propagation that is considered in Part 1 of this thesis.

3.3 Description of Optical Pulses

In this part of the thesis a scalar approach is adopted which implies that the optical field maintains its polarisation along the fibre length so that the electric field vector $\mathbf{E}(\mathbf{r},t)$ associated with a pulse can be represented as:

$$\mathbf{E}\left(\mathbf{r},t\right) = \frac{1}{2}\hat{x}\left[E\left(\mathbf{r},t\right)\exp\left(-\mathrm{i}\omega_0 t\right) + \mathrm{c.c.}\right]. \tag{3.5}$$

Here $\hat{x}$ is the polarisation unit vector, $E\left(\mathbf{r},t\right)$ is the slowly varying complex envelope, ω_0 is the carrier angular frequency of the field and $\mathrm{c.c.}$ denotes the complex conjugate. The underlying assumption of Eq. (3.5) is that the field is quasi-monochromatic, i.e., the spectral width $\Delta\omega$ is much smaller than the centre frequency ω_0 [4].

In the search for solutions for the optical field, it is useful to separate the envelope $E\left(\mathbf{r},t\right)$ in the form:

$$E\left(\mathbf{r},t\right) = F\left(x,y\right)\Psi\left(z,t\right)\exp\left(\mathrm{i}\beta_0 z\right), \tag{3.6}$$

where $F\left(x,y\right)$ is the transverse mode distribution, $\beta_0 \equiv \beta\left(\omega_0\right)$ is the momentum wavenumber at the carrier frequency and $\Psi\left(z,t\right)$ is a slowly varying function of z. Substitution of Eq. (3.6) into the wave equation then leads to two equations for $F\left(x,y\right)$ and $\Psi\left(z,t\right)$ [4]. The wavenumber β_0 is determined by solving the eigenvalue equation for the modes $F\left(x,y\right)$ whilst the temporal characteristics of the optical pulse are obtained via the solutions for $\Psi\left(z,t\right)$.

Considerable insight into the temporal features of the pulse can then be obtained by separating the complex signal $\Psi(z,t)$ into its amplitude A and phase Φ:

$$\Psi(z,t) = A(z,t)\exp\left[\mathrm{i}\Phi(z,t)\right], \tag{3.7}$$

where $A(z,t) = |\Psi(z,t)|$ is positive definite. From Eqs. (3.5) and (3.7) it is apparent that the instantaneous frequency of the electric field is:

$$\omega(z,t) = \omega_0 + \Omega_{\mathrm{c}}(z,t) = \omega_0 - \frac{\partial\Phi}{\partial t} \qquad \text{or} \qquad \Omega_{\mathrm{c}}(z,t) = -\frac{\partial\Phi}{\partial t}, \tag{3.8}$$

where the angular frequency ω is related to the frequency ν through $\omega = 2\pi\nu$, and $\Omega_{\mathrm{c}}(z,t)$ is the chirp function which represents the instantaneous frequency deviation from the carrier frequency [4].

It is also useful to consider the envelope of the field in the frequency domain $\tilde{\Psi}(z,\nu)$, obtained from the Fourier transform of $\Psi(z,t)$, defined as:

$$\tilde{\Psi}(z,\nu) = \int_{-\infty}^{\infty} \Psi(z,t)\exp\left(\mathrm{i}2\pi\nu t\right)\mathrm{d}t. \tag{3.9}$$

Analogous to Eq. (3.7), $\tilde{\Psi}(z,\nu)$ can be written as:

$$\tilde{\Psi}(z,\nu) = \tilde{A}(z,\nu)\exp\left[\mathrm{i}\tilde{\Phi}(z,\nu)\right], \tag{3.10}$$

where $\tilde{A}$ and $\tilde{\Phi}$ are the amplitude and phase in the frequency domain, respectively. The group delay $T(\omega)$ is then defined as [15]:

$$T(\omega) = \frac{\partial\tilde{\Phi}}{\partial\omega}, \tag{3.11}$$

which presents the relative time delay between the mean temporal location of the spectral components within the pulse.

From Eq. (3.9), it can be seen that in order to obtain $\tilde{A}(z,\nu)$ from $A(z,t)$ [or similarly, $A(z,t)$ from $\tilde{A}(z,\nu)$], one must have complete knowledge of both the amplitude and phase in the original domain. However, a convenient way of characterising the relationship between a pulse in the temporal domain and its corresponding spectrum is through the root-mean-square (RMS) time-bandwidth product (TBP) [4]:

$$\mathrm{TBP} = \Delta\Omega\cdot\Delta\tau \geq \rho. \tag{3.12}$$

Here, the RMS temporal width is defined by

$$\Delta\tau = \left[\left\langle t^2\right\rangle - \left\langle t\right\rangle^2\right]^{1/2}, \tag{3.13}$$

where

$$\langle t^n \rangle = \frac{\int_{-\infty}^{\infty} t^n \left|\Psi\left(z,t\right)\right|^2 \mathrm{d}t}{\int_{-\infty}^{\infty} \left|\Psi\left(z,t\right)\right|^2 \mathrm{d}t},$$

and a similar relation exists for the RMS spectral width $\Delta\Omega$ in terms of ω. In Eq. (3.12), ρ is a real positive parameter that depends on the pulse shape. In general, Eq. (3.12) suggests that the more highly chirped the pulse, the larger the TBP. In the case where Eq. (3.12) is an equality, the pulse possesses a flat phase and is said to be "transform limited" (see Appendix A). The RMS time-bandwidth products for the commonly encountered Gaussian and hyperbolic secant (sech) pulse profiles are given in Table 3.3, where T_0 is the half width at the $1/\mathrm{e}$–intensity point.

Profile	Temporal Amplitude	Spectral Amplitude	Time-Bandwidth Product
Gaussian	$\exp\left(-t^2/2T_0^2\right)$	$\exp\left(-2\pi^2 T_0^2 \nu^2\right)$	0.5
sech	$\mathrm{sech}\left(t/T_0\right)$	$\mathrm{sech}\left(\pi^2 T_0 \nu\right)$	0.5227

Table 3.1: Time-bandwidth products for Gaussian and hyperbolic secant temporal profiles.

3.4 Chromatic Dispersion

Chromatic dispersion arises due to the frequency dependence of the effective refractive index. Thus a pulse consisting of a finite band of wavelengths, over which the phase velocity v_p varies significantly, will experience a temporal separation of its different spectral components during propagation. In an optical fibre there are two effects that lead to chromatic dispersion: (i) the material dispersion, which is intrinsic to any lossy medium, and (ii) the waveguide dispersion, which can be used to tailor the total chromatic dispersion.

3.4.1 Material Dispersion

The material dispersion of a propagation medium has its origins in the frequency dependent response of the bound electrons of the dielectric to the incident optical field. Far from the resonant frequencies of the medium, the re-

fractive index of a fibre is well described by the Sellmeier equation [16]:

$$n^2(\omega) = 1 + \sum_{j=1}^{m} \frac{B_j \omega_j^2}{\omega_j^2 - \omega^2}, \tag{3.14}$$

where B_j is the strength of the resonance at ω_j. For bulk fused silica, the three resonances of importance have the parameters [17]:

$$\begin{array}{lll} B_1 = 0.6961663 & B_2 = 0.4079426 & B_3 = 0.8974794 \\ \lambda_1 = 0.0684043\,\mu\mathrm{m} & \lambda_2 = 0.1162414\,\mu\mathrm{m} & \lambda_3 = 9.896161\,\mu\mathrm{m} \end{array}$$

where $\lambda_j = 2\pi c/\omega_j$, and c is the velocity of light in a vacuum.

The effects of dispersion can be included in the propagation equations through the wavenumber $\beta(\omega) = n(\omega)\,\omega/c$. To simplify the mathematical description this can be expanded in a Taylor series about ω_0 as:

$$\beta(\omega) = \beta_0 + \beta_1(\omega - \omega_0) + \frac{1}{2}\beta_2(\omega - \omega_0)^2 + \frac{1}{6}\beta_3(\omega - \omega_0)^3 + \cdots, \tag{3.15}$$

where

$$\beta_m = \left[\frac{\mathrm{d}^m \beta}{\mathrm{d}\omega^m}\right]_{\omega=\omega_0} \qquad (m = 0, 1, 2, 3, ...), \tag{3.16}$$

which is valid under the quasi-monochromatic approximation [Section 3.3]. It is worth noting that some limitations on the use of this expansion are discussed in Ref. [18]. Generally the cubic and higher order terms in this expansion are negligible for pulses with small bandwidths as $\Delta\omega << \omega_0$ and it is only necessary to consider β_1 and β_2. Eq. (3.15) then yields the relations:

$$\begin{aligned} \beta_1 &= \frac{1}{c}\left(n + \omega\frac{\mathrm{d}n}{\mathrm{d}\omega}\right) = \frac{1}{v_g}, \\ \beta_2 &= \frac{1}{c}\left(2\frac{\mathrm{d}n}{\mathrm{d}\omega} + \omega\frac{\mathrm{d}^2 n}{\mathrm{d}\omega^2}\right) = -\frac{1}{v_g^2}\frac{\mathrm{d}v_g}{\mathrm{d}\omega}, \end{aligned} \tag{3.17}$$

where v_g is the group velocity at ω_0. From the first expression it follows that β_1 determines the speed of the pulse envelope. In the second expression, β_2 determines how the group velocity of the pulse changes as a function of the frequency. Consequently, β_2 is referred to as the group velocity dispersion (GVD) parameter. This latter coefficient vanishes in fused silica at a wavelength $\lambda_{\mathrm{zd}} \simeq 1.27\,\mu\mathrm{m}$ called the zero dispersion wavelength. For wavelengths such that $\lambda_0 < \lambda_{\mathrm{zd}}$, $\beta_2 > 0$ and the fibre is said to exhibit normal dispersion for which the red shifted frequency components travel faster than those that

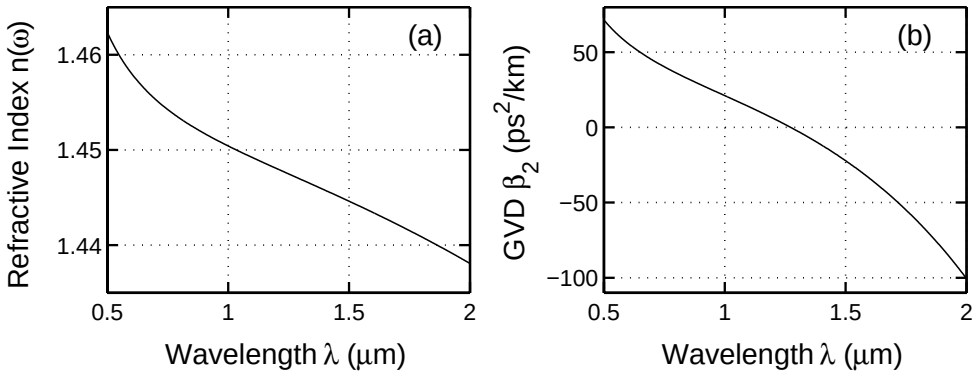

Figure 3.2: (a) Refractive index n and (b) the resultant GVD β_2 for fused silica, as functions of wavelength.

are blue shifted. In contrast, the opposite occurs in the anomalous dispersion regime where $\lambda_0 > \lambda_{\text{zd}}$ and $\beta_2 < 0$. Using Eqs. (3.14) and (3.17), Fig. 3.2 shows (a) the variation of n and (b) the resultant β_2, as functions of wavelength, clearly showing the different regions of the GVD.

Although, as mentioned above, in most cases the contribution of the β_2 term dominates, for wavelengths close to λ_{zd} or alternately, for pulses with significant bandwidths, it becomes necessary to include the higher order term proportional to β_3 in Eq. (3.15). This can be understood from Fig. 3.2(b) where it can be seen that for pulses with a large bandwidth, β_2 varies significantly over the wavelengths contained within the spectrum. Clearly, the wavelength dependence of β_2 will play some role in the pulse broadening. From Eq. (3.16):

$$\beta_3 = \frac{\mathrm{d}^3\beta}{\mathrm{d}\omega^3} = \frac{\mathrm{d}\beta_2}{\mathrm{d}\omega}, \tag{3.18}$$

which implies that β_3 is related to the dispersion slope. Consequently, the inclusion of β_3 can be viewed as a way of incorporating the wavelength dependence of β_2.

3.4.2 Waveguide Dispersion

In optical fibres the tails of the transverse mode extend into the cladding (see Fig. 3.1) by an amount dependent on the wavelength. Due to the lower refractive index of the cladding, this leads to a small perturbation to the effective refractive index given by [14]:

$$\delta n\left(\omega\right) = \Gamma_2\left(\omega\right)\Delta n, \tag{3.19}$$

where $\Gamma_2(\omega)$ is the fraction of power flowing in the cladding and Δn is assumed to be independent of wavelength. To first order $\Gamma_2(\omega) \propto \kappa/\omega^2$, where κ is a positive constant which depends on the fibre design parameters such as the core radius. It then follows from Eq. (3.17) that the approximate change in dispersion $\delta\beta_2(\omega)$ is given by:

$$\delta\beta_2(\omega) = \frac{1}{c}\left(2\frac{\mathrm{d}(\delta n)}{\mathrm{d}\omega} + \omega\frac{\mathrm{d}^2(\delta n)}{\mathrm{d}\omega^2}\right) = \frac{\Delta n}{c}\left(2\frac{\mathrm{d}\Gamma_2}{\mathrm{d}\omega} + \omega\frac{\mathrm{d}^2\Gamma_2}{\mathrm{d}\omega^2}\right) = \frac{2\Delta n}{c}\frac{\kappa}{\omega^3}. \quad (3.20)$$

Eq. (3.20) shows that the effect of waveguide dispersion is to increase the group velocity dispersion in fibres, which consequently shifts the zero dispersion wavelength so that in typical optical fibres $\lambda_{\mathrm{zd}} \simeq 1.31\,\mu\mathrm{m}$. An additional feature of Eq. (3.20) is that it illustrates the Δn dependence of β_2, and this suggests that the dispersion can also be modified by introducing dopants (see Section 3.6). These results also indicate that the waveguide dispersion can be exploited to shift, or flatten, the dispersion curve [19], and this has important implications for the field of telecommunications.

3.5 Nonlinear Effects in Optical Fibres

When intense electromagnetic fields propagate through a medium they cause the bound electrons to oscillate in an anharmonic manner. As a result, the induced polarisation $\mathbf{P}$ no longer depends linearly on the incident field $\mathbf{E}$ and must be extended to the more general expression [20]:

$$\begin{aligned} P_i(\omega_1) &= \chi^{(1)}_{ij}(\omega_1;\omega_1) E_j(\omega_1) + \chi^{(2)}_{ijk}(\omega_1;\omega_1-\omega_2,\omega_2) E_j(\omega_1-\omega_2) E_k(\omega_2) \\ &+ \chi^{(3)}_{ijkl}(\omega_1;\omega_1-\omega_2-\omega_3,\omega_2,\omega_3) E_j(\omega_1-\omega_2-\omega_3) E_k(\omega_2) E_l(\omega_3) \\ &+ \ldots, \end{aligned} \quad (3.21)$$

where $\chi^{(j)}$ is the $(j+1)$ th rank susceptibility tensor, $P_i(\omega)$ and $E_i(\omega)$ are the Fourier components of the fields P_i and E_i, respectively, and the Einstein summation convention applies. Although for simplicity Eq. (3.21) assumes that the polarisation can be related to the field via a power series, it is nevertheless extremely useful for describing a large number of nonlinear phenomena.

The linear susceptibility is still the dominant term in this expansion and this gives rise to the refractive index n and the attenuation coefficient α through:

$$n(\omega) = 1 + \frac{1}{2}\mathrm{Re}\left[\chi^{(1)}(\omega)\right], \quad (3.22)$$

$$\alpha(\omega) = \frac{\omega}{nc}\mathrm{Im}\left[\chi^{(1)}(\omega)\right]. \tag{3.23}$$

The second order susceptibility $\chi^{(2)}$ is responsible for effects such as second harmonic generation and sum frequency three wave mixing, but this vanishes for fused silica glass due to its inversion symmetry. As a result the lowest order nonlinear effects in optical fibres originate from the third order susceptibility $\chi^{(3)}$, which gives rise to effects such as nonlinear refraction, third harmonic generation and four-wave mixing. In general, with most common fibres there is insufficient phase matching to observe the latter two processes and the majority of nonlinear effects result from the nonlinear refraction.

3.5.1 Nonlinear Refraction

Nonlinear refraction gives rise to the intensity dependence of the refractive index so that n becomes [4]:

$$\tilde{n}\left(\omega, |E|^2\right) = n(\omega) + n_2 |E|^2, \tag{3.24}$$

where $n(\omega)$ is given by Eq. (3.22), $|E|^2$ is the intensity of the field and n_2 is the nonlinear index coefficient given by

$$n_2 = \frac{3}{8n}\mathrm{Re}\left[\chi^{(3)}_{xxxx}\right]. \tag{3.25}$$

The assumption of a linearly polarised field implies that only the $xxxx$ component of the $\chi^{(3)}$ tensor contributes to the nonlinear index n_2. The effect of the second term in Eq. (3.24) is to cause an additional phase shift

$$\Delta\Phi_{\text{SPM}} = n_2 k_0 |E|^2 L, \tag{3.26}$$

where L is the fibre length. Thus the field experiences a self-induced phase shift referred to as self-phase modulation (SPM). It is this phase shift that is responsible for the spectral broadening of short pulses and in general, due to the symmetric nature of the pulse profiles, will also be symmetric. At this point it is useful to note that n_2 appears in the propagation equations through the fibre specific parameter γ defined as:

$$\gamma = \frac{n_2 \omega_0}{c A_{\text{eff}}}, \tag{3.27}$$

where A_{eff} is the effective mode area given by

$$A_{\text{eff}} = \frac{\left[\int_{-\infty}^{\infty}\int_{-\infty}^{\infty} |F(x,y)|^2 \,\mathrm{d}x\mathrm{d}y\right]^2}{\int_{-\infty}^{\infty}\int_{-\infty}^{\infty} |F(x,y)|^4 \,\mathrm{d}x\mathrm{d}y}. \tag{3.28}$$

If two optical fields are copropagating in a fibre at different wavelengths, the total electric field $\mathbf{E}$ is now given by:

$$\mathbf{E}(\mathbf{r},t) = \frac{1}{2}\hat{x}\left[E_1(\mathbf{r},t)\exp(-\mathrm{i}\omega_1 t) + E_2(\mathbf{r},t)\exp(-\mathrm{i}\omega_2 t) + \text{c.c.}\right].$$

Thus the nonlinear phase shift induced on the first field by the second is

$$\Delta\Phi_{\text{XPM}} = 2n_2 k_0 |E_2|^2 L, \tag{3.29}$$

and this effect is known as cross-phase modulation (XPM). It follows from Eqs. (3.26) and (3.29) that if the two fields are of equal intensity, then the XPM phase shift is twice as large as that induced by SPM. The defining feature of the XPM phase shift is that, in general, it leads to an asymmetry in the pulse spectrum. This is because the contributing portion of the second field to the phase shift changes as the pulses move through each other.

3.6 Doped Fibre Amplifiers

The incorporation of rare-earth ions, such as Yb^{3+} and Er^{3+}, as dopants in a silica fibre provides a source of gain which allows such a medium to amplify an optical field as it propagates. In order to improve the efficiency of the pumping, the inclusion of rare-earth dopants is often accompanied by a high concentration of codopants. As it has just been shown, both the dispersion and the nonlinear effects that govern the propagation are fibre specific parameters. This suggests that the inclusion of dopants will lead to a qualitative change in the propagation in comparison to a SMF.

In Section 3.4 it was noted that the contribution due to the waveguide dispersion depends on Δn and the core radius. The inclusion of rare-earth ions and codopants such as GeO_2, Al_2O_3, P_2O_5 (or a combination of these) increases the refractive index difference in a fibre amplifier, which leads to a shift in the zero dispersion wavelength to longer wavelengths [Eq. (3.20)]. In addition,

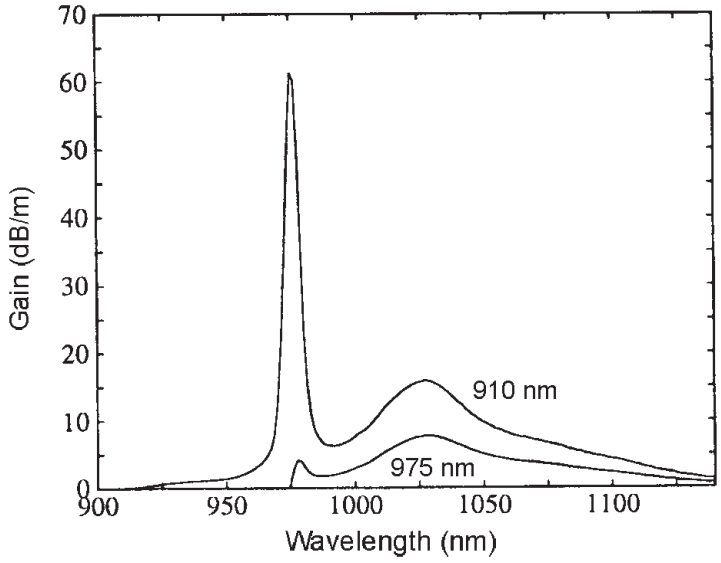

Figure 3.3: Gain spectra for a Yb^{3+}:doped germanosilicate fibre amplifier, for $910\,\mathrm{nm}$ and $975\,\mathrm{nm}$ pumps, from Ref. [22].

fibres with higher refractive index differences generally have smaller core diameters which further shifts the dispersion [21]. A small shift in the dispersion curve can also be attributed to a slight change in the material dispersion and increasing the codopant content can enhance this effect, but in general this is negligible.

The equation for the nonlinearity coefficient γ [Eq. (3.27)] then showed that this depends on the effective mode area A_{eff} so that it also depends on the radius of the amplifier core. Thus the reduction in the core radius suggested above implies a decrease in A_{eff} and hence an increase in the absolute value of γ compared to that of a SMF. Furthermore, the introduction of dopants and codopants into the core can cause a small change in γ by altering the nonlinear refractive index n_2 of the medium slightly [4].

A typical gain profile $g\,(z_0, \lambda)$ for a rare-earth fibre amplifier doped with Yb^{3+} ions is shown in Fig. 3.3 [22]. This illustrates the high gains attainable over a broad gain bandwidth which is an attractive feature for ultrashort pulse amplification. In general, the gain is a function of distance z along the fibre, and saturates with increasing pump power. However, typical pulse energies are much smaller than the saturation energy and so $g\,(z, \lambda)$ can be replaced by $g\,(\lambda)$. In addition, if $g\,(\lambda)$ does not vary significantly over the spectral width of

the optical signal then $g(\lambda) \simeq g(\lambda_0)$.

One further consideration is the attenuation of the pump beam as it propagates down the amplifier. This attenuation implies that g will have an additional z dependence which will be a function of the pumping configuration employed in the amplification. The choice of the pumping geometry will in general depend on the nature of the experiment. The most commonly encountered geometries are those of: (i) pumping codirectionally with the signal beam so that the gain decreases along the length of the amplifier, (ii) pumping counterdirectionally so that the gain increases along the amplifier and (iii) pumping bidirectionally so that the gain remains approximately constant over the length of the amplifier.

3.7 Nonlinear Schrödinger Equation

As discussed in Section 3.1, the effects of dispersion, nonlinearity, loss and gain on the propagation of a pulse in an optical fibre can be combined in a single propagation equation. For a scalar field, the NLSE is given by:

$$\mathrm{i}\frac{\partial}{\partial z}\Psi = \frac{\beta_2}{2}\frac{\partial^2}{\partial T^2}\Psi + \mathrm{i}\frac{\beta_3}{6}\frac{\partial^3}{\partial T^3}\Psi - \gamma\left|\Psi\right|^2\Psi + \mathrm{i}\left[\frac{g-\alpha}{2}\right]\Psi, \tag{3.30}$$

where z is the propagation length and $T = t - \beta_1 z = t - z/v_g$ so that the pulse propagates in a temporal reference frame whose origin moves with the centre of the pulse.[2] For the majority of fibres considered in this part of the thesis, the losses are typically around $1 \times 10^{-3}\,\mathrm{dBm}^{-1}$ so that α can be set to zero for short propagation lengths.

In addition to the assumptions discussed in the preceding sections where the dispersion and nonlinear effects were introduced, there is a further approximation inherent in the derivation of Eq. (3.30). This is that the effect of the nonlinearity is included as a perturbation to the linear solution. This approximation is justified in optical fibres where the linear polarisation is much larger than the nonlinear polarisation, even at very high intensities.

At this point it is useful to introduce propagation lengths which quantify the importance of the dispersive or nonlinear effects on the evolution of the pulse

[2] This is often referred to as the retarded frame.

along the fibre. The relations,

$$L_{\mathrm{D}} = \frac{T_0^2}{|\beta_2|} \quad \text{and} \quad L_{\mathrm{NL}} = \frac{1}{\gamma P_0},$$

where P_0 is the initial peak power, describe the dispersion and nonlinear lengths, respectively.

3.8 Analytic Solutions to the NLSE

In general, solutions to the full NLSE given in Eq. (3.30) cannot be obtained analytically and instead must be found numerically. However, some important analytic expressions exist in situations where certain terms can be neglected.

Considering a lossless SMF, when the propagation distance satisfies $z \sim L_{\mathrm{D}}$ and $z << L_{\mathrm{NL}}$, Eq. (3.30) becomes

$$\mathrm{i}\frac{\partial}{\partial z}\Psi = \frac{\beta_2}{2}\frac{\partial^2}{\partial T^2}\Psi, \tag{3.31}$$

which can be solved in the Fourier domain to give:

$$\tilde{\Psi}(z,\nu) = \tilde{\Psi}(0,\nu)\exp\left[\frac{\mathrm{i}}{2}\beta_2(2\pi\nu)^2 z\right]. \tag{3.32}$$

Thus it can be seen that the effect of GVD only propagation is to introduce a quadratic spectral phase. Although this modification to the phase will not alter the shape of the spectrum, it causes the spectral components to separate in time which results in a temporal broadening of the pulse.

The solution for the complex field in the time domain can then be found by calculating the inverse Fourier transform of Eq. (3.32):

$$\Psi(z,T) = \int_{-\infty}^{\infty} \tilde{\Psi}(z,\nu)\exp(-\mathrm{i}2\pi\nu T)\,\mathrm{d}\nu. \tag{3.33}$$

For an incident Gaussian pulse, such that $\Psi(0,T) = \sqrt{P_0}\exp\left(-1/2\,(T/T_0)^2\right)$, Eq. (3.33) can be solved exactly to yield the solution:

$$\Psi(z,T) = \frac{\sqrt{P_0}T_0}{\left(T_0^2 - \mathrm{i}\beta_2 z\right)^{1/2}}\exp\left(-\frac{T^2}{2\left(T_0^2 - \mathrm{i}\beta_2 z\right)}\right). \tag{3.34}$$

Thus, in a dispersive medium, a Gaussian pulse maintains its shape on propagation but with its width scaling as $T_0\left[1+(z/L_{\mathrm{D}})^2\right]^{1/2}$. However, even for

non-Gaussian pulses, where closed form solutions to Eq. (3.33) for arbitrary z cannot be found, it is possible to use the method of stationary phase to show that in the limit of large z [23]:

$$\Psi(z,T) \simeq \frac{1+\mathrm{i}\left(\beta_2/|\beta_2|\right)}{\sqrt{2}}\left(\frac{1}{2\pi|\beta_2|z}\right)^{1/2}\tilde{\Psi}\left(0,\frac{T}{\beta_2 z}\right)\exp\left(-\frac{\mathrm{i}}{2}\frac{T^2}{\beta_2 z}\right). \quad (3.35)$$

Thus any pulse that propagates in a linear dispersive medium ultimately develops a temporal profile that has the same form as its spectrum with a linear chirp.

Now considering the situation where the propagation distance satisfies $z \sim L_{\mathrm{NL}}$ and $z << L_{\mathrm{D}}$, Eq. (3.30) can be written as

$$\mathrm{i}\frac{\partial}{\partial z}\Psi = -\gamma|\Psi|^2\Psi. \quad (3.36)$$

For sufficiently small z it can be assumed that $|\Psi|^2$ remains unchanged so that Eq. (3.36) has the solution:

$$\Psi(z,T) = \Psi(0,T)\exp\left[\mathrm{i}\gamma|\Psi|^2 z\right], \quad (3.37)$$

and thus the effect of SPM alone is to cause an intensity dependent temporal phase. By noting that this phase induces an intensity dependent chirp, it can be seen that the effect of SPM is to introduce new frequency components into the pulse which results in spectral broadening.

To illustrate the separate effects of dispersive and nonlinear propagation, Fig. 3.4 shows the evolution of a transform limited Gaussian pulse, such that $L_{\mathrm{D}} = 1/2\,\mathrm{m}$ and $L_{\mathrm{NL}} = 1/5\,\mathrm{m}$, for (a) dispersive propagation in the normal dispersion regime and (b) nonlinear propagation.

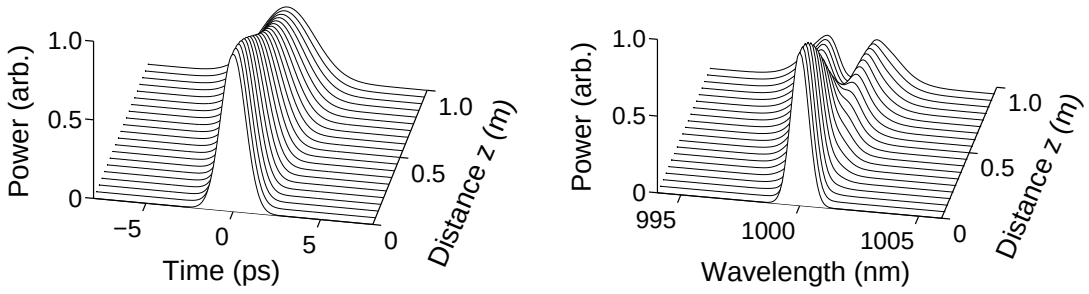

(a) Dispersive Propagation (b) Nonlinear Propagation

Figure 3.4: Evolution of (a) the temporal intensity under dispersive propagation ($\beta_2 > 0$) only and (b) the spectral intensity under nonlinear propagation only.

3.8.1 Soliton Solutions to the NLSE

For systems where it becomes necessary to consider the combined effects of dispersion and nonlinearity ($L_{\mathrm{D}} \sim L_{\mathrm{NL}} \sim z$), interesting phenomena can arise from the interplay between GVD and SPM. In such instances, ignoring gain, loss and higher order dispersion, Eq. (3.30) takes the form:

$$\mathrm{i}\frac{\partial}{\partial z}\Psi = \frac{\beta_2}{2}\frac{\partial^2}{\partial T^2}\Psi - \gamma\left|\Psi\right|^2\Psi. \tag{3.38}$$

This equation belongs to a special class of equations that can be solved exactly using the inverse scattering method [24]. The success of this approach lies in identifying a suitable scattering problem whose potential is the solution sought. The field at any point z can then be found via the evolution of the scattering data, which can simply be obtained by solving the linear scattering problem.

Using this method Eq. (3.38) was found to have an important class of solutions known as solitons [10]. These soliton pulses have the property that they can propagate over long distances in a fibre without undergoing distortions as a result of an effective cancellation of the dispersive and nonlinear effects. Specifically, the term soliton is restricted to solutions found via inverse scattering techniques in which the energy propagates in the form of a localised packet (without gain or loss) and which remain unaffected after collisions with each other [25]. A more general term is a solitary wave and these will be discussed in the following section. Owing to their robustness in nonlinear systems, solitons have been studied extensively in many fields of physics. In the context of pulse propagation in optical fibres, solitons are not only of great fundamental importance but they have also found wide application in many technologies. As it is about to be shown, the qualitative features of the solutions depend strongly on the sign of the dispersion.

In the anomalous dispersion regime, Eq. (3.38) supports soliton solutions which propagate in a cycle returning to the initial form after one soliton period $z_0 = \pi L_{\mathrm{D}}/2$ [4].[3] The exception to this is the fundamental soliton whose shape remains unchanged over the propagation and, provided $\sqrt{\gamma T_0^2 P_0/\left|\beta_2\right|} = 1$, has

[3] These are sometimes referred to as bright solitons in the literature to distinguish them from the solutions where $\beta_2 > 0$.

the form:

$$\Psi(z,T) = \sqrt{P_0}\,\mathrm{sech}\left(\frac{T}{T_0}\right)\exp\left(\mathrm{i}\frac{z}{2L_\mathrm{D}}\right). \tag{3.39}$$

Here the condition placed on the dispersion and nonlinear lengths illustrates the strong dependence of the soliton pulse parameters on the fibre parameters.

In the normal dispersion regime Eq. (3.38) also supports soliton solutions which are referred to as dark solitons. Here the term dark soliton is used since the intensity profile is in the form of a dip embedded on a uniform background. The general solution is given by:

$$\Psi(z,T) = A_0\left[B^{-2} - \mathrm{sech}^2\left(\frac{A_0 T}{T_0}\right)\right]^{1/2}\exp\left[\mathrm{i}\varphi(T') + \mathrm{i}\left(\frac{A_0}{B}\right)^2\frac{z}{L_\mathrm{D}}\right], \tag{3.40}$$

where $T' = A_0 T/T_0 + (A_0^2/B)\left(1-B^2\right)^{1/2} z/L_\mathrm{D}$. The parameter A_0 determines the level of the background and B (the so-called "blackness parameter") governs the depth of the dip ($|B| \leq 1$). The temporal phase varies across the dark soliton, with the magnitude of the phase shift depending on B through:

$$\varphi(T') = \sin^{-1}\left\{\frac{B\tanh(T')}{\left[1 - B^2\,\mathrm{sech}^2(T')\right]^{1/2}}\right\}.$$

For $B = 1$ the intensity goes to zero at the centre of the dip and the soliton is often referred to as a black soliton. Whereas for $|B| < 1$, the intensity of the dip does not extend all the way to zero and the solutions are referred to as gray solitons.

A significant difference between the soliton of Eq. (3.39) and that of Eq. (3.40) is that fundamental solitons are even pulses, with a constant phase across the

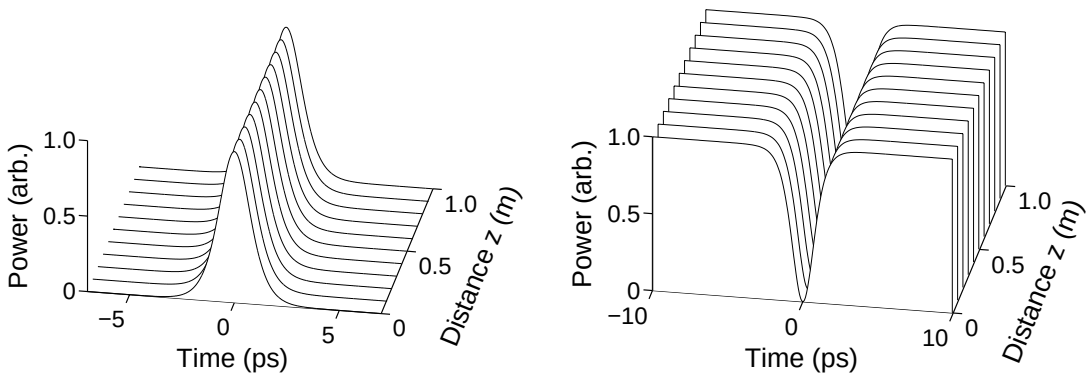

(a) Fundamental Soliton (b) Black Soliton

Figure 3.5: Evolution of (a) a bright soliton ($\beta_2 < 0$) and (b) a black soliton ($\beta_2 > 0$).

entire pulse, and black solitons are odd pulses, with a π phase jump at the centre (where the intensity is zero).[4] To illustrate the differences between the two solutions, Fig. 3.5 shows the evolution of (a) a fundamental soliton and (b) a black soliton.

3.8.2 Solitary Wave Solutions to the Ginzburg-Landau Equation

In situations where the fibre possesses gain, loss, and/or when higher order dispersive effects must be considered, the propagation equation may no longer be integrable by such inverse scattering techniques and so does not possess soliton solutions in the strict mathematical sense. However, these equations can often be found to have solitary wave solutions that can propagate undistorted such that their shape does not change but which may undergo scaling of their amplitude or width. An example of such solitary wave solutions are the autosolitons which exist for a modified form of Eq. (3.30) called the Ginzburg-Landau equation [26]:

$$\mathrm{i}\frac{\partial}{\partial z}\Psi = \frac{1}{2}\left(\beta_2 + \mathrm{i}g\right)\frac{\partial^2}{\partial T^2}\Psi - \gamma\left|\Psi\right|^2\Psi + \mathrm{i}\frac{g}{2}\Psi. \tag{3.41}$$

Here the dispersive term proportional to $\mathrm{i}g/2$ is related to the finite gain bandwidth and is referred to as gain dispersion. This equation is often studied in the context of short pulse propagation in optical fibre amplifiers with the solutions being referred to as amplifier solitons [5].

As mentioned in Chapter 2, the amplifier soliton solutions were found via a method of trial and error to be [27]:

$$\Psi\left(z,T\right) = \sqrt{P_0}\,\mathrm{sech}\left(pT\right)\exp\left[\mathrm{i}\Phi\left(z,T\right)\right], \tag{3.42}$$

where the phase Φ is given by:

$$\Phi\left(z,T\right) = \Gamma z - q\ln\left[\cosh\left(pT\right)\right], \tag{3.43}$$

and the constants P_0, p, q and Γ are determined via:

$$P_0 = \frac{p^2}{2}\frac{\beta_2}{\gamma}\left[s\left(q^2-2\right)+3qg\right], \qquad p^2 = \frac{-g}{g\left(1-q^2\right)+2sq}, \tag{3.44}$$

[4] The description of the pulse as odd refers to its amplitude.

$$q = \frac{3s \pm \sqrt{(9 + 8g^2)}}{2g}, \qquad \Gamma = \frac{-p^2}{2\beta_2}\left[s\left(1 - q^2\right) - 2qg\right], \tag{3.45}$$

where $s = \mathrm{sgn}\,(\beta_2)$. These pulses represent a solution that will propagate in an amplifier, whilst maintaining both their shape and energy, where the amplifier gain is balanced by the loss introduced by the gain dispersion. An important property of these amplifier solitons is that, in contrast to the soliton solutions, these pulses have a time dependent phase. Significantly, however, because of the gain limiting effects, amplifier solitons are undesirable in most amplifier systems and particularly in those that require the pulses to be amplified to a high energy.

To illustrate the significance of these solitary wave solutions, Fig. 3.6(a) shows the evolution of an arbitrary input pulse in an amplifier with a finite gain bandwidth. It can be seen that after the initial propagation, where the pulse experiences gain, the evolution stabilises and a solitary wave is formed. Furthermore, by comparing the output pulse from the amplifier with the solutions of Eqs. (3.42)–(3.45), Fig. 3.6(b) confirms that this pulse has indeed evolved to be an amplifier soliton.

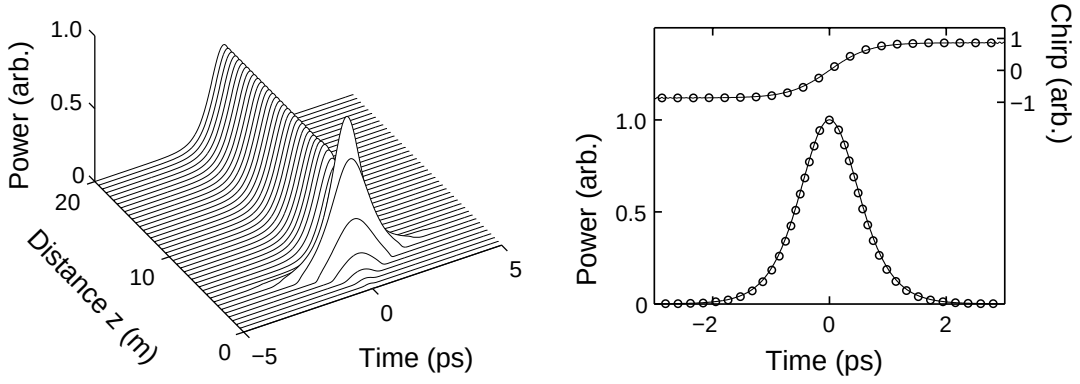

(a) Solitary Wave Evolution (b) Amplifier Soliton

Figure 3.6: (a) Evolution of an autosoliton pulse in an optical fibre amplifier with a finite gain bandwidth. (b) Intensity profile (left axis) and chirp (right axis) of the output amplifier soliton together with the theoretical predictions (circles).

3.9 Numerical Solutions to the NLSE

In the previous section it has been shown that analytic solutions only exist for special reduced forms of Eq. (3.30), and that they often depend critically on the parameters of the system. Thus for more complicated systems and / or an arbitrary choice of initial conditions, it is unlikely that any analytic solutions will exist. As a result, most of the progress which has been made in unveiling the properties of propagation in realistic systems is due to numerical simulations.

Several numerical techniques exist for solving the NLSE but the fastest and the most extensively employed is the split-step Fourier method [4], and it is this technique that is used in this thesis. The essence of this method lies in identifying that the terms in Eq. (3.30) can be separated into those that are easily solved in the temporal domain (i.e., the nonlinear terms) and those that are more efficiently solved in the spectral domain (i.e., the linear terms). Eq. (3.30) can then be rewritten in the form:

$$\mathrm{i}\frac{\partial \Psi}{\partial z} = \left(\hat{D} + \hat{N}\right)\Psi, \tag{3.46}$$

where the dispersive[5] and nonlinear operators are

$$\hat{D} = \frac{\beta_2}{2}\frac{\partial^2}{\partial T^2} + \mathrm{i}\frac{\beta_3}{6}\frac{\partial^3}{\partial T^3} + \mathrm{i}\left[\frac{g-\alpha}{2}\right], \tag{3.47}$$

$$\hat{N} = -\gamma\left|\Psi\right|^2, \tag{3.48}$$

respectively. Although the dispersive and nonlinear effects act together along the length of the propagation, for a sufficiently small z step (h) it can be assumed that they act independently. Thus each propagation segment $z \rightarrow z+h$ is split into two steps where in each step an operator corresponding to the combined effects in the respective domain is applied. Mathematically this is expressed as:

$$\Psi\left(z+h,T\right) \simeq \exp\left(h\hat{D}\right)\exp\left(h\hat{N}\right)\Psi\left(z,T\right), \tag{3.49}$$

where the execution of the dispersive operator is carried out in the Fourier domain via:

$$\exp\left(h\hat{D}\right)\Psi'\left(z,T\right) = \left\{F^{-1}\exp\left[h\hat{D}\left(\mathrm{i}\omega\right)\right]F\right\}\Psi'\left(z,T\right). \tag{3.50}$$

[5]The effects of absorption and / or gain are included in this linear operator.

Here F is the Fourier transform operation and $\hat{D}(\mathrm{i}\omega)$ is the operator $\hat{D}$ of Eq. (3.47) in Fourier space. This process is then repeated until the required propagation distance has been covered.

To illustrate typical propagation with the combined effects of dispersion and nonlinearity this technique is used to propagate a Gaussian pulse under conditions where $L_{\mathrm{D}} = 5L_{\mathrm{NL}}/2$ ($\beta_2 > 0$, $g = 0$ and the individual effects can be seen in Fig. 3.4). Fig. 3.7(a) shows the evolution of the temporal intensity and (b) shows the evolution of the spectral intensity. Comparing these evolutions with those of Fig. 3.4 it can be seen that, in the normal dispersion regime, the combination of GVD and SPM increases the rate at which the temporal profile broadens. Subsequently, this acts to reduce the peak power of the pulse and hence decreases the rate of the spectral broadening. Additionally, it is clear that the multi-peak structure seen with only SPM is also suppressed, and this is due to the reduction in the SPM induced phase shift. Thus the dispersion induced broadening reduces the effects of the nonlinear propagation so that $L_{\mathrm{NL}} << L_{\mathrm{D}}$ is needed to achieve a large nonlinear response.

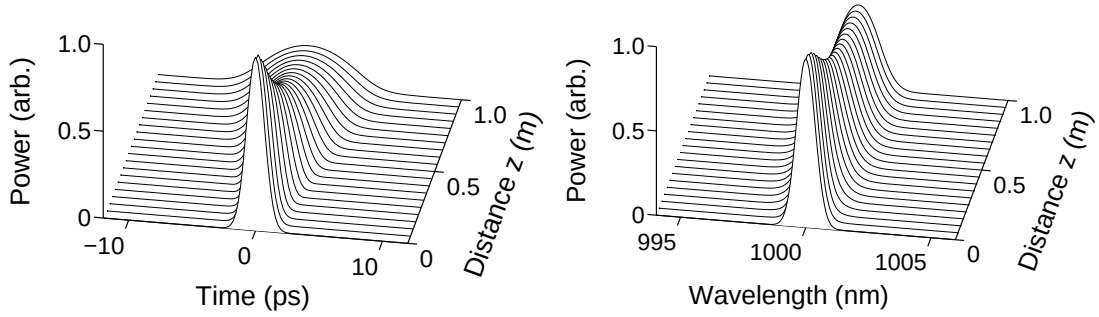

(a) Temporal: GVD and SPM

(b) Spectral: GVD and SPM

Figure 3.7: Numerical evolution of the intensity profile with the combined effects of GVD and SPM, (a) in the temporal domain and (b) in the spectral domain.

Extending the above simulation to include the effects of a constant gain profile, the propagation now describes the evolution of a pulse in an optical fibre amplifier. Fig. 3.8 shows the evolution with $L_{\mathrm{D}} = 5L_{\mathrm{NL}}/2$ ($\beta_2 > 0$) and $g = 2\,\mathrm{m}^{-1}$ where again (a) is the temporal intensity and (b) is the spectral intensity. This shows that the inclusion of gain results in a further increase in the rate of the broadening in both domains. This is to be expected as the increase in the peak

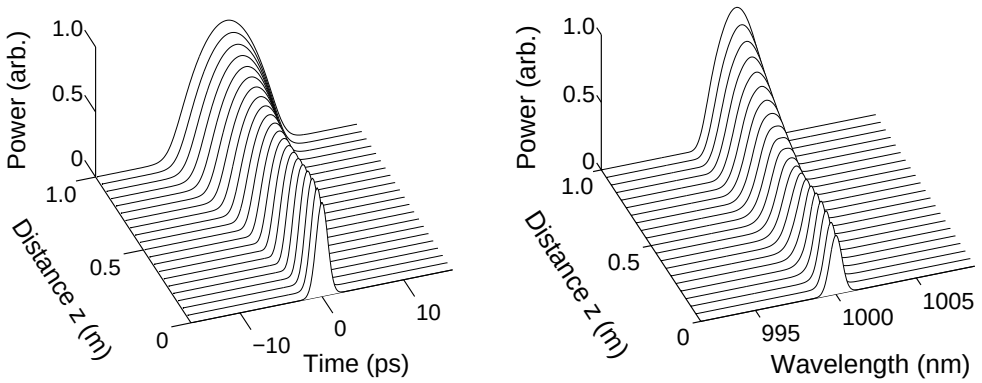

(a) Temporal: With Gain (b) Spectral: With Gain

Figure 3.8: Numerical evolution of the intensity profile with the combined effects of GVD, SPM and gain, (a) in the temporal domain and (b) in the spectral domain.

power leads to an increase in the nonlinear effects.

The different evolution processes can be summarised by the evolution of the RMS time-bandwidth product [Eq. (3.12)]. Fig. 3.9 shows the resultant products for GVD only, SPM only, GVD and SPM and the combined effects of GVD, SPM and gain, as functions of the propagation distance. It is clear that for $g = 0$, in all cases the broadening increases linearly for large propagation distances, whereas for $g \neq 0$ the rate of the broadening continues to increase as the peak power grows.

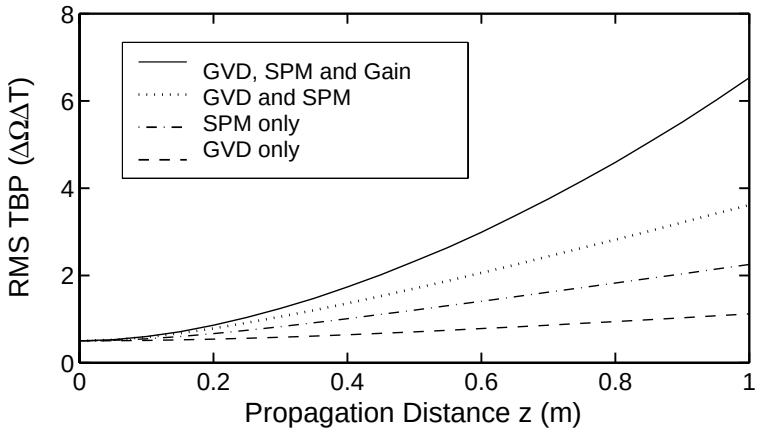

Figure 3.9: Evolution of the RMS time-bandwidth product for GVD only, SPM only, GVD and SPM, and the combined effects of GVD, SPM and gain.

3.10 Generalised NLSE

Although the NLSE introduced in Section 3.7 is extremely successful in explaining a large number of linear and nonlinear effects seen in optical fibres, it often needs modification in order to explain some of the more subtle effects which present themselves during pulse propagation. These effects occur when the spectral width $\Delta\omega$ of the pulse becomes large, and hence several approximations made in deriving the propagation equations are no longer valid. The following investigates modifications to the NLSE necessary to include the effects of a complex Lorentzian gain profile and a delayed nonlinear response.

3.10.1 Complex Lorentzian Gain Model

The Ginzburg-Landau equation, as described in Section 3.8.2, is based on a parabolic gain approximation where the dopant susceptibility is truncated after the second order terms. In general, this leads to an overestimation of the losses in the wings of the spectrum and consequently Eq. (3.41) is only valid for situations where the spectral width of the pulse remains within the gain bandwidth [7]. A more rigorous model to describe a system with a finite bandwidth requires that the amplification process is modelled by the Maxwell-Bloch equations which include the effects of dynamic gain saturation [4]. However, since the upper state lifetimes of rare-earth amplifiers are of the order of several milliseconds, the population inversion remains nearly constant across a propagating picosecond pulse and, in such cases, the system can be very accurately described by the NLSE with a complex Lorentzian gain profile [28].

In reality, the gain profile of a rare-earth doped fibre amplifier is far more complicated than a simple Lorentzian and, in fact, consists of peaks of several overlapping transitions which suffer both strong homogeneous and inhomogeneous broadening [Fig. 3.3]. However, for the purposes of this thesis, as the primarily concern is with the general features of how a frequency dependent gain profile influences the pulse shaping, it suffices to model the gain medium as a homogeneously broadened single transition.

Considering a model which will describe the propagation of a pulse in a homogeneously broadened two-level amplifying medium (in the low-gain satura-

tion limit), for a pulse injected into the amplifier on resonance the propagation equation is given by [7]:

$$\mathrm{i}\frac{\partial}{\partial z}\Psi = \frac{\beta_2}{2}\frac{\partial^2}{\partial T^2}\Psi - \gamma\left|\Psi\right|^2\Psi - \mathrm{i}\frac{\alpha}{2}\Psi + \frac{1}{2}\int_{-\infty}^{\infty}\chi_{\mathrm{D}}\left(\nu\right)\tilde{\Psi}\left(z,\nu\right)\exp\left(-\mathrm{i}2\pi\nu T\right)\mathrm{d}\nu. \tag{3.51}$$

By writing the susceptibility as

$$\chi_{\mathrm{D}}\left(\nu\right) = \frac{g\left(\mathrm{i}-2\pi\nu T_2\right)}{1+\left(2\pi\nu T_2\right)^2}, \tag{3.52}$$

where T_2 is the dipole relaxation time, it is easy to see that the imaginary part represents the resonant Lorentzian gain profile, with a peak gain of g, and the real part represents the resonant dispersion, introduced by the amplifier dopants. Eq. (3.51) can be solved numerically via the split-step Fourier method by calculating the resonant term in the frequency domain.

3.10.2 Delayed Nonlinear Response

The nonlinear effects discussed in Section 3.5.1 are elastic in the sense that no energy is exchanged between the electric field and the propagation medium. The following now considers a situation in which the optical field transfers part of its energy to the nonlinear medium. This occurs when a photon of the incident field is annihilated to create a photon at the downshifted Stokes frequency and a phonon of the exact energy and momentum necessary so that both of these quantities are conserved.[6] This generally occurs in a situation where a pump beam is copropagating with a probe beam at the Stokes frequency, in which case it is referred to as stimulated Raman scattering (SRS). However, if a pulse possesses a broad enough spectrum so that the Stokes frequency is within the bandwidth of the pulse ($\gtrsim 1\,\mathrm{THz}$), the Raman gain can amplify the low energy frequency components by transferring energy from the high frequency components of the same pulse. This latter case is often referred to as intrapulse Raman scattering and it is this effect that leads to the well known soliton self-frequency shift [4, 29].

To extend the system to include the effects of a delayed Raman response, a

[6] A higher energy photon can be created at the anti-Stokes frequency if a phonon of the right energy and momentum is available.

nonlinear polarisation of the form [30]:

$$P_{\mathrm{NL}}(\mathbf{r},T)=\varepsilon_0\chi^{(3)}E(\mathbf{r},T)\int_{-\infty}^{T}R(T-T')\,E^2(\mathbf{r},T')\,\mathrm{d}T' \tag{3.53}$$

is assumed, where $R(T)$ is the nonlinear response function which is normalised to $\int R(T)\,\mathrm{d}T=1$ and the upper limit of integration extends only up to T since the response function $R(T-T')$ must become zero for $T'>T$ to ensure causality.[7] Including this in the propagation equation leads to the modified NLSE [4]:

$$\begin{aligned}\mathrm{i}\frac{\partial}{\partial z}\Psi &= \frac{\beta_2}{2}\frac{\partial^2}{\partial T^2}\Psi+\mathrm{i}\frac{\beta_3}{6}\frac{\partial^3}{\partial T^3}\Psi+\mathrm{i}\left[\frac{g-\alpha}{2}\right]\Psi\\ &- \gamma\left(1+\frac{\mathrm{i}}{\omega_0}\frac{\partial}{\partial T}\right)\Psi\int_0^{\infty}R(T')\left|\Psi(z,T-T')\right|^2\mathrm{d}T'.\end{aligned} \tag{3.54}$$

An important feature of Eq. (3.54) is the inclusion of the time derivative operator in the nonlinear term. This term describes the Stokes' losses associated with the material excitation during the Raman self-scattering process, the frequency dependence of the nonlinearity and the self-steepening effect. Although it is often neglected in Raman analysis of pulses with small bandwidths [29], it is in fact necessary to ensure that the photon number, and not the optical energy, is conserved so that the Raman interaction is described correctly. The response function $R(T)$ should include both the electronic and vibrational (Raman) contributions. If the electronic contribution is assumed to be instantaneous, then the functional form of $R(T)$ can be written as:

$$R(T)=(1-f_R)\,\delta(T)+f_R h_R(T),$$

where $\delta(T)$ is the Dirac delta function and f_R represents the fractional contribution of the delayed Raman response governed by $h_R(T)$ [31]. The form of the Raman response function $h_R(T)$ can be obtained experimentally, or through an approximate analytic form which is modelled on experimental response functions [30]. In this thesis an experimentally determined response function obtained for a silica fibre is used [32], where $f_R=0.18$ and $h_R(T)$ is given in Fig. 3.10. Here Fig. 3.10(a) is the temporal variation and (b) is the Raman gain spectrum corresponding to the Stokes gain. Significantly, although both doped and undoped fibres are considered in this thesis, the inclusion of rare-earth dopants has a negligible effect on the response function of silica fibres.

[7] Both the electric field and the induced polarisation vectors are assumed to point along the same direction so that a scalar notation can be used.

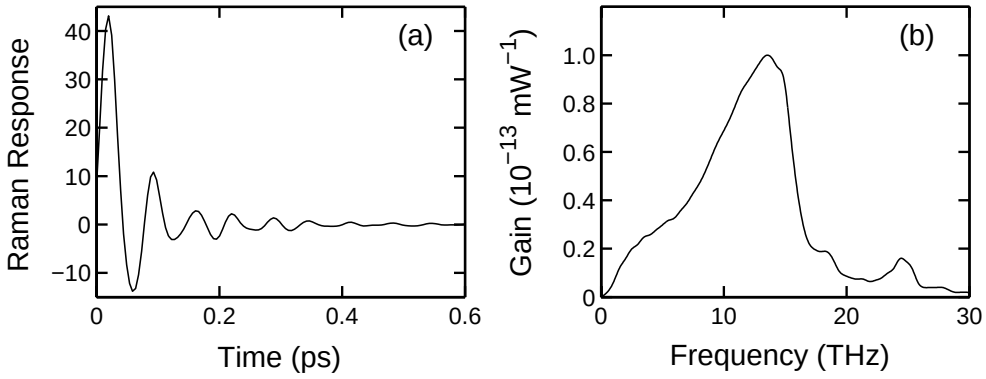

Figure 3.10: (a) Temporal variation and (b) Raman gain spectrum (corresponding to the Stokes gain) of the Raman response function used in this thesis.

Numerical Solutions

Eq. (3.54) can be solved numerically via the split-step Fourier method, described in Section 3.9, but with special treatment of the Raman term [30]:

$$\mathrm{i}\frac{\partial}{\partial z}\Psi = -\gamma\left(1+\frac{\mathrm{i}}{\omega_0}\frac{\partial}{\partial T}\right)\Psi R * |\Psi|^2\,, \tag{3.55}$$

where $*$ has been used to denote the convolution,

$$R * |\Psi|^2 = \int_0^\infty R\left(T'\right)|\Psi(z,T-T')|^2\,\mathrm{d}T'. \tag{3.56}$$

Defining:

$$V\left(z,T\right) = \Psi\left(z,T\right)\exp\left[-\mathrm{i}\left(z-z_0\right)\gamma R * |\Psi_0|^2\right], \tag{3.57}$$

where

$$V_0 = \Psi_0 = \Psi\left(z_0,T\right), \tag{3.58}$$

it can be noted that as $R * |\Psi_0|^2 \in \mathbb{R}$, this implies that $|V|^2 = |\Psi|^2$ and hence $R * |V|^2 = R * |\Psi|^2$. The derivative of V is then calculated as:

$$\begin{aligned}\frac{\partial V}{\partial z} &= \frac{\partial \Psi}{\partial z}\mathrm{e}^{-\mathrm{i}(z-z_0)\gamma R*|\Psi_0|^2} + \Psi\left(-\mathrm{i}\gamma R * |\Psi_0|^2\right)\mathrm{e}^{-\mathrm{i}(z-z_0)\gamma R*|\Psi_0|^2}\\ &= \mathrm{i}\gamma\left(1+\frac{\mathrm{i}}{\omega_0}\frac{\partial}{\partial T}\right)R * |\Psi|^2\,\Psi\mathrm{e}^{-\mathrm{i}(z-z_0)\gamma R*|\Psi_0|^2} - \mathrm{i}\gamma R * |\Psi_0|^2\,\Psi\mathrm{e}^{-\mathrm{i}(z-z_0)\gamma R*|\Psi_0|^2}\\ &= \mathrm{i}\gamma V R * \left(|V|^2 - |V_0|^2\right) - \frac{\gamma}{\omega_0}\frac{\partial}{\partial T}\left(V R * |V|^2\right).\end{aligned} \tag{3.59}$$

To integrate this system a second order Runge-Kutta scheme is used, where the integration of

$$\frac{\partial V}{\partial z} = \xi\left(z,V\right)$$

from z_n to $z_{n+1} = z_n + \delta z$ is performed as:

$$V_{n+1} \approx V_n + \delta z \times \xi \left\{ z_n + \delta z/2, V_n + \delta z/2 \times \xi \left(z_n, V_n \right) \right\}. \tag{3.60}$$

This equation can be solved in a two step process where, using Eq. (3.59), the intermediate step $(n + \frac{1}{2})$ is obtained as:

$$\begin{aligned} V_{n+\frac{1}{2}} &= V_n + \delta z/2 \times \xi \left(z_n, V_n \right) \\ &= V_n - \frac{\gamma \delta z}{2\omega_0} \frac{\partial}{\partial T} \left(V_n R * |V_n|^2 \right), \end{aligned} \tag{3.61}$$

so that,

$$V_{n+1} = V_n + \mathrm{i}\gamma\delta z V_{n+\frac{1}{2}} R * \left(\left| V_{n+\frac{1}{2}} \right|^2 - |V_n|^2 \right) - \frac{\gamma \delta z}{\omega_0} \frac{\partial}{\partial T} \left(V_{n+\frac{1}{2}} R * \left| V_{n+\frac{1}{2}} \right|^2 \right). \tag{3.62}$$

The field $\Psi \left(z, T \right)$ is then reconstructed from Eq. (3.62) using Eq. (3.57) before being operated on by the dispersive operator, as described by Eq. (3.50).

Chapter 4

Self-Similar Parabolic Pulse Solutions to the NLSE with Gain

4.1 Introduction

As discussed in Chapter 2, recent calculations using self-similarity methods have led to the discovery of an important class of solutions to the NLSE with normal dispersion and gain. These pulses, which have a parabolic intensity profile, will maintain a strictly linear chirp so that they propagate self-similarly in highly nonlinear, normal dispersion, media subject to simple scaling rules. Importantly, it is the ability of these solutions to undergo distortion free amplification to high powers, and to be efficiently compressed to ultrashort pulse widths, that has motivated the investigations presented in the first part of this thesis. For this reason, this chapter presents a review of some of the important results regarding parabolic pulses and discusses the significant features of the solutions. To facilitate the theoretical analysis, the discussion begins with a brief introduction to the mathematical formalism of self-similarity techniques.

4.2 An Introduction to Self-Similarity

It is often the case that the evolution of a physical system will exhibit some form of symmetry such that the behaviour of the system at one stage can

be mapped onto its behaviour at some other stage through a suitable scaling transformation. It may be that the properties of this system exhibit unchanging or periodic characteristics, such as the case of soliton solutions (see Section 3.8), or that their evolution with time or distance obeys a simple power-law relationship. In any case, irrespective of the details of the symmetries (or "similarities") possessed by a particular physical system, their identification is the key to establishing a useful mathematical description of the system.

4.2.1 Self-Similarity and Scaling in Physics

A self-similar solution is one in which the functional form of the solution is invariant so that the solution at one point (in space or time for example) can be found from a solution at another point by a similarity transformation. Despite its apparent complexity, self-similarity is a concept that is taught in high school geometry classes in the context of "similar triangles," which have the same angles, but sides of different lengths. In such a case, it is straightforward to map one triangle on to the other by a simple linear scaling transformation.

A slightly more complex example is the evolution of the radius of the acoustic shock-wave produced as a result of a nuclear explosion. A nuclear explosion is, of course, a very complicated event whose complete description must take into account many different factors such as the particular radioactive isotopes used and the geometry of the explosive device. However, the evolution of the radius r_f of the generated acoustic shock-wave is found to obey a remarkably simple scaling law, where the rate of expansion is determined only by the energy released in the explosion, and not the specifics of the system. The result is:

$$r_f = \left(\frac{Et^2}{\rho_0}\right)^{1/5}, \tag{4.1}$$

where E is the energy of the explosion, ρ_0 is the density of the air and t is the time after the explosion [33]. The realisation that a complex event such as an explosion possesses such a simple underlying structure is both very satisfying from a physical point of view, but also of immense practical importance. For example, Eq. (4.1) allowed opposing sides during the Cold War to estimate the energy released in nuclear tests based only on analysis of available television footage.

Although self-similarity has long been a focus of studies involving nonlinear physical phenomena in fields ranging from hydrodynamics to solid state physics, such techniques have yet to be strongly established in the field of optics. However, in recent years some important results have been obtained and this has sparked a tremendous growth in the current interest of these techniques. For interest, some of the results obtained in the field of nonlinear optics are summarised below.

Radial Pattern Formation in a Laser Cavity

One of the first demonstrations of self-similarity techniques in optics was conducted in 1991 by Afanas'ev *et al.* [34]. In their calculations they investigated the self-action of counterpropagating axially symmetric light beams within the nonlinear medium of a laser cavity. They found that a number of self-similar solutions can exist in different experimental regimes which depend on the parameters of the input beam and the nonlinear medium. In particular, these solutions can describe the self-focusing or defocusing of the propagating beams under single or double focus conditions.

Phase Grating Formation in Optical Fibres

Motivated by the discovery of self-organised grating formation in optical fibres, An and Sipe investigated a model to describe the dynamics of grating formation by visible light [35]. Using this model they showed that the grating formation can be described by a single universal parameter (or a self-similarity variable) so that the parameters which describe the grating state evolve self-similarly subject to a variation in their scaling rates. Thus the growth of a grating will ultimately approach a fixed point and this corresponds to a perfectly phase matched stable grating.

Transient Stimulated Raman Scattering

Transient stimulated Raman scattering (TSRS) occurs in the limit where the pulse durations are short compared to the dipole deexcitation time T_2. In this limit the system can be said to have "memory" in the sense that the medium

will retain information long after the pulses have passed. Thus when investigating the solutions of such systems it is important to study the long distance behaviour. Indeed, it was this approach that lead to the discovery by Menyuk *et al.* that, after an initial period of transient behaviour, the soliton pulses normally associated with SRS [36] disappear and the solutions tend towards a self-similar solution [37]. Importantly, they found that the exact form of the self-similar solution toward which the system tends is determined entirely by the initial fields at early times.

Self-Similar Evolution of Self-Written Waveguides

Self-written waveguides can be written in a photosensitive material using the intensity dependent refractive index change induced by a propagating light beam. Significantly, whilst numerically investigating the self-writing of channel waveguides, in 1998 Monro *et al.* showed that as the waveguide evolved its shape appeared to remain approximately constant, but with a scaling of its depth and width [38]. As a result, this motivated them to use similarity techniques to search for the solutions for the self-similar mode shape and the corresponding refractive index profile. By studying the evolution of arbitrary input pulses they could confirm that the predicted self-similar solutions were indeed stable solutions to the self-writing process.

4.2.2 Mathematical Methods

Mathematically, self-similar solutions are found by the technique of "symmetry reduction." This involves reformulating the problem in terms of a certain combination of the original variables, called a similarity variable, so that the number of degrees of freedom of the system is reduced. This means that the original problem of solving partial differential equations can be recast into a problem of solving a reduced system of differential equations, which greatly simplifies the analytic treatment. Exactly how this reformulation is carried out varies from problem to problem.

In general, the similarity variables can be found using techniques based on Lie algebra theory [11]. This analysis is based on the fact that self-similar solutions

are invariant under some symmetry group of the system of partial differential equations. Consequently, finding the global invariants of the group equates to finding the similarity variable, and thus results in a reduction in the differential equations.

However, this type of formal approach is often unnecessary if the solution to a similar problem has already been found. In such cases it is often more convenient to construct the similarity variable based on the findings of the previous solution. Indeed, this was the case for the parabolic pulse solutions found by Kruglov *et al.* (to be described in Section 4.4), where the theoretical analysis was based on the combined results of high intensity wave-breaking-free propagation in normal dispersion fibres [9] with those obtained for radial pattern formation in a laser cavity [34]. It is important to note that in choosing this approach one must be wary of subtle differences in the two systems which can lead to an incorrect reformulation of the problem. Thus when constructing a similarity variable in this manner one must use a large amount of physical intuition and in particular, be very cautious of an incorrect choice of the governing parameters which will lead to inconsistencies in the solution. However, irrespective of the techniques used to obtain the scaling laws, the essential physical behaviour of all such self-similar systems is identical: the scaling laws map the evolution at one point exactly onto the evolution at another.

4.3 Parabolic Pulse Propagation in Normal Dispersion Fibres

The theoretical analysis describing parabolic pulse evolution in normal dispersion optical amplifiers was motivated by previous observations of self-similar behaviour of parabolic pulses in normal dispersion fibres by Anderson *et al.* [9] and Tamura and Nakazawa [39]. To establish the foundations for the analytical calculations, this section describes these precursory papers, and the significance of the results, in more detail.

4.3.1 Parabolic Pulse Propagation in the High Intensity Limit

As mentioned in Chapter 2, the interaction between dispersive and nonlinear effects acting on a high intensity pulse in a normal dispersion optical fibre can lead to severe pulse distortions due to the effect of optical wave breaking [Appendix B]. To this end, in 1993 Anderson *et al.* presented an investigation into the conditions under which wave breaking effects could be avoided [9]. Significantly, their results showed that the particular class of solution for which this was the case was in fact a linearly chirped parabolic pulse.

Their analysis was based on a simplified form of the NLSE given by Eq. (3.30) with $\beta_3 = g = \alpha = 0$, with the condition of normal dispersion $\beta_2 > 0$. By writing the field in terms of the real amplitude A and phase Φ: $\Psi(z,T) = A(z,T)\exp[\mathrm{i}\Phi(z,T)]$, the NLSE could then be expressed in terms of the coupled equations:

$$-\frac{\partial\Phi}{\partial z} = \frac{\beta_2}{2}\left[\frac{1}{A}\frac{\partial^2 A}{\partial T^2} - \left(\frac{\partial\Phi}{\partial T}\right)^2\right] - \gamma A^2, \tag{4.2}$$

$$\frac{\partial(A^2)}{\partial z} = \beta_2\frac{\partial}{\partial T}\left(A^2\frac{\partial\Phi}{\partial T}\right). \tag{4.3}$$

An important aspect of the analysis of Anderson *et al.* was the realisation that much physical insight into the evolution of a propagating pulse is obtained by recasting the above equations in terms of the chirp function, $\Omega_\mathrm{c} = -\partial\Phi/\partial T$ [Eq. (3.8)]. Making the appropriate substitutions in the above equations yields:

$$\frac{\partial\Omega_\mathrm{c}}{\partial z} = \frac{\partial}{\partial T}\left[\frac{\beta_2}{2}\left(\frac{1}{A}\frac{\partial^2 A}{\partial T^2} - \Omega_\mathrm{c}^2\right) - \gamma A^2\right], \tag{4.4}$$

$$\frac{\partial(A^2)}{\partial z} = -\beta_2\frac{\partial}{\partial T}\left(A^2\Omega_\mathrm{c}\right), \tag{4.5}$$

which clearly shows how the evolution of the chirp and the intensity of the propagating pulse are coupled together. A solution to these equations which avoids the effect of optical wave breaking is one which, even though it expands temporally, nonetheless preserves its shape as it propagates. This will be the case if the pulse possesses a linear chirp such that the rate of change of the time separation is the same for all parts of the pulse. Thus the pulse propagates self-similarly in z. With this condition for the chirp, the form of the intensity profile can then be determined via Eqs. (4.4)–(4.5).

From Eq. (4.4), the initial evolution of the chirp function can be approximated as:

$$\begin{aligned}\Omega_{\mathrm{c}}(z,T) &\approx \Omega_{\mathrm{c}}(0,T) \\ &+\frac{\partial}{\partial T}\left\{\frac{\beta_2}{2}\left[\frac{1}{A(0,T)}\frac{\partial^2 A(0,T)}{\partial T^2}-\Omega_{\mathrm{c}}^2(0,T)\right]-\gamma A^2(0,T)\right\}z.\end{aligned} \tag{4.6}$$

For an unchirped input pulse, $\Omega_{\mathrm{c}}(0,\tau)=0$, requiring that the chirp must develop to be linear in time yields:

$$\frac{\beta_2}{2}\frac{1}{A(0,T)}\frac{\partial^2 A(0,T)}{\partial T^2}-\gamma A^2(0,T)=C_0+C_1T^2, \tag{4.7}$$

where $A(0,T)$ is an even function of T, and C_0 and C_1 are constants. If the initial pulse satisfies Eq. (4.7), the chirp will remain linear and consequently the pulse will preserve its shape as it propagates.

In the limit of a high intensity pulse, the nonlinear effects will dominate over the dispersive effects so that the first term on the left hand side of Eq. (4.7) can be neglected. This directly yields the intensity profile as:

$$A^2(0,T)=A_0^2\left(1-\frac{T^2}{T_0^2}\right), \tag{4.8}$$

where the constants C_0 and C_1 are replaced by the more physically meaningful pulse parameters A_0 and T_0, being the peak amplitude and the zero crossing of the intensity profile at $z=0$. Thus the form of a pulse which will propagate self-similarly in a normal dispersion fibre, free from the effects of optical wave breaking, is a pulse with a parabolic intensity profile and a linear frequency chirp. Importantly, whilst it is true that any pulse that maintains a linear chirp will propagate self-similarly, such as the Gaussian pulse solutions to the linear equation [Eq. (3.31)], most profiles cannot sustain such a chirp in the presence of nonlinearity, and eventually undergo pulse distortion. The distinguishing feature of the high power parabolic pulse in this regard is the fact that both the induced phase due to GVD and SPM have a parabolic form (and the same sign) and thus the linear chirp is preserved [23].

4.3.2 Simulations of Parabolic Pulse Generation in a Fibre Amplifier

Despite the physical significance of the analysis by Anderson *et al.*, the results appeared to be of limited practical application due to the apparent impossibil-

ity of constructing a pulse with a parabolic intensity profile. However, in 1996 Tamura and Nakazawa published a paper where they pointed out the significance of the results in Ref. [9] for the evolution of optical pulses in high gain fibre amplifiers operating in the normal dispersion regime [39]. Using numerical simulations of the NLSE, Tamura and Nakazawa considered the evolution of an input fundamental soliton pulse in an amplifier with a constant longitudinal gain profile and $\beta_3 = \alpha = 0$ [Eq. (3.30)].

Their results showed that after about one dispersion length, the input pulse appeared to evolve into a parabolic pulse and furthermore, continued to propagate in the amplifier in a self-similar manner without any change in shape even though its intensity continued to be amplified. Although Tamura and Nakazawa did attempt to verify these results experimentally in an Er^{3+}:doped fibre amplifier, they were limited with their pulse diagnostic techniques (see Section 5.3.4). They did, however, show that the autocorrelation function of the output pulses was nontriangular, which indicated that the pulse was not undergoing the usual pulse shaping associated with normal dispersion fibre propagation and optical wave breaking. Although these results were not conclusive, they were a clear indication that the generation of pulses with parabolic intensity profiles, which possess a strictly linear chirp, may be possible in a normal dispersion optical amplifier. This was enough to motivate further study into the formation and propagation of parabolic pulses which will be discussed in the following section.

4.4 Parabolic Pulse Solutions in an Amplifier

This section describes the theoretical calculations used to analyse the parabolic pulse solutions of the NLSE with gain and normal dispersion. These calculations form a series of investigations conducted within the Applied Optics Group of The University of Auckland [12, 13, 40].[1] In this analysis two regimes of propagation were considered: (i) in an amplifier with a constant gain profile in the asymptotic limit $z \to \infty$ and (ii) in an amplifier with an arbitrary gain profile in the high intensity limit $z > z_0$. Despite the slight differences in the analysis, in both cases the form of the solution is the same yielding a linearly

[1] This work was conducted during the course of my Masters degree in Physics.

chirped pulse with a parabolic intensity profile.

4.4.1 Asymptotic Solutions for an Amplifier with a Constant Gain Profile

The theoretical analysis for the asymptotic parabolic pulse solutions was based on the evolution of pulses in an amplifier with spectral bandwidths less than the amplifier bandwidth and a constant longitudinal gain profile. Ignoring fibre loss and higher order dispersion terms ($\alpha = \beta_3 = 0$), the equation governing the propagation of pulses in this system is of the form [Eq. (3.30)]:

$$\mathrm{i}\frac{\partial}{\partial z}\Psi = \frac{\beta_2}{2}\frac{\partial^2}{\partial T^2}\Psi - \gamma\left|\Psi\right|^2\Psi + \mathrm{i}\frac{g}{2}\Psi. \tag{4.9}$$

Based on the previous work of Anderson *et al.*, the search for solutions to this system also began by substituting the expanded field [$\Psi = A\exp\left(\mathrm{i}\Phi\right)$] into Eq. (4.9). This now yields the following coupled equations in A and Φ:

$$\frac{\partial A}{\partial z} = \beta_2\frac{\partial A}{\partial T}\frac{\partial \Phi}{\partial T} + \frac{\beta_2}{2}A\frac{\partial^2\Phi}{\partial T^2} + \frac{g}{2}A, \tag{4.10}$$

$$\left[\frac{\beta_2}{2}\left(\frac{\partial\Phi}{\partial T}\right)^2 - \frac{\partial\Phi}{\partial z}\right]A = \frac{\beta_2}{2}\frac{\partial^2 A}{\partial T^2} - \gamma A^3. \tag{4.11}$$

As mentioned in Section 4.2.2, the solutions to this system were found via techniques based on symmetry reduction where the similarity variables were constructed based on the previous findings of Refs. [9, 34]. In particular, with the requirement of normal dispersion ($\beta_2 > 0$), motivated by the results obtained for Eqs. (4.2) and (4.3), linearly chirped solutions having the form:

$$A(z,T) = f(z)F(z,T) = f(z)F(\vartheta), \tag{4.12}$$

$$\Phi(z,T) = \varphi(z) + C(z)T^2, \tag{4.13}$$

were sought where the self-similarity variable ϑ is given by:

$$\vartheta = f^2(z)\exp(-gz)T. \tag{4.14}$$

Here, the explicit form of the amplitude was constructed so that for the particular form of ϑ, it satisfied the energy conservation integral of Eq. (4.9):

$$U\left(z\right) = U_0\exp\left(gz\right), \tag{4.15}$$

where $U(z) = \int_{-\infty}^{\infty} |\Psi(z,T)|^2 \, \mathrm{d}T$ and $U_0 = U(0)$.

With the form of the solutions as given by Eqs. (4.12)–(4.14), it was found that in the limit $z \to \infty$ there exists an exact asymptotic solution such that [12]:

$$\Psi(z,T) = A_0(z) \sqrt{1 - \left[\frac{T}{T_0(z)}\right]^2} \exp\left[\mathrm{i}\Phi(z,T)\right], \qquad |T| \leq T_0(z), \tag{4.16}$$

with $\Psi(z,T) = 0$ for $|T| > T_0(z)$, and where:

$$\Phi(z,T) = \Phi_0 + \frac{3\gamma A_0^2(z)}{2g} - \frac{gT^2}{6\beta_2}, \qquad |T| \leq T_0(z). \tag{4.17}$$

The scaling of the peak amplitude $A_0(z)$ and the effective width $T_0(z)$ are related to the system parameters as:

$$A_0(z) = \frac{1}{2}\left(\frac{gU_0}{\sqrt{\gamma\beta_2/2}}\right)^{1/3} \exp\left(\frac{gz}{3}\right), \tag{4.18}$$

$$T_0(z) = \frac{6\sqrt{\gamma\beta_2/2}}{g} A_0(z). \tag{4.19}$$

The interpretation of the various terms of this solution is facilitated by referring to Fig. 4.1. Since, experimentally, it is common to examine pulse shapes on a logarithmic scale to distinguish low amplitude features in the wings, the

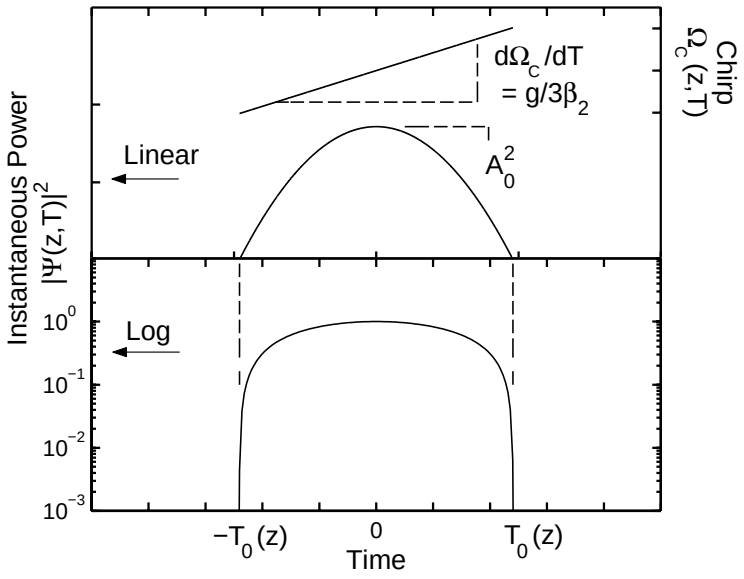

Figure 4.1: Generic figure of the asymptotic parabolic pulse solution. Top: intensity profile (left axis) and chirp (right axis). Bottom: normalised intensity on a logarithmic scale.

figure includes both linear and logarithmic intensity plots. In particular, the logarithmic plot highlights an interesting feature of a parabolic pulse which is the steepness of the slope on the edges of the intensity profile.

This parabolic pulse represents a solution to Eq. (4.9) which maintains its linear chirp so that it propagates self-similarly (retaining its parabolic shape) subject to the exponential scaling of its peak amplitude $A_0(z)$ and effective width parameter $T_0(z)$. Significantly, the solutions show that it is only the energy of the initial pulse, and not its specific shape, that determines the amplitude and width of the asymptotic parabolic pulse. It is worth noting that these results provided theoretical confirmation of Tamura and Nakazawa's observation that a linearly chirped parabolic pulse arises naturally as a consequence of the propagation of a pulse in a normal dispersion amplifier, as discussed in Section 4.3.2.

To demonstrate these results, propagation in an amplifier with: $\beta_2 = 25 \times 10^{-3}\,\mathrm{ps^2 m^{-1}}$, $\gamma = 5.8 \times 10^{-3}\,\mathrm{W^{-1} m^{-1}}$, $g = 1.9\,\mathrm{m^{-1}}$ and a length $L = 6\,\mathrm{m}$ is simulated.[2] Fig. 4.2 shows the evolution of a $12\,\mathrm{pJ}$, $200\,\mathrm{fs}$ full width half maximum (FWHM) Gaussian input pulse in this amplifier. This figure illustrates the expected increase in the peak intensity and the pulse width, as well as the parabolic form of the pulse in the latter stages of the amplifier. The parabolic nature of the output pulse is then confirmed in Fig. 4.3(a) where the

[2]The parameters were chosen based on realistic parameters for an Yb^{3+}:doped fibre amplifier [12].

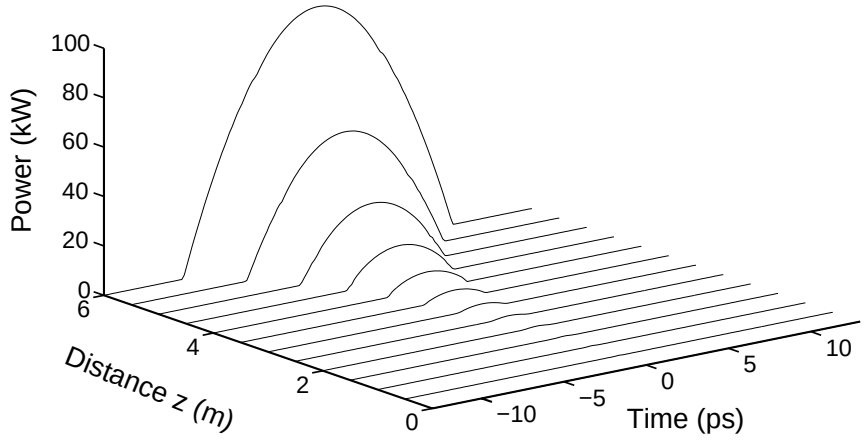

Figure 4.2: Evolution of a parabolic pulse in an optical fibre amplifier.

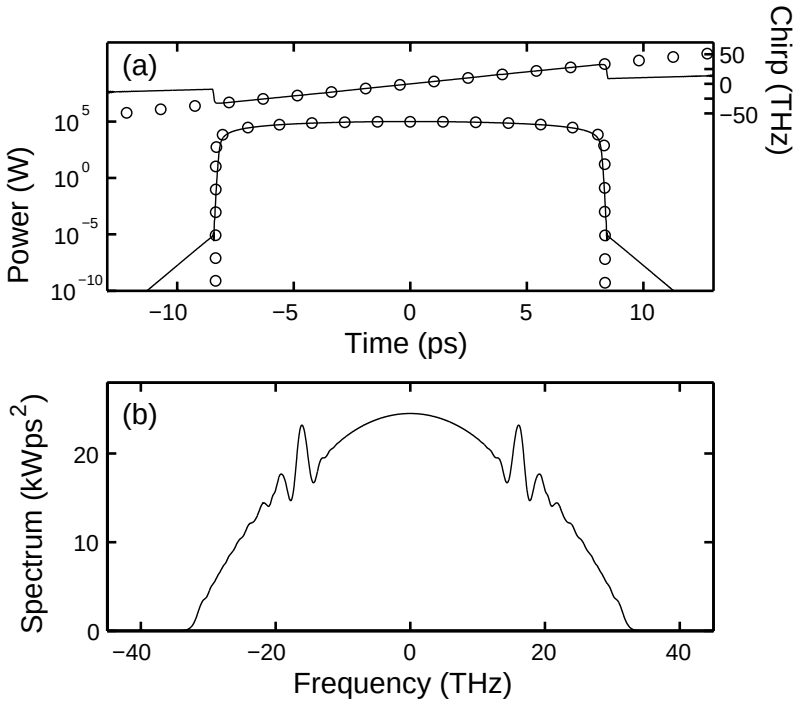

Figure 4.3: (a) Intensity profile (left axis - logarithmic scale) and chirp (right axis - linear scale) of the output pulse from Fig. 4.2, together with the theoretical predictions (circles). (b) Corresponding spectrum.

simulated pulse (solid lines) is compared with the theoretical predictions of Eqs. (4.16)–(4.19) (circles). Although at $|T| = T_0(z)$ the solution of Eq. (4.16) has an infinite slope, this is only the case in the asymptotic limit. At intermediate propagation distances both simulations and analytic analysis predict the appearance of low amplitude wings which decay exponentially as a function of T and indeed such wings can be seen on the simulation results in Fig. 4.3(a) at power levels less than $10^{-5}\,\mathrm{W}$ [40].

The corresponding spectrum is plotted below in Fig. 4.3(b). It can be noted that the oscillations present on the edges of the spectrum are not manifestations of optical wave breaking as they are not accompanied by the presence of oscillations on the edge of the temporal profile [Appendix B]. They are, in fact, due to slight fluctuations in the quadratic phase which results in small oscillations on the linear chirp [40]. Such phase modulations are not unexpected because of the strong nonlinear pulse shaping as the pulse evolves from the initial pulse profile to the asymptotic parabolic pulse solution. Thus these oscillations are a characteristic feature of the transition of a pulse to the parabolic regime.

Finally, to demonstrate the asymptotic nature of the parabolic pulse solutions it is useful to consider the evolution of Gaussian input pulses with a fixed input energy $U_0 = 12\,\mathrm{pJ}$, but with a range of pulse durations from $100\,\mathrm{fs} - 5\,\mathrm{ps}$ (FWHM). The amplifier parameters are the same as those used in Figs. 4.2 and 4.3. As a means of comparing the evolution of these different input pulses, Fig. 4.4 shows the (a) peak amplitude and (b) effective width parameter, as functions of the propagation distance in the amplifier, obtained from the simulation results together with the analytic predictions (see legend). It is clear from these results that for an amplifier of fixed gain, the rate at which a pulse evolves to the parabolic pulse solution depends strongly on the choice of the input pulse width. This is to be expected as, for a fixed energy, a broader temporal width implies a lower peak power. It is therefore expected that the initial nonlinear evolution will be substantially different for the various input pulses. Indeed, it can be noticed that the pulse with the largest input pulse width (and hence the lowest peak power) is the slowest pulse to converge to the parabolic pulse solution. Nevertheless, it is clear that in all cases the evolution of the pulse in the amplifier does indeed approach the asymptotic limit.

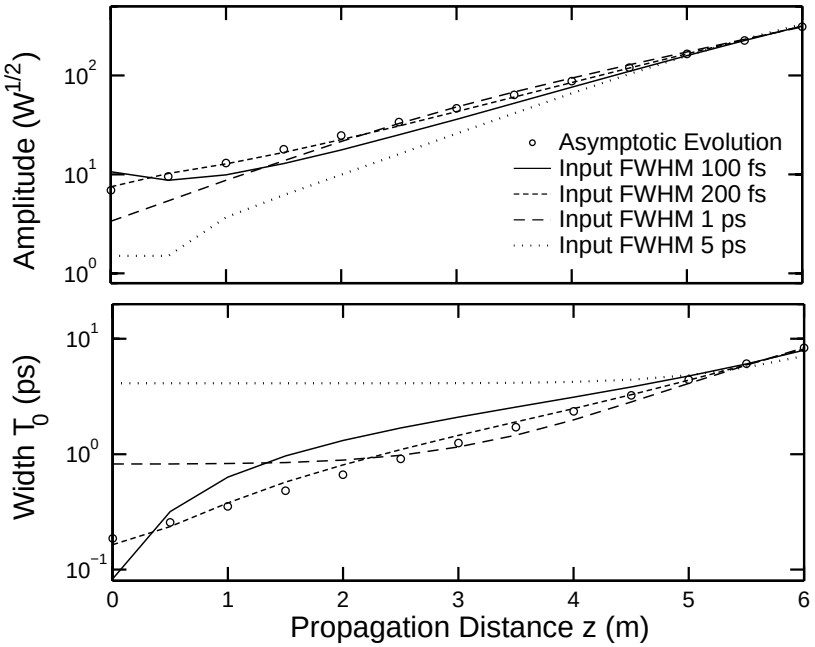

Figure 4.4: Simulation results showing the evolution of the peak pulse amplitude (top) and the effective temporal width (bottom), as functions of the propagation distance, for Gaussian pulses of duration $100\,\mathrm{fs} - 5\,\mathrm{ps}$. The results are compared with the asymptotic predictions (see legend).

4.4.2 Solutions for an Amplifier with an Arbitrary Gain Profile

For an amplifier with an arbitrary longitudinal gain profile $g(z)$ the theoretical analysis was based on the generalised form of Eq. (4.9):

$$\mathrm{i}\frac{\partial}{\partial z}\Psi = \frac{\beta_2}{2}\frac{\partial^2}{\partial T^2}\Psi - \gamma\left|\Psi\right|^2\Psi + \mathrm{i}\frac{g(z)}{2}\Psi. \tag{4.20}$$

Again, with the field expanded in terms of the amplitude A and phase Φ, self-similar solutions of the form given by Eqs. (4.12) and (4.13) were sought. However, unlike the previous analysis for a constant gain profile, this time the investigations were based on a search for exact self-similar solutions in the regime $z > z_0$. Here z_0 defines the start of the parabolic regime and this corresponds to the pulse entering a high intensity regime where the nonlinear effects dominate over the dispersive. From dimensional analysis and the group symmetry properties of Eq. (4.20), the explicit form of the self-similarity variable ϑ was found to be [13]:

$$\vartheta = \frac{U(z_0)}{U(z)}f^2(z)\,T, \tag{4.21}$$

where the evolution of the energy is now

$$U(z) = U(z_0)\exp\left[\int_{z_0}^{z} g(z')\,\mathrm{d}z'\right]. \tag{4.22}$$

Significantly, the form of the solutions for an arbitrary gain profile were found to be identical to that previously obtained for a constant gain [Eq. (4.16)]:

$$\Psi(z,T) = A_0(z)\sqrt{1-\left[\frac{T}{T_0(z)}\right]^2}\exp\left[\mathrm{i}\Phi(z,T)\right], \qquad |T| \le T_0(z), \tag{4.23}$$

and $\Psi(z,T) = 0$ for $|T| > T_0(z)$, but with a quadratic phase now given by:

$$\Phi(z) = \Phi_0 + \frac{3\gamma}{4}\int_{z_0}^{z}\frac{U(z')}{T_0(z')}\mathrm{d}z' - \frac{1}{2\beta_2}\frac{\mathrm{d}}{\mathrm{d}z}\ln\left[T_0(z)\right]T^2, \qquad |T| \le T_0(z). \tag{4.24}$$

The scaling of the amplitude $A_0(z)$ and width $T_0(z)$ can then be determined via the relations:

$$A_0(z) = \left(\frac{3U(z)}{4T_0(z)}\right)^{1/2}, \tag{4.25}$$

$$\frac{\mathrm{d}^2T_0(z)}{\mathrm{d}z^2} = \left(\frac{3}{2}\right)\frac{\beta_2\gamma U(z)}{T_0^2(z)}, \tag{4.26}$$

where Eq. (4.26) is subject to the boundary condition:

$$\left.\frac{\mathrm{d}T_0(z)}{\mathrm{d}z}\right|_{z_0} = T_0(z_0)\left.\frac{\mathrm{d}}{\mathrm{d}z}\ln\left[T_0(z)\right]\right|_{z_0}. \tag{4.27}$$

Thus the solution for the case of a longitudinal distributed gain profile is still a parabolic pulse with a linear chirp but now the scaling of its amplitude and width are determined by the form of the gain profile $g(z)$. Importantly, this solution holds for any function $g(z)$ and in particular g can be zero, which corresponds to an undoped normal dispersion fibre (see Section 4.3.1), or negative (i.e., a fibre with loss) so long as the pulse intensity is high.

To illustrate the significance of the shape of the longitudinal gain on the self-similar solutions of Eqs. (4.23)–(4.27), the top curves of Fig. 4.5 show the evolution of identical Gaussian input pulses in amplifiers with three different gain profiles corresponding to: (a) pumping counterdirectionally so that the gain increases along the amplifier, (b) pumping bidirectionally with constant gain along the amplifier, and (c) pumping codirectionally with decreasing gain along the amplifier. Explicitly, the respective gain profiles are: (a) $g(z) = g_a \exp(z/z_a)$ with $g_a = 0.687\,\mathrm{m}^{-1}$ and $z_a = 3\,\mathrm{m}$, (b) $g(z) = g_a$ with $g_a = 1.44\,\mathrm{m}^{-1}$, and (c) $g(z) = g_a \exp(-z/z_a)$ with $g_a = 2.606\,\mathrm{m}^{-1}$ and $z_a = 3\,\mathrm{m}$. Here the initial gain coefficients g_a were chosen such that in all cases the total integrated gain was $25\,\mathrm{dB}$ and the remaining amplifier parameters were: $\beta_2 = 35 \times 10^{-3}\,\mathrm{ps}^2\mathrm{m}^{-1}$, $\gamma = 6 \times 10^{-3}\,\mathrm{W}^{-1}\mathrm{m}^{-1}$ and $L = 4\,\mathrm{m}$ [13]. Although, as expected, the scaling of the pulses in the amplifiers differ quite considerably, nevertheless comparison of the output pulses (solid lines - middle curves) with the theoretical predictions (circles) confirms their parabolic nature. In addition, it can also be noticed that the corresponding output spectra (bottom curves) differ in shape and width indicating that the choice of pumping geometry will play an important role in situations where the bandwidth of the amplifier is significant. The differences in the spectral widths can be understood by noting that for the case where the gain increases (decreases) along the length of the amplifier, the incident pulse is amplified slowly (rapidly) to high power and subsequently experiences the largest amount of SPM in the final (initial) stages of its evolution so that it develops the smallest (broadest) spectral width [41].

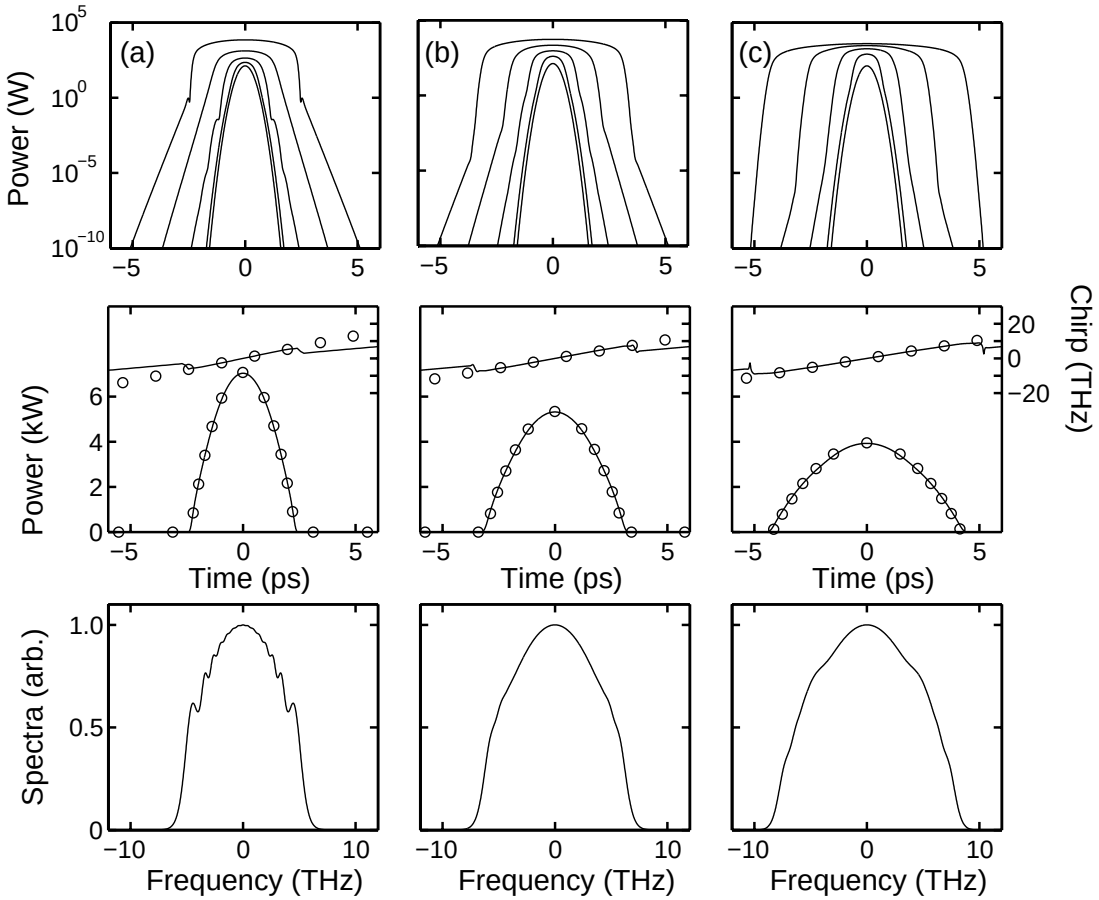

Figure 4.5: Top: parabolic evolution for (a) increasing gain, (b) constant gain and (c) decreasing gain. Middle: intensity (left axis) and chirp (right axis) of the amplifier outputs obtained from simulation results (solid curves), compared with the theoretical predictions (circles). Bottom: the corresponding spectra.

4.5 Experimental Confirmation

As part of the confirmation of the analytic parabolic pulse solutions presented in Section 4.4, preliminary experimental verification of the results was also provided in Ref. [12].[3] These experiments were conducted by Dr M. Fermann and Dr B. Thomsen at IMRA America in collaboration with the Applied Optics Group in Auckland, and a schematic diagram of their experimental setup is shown in Fig. 4.6. In their experiments they considered the amplification of $12\,\mathrm{pJ}$, $200\,\mathrm{fs}$ (FWHM) Gaussian input pulses generated in a fibre based pulse source, at a wavelength of $1.06\,\mu\mathrm{m}$ [42]. These pulses were then injected into a $3.6\,\mathrm{m}$ long high gain Yb^{3+}:doped fibre with dispersion and nonlinearity coeffi-

[3]For a more complete description of the experiments and a comparison with the theory, the interested reader is referred to Ref. [41].

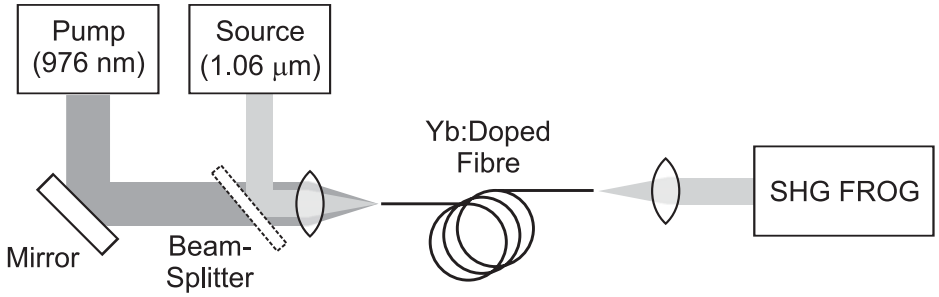

Figure 4.6: Schematic diagram of the experimental setup for parabolic pulse generation in an Yb^{3+}:doped fibre amplifier.

cients of $\beta_2 = 25\times10^{-3}\,\mathrm{ps^2m^{-1}}$ and $\gamma = 5.8\times10^{-3}\,\mathrm{W^{-1}m^{-1}}$, which could provide a maximum gain of $30\,\mathrm{dB}$. The complete characterisation of the output pulses was carried out using a second harmonic generation (SHG) frequency-resolved optical gating (FROG) technique, which will be discussed in Section 5.3.4.

The output pulse profile and chirp obtained from the FROG retrieval algorithm are plotted in Fig. 4.7(a) together with the analytic predictions of Eqs. (4.16)–(4.19) (dashed lines) and the results of numerical simulations (circles). Despite the weak oscillations in the wings, which were attributed to resonant effects, clearly in all cases the intensity and chirp are in good agreement. Further confirmation of this agreement is also provided by the similarities in the shapes of the corresponding spectra seen in Fig. 4.7(b).

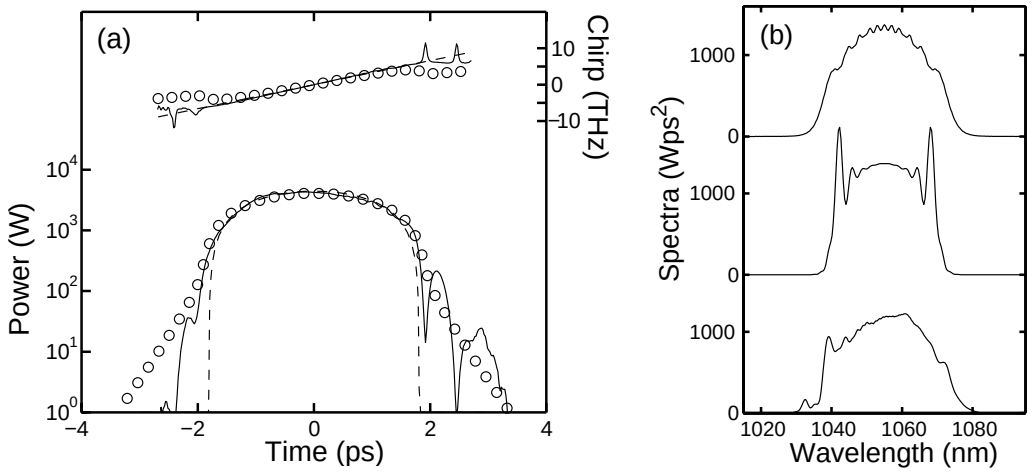

Figure 4.7: (a) Measured intensity (logarithmic scale - solid lines) and chirp (linear scale - solid lines), compared with simulation results (circles) and the theoretical predictions (dashes). (b) Pulse spectra from experiment (bottom), simulations (middle) and theory (top). Experimental data obtained from Ref. [12].

In addition to these measurements, they also considered launching the amplified pulses shown in Fig. 4.7 into a $2\,\mathrm{m}$ long undoped fibre (SMF) with normal dispersion. From the FROG traces of the output from the fibre they were able to show that the pulses had maintained their parabolic form indicating that they were indeed propagating self-similarly as predicted by the analysis of Anderson *et al.* [Section 4.3.1].

Chapter 5

Parabolic Pulse Generation in a Fibre Amplifier Chain

5.1 Introduction

In the previous chapter, the parabolic pulse solutions that exist for the nonlinear Schrödinger equation (NLSE) with gain were presented which showed that they evolved naturally via amplification in a fibre amplifier. This chapter describes experiments to investigate the generation of high energy parabolic pulses in a fibre amplifier chain where each of the amplifiers have different dispersion and nonlinear properties. The experimental results are complemented by a numerical anaylsis to establish the limitations and assist with the optimisation of the system.

5.2 Description of the Project

The research described in this chapter evolved out of an industrially funded project to develop a practical, high power short pulse Yb^{3+}:doped fibre based laser and amplifier system. The Yb^{3+}:doped fibre source was developed by Dr L. Lefort and Dr J. Price in the form of a passively mode-locked fibre based oscillator. This produced pulses with widths of $\sim 2.5\,\mathrm{ps}$ (FWHM) and energies of $\sim 60\,\mathrm{pJ}$. The aim of the amplifier system was to then boost these energies to

produce $\sim 10\,\mu$J output pulses which could be efficiently compressed down to ~ 200 fs. However, as the build up of amplified spontaneous emission (ASE) limits the gain from a single fibre amplifier to around $30-40$ dB [43], this would not be sufficient for the pulses to reach the microjoule level. Thus it was necessary to employ a cascaded system consisting of a series of three Yb^{3+}:doped amplifiers.

Because of the high peak powers generated within the amplifiers it soon became apparent that it would be beneficial to exploit the self-similar nature of parabolic pulses in order to avoid deleterious nonlinear distortions. The significant feature of using a cascaded system is that each amplifier in the chain has different dispersion and nonlinear coefficients as well as different gain characteristics. As the development of a parabolic pulse relies strongly on the interplay between the gain, dispersion and nonlinear properties of the amplifier this poses the question of whether parabolic pulses are sufficiently robust to form in an amplifier chain. In addition, as the pulses undergo coupling losses between each amplification stage this introduces an additional problem in that, as discussed in Section 4.4, the final parabolic pulse is dependent on the input pulse energy and thus these discrete jumps in the pulse energy will affect the evolution.

The experimental component of this project described in the following sections was carried out primarily by Dr J. Price and Dr A. Malinowski. My role in this work was to simulate the system and analyse the results in order to establish the limitations and aid with the optimisation of the system.

5.3 Experimental Setup

As discussed, the experiments were based on the amplification of picosecond pulses in a cascaded Yb^{3+}:doped fibre amplifier system. A schematic diagram of the experimental set up is presented in Fig. 5.1. Owing to the complexity of the system the individual components will be described separately in the following sections.

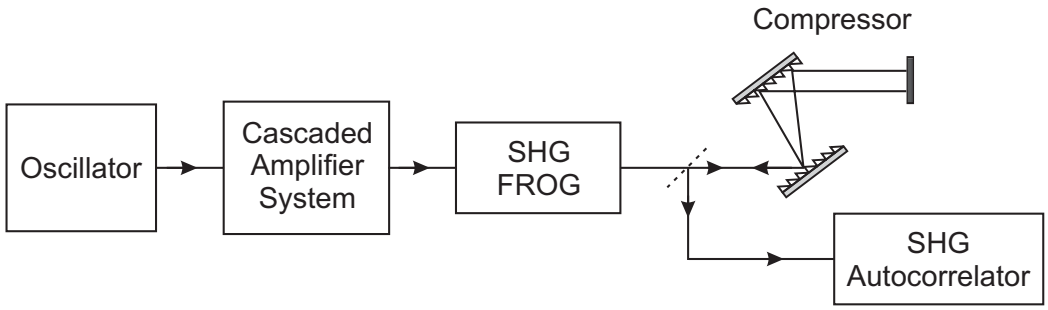

Figure 5.1: Schematic diagram of the experimental setup.

5.3.1 Pulse Source

The input pulse source was developed within the ORC and a detailed technical description can be found in Ref. [44]. A schematic of the source is illustrated in Fig. 5.2. The laser is based on a simple Fabry-Perot cavity design with a grating based dispersive delay line, and is pumped by a fibre coupled diode operating at $976\,\mu\mathrm{m}$ to produce gain at $1.055\,\mu\mathrm{m}$. The mode-locking operation is based on the stretched-pulse principle using nonlinear polarisation evolution as a fast saturable absorber [45]. Reliable self-start mode-locking is facilitated by incorporating a semiconductor saturable absorber mirror (SESAM). Two polarisers and associated waveplates are also included to control the bias of the polarisation switch and adjust the output coupling. The polarisation switch is the polarisation beam splitter PBS1, where the rejected part of the pulse appears at Port 1. The half-waveplate between PBS1 and PBS2 controls the output coupling strength of the ports so that pulses can either be extracted from Port 2 with a negative chirp or Port 3 with a positive chirp. In our experiments we chose to use the positively chirped output pulses from Port 3 which had a duration of $2.5\,\mathrm{ps}$ (FWHM) and a maximum energy of $60\,\mathrm{pJ}$.

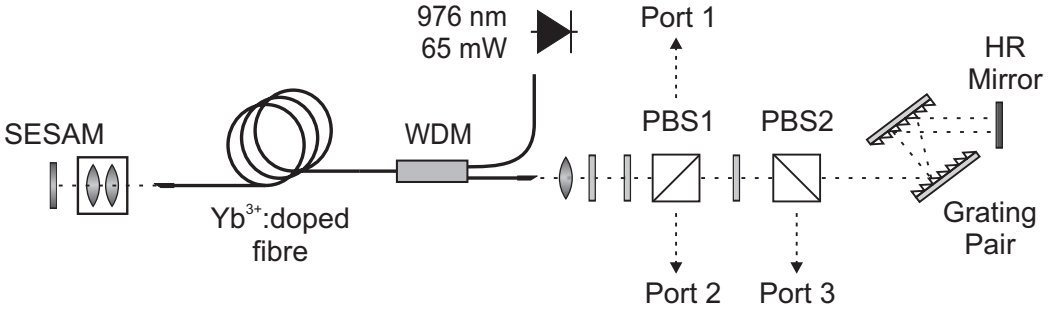

Figure 5.2: Experimental configuration of the picosecond pulse source at $1.055\,\mu\mathrm{m}$. PBS=polarising beam splitter and HR=highly reflecting.

5.3.2 Cascaded Amplifier System

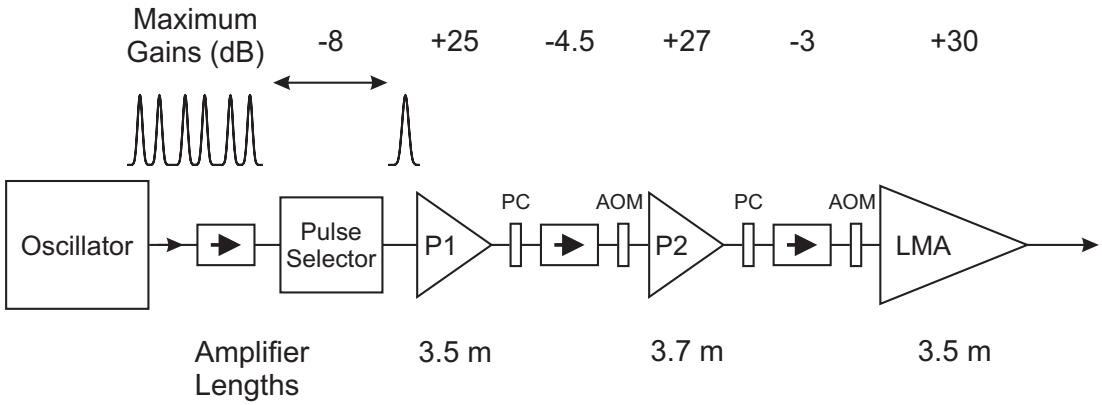

Figure 5.3: Experimental configuration of the cascaded amplifier system to generate parabolic pulses.

As mentioned above, the seed pulses were generated via a Yb^{3+}:based fibre oscillator which produced $\sim 60\,\mathrm{pJ}$, $2.5\,\mathrm{ps}$ (FWHM) positively chirped output pulses. These pulses were then launched into the three stage cascaded amplifier system. To prevent the build up of ASE in the system an isolator and an accousto-optic modulator (AOM) pair were placed between each amplifier stage. Polarisation controllers (PC) were also used to ensure optimum transmission through the isolators.

The first two preamplifiers, P1 and P2, were standard single mode Yb^{3+}:doped fibres with parameters similar to those used in previous studies of parabolic pulse amplification [12, 13]. These were pumped codirectionally to reduce the noise level. The final amplifier, however, was a large mode area (LMA) quasi-single mode amplifier with a core diameter of $30\,\mu\mathrm{m}$.[1] This was designed specifically to reduce the nonlinear effects in the final amplification stage, but otherwise the remaining parameters are the same as those of the preamplifiers. In contrast to the preamplifiers, this was pumped counterdirectionally so as to restrict the growth of the spectral width [Section 4.4.2].

To estimate the effective bandwidths of the amplifiers, the widths of the output pulse spectra were measured after propagation at low powers, where the nonlinear effects are negligible. As the gain bandwidth of Yb is typically of the order $\sim 40\,\mathrm{nm}$ [22], the small bandwidths of the preamplifiers that were

[1] This amplifier was doped such that the gain of the fundamental mode was enhanced relative to the higher order modes.

measured were likely to have been influenced by the polarising isolators used in the free space coupling processes. For reference, the parameters describing each of the three amplifiers are given explicitly in Table 5.1.

	β_2 $(\mathrm{ps}^2\mathrm{m}^{-1})$	β_3 $(\mathrm{ps}^3\mathrm{m}^{-1})$	γ $(\mathrm{W}^{-1}\mathrm{m}^{-1})$	$\Delta\lambda$ (nm)
P1	30×10^{-3}	2.5×10^{-5}	6.9×10^{-3}	10
P2	30×10^{-3}	2.5×10^{-5}	6.9×10^{-3}	15
LMA	30×10^{-3}	2.5×10^{-5}	2×10^{-4}	40

Table 5.1: Fibre parameters for the amplifiers in Fig. 5.3.

5.3.3 Linear Pulse Compressor

To obtain the required femtosecond durations, it is necessary to compress the output pulses from the LMA amplifier and, to this end, a simple linear compression device was employed. In such a system, if the pulse initially possesses a chirp (which is approximately linear) that has the opposite sign to that imposed by the GVD of the compressor then the two tend to cancel each other, resulting in an output pulse that is temporally narrower than the input pulse. Here we employed a simple grating pair compressor which is the most commonly used device to provide anomalous GVD to optical pulses with a positive linear chirp.

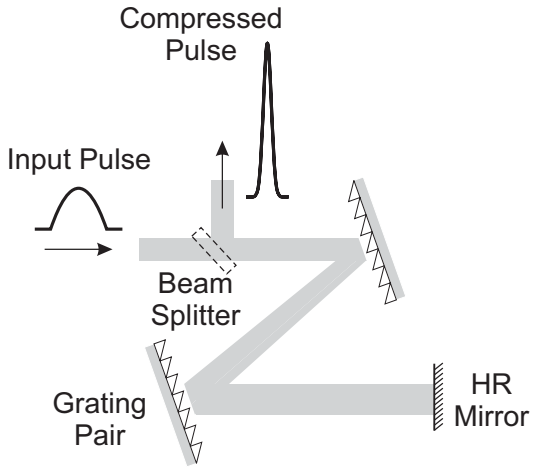

Figure 5.4: Schematic drawing of a linear grating pair compressor in the double-pass configuration.

Fig. 5.4 shows a schematic drawing of the grating pair setup used in our system. A double pass configuration is employed so that the pulse is recollimated into its original cross section. In this system the pulse is incident on one grating of the pair of two parallel gratings. As each frequency component associated with the pulse is diffracted at a slightly different angle, the different components travel slightly different path lengths through the grating pair. As a result, they experience different time delays so that the blue shifted components arrive earlier than the red shifted components. Consequently, for a positively chirped pulse, the trailing edge catches up with the leading edge so that the pulse is compressed during the passage through the grating pair. The optimum compression of the chirp (i.e., the point where the anomalous dispersion of the grating exactly cancels the positive chirp of the pulse) can be obtained simply through careful choice of the grating separation.

5.3.4 Characterisation Techniques

The output pulses from the LMA amplifier were characterised in the temporal domain via the technique of frequency-resolved optical gating (FROG). However, as the compressed pulses should have a flat phase, these were simply characterised using a standard autocorrelation method. As the comparison of our experimental data with an analytic parabolic pulse relies heavily on the accurate characterisation of the measured pulses, the following provides a brief description of both the FROG and autocorrelation techniques.

Frequency-Resolved Optical Gating

Although several varieties of FROG exist, the results in this chapter were obtained via second harmonic generation (SHG) FROG [46]. In SHG FROG, a Michelson-type interferometer is used to split the pulse to be measured into two identical replicas which are then combined in a $\chi^{(2)}$ nonlinear medium. The envelope of the signal field has the form:

$$E_{\text{sig}}(t,\tau) = E(t)\,E(t-\tau)\,, \tag{5.1}$$

where τ is the time delay between the two beams and the carrier frequency of the field is neglected as it simply represents an arbitrary phase shift. The signal

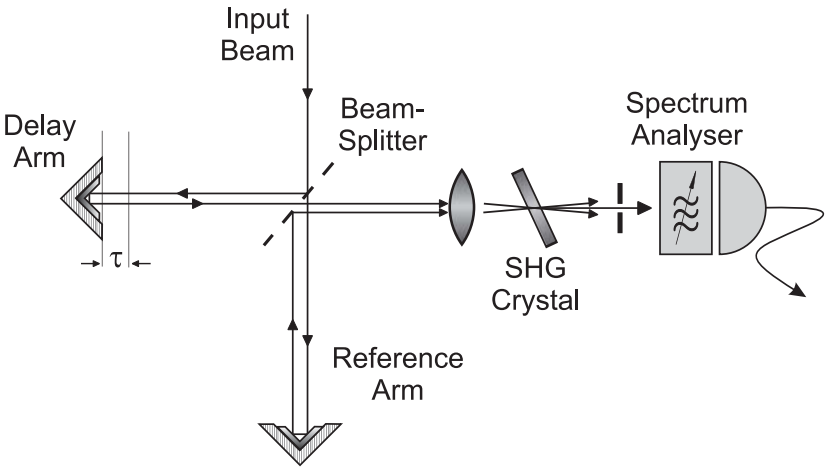

Figure 5.5: Experimental setup for SHG FROG.

field of Eq. (5.1) is incident on a spectrometer where it is spectrally resolved as a function of delay to yield the FROG trace:

$$I_{\text{FROG}}(\omega,\tau) = \left|E_{\text{sig}}(\omega,\tau)\right|^2 = \left|\int_{-\infty}^{\infty} \mathrm{d}t E_{\text{sig}}(t,\tau)\exp(\mathrm{i}\omega t)\right|^2, \tag{5.2}$$

which is a positive real-valued function of the variables ω and τ. The experimental setup for SHG FROG is shown in Fig. 5.5.

Although the measurement of such a FROG trace is a relatively simple exercise experimentally, solving the inverse problem to determine the complex electric field of the incident pulse requires rather sophisticated numerical methods based on two dimensional phase retrieval. In our case, this was carried out using an iterative "generalised projections" retrieval algorithm whose task is to estimate the discrete complex field $E_{\text{R}}(t)$ (where the subscript R denotes the retrieved field) which generates the best approximation $|E^{\text{R}}_{\text{sig}}(\omega,\tau)|^2$ to $I_{\text{FROG}}(\omega,\tau)$ in a least squares sense [15].

It is important to note that both $E(t)$ and its time reversed conjugate $E^*(-t)$ produce identical SHG FROG traces, which causes a time-phase reversal ambiguity. This ambiguity can be removed either by additional propagation experiments in media of known dispersion or by *a priori* knowledge of the characteristics of the pulse to be measured. This latter condition was the case for our experiments where we anticipate that the output pulses from the amplifier will always possess a large positive chirp.

Autocorrelation Measurements

The most widely used autocorrelation technique is again based on the phenomenon of SHG [14]. A sketch of the SHG autocorrelation setup is shown in Fig. 5.6. As in the case of a SHG FROG, a Michelson-type interferometer is used to split the pulse to be measured into two identical replicas where one of the pulses can be advanced (or delayed) by τ seconds relative to the other. The two pulses are then recombined in a nonlinear crystal to produce a second harmonic pulse which is incident on a "slow" detector.

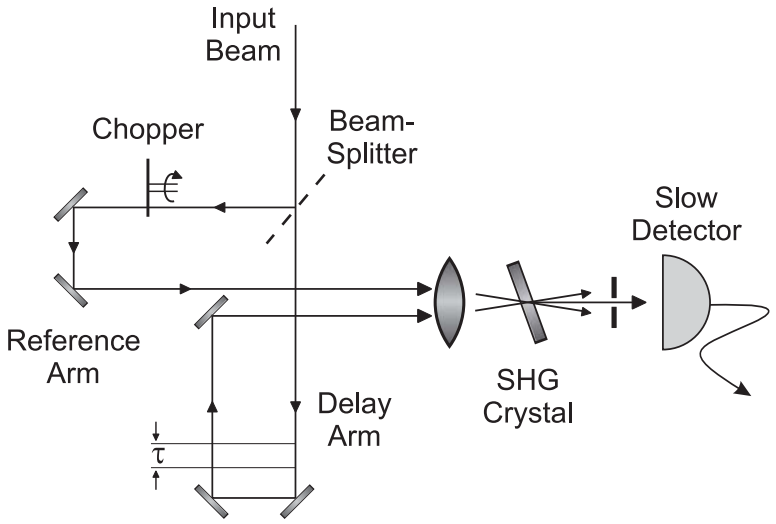

Figure 5.6: Experimental setup for SHG autocorrelation measurements.

The second harmonic field radiated from the nonlinear crystal is proportional to the square of the complex amplitude of the incident fundamental field:

$$E_{2\omega}(t) \propto E_{\omega}^{2}(t) + E_{\omega}^{2}(t-\tau)\mathrm{e}^{-2\mathrm{i}\omega\tau} + 2E_{\omega}(t)E_{\omega}(t-\tau)\mathrm{e}^{-\mathrm{i}\omega\tau}. \tag{5.3}$$

The current produced by the detector is then proportional to the incident intensity so that:

$$\begin{aligned} i_d(t) &\propto E_{2\omega}(t)E_{2\omega}^{*}(t) \\ &= \left[E_{\omega}(t)E_{\omega}^{*}(t)\right]^2 + \left[E_{\omega}(t-\tau)E_{\omega}^{*}(t-\tau)\right]^2 \\ &+ 4E_{\omega}(t)E_{\omega}^{*}(t)E_{\omega}(t-\tau)E_{\omega}^{*}(t-\tau) + s(\tau), \end{aligned} \tag{5.4}$$

where $s(\tau)$ is composed of oscillating terms that can be averaged out over integration in the delay τ. Since the temporal (t) variation of the first three terms

is on the scale of picoseconds (or less), the much slower optical detector integrates the current with the result that the actual output is a function of the delay only. Thus the normalised detector output is simply:

$$i_d(\tau) = 1 + 2\frac{\langle I(t)I(t-\tau)\rangle}{\langle I^2(t)\rangle}. \tag{5.5}$$

A plot of $i_d(\tau)$ versus τ will produce a symmetric normalised pulse with a central width of τ_0. The determination of the true pulse width ΔT_0 (FWHM) from the width of the autocorrelation trace is somewhat ambiguous. However, from integration of Eq. (5.5) the ratio $\Delta T_0/\tau_0$ can be calculated and for a Gaussian pulse: $\Delta T_0/\tau_0 = \sqrt{2}$, whilst for a hyperbolic secant pulse: $\Delta T_0/\tau_0 = 1.55$.

5.4 Results and Analysis

In our investigations we focused on two different regimes where: (a) the gain in P2 and the LMA amplifier were similar and (b) the gain in P2 is considerably less than that in the LMA amplifier. The total pulse gain in each amplifier and the final output pulse energies are given in Table 5.2. Clearly, both the output pulse energies are only of the order of hundred's of nanojoules, which is considerably less than the required $\sim 10\,\mu$J. However, as we will discuss below, despite investigating various pumping configurations, in all cases we found the output energies were restricted to this regime.

	P1 (dB)	P2 (dB)	LMA (dB)	Energy (nJ)
(a)	22.6	12.5	14.8	177
(b)	22.6	4.3	25.8	334

Table 5.2: Total pulse gains at each amplifier stage and the output pulse energies for situations where: (a) the gain in P2 is similar to that in the LMA amplifier and (b) the gain in P2 is much less than the LMA amplifier.

The temporal (top) and spectral (bottom) characteristics of the measured output pulses, obtained from the retrieved FROG trace, are plotted in Fig. 5.7. A comparison between the defining parameters of the temporal pulses and those predicted for a parabolic pulse, calculated from Eqs. (4.24)-(4.27), is given in Table 5.3. We note that in our calculations we only considered parabolic pulse

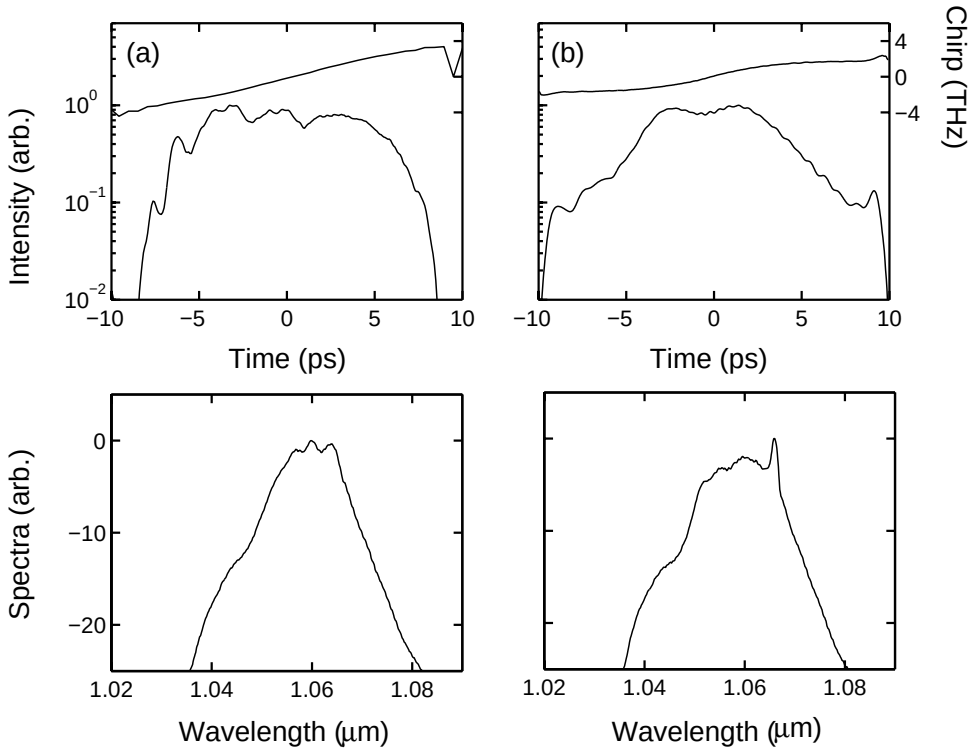

Figure 5.7: Top: intensity (left axis - logarithmic scale) and chirp (right axis - linear scale) of the LMA fibre output obtained from FROG data. Bottom: the corresponding spectra.

evolution in the LMA amplifier. Furthermore, as we approximate the peak gain by an exponentially increasing profile, the parabolic predictions can only serve as an indication of any parabolic evolution. Although the agreement between the widths and the peak powers is reasonable, from the chirps we see that neither of these pulses is strictly parabolic. The slow convergence to the parabolic regime can be partially attributed to the large input pulse widths because, as discussed in Section 4.4.1, although the final parabolic pulse only depends on the input pulse energy, the rate of convergence does depend on the initial pulse parameters. Nevertheless, in both cases the pulses exhibit a

	Input		Measured			Parabolic		
	U_0 (nJ)	T_0 (ps)	T_0 (ps)	P_0 (kW)	Ω_c (THz)	T_0 (ps)	P_0 (kW)	Ω_c (THz)
(a)	5.9	5.2	~ 7	~ 25	~ 0.60	7.4	18	0.82
(b)	0.88	4.4	~ 6	~ 55	~ 0.54	6.5	40	1.3

Table 5.3: Comparison between the measured pulse parameters and those predicted for a parabolic pulse.

linear chirp over the central region.

Although Table 5.3 indicates that neither pulse is particularly more parabolic than the other, on examination of the spectra we see that whilst the spectrum for case (a) is fairly featureless, the spectrum for case (b) is in fact showing signs of the oscillations typically seen on the spectral edges of a parabolic pulse (see Fig. 4.3). Thus this suggests that pulse (b) has advanced further into the parabolic regime. However, this seems in contradiction with the comparison between the chirp slopes where the measured chirp of pulse (a) is in better agreement with the parabolic predictions. A possible explanation for this is that in case (b) the pulse is actually evolving from the parabolic regime and entering an amplifier soliton regime. As discussed in Section 3.8.2, the formation of amplifier solitons can occur in an amplifier due to the effects of a finite gain bandwidth. Significantly, it has also been shown that in normal dispersion amplifiers stable solitary wave propagation is often associated with an initial period of propagation where the pulse exhibits parabolic characteristics [8]. Indeed, by comparing the output pulse from case (b) with a typical amplifier soliton in Fig. 5.8, obvious similarities can be seen in both the intensity profile and the chirp. Importantly, this would explain the observation that despite our attempts to increase the output pulse energy, these are typically restricted to the order of hundreds of nanojoules.

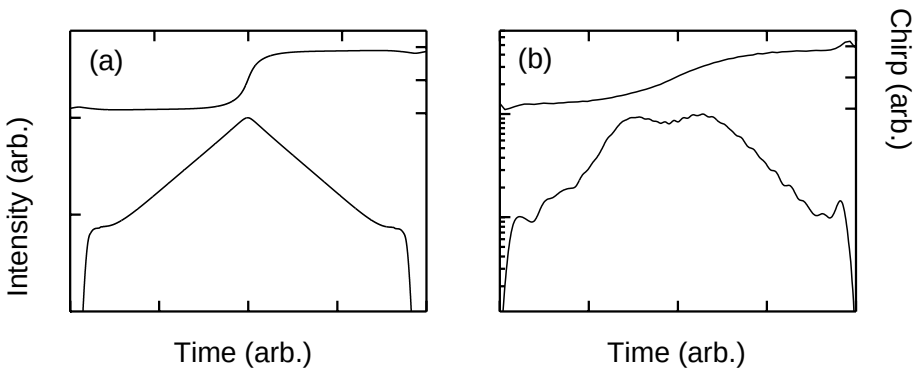

Figure 5.8: Comparison between (a) a typical amplifier soliton and (b) the output pulse of Fig. 5.7(b), plotted on logarithmic scales.

The autocorrelations of the compressed pulses are plotted in Fig. 5.9. These both have autocorrelation FWHM widths of $\sim 450\,\mathrm{fs}$ indicating compressed pulse widths of $\sim 300\,\mathrm{fs}$ (assuming a Gaussian profile). Although the widths of the central peaks are similar, the pedestals are greatly reduced for pulse (b)

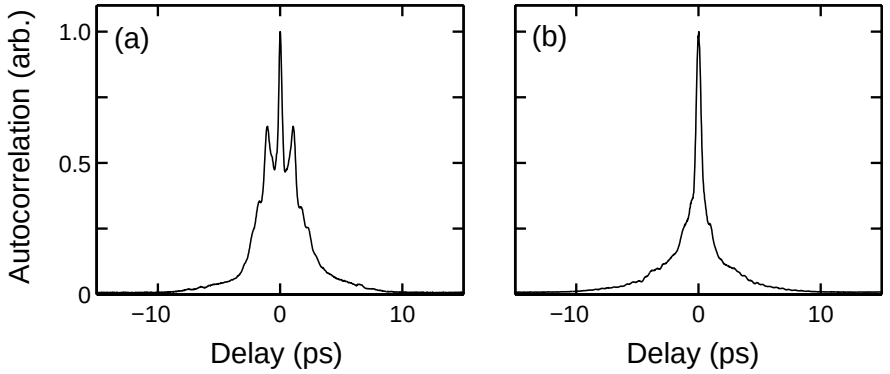

Figure 5.9: Measured autocorrelation traces corresponding to the compression of the pulses in Fig. 5.7.

[$\sim 70\,\%$ of the pulse energy in the central peak as opposed to $\sim 35\,\%$ for pulse (a)]. Again this indicates that pulse (b) has, at some stage in its propagation, evolved further into the parabolic regime.

Although the output pulse energies for the two cases differ quite considerably, we have found that for case (a) increasing the gains simply acts to further distort the output pulse. A possible explanation for this can be understood by noting that P2 has a large nonlinear coefficient (compared to the LMA amplifier) and is pumped codirectionally so that the pulse sees most of the gain in the initial amplification stages. Thus by placing a large gain in P2, there is a rapid initial growth of the spectrum so that it quickly approaches the width of the gain bandwidth (see Fig. 4.5) leading to bandwidth limiting effects [8]. However, in case (b), due to the low gain in P2, the pulse enters the LMA amplifier with a relatively low peak power and this combined with the small nonlinearity coefficient in this amplifier means that most of the amplification occurs within the gain bandwidth. Thus these results suggest that in order to understand how we might reach the desired pulse energies of $\sim 10\,\mu$J, a detailed investigation of the evolution of the pulses in each stage of the amplifier system is required.

5.5 Numerical Investigations of Modified Systems

The results presented in Section 5.4 suggest that the main limitation to our setup is the small gain bandwidths of the preamplifiers. Thus we expect that

to reach the microjoule regime we will need to find a way to increase these and / or redistribute the gain in the amplifiers. To illustrate this we simulate a system based on that described in Fig. 5.3, but using slightly larger gain bandwidths in the preamplifiers and distributing the gain so that there is more gain in the amplifiers which have larger bandwidths. Specifically we consider a system with amplifier bandwidths of $15\,\mathrm{nm}$, $20\,\mathrm{nm}$ and $40\,\mathrm{nm}$ and gains of $6\,\mathrm{dB}$, $20\,\mathrm{dB}$ and $40\,\mathrm{dB}$ for P1, P2 and the LMA amplifier, respectively. The remaining amplifier parameters were unchanged. Propagation in the amplifiers was modelled on Eq. (3.51) from Section 3.10.1, but with the modification of a z dependent peak gain to approximate the different pumping geometries (as discussed in Section 4.4).

The output pulse and spectrum are plotted in Fig. 5.10. This pulse has an energy of $10\,\mu\mathrm{J}$ so that it satisfies the output energy requirements of the experimental project. Furthermore, the appearance of linear wings on the intensity profile and the oscillations on the edges of the spectrum, suggest that the pulse is in the early stages of evolution towards the parabolic regime (see Fig. 4.3). Thus these results indicate that despite the increased gains, there has not been a substantial increase of the bandwidth limiting effects.

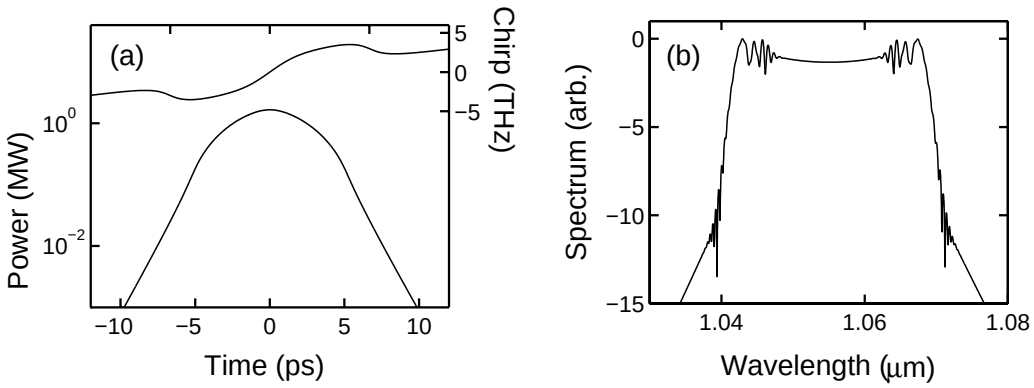

Figure 5.10: (a) Intensity (left axis - logarithmic scale) and chirp (right axis - linear scale) obtained from numerical simulations of a modified system based on Fig. 5.3. (b) The corresponding spectrum.

The corresponding calculated autocorrelation of the compressed pulse is shown in Fig. 5.11. Clearly, not only does this pulse show a significant reduction in the pedestals over those of the experimental pulses (see Fig. 5.9), but it also has a true compressed width of $\sim 200\,\mathrm{fs}$ (FWHM) which also satisfies the project requirements. We can expect these results to be further improved with addi-

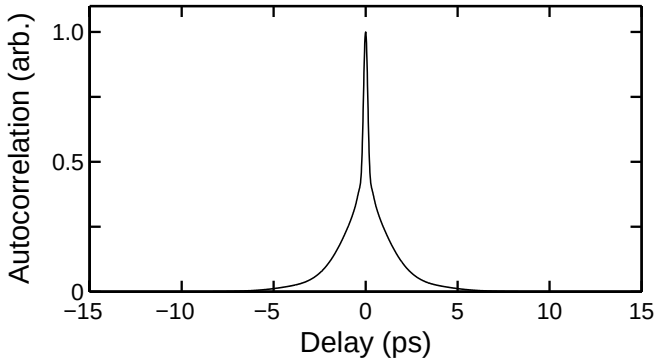

Figure 5.11: Calculated autocorrelation corresponding to the compression of the simulated pulse of Fig. 5.10.

tional increments of the preamplifier bandwidths.

In addition, we have also performed numerous simulations in attempt to establish modifications to the system which could improve our results. As an example, Fig. 5.12 shows the effect on the energy and the compressed output pulse width as functions of the core size of the LMA amplifier and the pream-

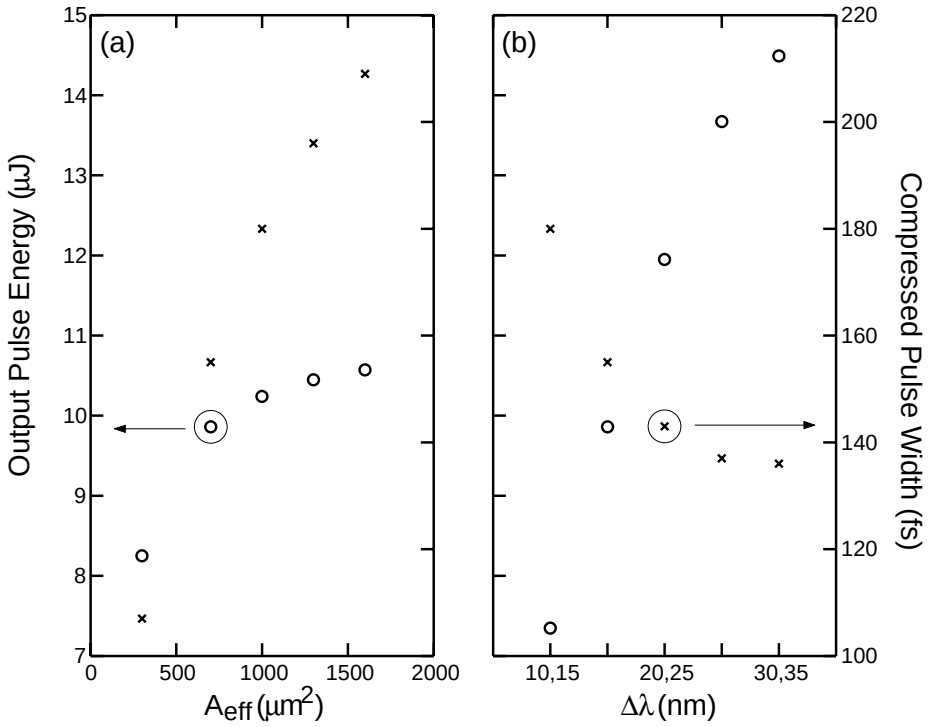

Figure 5.12: Output pulse energy (left axis - circles) and compressed pulse width (right axis - crosses) as functions of (a) the effective area of the LMA and (b) the bandwidths of the preamplifiers where the x labels are the bandwidths of P1 and P2, respectively.

plifier bandwidths.[2] From the left hand curves we see that increasing A_{eff} increases both the output pulse energy and the compressed pulse width. This is because the smaller effective nonlinearities reduce the spectral broadening so that the spectrum is better contained within the gain bandwidth. Consequently, for a fixed gain, the rates of increase saturate as the spectrum becomes narrower. In contrast, not only does increasing the preamplifier bandwidths increase the output pulse energy, but because it allows for enhanced spectral broadening it also reduces the compressed pulse width (right hand curves). As expected, this effect is ultimately limited by the bandwidth of the LMA amplifier.

5.5.1 Two Amplifier System

Further aspects to this work have included experimental and numerical investigations into the performance of the system with only one preamplifier. Although this reduces the total gain available in the system, it removes one of the coupling losses so that not much should be lost in terms of achievable pulse energy. Fig. 5.13(a) shows temporal (top) and spectral (bottom) profiles of simulation results for a system identical to case (b) from Section 5.4 [see Fig. 5.7(b)], but with P2 removed. We note that the decision to remove P2 over P1 was motivated by the fact that this eliminated one of the free space coupling sections. Although this pulse appears significantly less distorted than the pulse in Fig. 5.7(b), the output pulse energy is only $53\,\text{nJ}$ so that this can simply be attributed to a reduction in the total gain. Repeating this simulation, but with the gains increased to $30\,\text{dB}$ in P1 and $40\,\text{dB}$ in the LMA amplifier, an output pulse energy of $3.1\,\mu\text{J}$ was achieved and the corresponding output pulse can be seen in Fig. 5.13(b). However, on comparison with Fig. 5.7(b) it is clear that this pulse has suffered similar bandwidth limiting distortions. Thus these results have simply emphasised the problems discussed above. As a result, the system was returned to the original configuration with both preamplifiers.

[2]The remaining amplifier parameters are the same as those used in Fig. 5.10.

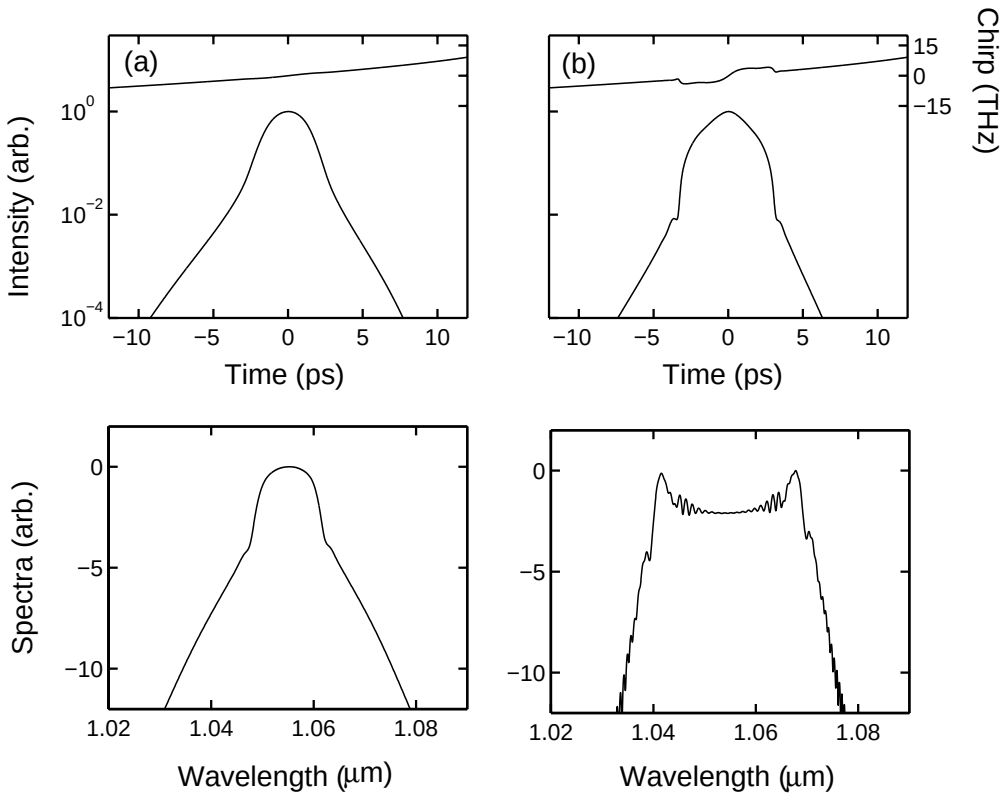

Figure 5.13: Top: output pulses (left axis - logarithmic scale) and chirps (right axis - linear scale) of pulses simulated in a two amplifier system where the gains are (a) 22.6 dB, 25.8 dB and (b) 30 dB, 40 dB, for P1 and the LMA amplifier, respectively. Bottom: the corresponding pulse spectra.

5.6 Future Directions

In response to these findings, work is currently being conducted within the ORC by members of Prof. D. Richardson's fibre fabrication group to design new preamplifiers with larger effective bandwidths but whilst maintaining the large effective nonlinearities. As previously mentioned, because it is likely that the polarising isolators used in the free space coupling are contributing to the observed small effective bandwidths, design of the new preamplifiers must include improving their ability to maintain the polarisation of the amplified field as well as flattening their gain profiles.

Chapter 6

Parabolic Evolution in Microstructured Fibre Raman Amplifiers

6.1 Introduction

The previous two chapters have discussed parabolic pulse generation in doped fibre amplifiers. This chapter now moves to consider parabolic pulse generation using an undoped microstructured fibre Raman amplifier. After a description of the Raman amplifier system, numerical simulations to demonstrate parabolic pulse generation in a highly nonlinear, normally dispersive microstructured fibre will be presented. The preliminary experimental results indicate that parabolic pulse generation in these fibres is indeed possible via Raman amplification.

6.2 Raman Amplifier System

To date, the theoretical studies of parabolic pulse generation have considered the evolution of pulses in a rare-earth doped fibre amplifier so that the propagation is described by the nonlinear Schrödinger equation (NLSE) with a gain term [Section 4.4]. As a result, all related numerical and experimental investi-

gations have also been based on their formation in such amplifiers. The results have shown that the most efficient parabolic pulse generation occurs when the nonlinear propagation dominates over the dispersive propagation and that this requires a gain medium with a large gain bandwidth to support the growing spectral width of the pulse. Indeed, as it was shown in Chapter 5, for efficient parabolic pulse formation to occur the spectral width of the pulse must remain within the gain bandwidth of the amplifier.

This chapter now considers a new approach to parabolic pulse generation using amplification in an undoped fibre based on the Raman effect. Such an amplifier would enable the exploitation of the broad Raman amplification band where bandwidths of more than $100\,\mathrm{nm}$ have been demonstrated [47]. In addition, as the Raman effect is not confined to any particular wavelength, this technology can be used to provide gain at wavelengths where no conventional amplifiers are possible and more importantly, can form the basis of a tunable high power pulse source. Such pulse sources will find wide spread applications in all optical processes such as wavelength division multiplexing (WDM) [48], terahertz optical asymmetric demultiplexing (TOAD) [49], and optical logic [50].

Commercial Raman amplifiers based on standard fibre are available and are typically pumped via continuous wave (CW) sources operating at several Watt power levels. It has been shown by Finot *et al.* that in such a regime propagation lengths of the order of kilometers are required for the pulse to become parabolic due to the small gain [51]. To over come this problem, the following investigations consider using a high power pulsed pump source and, to further enhance the nonlinear effects, a microstructured fibre with a large effective nonlinearity [52]. Importantly, unlike high nonlinearity fibres with a large n_2 [see Eq. (3.25)] which can have a reduced Raman gain bandwidth [53], the bandwidth of the single material microstructured fibres considered in this chapter is simply that of pure silica. In addition, the dispersive properties of a microstructured fibre can be tailored such that they have normal dispersion, necessary for parabolic pulse propagation, over a wide range of wavelengths extending up to and beyond the optical communications window of $1.5\,\mu\mathrm{m} - 1.6\,\mu\mathrm{m}$.

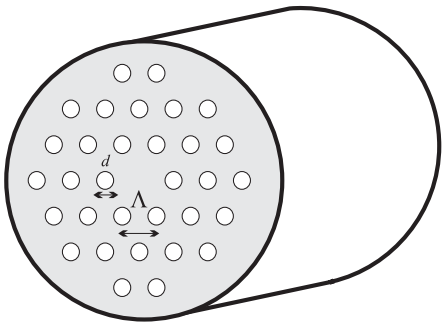

Figure 6.1: Microstructured fibre cross section with the air holes arranged in a hexagonal lattice in the cladding region.

6.2.1 Microstructured Fibres

The microstructured fibres considered in this chapter consist of a central fused silica core surrounded by a regular array of air holes which extend down the length of the fibre. A sketch of an idealised microstructured fibre, where the air holes are arranged in an hexagonal lattice, is given in Fig. 6.1. The design parameters of a microstructured fibre are specified by the hole diameter (d) and the hole-to-hole spacing (Λ) which are typically on the scale of the wavelength of light. With careful choice of the number, size and orientation of the air holes the confinement and dispersion characteristics of the fibre can be tailored to obtain nonlinear and dispersion parameters not available in conventional fibre structures.

For a typical microstructured fibre, as illustrated in Fig. 6.1, the average index of the core region is greater than that of the surrounding cladding so that, similar to a conventional fibre, light is guided by a modified form of total internal reflection [Section 3.2]. However, in a microstructured fibre the combination of the large air / glass index difference and the small structural dimensions make the effective cladding index a strong function of wavelength. This wavelength dependence can be explained by noting that at longer wavelengths the modes extend further into the air holes thus reducing the effective index of the cladding and increasing the core-cladding index contrast.

The fabrication process used to construct the microstructured fibres discussed in this chapter is illustrated in a schematic diagram in Fig. 6.2. First, an array of capillaries is stacked in a hexagonal configuration around a solid rod, which defines the core. The resulting stack (preform) is then drawn down to the

appropriate fibre dimensions using a conventional fibre drawing tower [54]. The parameters d and Λ are controlled via the choice of the wall thickness and the tube diameter of the capillaries, and the conditions (such as the speed) under which the fibre is drawn. The microstructured fibre used in Section 6.4 was fabricated by Dr K. Furusawa.

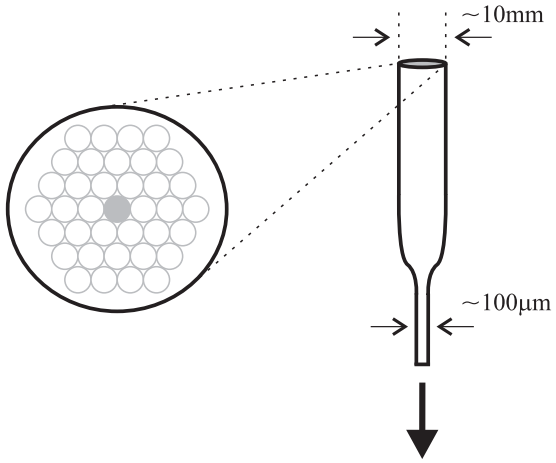

Figure 6.2: Schematic diagram for the procedure used for microstructured fibre fabrication.

To establish the modal properties of a microstructured fibres a full-vector orthogonal function model is employed, as described in Ref. [55]. In this approach, the modal fields and refractive index profile are decomposed into plane wave components so that the wave equation can be reduced to an eigenvalue equation. Solutions to this equation yield the mode profiles and their corresponding propagation constants. The modelling of the microstructured fibres discussed in Section 6.3 was conducted by Dr T. Monro.

6.3 Simulating the Raman Amplifier System

This section describes the numerical model used to analyse the Raman amplifier system and presents a detailed discussion of the results. It will be shown that parabolic pulse formation is possible in a range of microstructured fibres with normal dispersion. The dependence of the parabolic pulse solution on the parameters of the microstructured fibre is also discussed.

6.3.1 Numerical Model and Fibre Parameters

Given the modal properties of a microstructured fibre, pulse propagation can be described by the standard NLSE. Including the effects of Raman amplification, the evolution can be described by the propagation equation given in Section 3.10.2:

$$\begin{aligned} \mathrm{i}\frac{\partial}{\partial z}\Psi &= \frac{\beta_2}{2}\frac{\partial^2}{\partial T^2}\Psi + \mathrm{i}\frac{\beta_3}{6}\frac{\partial^3}{\partial T^3}\Psi - \mathrm{i}\frac{\alpha}{2}\Psi \\ &- \gamma\left(1+\frac{\mathrm{i}}{\omega_0}\frac{\partial}{\partial T}\right)\Psi\int_0^\infty R\left(T'\right)\left|\Psi\left(z,T-T'\right)\right|^2\mathrm{d}T', \end{aligned} \tag{6.1}$$

where, as discussed in Chapter 3, β_2 is the group velocity dispersion parameter, β_3 is the third order dispersion, α is the loss, γ is the effective nonlinearity of the microstructured fibre and ω_0 is the carrier frequency. Here the field Ψ, in comoving coordinates of the pump beam, is expressed in terms of the amplitude A_j and the phase Φ_j ($j = p, s$) of the pump and the signal beams as:

$$\Psi\left(z,T\right) = A_p\left(z,T\right)\exp\left[\mathrm{i}\Phi_p\left(z,T\right)\right] + A_s\left(z,T\right)\exp\left[\mathrm{i}\Phi_s\left(z,T\right)\right], \tag{6.2}$$

where the signal field is downshifted in frequency by $13.2\,\mathrm{THz}$ from the pump beam, corresponding to the peak of the Raman gain spectrum [Fig. 3.10].

The simulations consider a range of small core pure silica microstructured fibre designs with the aim of determining whether they are suitable hosts for parabolic pulse generation. Values for the effective mode area A_{eff} and the propagation constant β are shown in Fig. 6.3 for the three microstructured fibres used in the simulations. The transverse refractive index profile for a fibre with $d/\Lambda = 0.8$ is shown in the inset of Fig. 6.3(b). Specifically, fibres with Λ in the range $0.9\,\mu\mathrm{m} - 1.2\,\mu\mathrm{m}$ and ratios d/Λ of $0.8 - 0.85$ are considered, where the numerical predictions indicate normal dispersion at wavelengths in the range $1.5\,\mu\mathrm{m} - 1.7\,\mu\mathrm{m}$. As small (sub-$\lambda$) values of Λ lead to small core sizes and large values of d/Λ give a large NA [Eq. (3.4)], the combined effects result in tight modal confinement thus offering large effective nonlinearities. It should be recalled that the propagation constant β is related to the group velocity dispersion (GVD) and the third order dispersion parameters via Eq. (3.16) and that A_{eff} is related to γ via Eq. (3.27). For reference, the nonlinear and dispersion parameters of the three fibres in Fig. 6.3 are given explicitly in Table 6.1. Such fibres are similar to that used previously as a Raman amplifier [52].

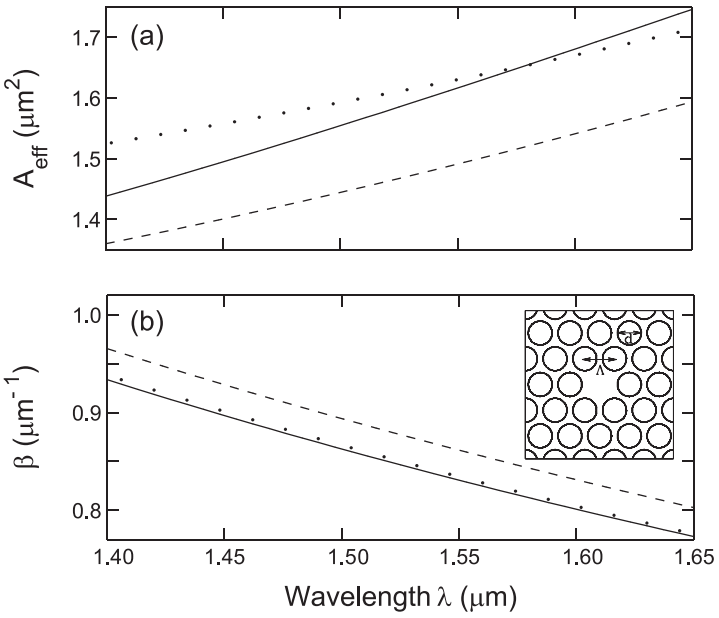

Figure 6.3: (a) Effective areas A_{eff} and (b) propagation constants β, as functions of wavelength, for fibre A (solid curves), fibre B (dashed curves) and fibre C (dotted curves). Inset: refractive index profile of a fibre with $d/\Lambda = 0.8$.

	Λ (μm)	d/Λ	β_2 (ps^2m^{-1})	β_3 (ps^3m^{-1})	γ ($\text{W}^{-1}\text{m}^{-1}$)
Fibre A	0.9	0.8	0.4980	-0.0013	0.0517
Fibre B	1.2	0.8	0.0929	-0.0010	0.0524
Fibre C	1.0	0.85	0.3412	-0.0018	0.0564

Table 6.1: Dispersion and nonlinearity parameters for the fibres corresponding to the profiles in Fig. 6.3, calculated at $\lambda = 1.647\,\mu\text{m}$.

6.3.2 Parabolic Pulse Generation

The numerical simulations are based on a Raman interaction pumped with a $20\,\text{W}$, $\sim 1\,\text{ns}$ (FWHM) $m = 20$ super-Gaussian (square) pulse at $1.536\,\mu\text{m}$, typical of the output from a diode pumped high power Er^{3+}:doped fibre amplifier chain (see Section 6.4.1). The Gaussian signal pulses of $5\,\text{W}$, $1\,\text{ps}$ duration (FWHM) are injected at $1.647\,\mu\text{m}$ into the three fibres with lengths of $16\,\text{m}$ so that the total pulse gains are of the order of $\sim 30\,\text{dB}$. The output signal pulses (top curves) and spectra (bottom curves) resulting from amplification in the three fibres are plotted in Fig. 6.4, corresponding to total pulse gains of: (A) $\sim 29\,\text{dB}$, (B) $\sim 25\,\text{dB}$ and (C) $\sim 29\,\text{dB}$. These results illustrate the significance of the fibre parameters on the total pulse gain and the final pulse shape. Despite these differences, it is clear that in all cases the pulse displays the char-

acteristic features of a pulse entering the parabolic regime including both the low intensity exponentially decaying wings and the oscillations on the edges of the spectrum (see Fig. 4.3 in Section 4.4).

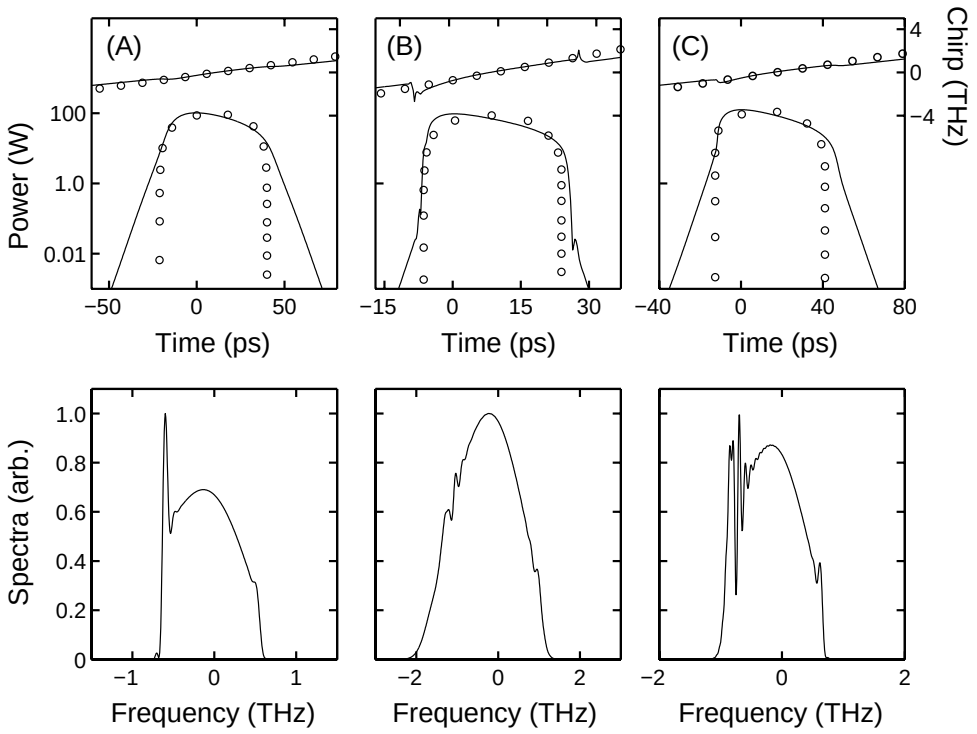

Figure 6.4: Top: intensity (left axis - logarithmic scale) and chirp (right axis - linear scale) of the fibre outputs obtained from simulated propagation in fibres A, B and C (solid lines) together with the corresponding parabolic and linear fits (circles). Bottom: the output spectra.

In order to illustrate the extent to which each of the pulses has developed into the parabolic regime, the top curves of Fig. 6.4 also include parabolic and linear fits (obtained via a minimisation scheme based on the Nelder-Mead Simplex method [56]) to the intensity profile and the chirp, respectively (circles). These fits indicate that the pulse which has evolved to be the most parabolic is that corresponding to fibre B. This is to be expected as this fibre has the smallest GVD parameter relative to the fibre nonlinearity so that the nonlinear effects are more pronounced. However, it is also apparent that in all cases the pulse has developed asymmetrically. Although some of the asymmetry in the output pulse can be attributed to the third order dispersion [4], and the shape of the gain spectrum [Fig. 3.10], it is in fact primarily due to pump depletion where the leading edge of the pulse experiences more gain than the trailing edge.

This effect is significant because the signal intensity eventually exceeds that of the pump intensity [4] and, due to the large gains necessary to amplify a pulse to the parabolic regime, it is a difficult problem to avoid. Indeed, the peak powers of the output pulses are: (A) $102\,\mathrm{W}$, (B) $96\,\mathrm{W}$ and (C) $125\,\mathrm{W}$, so that they are all much greater than the initial pump power of $20\,\mathrm{W}$. Furthermore, on comparing the output pulse profiles in Fig. 6.4, it is clear that the relative sizes of the peak powers are in agreement with the size of the induced asymmetry in the pulses, with the pulse generated in fibre C displaying the largest asymmetry. In this context, it is worth noting that given the high peak powers reached by the signal pulse it could be possible for it to pump a second Raman pulse, downshifted from itself by $13.2\,\mathrm{THz}$, out of the amplifier noise, thus creating a cascaded Raman effect. However, observations indicate that over the relatively short propagation lengths considered in the simulations, the gain that the signal provides to the noise is not sufficient for a second Raman pulse to form or, more importantly, to degrade the quality of the generated parabolic pulse.

6.3.3 The Effects of Third Order Dispersion

An important consequence of the effects of the pump depletion is that the formation of a parabolic pulse is highly dependent on the sign of the third order dispersion. Indeed, the simulations have shown that when $\beta_3 < 0$ then the asymmetry induced by the third order dispersion acts in the opposite direction to that induced by the pump depletion and thus can actually improve the quality of the output pulse. However, when $\beta_3 > 0$ the effects of the asymmetries combine, destroying the linearity of the chirp, and can lead to the pulse developing oscillations on the long sloping trailing edge. Such effects can be seen in Fig. 6.5 where (a) shows the intensity profile and chirp (plotted on linear scales) and (b) shows the spectrum of the output pulse generated under the same conditions as that in Fig. 6.4(C) but this time with $\beta_3 = 0.0018\,\mathrm{ps}^3\mathrm{m}^{-1}$. Although in standard single mode fibres β_3 is typically positive over most wavelengths, both positive and negative values of β_3 are possible in small core microstructured fibres. Clearly, from the slope of the dispersion profiles in Fig. 6.3(b), in all cases considered here $\beta_3 < 0$.

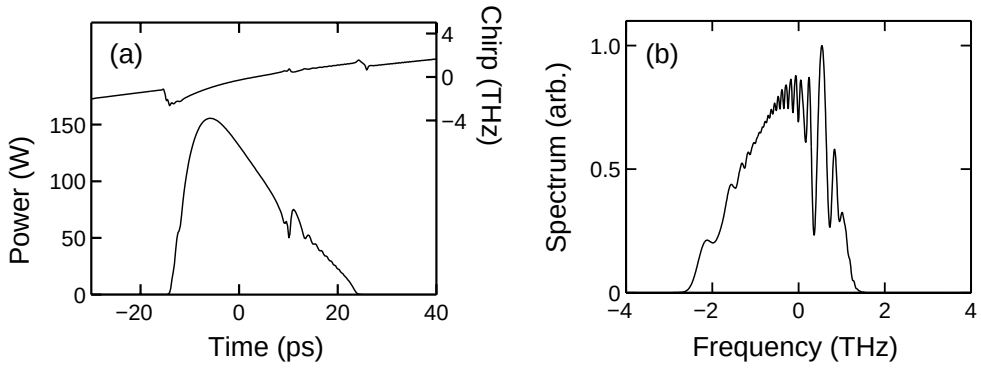

Figure 6.5: (a) Intensity (left axis) and chirp (right axis) of the output obtained from simulated propagation in fibre C but with $\beta_3 = 0.0018\,\mathrm{ps}^3\mathrm{m}^{-1}$. (b) The corresponding spectrum.

6.3.4 Dependence on the Input Pulse Characteristics

From the results presented in Figs. 6.4 and 6.5 it is evident that the evolution of the signal pulse to the parabolic pulse regime depends strongly on the parameters of the microstructured fibre. Further design work could be performed to identify microstructed fibres that are optimised for parabolic pulse generation. However, previous investigations of parabolic evolution have shown that for a given amplifier with fixed parameters, there are certain input pulse parameters that allow for a more efficient convergence to the parabolic regime [40]. Based on these results, additional simulations have been conducted to establish the input signal and pump pulse parameters which optimise the evolution to the parabolic pulse solution with the hope that a faster convergence to the parabolic regime will make the specific fibre design less critical.

Despite the complexity of the Raman term in Eq. (6.1), in the limit of low pump depletion it can in fact be well approximated by the NLSE with a simple gain term as given in Eq. (3.30). Consequently, in this limit it can be expected that the amplified pulses can be described by the parabolic pulse solutions of Chapter 4. However, in the high gain systems investigated here, the effects of pump depletion cannot be ignored and it must be expected that the parabolic pulse solutions will deviate from the analytic predictions based on the simplified equation. Nevertheless, as the previous results have shown, clearly the pulses in this system are still evolving to have a parabolic form. Thus, as a means of quantifying the level to which a pulse has become parabolic, a root-mean-square (RMS) intensity error can be introduced between the numerically sim-

ulated pulse $I_{\mathrm{NUM}}(T) = |\Psi(L,T)|^2$, where L is the fibre length, and the fitted parabolic pulse $I_{\mathrm{FIT}}(T)$ (as shown in Fig. 6.4) as [57]:

$$\varepsilon_{\mathrm{I}} = \sqrt{\frac{\frac{1}{N}\sum_{j=0}^{N}\left[I_{\mathrm{NUM}}(T_j) - I_{\mathrm{FIT}}(T_j)\right]^2}{\frac{1}{N}\sum_{j=0}^{N} I_{\mathrm{NUM}}^2(T_j)}}. \tag{6.3}$$

The results of the simulations have shown that the important pulse parameters are the input pulse width and the ratio of the peak powers of the pump and signal pulses. To illustrate the dependence of the pulse width, Fig. 6.6 shows a plot of the RMS intensity error as a function of the input width (FWHM) where in all cases the input pulse energy is $5.3\,\mathrm{pJ}$ (as used for the input pulses in Fig. 6.4), and the fibre parameters correspond to fibre A. This clearly shows that for a fixed input pulse energy there is an optimum input pulse width, in agreement with the earlier observations of Ref. [40], and for this system the width is $\sim 6\,\mathrm{ps}$.

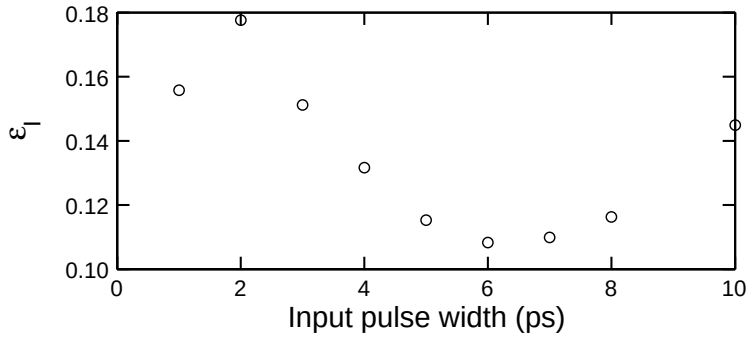

Figure 6.6: RMS intensity error as a function of input pulse duration (FWHM) for a fixed signal pulse energy. The fibre parameters correspond to fibre A.

The remaining curves plotted in Fig. 6.7 then show a comparison between two parabolic pulses generated with the same input pulse and fibre parameters as used to generate Fig. 6.4(A) (i.e., a signal peak power of $5\,\mathrm{W}$) but with pump powers of (a) $40\,\mathrm{W}$ and (b) $100\,\mathrm{W}$. As larger pump powers offer larger gains per unit length, the fibre lengths were chosen to be $8\,\mathrm{m}$ and $3\,\mathrm{m}$ for (a) and (b), respectively, so that in both cases the signal pulse experienced a gain of $\sim 28\,\mathrm{dB}$. Although the intensity misfits for these output pulses are similar, (a) $\varepsilon_{\mathrm{I}} = 0.17$ and (b) $\varepsilon_{\mathrm{I}} = 0.15$, the steep sloping edges on the pulse in Fig. 6.7(b)

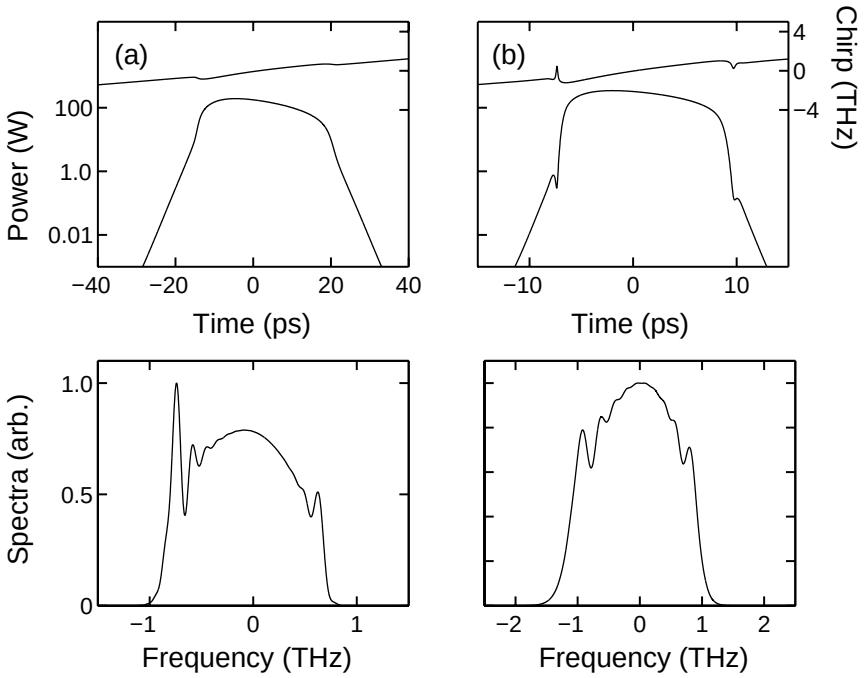

Figure 6.7: Top: intensity (left axis - logarithmic scale) and chirp (right axis - linear scale) of the fibre outputs obtained from simulations with (a) 40 W and (b) 100 W pump pulses, respectively. Bottom: the corresponding spectra. In both cases the fibre parameters correspond to fibre A.

indicate that this pulse is more parabolic [Section 4.4]. Thus these results suggest that a larger gain per unit length can enhance the rate of evolution to the parabolic regime.

6.3.5 Compression of a Raman Amplified Parabolic Pulse

Finally, to demonstrate the potential use of Raman amplified parabolic pulses for high power short pulse generation, the compression of the pulses in Fig. 6.4 is simulated via a simple linear grating pair (see Section 5.3.3). Importantly, it can be noted that the simulations have indicated that compressing the pulses to obtain the flattest spectral phase corresponds to the optimal compressed profile in that it simultaneously minimises the temporal phase variation across the central peak as well as the fraction of the total pulse energy contained in the pedestals (see Appendix A). Using this technique, the resultant compressed pulses can be seen in Fig. 6.8 where the corresponding output widths are (A) 900 fs, (B) 640 fs and (C) 920 fs. Here the long pedestals on the trailing edges can be partly attributed to the parabolic nature of the pulses as it has been

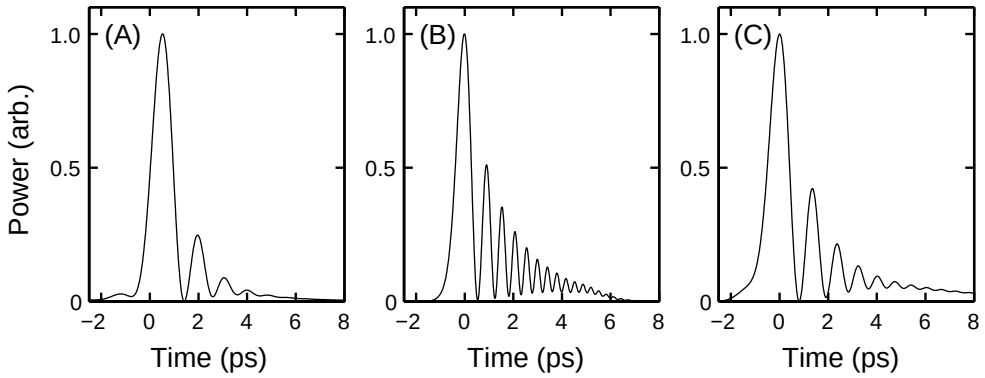

Figure 6.8: Intensity profiles of the output pulses from Fig. 6.4 after linear compression.

shown that the analytic form of a compressed parabolic pulse is in fact a Bessel function of the first kind [41]. Significantly, a characteristic feature of this result is that the amplitude and frequency of these oscillations increase with increasing spectral width. This is in agreement with the observations as the pulse corresponding to case B possess both the broadest spectrum ($2.1\,\mathrm{THz}$ compared to $0.9\,\mathrm{THz}$ for case A and $1.3\,\mathrm{THz}$ for case C) and the largest pedestals ($46\,\%$ of the total pulse energy compared to $28\,\%$ for case A and $42\,\%$ for case C). In addition, because of the asymmetry of these pedestals, they can also be attributed to the asymmetry in the uncompressed pulses. Thus it is expected that these results could be improved by employing specially designed fibre Bragg grating dispersion compensators [58]. Nonetheless, the ease with which these pulses can be compressed suggests that Raman amplified parabolic pulses offer an efficient source of high power short pulses unrestricted by wavelength.

6.4 Experimental Confirmation

The results of the numerical simulations presented in Section 6.3.2 have demonstrated parabolic pulse generation in microstructured fibre Raman amplifiers. This section now presents preliminary experimental confirmation of these numerical results. The experiments described in the following were performed with the help of Dr M. O'Connor who built and maintained the signal pulse source. Because of the specialised apparatus used in these experiments, this section begins with a detailed description of the experimental configuration.

6.4.1 Experimental Apparatus

The Microstructured Fibre

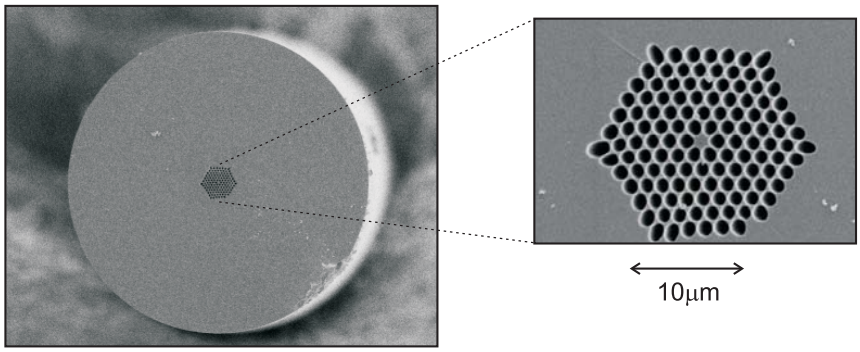

Figure 6.9: SEM image of the cross section of the microstructured fibre used in the experiments.

The amplifying fibre used in the experiments is a hexagonally stacked pure silica small core microstructured fibre. A scanning electron microscope (SEM) image of the fibre cross section is shown in Fig. 6.9.[1] From this image we could estimate d and Λ which in turn allowed us to calculate the nonlinearity and dispersion properties of the fibre. For reference, the relevant fibre parameters are listed in Table 6.2.

Parameter	Value
Hole diameter d	$1.1\,\mu\mathrm{m}$
Hole-to-hole spacing Λ	$1.2\,\mu\mathrm{m}$
Nonlinearity parameter γ	$90 \times 10^{-3}\,\mathrm{W}^{-1}\mathrm{m}^{-1}$
Dispersion parameter β_2	$63 \times 10^{-3}\,\mathrm{ps}^2\mathrm{m}^{-1}$
Loss α	$0.2\,\mathrm{dBm}^{-1}$
Length L	$5\,\mathrm{m}$

Table 6.2: Microstructured fibre parameters used in the experiments.

Because of the extremely small core size we expect the nonlinear effects in this fibre to be dramatically enhanced, and in particular we found it to exhibit some very unusual Raman properties. Specifically, one would expect that for

[1] A SEM is a microscope that uses electrons rather than light to form an image so that higher resolutions can be attained.

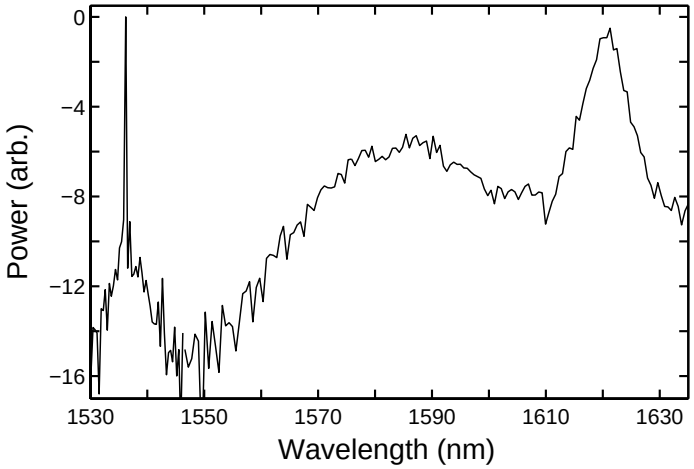

Figure 6.10: Raman spectrum for the microstructured fibre of Fig. 6.9 taken at the time of the measurements.

a pure silica fibre the peak of the Raman gain spectrum should appear downshifted from the pump by $13.2\,\mathrm{THz}$ so that for a $1.536\,\mu\mathrm{m}$ pump we should choose a signal beam at $1.649\,\mu\mathrm{m}$. However, from Fig. 6.10 which shows the Raman spectrum of this fibre at the time of our measurements, clearly this is not the case as the peak gain is in fact at $\sim 1.62\,\mu\mathrm{m}$. Furthermore, we also found that this Raman peak shifted in wavelength as the fibre was recleaved and the coupling was varied. This anomaly can possibly be attributed to the nonuniformity of the fibre cross section and examples of alternative Raman spectra obtained in this fibre are shown in Fig. 6.11. Nevertheless, as a complete investigation into the Raman properties of this fibre was beyond the scope of this thesis, we simply attributed this behaviour to the extreme nature of the fibre structure. In addition, it is worth noting that because of the small core

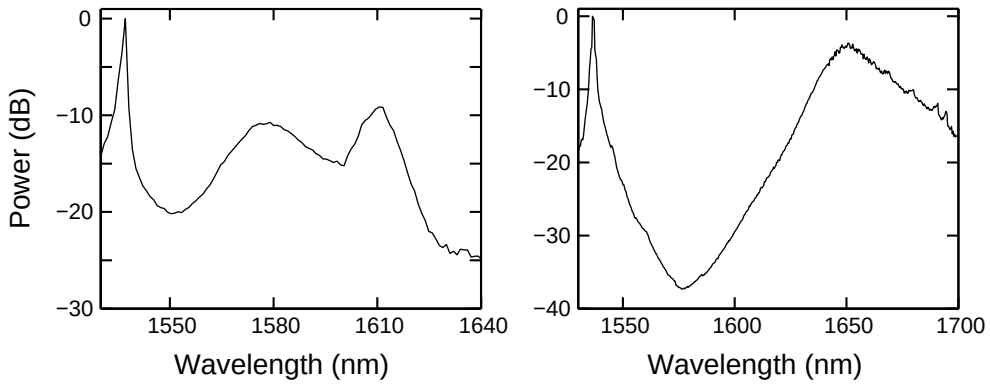

Figure 6.11: Alternative Raman spectra for the microstructured fibre of Fig. 6.9 showing the wavelength dependence of the coupling.

size, the coupling efficiencies obtained during this experiment were typically of the order of 10% or less and were highly dependent on the wavelength of the coupled light.

The Signal Pulse Source

To ensure efficient parabolic pulse amplification in the microstructured fibre described above we required a picosecond pulse source at the peak of the Raman gain curve: $\sim 1.62\,\mu\mathrm{m}$. To this end, Dr M. O'Connor developed a synchronously pumped optical parametric oscillator (OPO) based on wavelength conversion in a periodically poled lithium niobate ($LiNbO_3$) crystal (PPLN) (see Chapter 10 for a more complete description of PPLN). A detailed technical description of a similar OPO has been published in Ref. [59].

A schematic diagram of the signal pulse source is given in Fig. 6.12. The pump source is a mode-locked Nd:YLF laser (Microlase DPM-1000-120), coupled with a Nd:YLF amplifier system, which operates at a wavelength of $\lambda = 1.047\,\mu\mathrm{m}$ to produce $4\,\mathrm{ps}$ (FWHM) hyperbolic secant pulses at a repetition rate of $120\,\mathrm{MHz}$. These pulses are injected into the OPO ring cavity where the wavelength conversion occurs in a $19\,\mathrm{mm}$ long PPLN crystal with a grating period of $30\,\mu\mathrm{m}$. The crystal was housed in an oven (dashed box) where the temperature could be adjusted to tune through the converted wavelengths and for signal

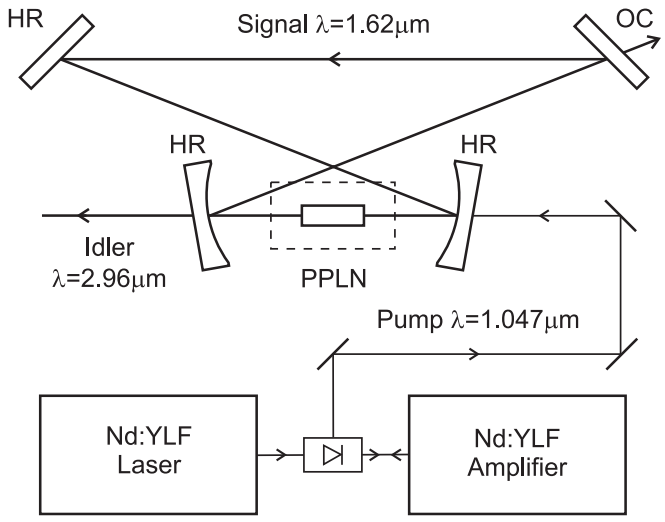

Figure 6.12: Experimental configuration of the OPO used to generate picosecond pulses at $1.62\,\mu\mathrm{m}$.

and idler waves of $\lambda_S = 1.62\,\mu\mathrm{m}$ and $\lambda_I = 2.96\,\mu\mathrm{m}$, the operating temperature was $135\,^{\circ}\mathrm{C}$. The cavity was surrounded by three highly reflecting (HR) mirrors and an output coupler (OC) with a 40% transmission fraction (at the signal wavelength) to produce $\sim 550\,\mathrm{mW}$ of average power.

At this point we note that the source that will be used to pump the Raman interaction only operates at a repetition rate of the order of $100\,\mathrm{kHz}$ (see following section). Thus if we were to consider launching the signal beam into the fibre at the maximum repetition rate of $120\,\mathrm{MHz}$, only 1 out of ~ 1200 pulses would be amplified. As slower detection devices [such as an optical spectrum analyser (OSA)] integrate the optical signals over a window in time, this averaging effect would make it almost impossible to detect the gain in a single amplified pulse. As a result, to reduce the number of pulses that enter the fibre stage an accousto-optic modulator (AOM) is used to chop the pulse train from the OPO into a series of pulse windows which occur at a repetition rate of $100\,\mathrm{kHz}$. A schematic illustration of this can be seen in Fig. 6.13. An example of a typical window of pulses for an AOM trigger width of $350\,\mathrm{ns}$, obtained from a $100\,\mathrm{MHz}$ digital oscilloscope, is plotted in Fig. 6.14(a).[2] Here the departure of the pulse window from the perfect rectangular function of Fig. 6.13 is due to the finite response time of the AOM and for window sizes less than $\sim 4\,\mu\mathrm{s}$ leads to a reduction in the peak power of even the most central pulses. With the AOM window fully open ($8.3\,\mu\mathrm{s}$) the maximum average signal power before the microstructured fibre launch was $30\,\mathrm{mW}$.

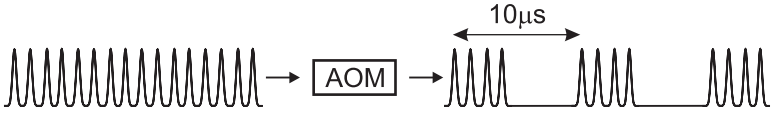

Figure 6.13: Reduction of the signal pulse repetition rate for launch into the Raman amplifier system.

Finally, Fig. 6.14(b) shows an autocorrelation trace of the input pulses into the Raman amplifier system. Assuming a hyperbolic secant pulse profile, the autocorrelation width of $6.12\,\mathrm{ps}$ indicates a true input pulse width of $\sim 4.0\,\mathrm{ps}$ (FWHM). The fine oscillatory structure on the envelope of the pulse is due to the chopping of the pulse train by the AOM.

[2] Although the pulse-to-pulse spacing is large enough to be resolved accurately, the small bandwidth of the scope causes an exaggeration of the pulse widths.

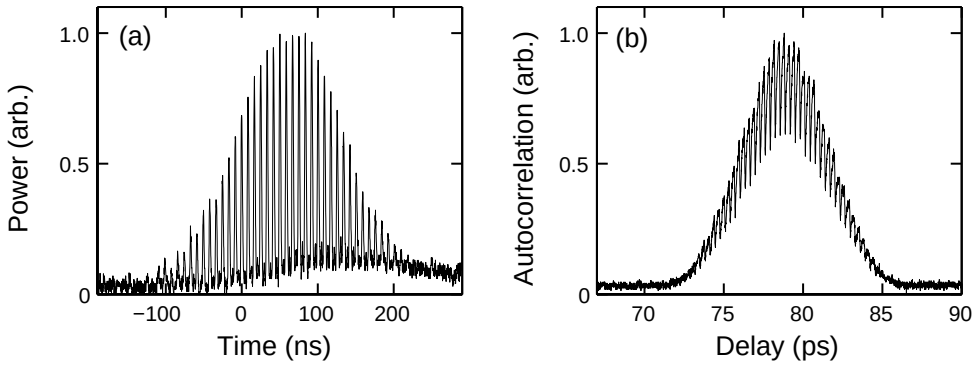

Figure 6.14: (a) Typical example of a window of signal pulses for input into the microstructured fibre. (b) Autocorrelation trace of the input pulses into the microstructured fibre.

The Pump Pulse Source

The pump pulse source was also developed within the ORC and a detailed technical description can be found in Ref. [60]. Fig. 6.15 shows a schematic diagram of the experimental setup. The laser is seeded by a simple laser diode providing $1\,\mathrm{mW}$ CW at $1.536\,\mu\mathrm{m}$ which is externally modulated to produce $5\,\mathrm{ns}$ square pulses. To compensate for the losses resulting from the chopping of the beam, an amplifier is also included in this preliminary stage. These pulses are then passed into a two stage, high gain Er^{3+}:doped fibre preamplifier before

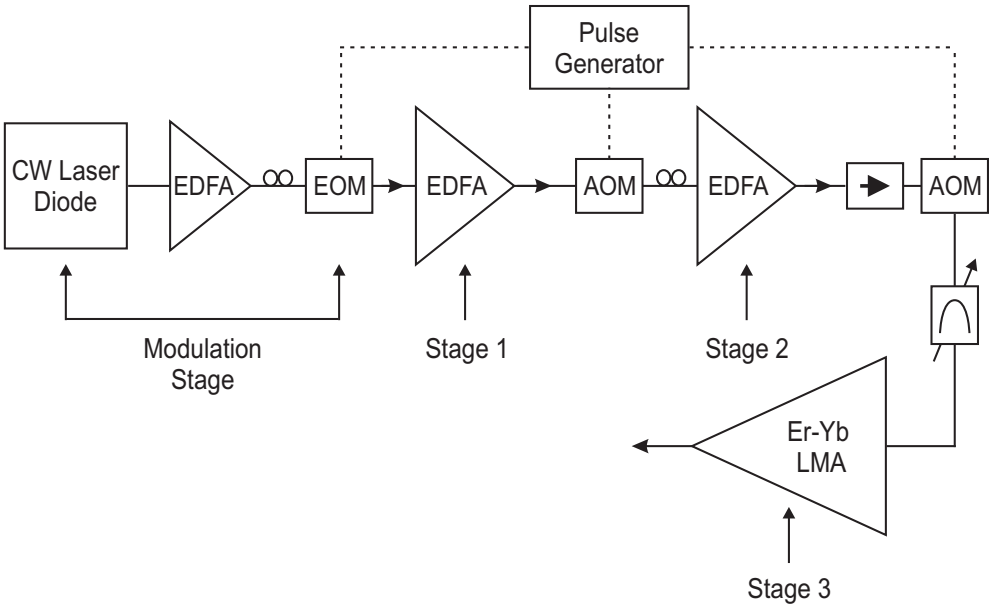

Figure 6.15: Experimental configuration of the high power pump pulse source to produce pulses at $1.536\,\mu\mathrm{m}$.

finally being launched into the large mode area (LMA) Er^{3+}–Yb^{3+}:doped fibre amplifier. The three amplifier stages were separated by two AOMs triggered to gate through the pulses whilst stopping the ASE from passing between adjacent stages. In addition, a $1\,\mathrm{nm}$ bandpass filter was placed before the LMA amplifier stage to eliminate the small amount of ASE in the time slot of the pulse. With the pulse generator operating at a repetition rate of $100\,\mathrm{kHz}$ this setup produced $5\,\mathrm{ns}$ pulses with peak powers of $\sim 1\,\mathrm{kW}$.

6.4.2 Experimental Setup

The complete experimental setup to generate parabolic pulses in a microstructured fibre Raman amplifier is illustrated in Fig. 6.16. The AOM in the signal setup was triggered off the pump source so that the signal pulses were launched into the microstructured fibre to overlap with the pump pulses. Polarisation controllers (PC) were included in the pump and signal launch paths so that both beams could be launched onto a single polarisation axis. Typically, the average pump power before the microstructured fibre launch was $250\,\mathrm{mW}$. Coupling into the fibre was achieved using a $2.75\,\mathrm{mm}$ focal length lens and coupling efficiencies of $\sim 10\%$ and $\sim 5\%$ were usually obtained for the pump and signal beams, respectively.[3] This resulted in a maximum pump peak power of $40\,\mathrm{W}$ and a maximum signal peak power of $4.5\,\mathrm{W}$ (when the AOM window was fully open: $8.3\,\mu\mathrm{s}$) in the microstructured fibre.

To verify that the pulses were in fact experiencing gain from the Raman interaction, before attempting to measure autocorrelation traces of the output pulses we first looked at the output from the fibre on the digital scope. As mentioned previously [Section 6.4.1], the small bandwidth of the scope causes an exaggeration of the observed pulse widths so that this is not a true representation of the output pulses. However, it is clear from Fig. 6.17(a) that the signal pulse which is overlapped by the pump pulse is experiencing gain. In order to see the unamplified pulses on this scale, this image was taken for a relatively low average input pump power of $100\,\mathrm{mW}$ (corresponding to a peak pump power in the fibre of $\sim 13\,\mathrm{W}$) and resulted in $\sim 8\,\mathrm{dB}$ of gain. Increasing the input pump power to $250\,\mathrm{mW}$ ($\sim 40\,\mathrm{W}$ of peak pump power in the fibre), the

[3] This assumes a launch optimised for the pump beam.

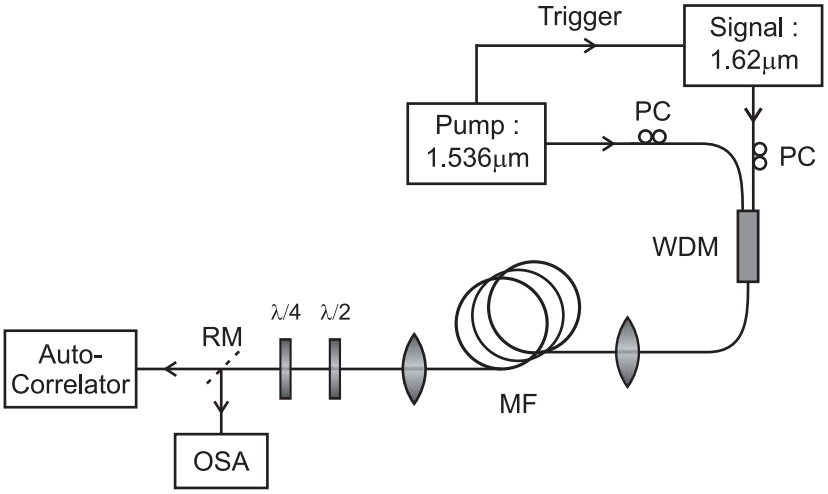

Figure 6.16: Schematic diagram of the experimental setup for parabolic pulse generation in a microstructured fibre Raman amplifier. WDM=wavelength division multiplexer, MF=microstructured fibre and RM=removable mirror.

amplified pulse in Fig. 6.17(b) is now sufficiently large that the unamplified pulses are undetectable on this scale, and this corresponded to a total pulse gain of $\sim 22\,\mathrm{dB}$.

Once we were satisfied that the signal pulses were experiencing Raman gain we then aligned the output to the autocorrelator. This was done with the AOM window fully open so that the power was at a maximum. A removable mirror was placed just before the entrance to the autocorrelator so that the output could be redirected to an OSA and thus we could obtain measurements of the pulses in the temporal and spectral domains under the same conditions.

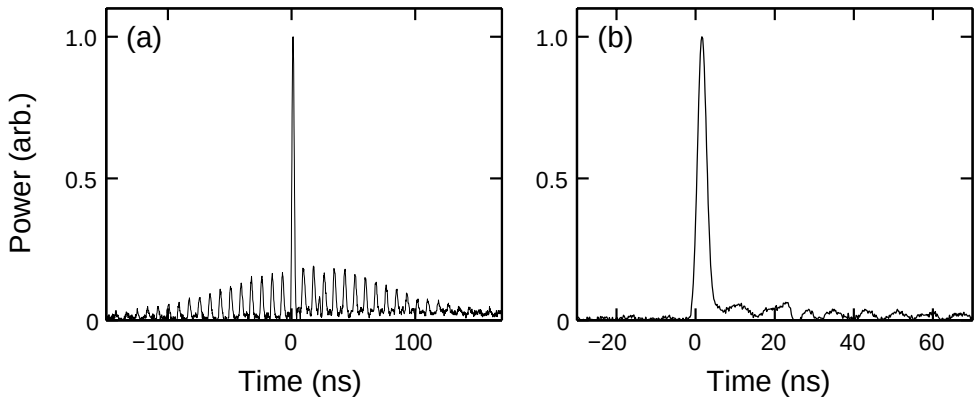

Figure 6.17: Oscilloscope traces showing signal pulses with: (a) $8\,\mathrm{dB}$ and (b) $22\,\mathrm{dB}$ of Raman gain.

We recall that as the defining features of a parabolic pulse are the steep edges of the temporal profile and its linear frequency chirp [Chapter 4], a thorough characterisation of a parabolic pulse requires the use of the FROG measurement technique which allows for the complete retrieval of both the intensity profile and the phase (as described in Section 5.3.4). However, at the time of these measurements a FROG device at $1.62\,\mu\mathrm{m}$ was not available. Thus in order to establish any parabolic nature of the amplified pulses it was important to consider both the temporal and spectral measurements where, in the time domain the steep parabolic edges will translate to an autocorrelation trace with steep edges, and in the frequency domain the strong chirp will result in a broad spectral width [Section 3.2].

6.4.3 Analysis of Experimental Data

With the experimental configuration set up to look at the fibre output on the OSA, the coupling and polarisation of the pump beam were optimised to obtain the largest Raman gain at $1.62\,\mu\mathrm{m}$. We found that, at the time of the measurements, this corresponded to an input pump power of $210\,\mathrm{mW}$ and a coupling efficiency of $\sim 8\,\%$ so that the peak power of the pump in the fibre was $\sim 25\,\mathrm{mW}$.

The measured autocorrelation trace of a Raman amplified pulse is shown in Fig. 6.18(a). This was taken for an AOM window size of $4\,\mu\mathrm{s}$ and with only $10\,\mathrm{mW}$ of average signal power before the fibre, we estimate an average coupled power of $\sim\ 1\,\mathrm{mW}$, corresponding to a peak signal power of $\sim\ 2\,\mathrm{W}$. Clearly there is a very large noise component to this pulse which makes it difficult to distinguish any defining features. This is due to the extremely low average power of the signal beam and, in fact, for this window size it was not possible to measure an autocorrelation trace of the signal pulses through the fibre without gain (i.e., with the pump turned off). Nevertheless, the steepness of the edges of this trace suggests that the pulse has departed from its input hyperbolic secant profile.

The output spectrum from the microstructured fibre showing both the pump at $1.536\,\mu\mathrm{m}$ and the amplified spectrum at $1.62\,\mu\mathrm{m}$ is plotted in Fig. 6.18(b). To estimate the Raman pulse gain we then closed the AOM window down even

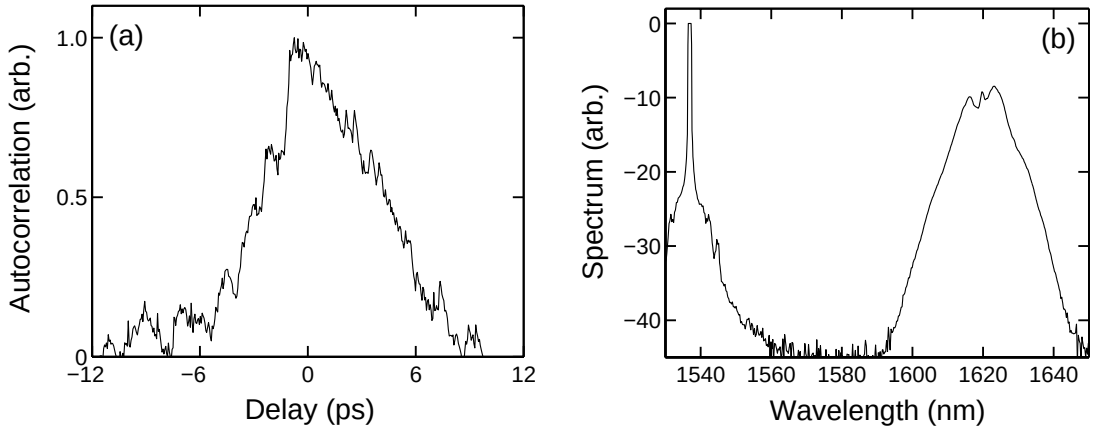

Figure 6.18: (a) Measured autocorrelation trace and (b) spectrum of a Raman amplified pulse.

further to $60\,\mathrm{ns}$, so that there were approximately 4 significant signal pulses in each train, and measured the spectrum of the signal pulses with and without the copropagating pump. The resulting pulse spectra can be seen in Fig. 6.19 and from these we calculated the Raman gain to be $\sim 16\,\mathrm{dB}$. Importantly we note that due to the reduction in the peak power, caused by the reduction of the AOM window, we can expect that this calculation will actually underestimate the true Raman pulse gain and this is facilitated by the suppression of the pulse shaping effects seen from Fig. 6.18(b) to Fig. 6.19(b). However, as it was not possible to measure the Raman gain directly from the temporal pulses, this was the best estimate that we could obtain.

To investigate these results in more detail, the system has been simulated based on the input pump and signal pulse properties, as estimated above, and with

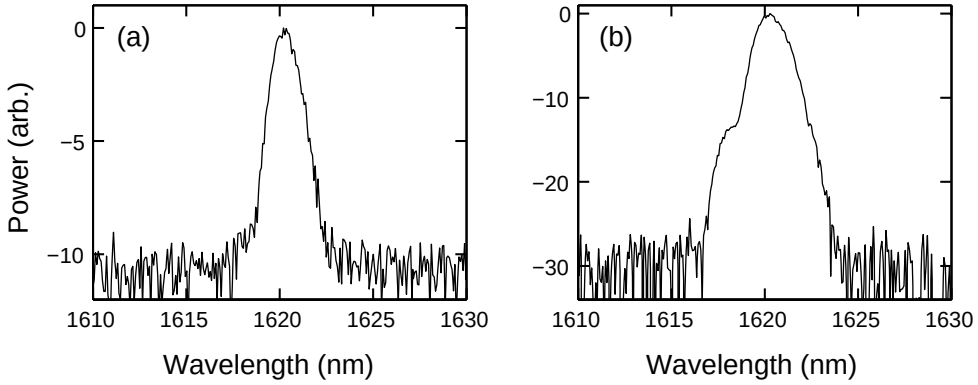

Figure 6.19: Signal pulse spectra corresponding to (a) no gain (pump off) and (b) gain (pump on) to estimate the total Raman gain.

the fibre parameters given in Table 6.2. Fig. 6.20(a) shows the intensity profile and chirp of the output pulse from the simulation (solid curves). The total output pulse gain was $15.9\,\mathrm{dB}$, consistent with the estimated measured gain. Clearly, not only is this pulse starting to look visually parabolic, it is also in good agreement with the parabolic fit to its intensity profile and the linear fit to its chirp (circles).[4] In addition, the corresponding spectrum of Fig. 6.20(b) appears to be developing the oscillations on its edges typically associated with the entrance to the parabolic regime [Section 4.4].

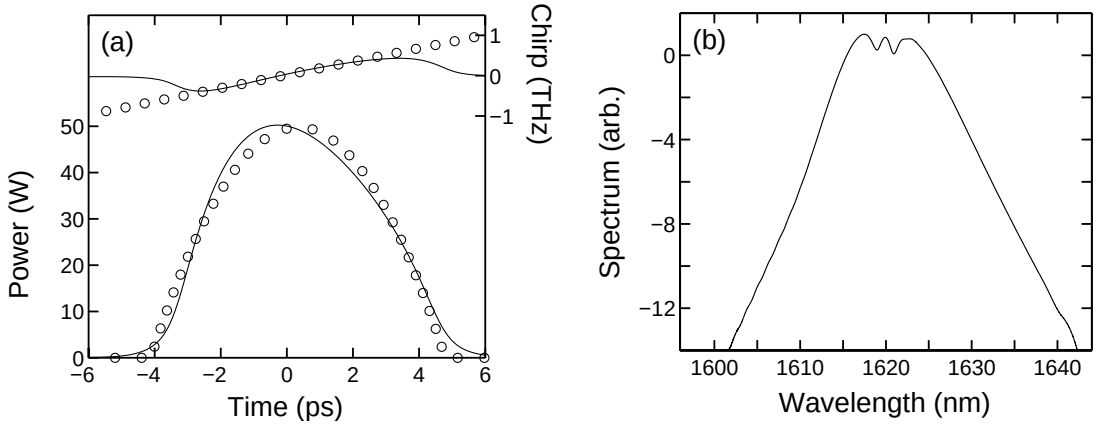

Figure 6.20: (a) Intensity profile (left axis) and chirp (right axis) of the simulated Raman amplified pulse together with parabolic and linear fits (circles). (b) Corresponding spectrum.

To compare our measured pulse with the simulation results, Fig. 6.21(a) shows the autocorrelation trace of the pulse from Fig. 6.18(a) (solid curve) together with the calculated autocorrelation of the pulse from Fig. 6.20(a) (dashes). Despite the noise induced asymmetry in the peak of the measured trace, there is still good agreement between the autocorrelations and specifically between their half maximum widths which are $7.2\,\mathrm{ps}$ (measured) and $7.3\,\mathrm{ps}$ (simulated). Furthermore, not only is there good agreement between the spectral widths ($8.3\,\mathrm{nm}$ and $8.4\,\mathrm{nm}$ for the measured and simulated spectra, respectively), there is also excellent qualitative agreement between the shape of the spectral profiles as seen in Fig. 6.21(b). Consequently, we can expect that the simulated pulse of Fig. 6.20 is a reasonable representation of the measured amplified pulse in Fig. 6.18 which indicates that parabolic pulses are indeed being gen-

[4] As in Section 6.3.2, the fits are obtained via a minimisation scheme based on the Nelder-Mead Simplex method.

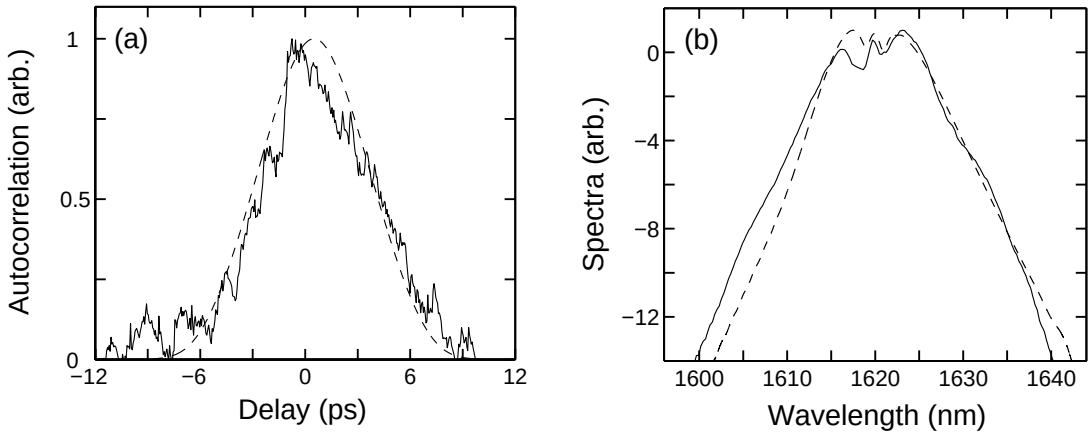

Figure 6.21: (a) Autocorrelation traces and (b) Raman amplified spectra of the measured pulse (solid curves) compared with the simulated parabolic pulse (dashed curves).

erated in our system.

Finally, to emphasise the parabolic nature of the output pulse, Fig. 6.22 compares the measured autocorrelation trace (solid line) with calculated autocorrelations for parabolic (dashes), Gaussian (dot-dashed) and hyperbolic secant (dotted) fits to the simulated pulse of Fig. 6.20, on a logarithmic scale. Clearly, the parabola offers the best fit to the experimental pulse, especially in the wings. Thus these results offer the first confirmation of a parabolic pulse generated via Raman amplification in a microstructured fibre.

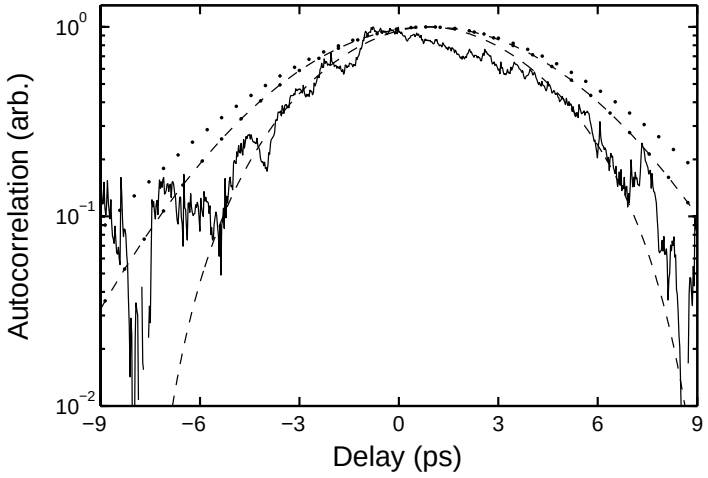

Figure 6.22: Autocorrelation trace of the experimentally measured pulse (solid curve) compared with calculated autocorrelations of parabolic (dashes), Gaussian (dot-dashes) and hyperbolic secant (dots) fits to the simulated pulse of Fig. 6.20.

6.4.4 Future Directions

The results presented in this section have indicated that the main limiting feature of this experiment is the very low coupling efficiency of the microstructured fibre, which is due to the extremely small core size. Unfortunately, to date, investigations of the dispersion properties of various microstructured fibres have shown that in the wavelength range $1.5\,\mu\mathrm{m} - 1.7\,\mu\mathrm{m}$ normal dispersion is typically associated with small core structures [61]. In the interest of establishing the structural features that give rise to the dispersion, and also the nonlinearity, of a microstructured fibre, members of Dr T. Monro's microstructured fibre group are currently working to solve the inverse problem of calculating possible fibre structures given a fixed dispersion profile. Thus it is hoped that in the near future we could exploit this technique to design fibres with dispersion and nonlinear properties that are optimised to our specific needs.

As well as the small coupling efficiencies, we also faced the additional problem that the signal source was passively mode locked so that this could not be synchronised exactly with the pump source. Thus in order to improve the efficiency of the measurements it would also be beneficial to design a signal source that could be triggered directly off our pump source, such as a Raman fibre laser [62], enabling single pulse measurements.

Finally, to make more rigorous comparisons between the experimental measurements and the parabolic theory it is important that our pulse diagnostic techniques are improved. Thus, to this end, we will need to develop a FROG setup (such as that described in Section 5.3.4) that operates at $\sim 1.62\,\mu\mathrm{m}$ so that we can obtain a complete retrieval of both the intensity and phase of the field. Furthermore, it is hoped that a better understanding of the output pulse characteristics, and hence the precise effects of the dispersion and nonlinearity, will aid in the design process of the microstructured fibres.

Chapter 7

Self-Similar Solutions of the NLSE with Distributed Coefficients

7.1 Introduction

The self-similar solutions discussed in the previous two chapters exist under the conditions of normal dispersion and gain. In this chapter a new class of solutions which exist for a much wider parameter range that extends to both signs of the dispersion parameter, and either gain or loss is investigated. These solutions have been found for a generalised form of the nonlinear Schrödinger equation (NLSE) with distributed coefficients which vary longitudinally down the length of the fibre or fibre amplifier. It will be shown that this system permits a broad class of exact self-similar solutions and that these include a set of solitary wave solutions. In order to establish the robustness of these solutions to realistic experimental conditions, a numerical investigation into their stability is also presented.

7.2 Background of the Project

Development of the techniques involved in optical fibre fabrication mean that it is now possible to fabricate fibres with longitudinally varying dispersion and nonlinear properties. Such tailored fibres have already been shown to have

important applications in the areas of pulse compression and amplification, as pulse degradation due to the nonlinear effects can be minimised. In particular, dispersion decreasing fibres have been used to demonstrate clean, high power short pulse generation via adiabatic soliton compression in both low gain fibre amplifiers and dispersion decreasing fibres [63].

Motivated by these results, in 1996 Moores conducted an analytical investigation into similar systems under which rapid compression was possible [64]. In his work he focused on pulse propagation in anomalous dispersion fibres or fibre amplifiers where either the gain or the dispersion parameter is a distributed function of the propagation distance. His results showed that high quality rapid compression is indeed possible and that the pulses are chirped throughout the compression with the size of the chirp being proportional to the rapidity of the amplification. However, as these results were obtained rather serendipitously, they could not be extended to consider more complex systems where two or more of the parameters varied along the fibre length.

This chapter presents the results of an independent analysis based on a more general system. Specifically, it will be shown that in systems where all of the parameters describing the fibre or fibre amplifier can vary longitudinally, there exists a new class of exact self-similar solutions. This work is the result of a collaboration with Prof. J. Harvey and Dr V. Kruglov of the Applied Optics Group at The University of Auckland. The theoretical component of this work was carried out by Dr V. Kruglov using similar techniques to those employed for the case of parabolic pulse propagation in normal dispersion amplifiers, as discussed in Chapter 4. My role was to conduct the numerical analysis to aid with the development and verification of these results, and to establish their stability under perturbations.

7.3 Nonlinear Schrödinger Equation with Variable Parameters

Pulse propagation in a fibre with distributed dispersion, nonlinearity and gain can be described by the standard NLSE, as introduced in Section 3.7, with z-

dependent coefficients so that:

$$\mathrm{i}\frac{\partial \Psi}{\partial z} = \frac{\beta_2(z)}{2}\frac{\partial^2 \Psi}{\partial T^2} - \gamma(z)\left|\Psi\right|^2\Psi + \mathrm{i}\frac{g\,(z)}{2}\Psi. \tag{7.1}$$

As discussed in Chapter 3, $\Psi\,(z,T)$ is the slowly varying envelope of the pulse in a co-moving frame, β_2 is the GVD parameter, γ is the nonlinearity parameter, g is the fibre gain (or loss if g is negative) and, to simplify the theoretical analysis, we assume that the higher order dispersive effects are negligible so that we can set $\beta_3 = 0$. The inclusion of a distributed gain function $g(z)$ has already been discussed in Section 4.4.2 in the context of the amplifier pumping geometry. To produce distributed dispersion in a fibre, longitudinal variation of the chemical composition, refractive index, or the core diameter is required. As the core diameter is controlled by the fibre drawing speed, this is by far the easiest parameter to control and thus dispersion variation is generally achieved by tapering the fibre. However, because the nonlinearity parameter depends on the mode size of the guided light [Eq. (3.27)], this is also controlled by the core diameter so that we expect a tapered fibre to have both distributed dispersion and nonlinearity. Although previous theoretical studies of pulse propagation in tapered fibres have neglected the effects of the distributed nonlinearity claiming that this effect is small, as the desire for shorter device lengths becomes greater, more extreme tapers will be required and these claims will no longer be accurate. Thus we expect to find that for such cases the full z-dependence of the coefficients in Eq. (7.1) must be considered.

7.4 Solutions to the Modified NLSE

In this section we consider the solutions to Eq. (7.1) under conditions where all of the fibre parameters are functions of the propagation distance. Following the analysis of Chapter 4, we start by writing the field Ψ in terms of its real amplitude A and phase Φ: $\Psi(z,T) = A(z,T)\exp\left[\mathrm{i}\Phi(z,T)\right]$. Substituting this into Eq. (7.1) we again obtain the coupled equations in A and Φ as:

$$A\frac{\partial \Phi}{\partial z} = \frac{\beta_2(z)}{2}\left[A\left(\frac{\partial \Phi}{\partial T}\right)^2 - \frac{\partial^2 A}{\partial T^2}\right] + \gamma(z)A^3, \tag{7.2}$$

$$\frac{\partial A}{\partial z} = \frac{\beta_2(z)}{2}\left[A\frac{\partial^2 \Phi}{\partial T^2} + 2\frac{\partial A}{\partial T}\frac{\partial \Phi}{\partial T}\right] + \frac{g(z)}{2}A. \tag{7.3}$$

As discussed in Section 4.2, with the assumption of self-similar evolution in the amplifier we can reduce the number of degrees of freedom of the system by rewriting the equations in terms of carefully chosen combinations of the original variables. Based on the results of the self-similar parabolic pulse solutions, for the generalised NLSE considered here we choose the two independent variables: $\Gamma(z)$ and $\tau = T/\Gamma(z)$ [41]. Using these we can represent the amplitude in the form:

$$A(z,T) = S(z)F(\tau), \tag{7.4}$$

and without loss of generality we can suppose that:

$$S(0) = 1 \qquad \text{and} \qquad \Gamma(0) = 1. \tag{7.5}$$

As it was shown in Section 4.4.2, for an equation of the form of (7.1) with a longitudinally varying gain profile, the evolution of the pulse energy in the amplifier satisfies the integral of motion:

$$U(z) = U_0 \exp\left[\int_0^z g(z')\mathrm{d}z'\right], \tag{7.6}$$

where $U_0 = U(0)$. With the form of the amplitude as given by Eq. (7.4) we find:

$$U(z) = S^2(z)\int_{-\infty}^{\infty} F^2\left(\frac{T}{\Gamma}\right)\mathrm{d}T = S^2(z)\Gamma(z)\int_{-\infty}^{\infty} F^2(\tau)\mathrm{d}\tau, \tag{7.7}$$

$$U_0 = S^2(0)\Gamma(0)\int_{-\infty}^{\infty} F^2(\tau)\mathrm{d}\tau = \int_{-\infty}^{\infty} F^2(\tau)\mathrm{d}\tau, \tag{7.8}$$

so that the integral of Eq. (7.6) yields:

$$S(z) = \frac{1}{\sqrt{\Gamma(z)}}\exp\left[\int_0^z \frac{g(z')}{2}\mathrm{d}z'\right]. \tag{7.9}$$

It follows from Eq. (7.4) that the self-similar form of the amplitude is thus:

$$A(z,T) = \frac{1}{\sqrt{\Gamma(z)}}F(\tau)\exp\left[\frac{1}{2}G(z)\right], \tag{7.10}$$

where we have defined

$$G(z) = \int_0^z g(z')\mathrm{d}z'. \tag{7.11}$$

To find the solution for the phase we first assume that it is quadratic in T:

$$\Phi(z,T) = \phi(z) + C(z)T^2. \tag{7.12}$$

The significance of this ansatz becomes clear by recalling that if a pulse possesses a linear chirp then the rate at which the temporal components expand or compress is the same for all parts of the pulse [Section 4.3.1]. Thus as the pulse propagates in the fibre its form will be preserved and hence it behaves self-similarly. As demonstrated by the analysis of Chapter 4, the value of this approach has been confirmed for the case of self-similar parabolic pulse propagation in both fibres and fibre amplifiers.

With this ansatz Eq. (7.2) can be rewritten as:

$$A\left(\frac{\mathrm{d}\phi(z)}{\mathrm{d}z}+\frac{\mathrm{d}C(z)}{\mathrm{d}z}T^2\right)=2\beta_2(z)AC^2(z)T^2-\frac{\beta_2(z)}{2}\frac{\partial^2 A}{\partial T^2}+\gamma(z)A^3. \tag{7.13}$$

This equation contains an explicit dependence on the variable T which disappears when the terms proportional to T^2 are equal. Thus we obtain the following pair of equations:

$$\frac{\mathrm{d}C(z)}{\mathrm{d}z}=2\beta_2(z)C^2(z), \tag{7.14}$$

$$A\frac{\mathrm{d}\phi(z)}{\mathrm{d}z}=-\frac{\beta_2(z)}{2}\frac{\partial^2 A}{\partial T^2}+\gamma(z)A^3. \tag{7.15}$$

We then rewrite the second coupled equation (7.3) as:

$$\frac{\partial A}{\partial z}=\beta_2(z)C(z)A-2\beta_2(z)C(z)T\frac{\partial A}{\partial T}+\frac{g(z)}{2}A. \tag{7.16}$$

With the form of the amplitude as given in Eq. (7.10), it follows that Eq. (7.16) can be satisfied if and only if the function $\Gamma(z)$ is defined via:

$$\frac{1}{\Gamma(z)}\frac{\mathrm{d}\Gamma(z)}{\mathrm{d}z}=-2\beta_2(z)C(z). \tag{7.17}$$

The solutions to Eqs. (7.14) and (7.17) follow as:

$$C(z)=\frac{C_0}{1-C_0D(z)}, \tag{7.18}$$

and

$$\Gamma(z)=1-C_0D(z), \tag{7.19}$$

where the initial chirp $C_0=C(0)\neq 0$, because the phase must be quadratic in T for all z, and the function $D(z)$ is

$$D(z)=2\int_0^z\beta_2(z')\mathrm{d}z'. \tag{7.20}$$

Via substitution of the form of the amplitude [Eq. (7.10)] into Eq. (7.15) we then obtain the differential equation for F to be:

$$\frac{\mathrm{d}^2F}{\partial\tau^2} + \frac{2\Gamma^2(z)}{\beta_2(z)}\frac{\mathrm{d}\phi(z)}{\mathrm{d}z}F - \frac{2\gamma(z)\Gamma(z)}{\beta_2(z)}\exp\left[G(z)\right]F^3 = 0. \tag{7.21}$$

As in the most general case the coefficients in Eq. (7.21) are functions of z whilst F only depends on the scaling variable τ, this equation only has nontrivial solutions ($F(\tau) \neq 0$) if and only if the coefficients are constants such that:

$$-\frac{2\Gamma^2(z)}{\beta_2(z)}\frac{\mathrm{d}\phi(z)}{\mathrm{d}z} = \lambda, \tag{7.22}$$

$$-\frac{\gamma(z)\Gamma(z)}{\beta_2(z)}\exp\left[G(z)\right] = \kappa. \tag{7.23}$$

Hence λ and κ can be calculated at $z = 0$:

$$\lambda = -\frac{2}{\beta_2(0)}\left.\frac{\mathrm{d}\phi}{\mathrm{d}z}\right|_{z=0} \qquad \text{and} \qquad \kappa = -\frac{\gamma(0)}{\beta_2(0)}, \tag{7.24}$$

and Eq. (7.21) can be rewritten as:

$$\frac{\mathrm{d}^2F}{\partial\tau^2} + 2\kappa F^3 = \lambda F. \tag{7.25}$$

The significance of writing Eq. (7.25) in this form is that it is clear that this equation can be regarded as an eigenvalue equation where λ is the eigenvalue to be determined. To complete the solution to the phase, Eq. (7.22) can be integrated to yield:

$$\phi(z) = \phi_0 - \frac{\lambda D(z)}{4\left[1 - C_0D(z)\right]}, \tag{7.26}$$

where ϕ_0 is a constant of the integration, and combining this with Eq. (7.18) we obtain:

$$\Phi\left(z,T\right) = \phi_0 - \frac{\lambda D(z)}{4\left[1 - C_0D(z)\right]} + \frac{C_0T^2}{1 - C_0D(z)}. \tag{7.27}$$

Importantly, as it was found from Eq. (7.17), the self-similar solutions described by Eqs. (7.10) and (7.27) do not exist for any combination of arbitrary shaped dispersion, nonlinearity and gain functions. To this end, it is useful to rewrite Eq. (7.19) in the form:

$$\rho(z) = \rho(0)\left[1 - C_0D(z)\right]\exp\left[G(z)\right], \tag{7.28}$$

where the function $\rho(z)$ is defined by:

$$\rho(z) = \frac{\beta_2(z)}{\gamma(z)}. \tag{7.29}$$

This equation [Eq. (7.28)] is the necessary and sufficient condition for the existence of the self-similar solutions of Eq. (7.1). Furthermore, it is also interesting to differentiate Eq. (7.28) to obtain:

$$g(z) = \frac{1}{\rho(z)}\frac{\mathrm{d}\rho(z)}{\mathrm{d}z} + \frac{2C_0\beta_2(z)}{1 - C_0D(z)}, \tag{7.30}$$

which, given the dispersion and nonlinearity profiles of the fibre, yields the required form of the gain. Combining these results we find that the complete description of the self-similar solutions to the NLSE with distributed coefficients is:

$$\Psi(z,T) = \frac{1}{\sqrt{1 - C_0D(z)}}F\left(\frac{T}{1 - C_0D(z)}\right)\exp\left[\frac{G(z)}{2}\right]\exp[\mathrm{i}\Phi(z,T)],$$

where

$$\Phi\left(z,T\right) = \phi_0 - \frac{\lambda D(z)}{4\left[1 - C_0D(z)\right]} + \frac{C_0T^2}{1 - C_0D(z)}. \tag{7.31}$$

Explicit Forms of the Self-Similar Solutions

In order to find the explicit forms of the possible sets of self-similar solutions we now consider integrating Eq. (7.25) for different signs of κ [i.e., different signs of the product $\beta_2(z)\gamma(z)$]. As the nonlinear coefficient is always positive in optical fibres ($\gamma > 0$), this corresponds to considering the two cases of anomalous ($\beta_2 < 0$) and normal ($\beta_2 > 0$) dispersion. Firstly for the case of anomalous dispersion ($\kappa > 0$), we find the amplitude through Eq. (7.10) to be:

$$A(z,T) = \frac{\sqrt{|\rho(z)|}}{T_0[1 - C_0D(z)]}\,\mathrm{sech}\left(\frac{T}{T_0[1 - C_0D(z)]}\right), \tag{7.32}$$

which is in fact in the form of a solitary wave solution where T_0 is the initial pulse width and $T_0^{-2} = \lambda$ [Eq. (7.27)]. For the case of normal dispersion ($\kappa < 0$), Eq. (7.25) then yields the amplitude in the form of a kink solution [4]:

$$A(z,T) = \frac{\sqrt{|\rho(z)|}}{T_0[1 - C_0D(z)]}\,\tanh\left(\frac{T}{T_0[1 - C_0D(z)]}\right), \tag{7.33}$$

where now $-2/T_0^2 = \lambda$. It is also possible to find a solution to Eq. (7.25) which is independent of T for either sign of κ and for such cases the amplitude is found to be:

$$A(z,T) = \frac{\Lambda\sqrt{|\rho(z)|}}{1 - C_0D(z)}, \tag{7.34}$$

where Λ is an arbitrary real parameter and $2\Lambda^2 \mathrm{sgn}\,(\kappa) = \lambda$.

In addition to these localised solutions, Eq. (7.25) also has six bounded periodic solutions which depend on an arbitrary parameter $0 < \mathrm{k} < 1$. Using the notations for the Jacobian elliptic functions [65], the solutions are, for $\kappa < 0$,

case 1: $-(1+\mathrm{k}^2)T_0^{-2} = \lambda$,

$$U(z,T) = \frac{\sqrt{|\rho(z)|}\mathrm{k}}{T_0[1-C_0D(z)]}\,\mathrm{sn}\left(\frac{T}{T_0[1-C_0D(z)]},\,\mathrm{k}\right), \tag{7.35}$$

case 2: $-(1+\mathrm{k}^2)T_0^{-2} = \lambda$,

$$U(z,T) = \frac{\sqrt{|\rho(z)|}\mathrm{k}}{T_0[1-C_0D(z)]}\,\mathrm{cd}\left(\frac{T}{T_0[1-C_0D(z)]},\,\mathrm{k}\right), \tag{7.36}$$

and for $\kappa > 0$,

case 3: $(2\mathrm{k}^2-1)T_0^{-2} = \lambda$,

$$U(z,T) = \frac{\sqrt{|\rho(z)|}\mathrm{k}}{T_0[1-C_0D(z)]}\,\mathrm{cn}\left(\frac{T}{T_0[1-C_0D(z)]},\,\mathrm{k}\right), \tag{7.37}$$

case 4: $(2-\mathrm{k}^2)T_0^{-2} = \lambda$,

$$U(z,T) = \frac{\sqrt{|\rho(z)|}}{T_0[1-C_0D(z)]}\,\mathrm{dn}\left(\frac{T}{T_0[1-C_0D(z)]},\,\mathrm{k}\right), \tag{7.38}$$

case 5: $(2\mathrm{k}^2-1)T_0^{-2} = \lambda$,

$$U(z,T) = \frac{\sqrt{|\rho(z)|}\mathrm{k}\sqrt{1-\mathrm{k}^2}}{T_0[1-C_0D(z)]}\,\mathrm{sd}\left(\frac{T}{T_0[1-C_0D(z)]},\,\mathrm{k}\right), \tag{7.39}$$

case 6: $(2-\mathrm{k}^2)T_0^{-2} = \lambda$,

$$U(z,T) = \frac{\sqrt{|\rho(z)|}\sqrt{1-\mathrm{k}^2}}{T_0[1-C_0D(z)]}\,\mathrm{nd}\left(\frac{T}{T_0[1-C_0D(z)]},\,\mathrm{k}\right). \tag{7.40}$$

In the case where β_2 is a constant (independent of z), the travelling solutions can also be found by a Galilean transformation [66]. These oscillatory solutions correspond to the transmission of amplitude modulated light which experiences a simultaneous amplification (or loss) and a modulation frequency shift under the influence of nonlinearity, dispersion and gain (or loss). To illustrate this solution set, Fig. 7.1 plots the Jacobian elliptic solutions for a constant β_2 for both $\kappa < 0$ (top curves) and $\kappa > 0$ (bottom curves), where $\mathrm{k} = 1/2$.

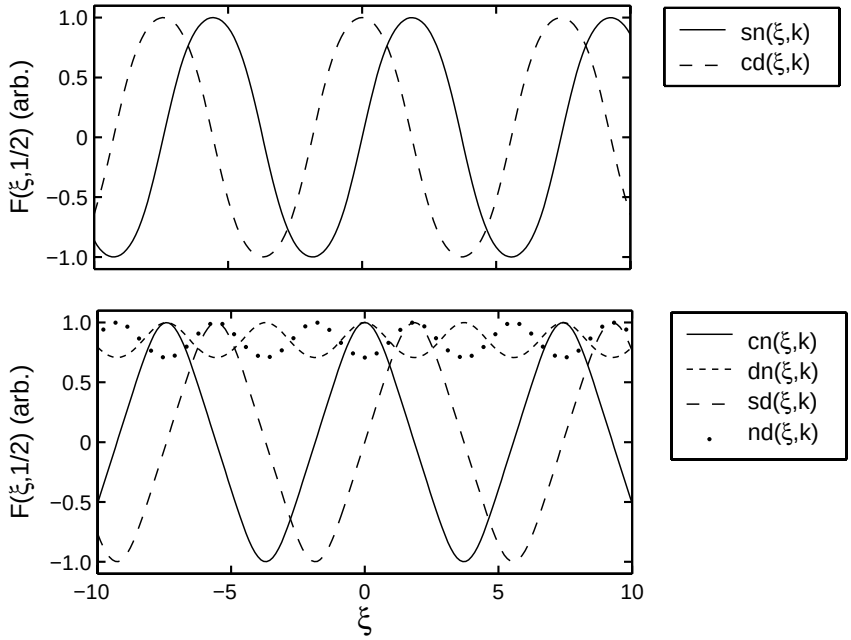

Figure 7.1: Oscillatory Jacobian elliptic solutions for constant β_2 where the top curves are for $\kappa < 0$ and the bottom are for $\kappa > 0$. In both cases $\mathrm{k} = 1/2$.

7.4.1 Solitary Wave Solutions with Distributed Dispersion and Nonlinearity

In this section we focus on the solitary wave solution of the generalised NLSE [Eq. (7.1)] found for the case of $\kappa > 0$, given by Eq. (7.32). Specifically we consider a system where the solution describes the evolution of optical pulses in dispersion decreasing fibres [67]. For definiteness, we suppose the fibre to have the physically realistic dispersion and the nonlinearity distributions:

$$\beta_2(z) = \beta_{2,0}\exp(-\sigma z), \quad \gamma(z) = \gamma_0\exp(\alpha z), \tag{7.41}$$

where $\beta_{2,0} < 0$ (as $\gamma_0 > 0$) and $\sigma > 0$. It follows from Eq. (7.30) that the gain function for self-similar solutions in this case is:

$$g(z) = -\alpha - \frac{\sigma(\nu-1)}{\nu - 1 + \mathrm{e}^{-\sigma z}}, \tag{7.42}$$

where we have introduced the parameter $\nu \equiv \sigma/2C_0\beta_{2,0}$ $(\neq 0)$. With this form of the gain profile, we find the amplitude of the solitary wave solution to be:

$$A(z,T) = A_0(z)\,\mathrm{sech}\left(\frac{T}{W(z)}\right), \tag{7.43}$$

where the evolution of the peak amplitude $A_0(z)$ and the pulse width $W(z)$ are given by:

$$A_0(z) = \frac{\nu}{T_0}\sqrt{\left|\frac{\beta_{2,0}}{\gamma_0}\right|}\left(\frac{\exp[-\frac{1}{2}(\alpha+\sigma)z]}{\nu-1+\mathrm{e}^{-\sigma z}}\right), \tag{7.44}$$

$$W(z) = \frac{T_0}{\nu}\left(\nu-1+\mathrm{e}^{-\sigma z}\right), \tag{7.45}$$

together with the phase:

$$\Phi(z,T) = \phi_0 - \frac{\beta_{2,0}\nu}{2\sigma T_0^2}\left(\frac{1-\mathrm{e}^{-\sigma z}}{\nu-1+\mathrm{e}^{-\sigma z}}\right) + \frac{\sigma}{2\beta_{2,0}}\left(\frac{T^2}{\nu-1+\mathrm{e}^{-\sigma z}}\right). \tag{7.46}$$

To demonstrate typical physical systems where these solutions apply we consider the two simplest cases corresponding to: (i) constant gain (i.e., where the amplifier is pumped from both ends) and (ii) constant loss (propagation in an undoped fibre). For case (i), referring to Eq. (7.42) it is clear that this takes place when $\nu = 1$ and $\alpha < 0$ so that $g = -\alpha = |\alpha|$. Here the energy of the pulse grows as $E(z) = E_0 \exp(|\alpha| z)$ whilst the width decreases $W(z) = T_0 \exp(-\sigma z)$. Thus this solution describes the compression of a pulse in a fibre amplifier. Furthermore, we note that by allowing the amplifier to have a distributed gain profile ($\nu \neq 1$) this solution provides other design possibilities for an amplifying pulse compressor.

For the second case (ii) of constant loss, again referring to Eq. (7.42) we require that $\nu = 1$ but now $\alpha > 0$ so that $g = -\alpha = -|\alpha|$ is negative. Despite the fact that the energy of the pulse now decays as $E(z) = E_0 \exp(-|\alpha| z)$, the width still decreases at the same rate, $W(z) = T_0 \exp(-\sigma z)$, so that again the pulse undergoes compression. Importantly, from these solutions we find that for systems with $\sigma > 0$ (dispersion decreasing fibre) the pulses will always undergo compression, whereas for $\sigma < 0$ (dispersion increasing fibre) the pulses will always broaden.

To illustrate the two cases discussed above, we consider the evolution of a pulse with an amplitude profile as described by Eq. (7.43) and a width of $T_0 = 4\,\mathrm{ps}$ ($7\,\mathrm{ps}$ FWHM) in a fibre of length $9\,\mathrm{m}$. We choose the fibre parameters to be: $\beta_{2,0} = -0.01\,\mathrm{ps^2 m^{-1}}$, $\gamma_0 = 0.01\,\mathrm{W^{-1} m^{-1}}$, $\sigma = 0.1\,\mathrm{m^{-1}}$, $g = -\alpha$ and $\alpha = \mp 0.25\,\mathrm{m^{-1}}$ corresponding to gain and loss, respectively. Fig. 7.2 shows the output pulses resulting from the simulations (solid curves) together with the theoretical predictions (circles) where in (a) the pulse has experienced $\sim 10\,\mathrm{dB}$

of gain and in (b) it has experienced $\sim 10\,\mathrm{dB}$ of loss. Clearly, in both cases the numerical simulations are in excellent agreement with the solitary wave solution. As expected, despite the different mechanisms involved, the rate at which the pulses compress is the same yielding output pulses with durations of $2.9\,\mathrm{ps}$ (FWHM). Defining the compression factor as: $F_\mathrm{c} = \Delta T_0/\Delta T_\mathrm{comp}$, where ΔT_0 and ΔT_comp are the input and output widths (FWHM) of the compressor [4], this corresponds to a compression factor of 2.5 for these pulses. Although the pulses have only undergone modest compression, because they are chirped they can be subjected to further compression to compensate for this. In fact, after additional linear compression (see Section 5.3.3) we find that the pulses have a width of $\sim 28\,\mathrm{fs}$ (FWHM), corresponding to a compression factor of $F_\mathrm{c} = 250$. This is pictured in Fig. 7.2(c) which shows the output pulse corresponding to the linear compression of the pulse in Fig. 7.2(a).

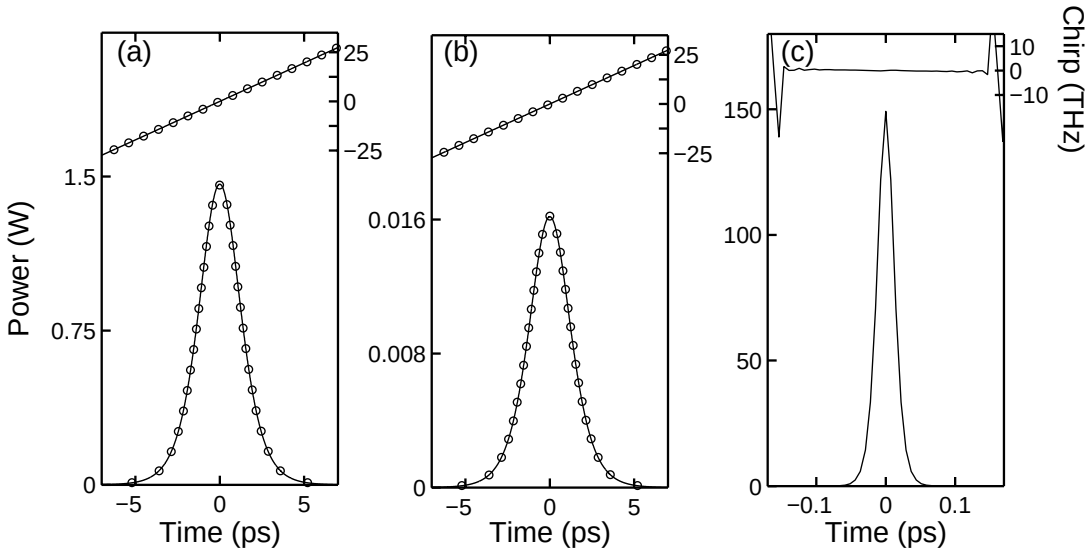

Figure 7.2: Intensity profiles (left axis) and chirps (right axis) of the output pulses from simulations (solid curves) in a fibre with both distributed dispersion and nonlinearity in the case of (a) constant gain and (b) constant loss (note the axis scales). The circles are the self-similar solitary wave solutions as predicted by the theory. (c) Output pulse from (a) after additional linear compression.

At this point we recall that previous attempts to simulate the nonlinear amplification of pulses in the anomalous dispersion regime, using constant parameters, have shown that the pulse tends to break up into a series of sub-pulses due to the combined effects of self-phase modulation and dispersion [4]. Importantly, these results have shown that by allowing the pulses to have an initial

chirp and the amplifier to have distributed coefficients, the pulses can undergo clean and efficient nonlinear compression producing high power short pulses.

7.4.2 Solitary Wave Solutions with Distributed Gain or Dispersion

We begin by returning to the solitary wave solution of Eq. (7.32) as found for $\kappa > 0$ and, assuming that the z-dependence of the nonlinear coefficient is negligible, we describe two cases corresponding to: (i) distributed gain and constant dispersion, and (ii) constant gain and distributed dispersion. We note that it was precisely these two systems that were previously investigated by Moores, as discussed in Section 7.2.

For case (i), solutions can be found for Eq. (7.1) with constant β_2 and γ provided the distributed gain function has the form [Eq. (7.30)]:

$$g(z) = \frac{g_0}{1 - g_0 z}. \tag{7.47}$$

With this gain profile it follows that the amplitude and phase of the chirped solitary wave are:

$$A(z,T) = \frac{\sqrt{|\beta_2|/|\gamma|}}{T_0[1 - g_0 z]} \operatorname{sech}\left(\frac{T}{T_0[1 - g_0 z]}\right), \tag{7.48}$$

and

$$\Phi(z,T) = \phi_0 - \frac{\beta_2}{2g_0 T_0^2[1 - g_0 z]} + \frac{g_0 T^2}{2\beta_2 - [1 - g_0 z]}. \tag{7.49}$$

For case (ii), the form of the dispersion profile that yields chirped solitary wave solutions with constant g and γ can again be found from Eq. (7.30) but by rearranging to make $\beta_2(z)$ the subject. This yields:

$$\beta_2(z) = \beta_{2,0} \exp[g_0 z - \eta(\exp(g_0 z) - 1)], \tag{7.50}$$

where $\eta = 2C_0\beta_{2,0}/g_0$ is a free parameter because C_0 is an arbitrary real parameter. In this case the solitary wave solution has amplitude and phase functions of the form:

$$A(z,T) = \frac{\sqrt{|\beta_2|/|\gamma|}}{T_0 \exp[-\eta(\exp(g_0 z) - 1)]} \operatorname{sech}\left(\frac{T}{T_0 \exp[-\eta(\exp(g_0 z) - 1)]}\right), \tag{7.51}$$

and

$$\Phi(z,T) = \phi_0 + \frac{1}{4C_0T_0^2} - \frac{\exp[\eta(\exp(g_0 z) - 1)]}{4C_0T_0^2} + \frac{C_0T^2}{\exp[-\eta(\exp(g_0 z) - 1)]}. \quad (7.52)$$

Comparing the above solutions with those of Ref. [64] it can be seen that, with the appropriate substitutions, these are identical. Thus by solving Eq. (7.1) we have been able to generalise the earlier predictions by Moores to include the possible effects of a variation in the mode size (and hence a distributed nonlinearity) and also the simultaneous variation of multiple fibre parameters.

To illustrate these results, Fig. 7.3 compares the outputs from simulations (solid curves) with the theoretical predictions (circles) for the two cases discussed above. In both instances we inject a $T_0 = 4\,\mathrm{ps}$ pulse with the appropriate form of the amplitude profile [Eq. (7.48) or Eq. (7.51)] into an amplifier of length $L = 9\,\mathrm{m}$ with parameters corresponding to a total pulse gain of $\sim 10\,\mathrm{dB}$. Fig. 7.3(a) shows the results for case (i) with $\beta_2 = -0.01\,\mathrm{ps^2 m^{-1}}$, $\gamma = 0.01\,\mathrm{W^{-1} m^{-1}}$ and $g_0 = 0.1\,\mathrm{m^{-1}}$, whilst Fig. 7.3(b) shows the results for case (ii) with $\beta_{2,0} = -0.01\,\mathrm{ps^2 m^{-1}}$, $\gamma = 0.01\,\mathrm{W^{-1} m^{-1}}$, $\sigma = 0.1\,\mathrm{m^{-1}}$, $g = 0.25\,\mathrm{m^{-1}}$ and $C_0 = \sigma/2\beta_{2,0}$. Clearly the simulation results are in excellent agreement with the theoretical predictions with the resulting output pulses having FWHM widths of (a) $698\,\mathrm{fs}$ and (b) $237\,\mathrm{fs}$, corresponding to compression factors of $F_\mathrm{c} = 10$ and $F_\mathrm{c} = 30$, respectively. Importantly we note that whilst in this instance case (ii) produced a shorter output pulse, as the final compressed width depends on the choice

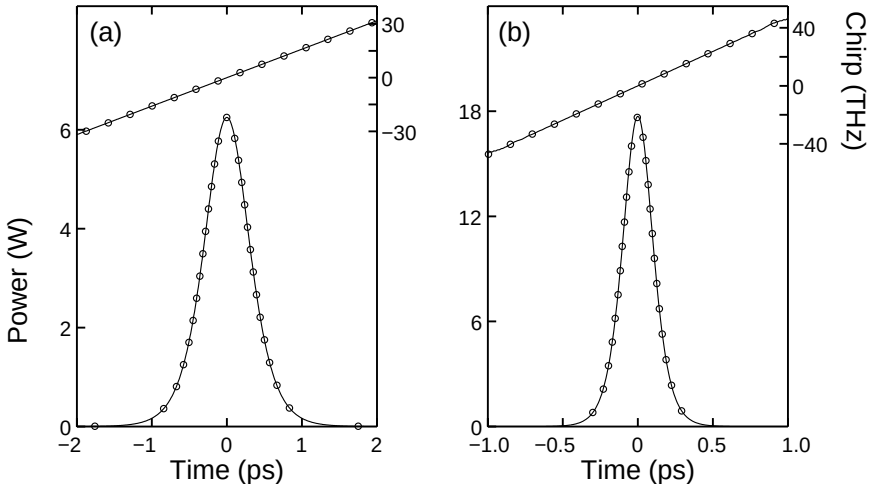

Figure 7.3: Intensity profiles (left axis) and chirps (right axis) of the simulated output pulses (solid curves) for (a) distributed gain and constant dispersion, and (b) constant gain and distributed dispersion. The circles are the self-similar solitary wave solutions as predicted by Eqs. (7.48)–(7.52) and by Ref. [64].

of input parameters this will not always be the case. In addition, as mentioned in the previous section, a further reduction of the pulse width can be achieved via linear compression of the residual chirp and in both cases the transform limited pulse has a duration of $\sim 28\,\mathrm{fs}$ (FWHM), again corresponding to compression factors of $F_\mathrm{c} = 250$.

We now wish to reconsider case (i) described above (i.e., distributed gain and constant dispersion), but this time applying the results to the oscillatory solutions of Eq. (7.37). It follows from the form of the gain profile, Eq. (7.47), that the amplitude and phase of the chirped oscillatory solution are:

$$A(z,T) = \frac{\sqrt{|\beta_2|/|\gamma|}\mathrm{k}}{T_0[1-g_0 z]}\,\mathrm{cn}\left(\frac{T}{T_0[1-g_0 z]},\,\mathrm{k}\right), \tag{7.53}$$

and

$$\Phi(z,T) = \phi_0 - \frac{\beta_2}{2g_0 T_0^2[1-g_0 z]} + \frac{g_0 T^2}{2\beta_2[1-g_0 z]}, \tag{7.54}$$

so that the form of the phase is identical to the phase of the solitary wave solution [Eq. (7.49)]. Significantly, we note that in the amplitude solution, T_0 refers to the width of the oscillations and not the length of the pulse train.

In order to demonstrate the important features of these oscillatory solutions Fig. 7.4 plots both the input truncated pulse train and corresponding output pulse train after propagation in a $0.9\,\mathrm{m}$ long amplifier with: $\beta_2 = -0.01\,\mathrm{ps}^2\mathrm{m}^{-1}$,

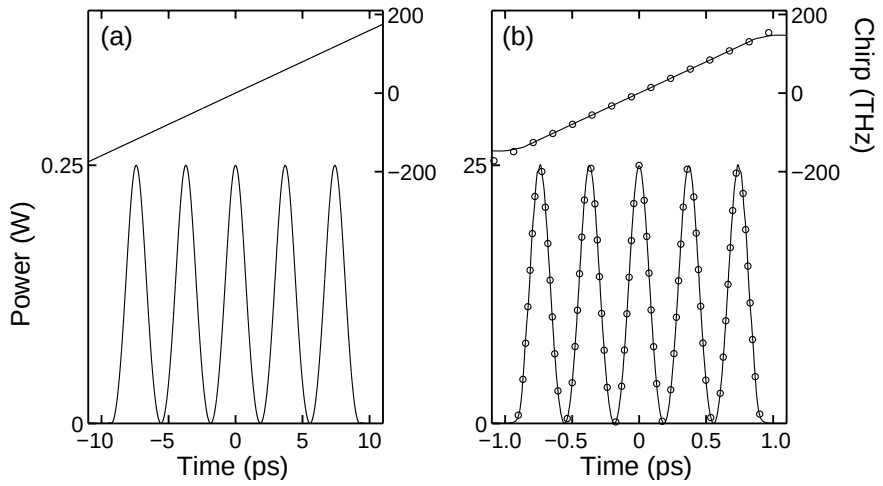

Figure 7.4: Intensity profiles (left axis) and chirps (right axis) of the self-similar oscillatory wave solutions corresponding to Eq. (7.37) where (a) is the input pulse train and (b) is the simulated output pulse train after propagation in an amplifier with distributed gain and constant dispersion. In (b) the circles are the theoretical predictions of Eqs. (7.53) and (7.54).

$\gamma = 0.01\,\mathrm{W^{-1}m^{-1}}$, $T_0 = 1$, $\mathrm{k} = 1/2$ and $g_0 = 1\,\mathrm{m^{-1}}$ (so that the gain is $10\,\mathrm{dB}$). The excellent agreement between the output profile and chirp (solid lines) with the theoretical predictions (circles) confirms the self-similar nature of the evolution. In addition, on comparing the rate of the oscillations of the input and output pulse trains (see x axes) it is clear that the modulation frequency at the output is 10 times larger than at the input which is a significant enhancement. Thus we expect these solutions to find application as a new way to generate very high frequency amplitude modulated light.

7.5 Stability of the Solutions

The results presented in Sections 7.4.1 and 7.4.2 have verified the excellent agreement between the theoretical predictions and simulations based on the generalised NLSE of Eq. (7.1). However, in these simulations we have considered the evolution of ideal input pulses in fibres with the exact distributed dispersion, nonlinearity and gain profiles. In addition, we have also neglected the higher order terms in the NLSE which will become important as the pulses compress to the femtosecond regime. Consequently, these results tell us little about the robustness of the system to perturbations and more importantly, of their suitability to real experimental situations. Thus in this section we investigate the solitary wave solutions under various non-optimum conditions to establish the stability of their evolution. Specifically, we consider the cases corresponding to a non-ideal input pulse, an incorrect gain profile, the influence of higher order dispersion and nonlinear effects and finally, the combined effect of the perturbations in an amplifier with experimentally realistic parameters.

7.5.1 Evolution of a Non-Ideal Input Pulse

A useful test of the stability of a self-similar solution is to investigate the evolution of a pulse with initial parameters that deviate from their ideal values. In this sense we know that solitons are stable as a soliton-like pulse with non-ideal input parameters will shed any excess energy (in the form of dispersive waves) as the pulse evolves to the exact soliton solution. In this section we consider three types of perturbation to the solitary wave solutions: (i) an in-

put peak power which is less than the ideal value, (ii) an input chirp with a slope that is less than the ideal value, and (iii) an ideal input pulse but with the addition of random noise on the amplitude and phase.

We investigate the system described in Section 7.4.1 corresponding to propagation in an amplifier with distributed dispersion and nonlinearity, but constant gain, so that the solitary wave solution is given by Eqs. (7.43)–(7.46) with $\nu = 1$ and $\alpha < 0$. Under these conditions, the optimum input peak power and chirp are:

$$P_{\rm opt} = \frac{1}{T_0^2}\left|\frac{\beta_{2,0}}{\gamma_0}\right| \quad \text{and} \quad \Omega_{\rm opt} = -\frac{\partial\Phi}{\partial T} = \frac{-\sigma T}{\beta_{2,0}}. \tag{7.55}$$

Unless otherwise stated, the input pulse and fibre parameters are the same as those used to generate Fig. 7.2(a). Both the input pulses (top curves) and output pulses (bottom curves) are plotted in Fig. 7.5 together with the predicted analytic solutions (circles). Fig. 7.5(a) shows the pulse generated from the amplification of an input pulse with a peak power of $0.95P_{\rm opt}$. The fact that the peak power of the simulated output is still less than that of the theoretical predictions is to be expected as in both cases (simulated and analytic) the pulses have seen the same effective gain. However, importantly the simulated pulse still has a peak power which is $95\,\%$ of the analytic solution and there has been no significant change to the shape of the pulse profile or the chirp. Thus this suggests that despite the non-optimum input power the pulse can still propagate self-similarly.

In Fig. 7.5(b) we then compare the results from the amplification of a pulse with an initial chirp of $0.95\Omega_{\rm opt}$. Unlike the previous case of a reduced input power, this time there is further deviation from the expected chirp with the output slope now being $89\,\%$ of the analytic prediction. Furthermore, we see that the intensity profile has also deviated from the theory and this is because the simulated pulse has undergone less compression than predicted. Although these deviations are small, they nonetheless highlight the fact that the self-similar evolution of the pulse is more sensitive to the initial slope of the chirp function than to the peak power.

Finally, Fig. 7.5(c) shows the output pulse generated from the amplification of an ideal input pulse but with $5\,\%$ random noise on the amplitude and phase. Despite there still being some remaining noise on the output pulse, it is clear that both the profile and the chirp are in excellent agreement with the theory.

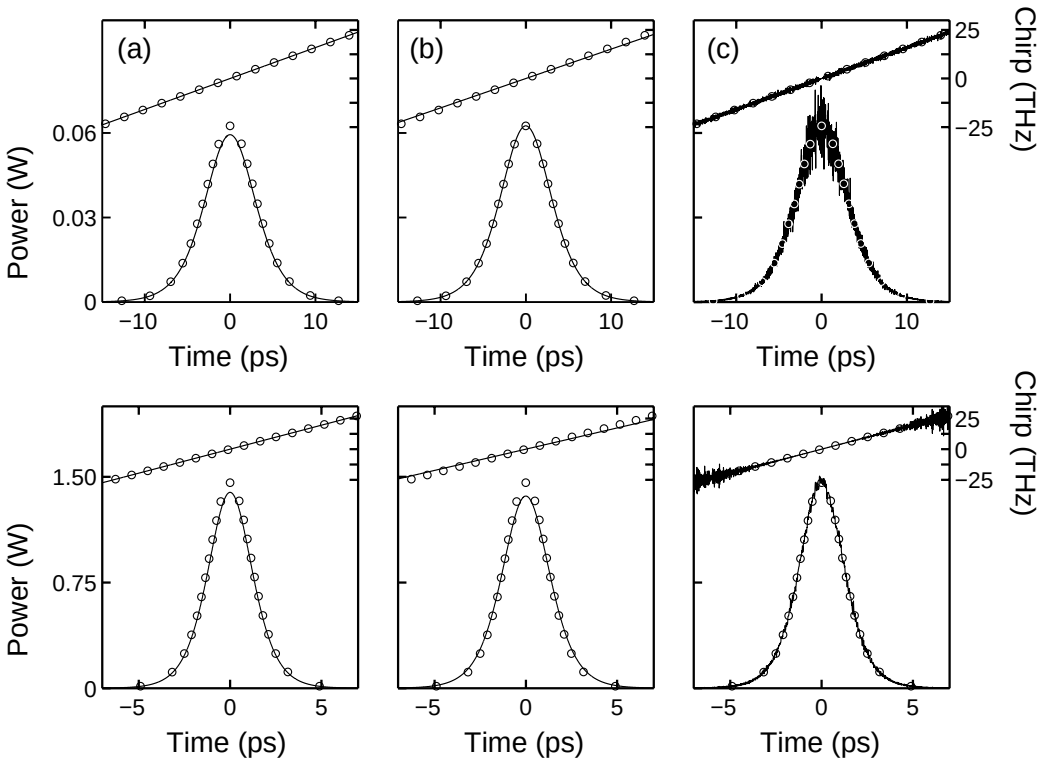

Figure 7.5: Top: intensity profiles (left axis) and chirps (right axis) of the input pulses where: (a) the peak power is $0.95P_{\rm opt}$, (b) the chirp is $0.95\Omega_{\rm opt}$, and (c) there is $5\,\%$ random noise on the amplitude and phase (solid curves). Bottom: intensity profiles and chirps of the pulses after amplification. In all cases the numerical pulses are compared with the theoretical predictions under ideal conditions (circles).

In addition, as the relative size of the noise on the output pulse is much less than that on the input pulse, this provides further confirmation of the stability of the solitary wave solutions in the presence of noise.

7.5.2 Evolution in an Amplifier with an Incorrect Gain Profile

As we saw in Section 7.4, once the dispersion and nonlinearity profiles of an amplifier are known the shape of the gain profile required to observe self-similar propagation can be found via Eq. (7.30). However, as the shape of the gain profile is largely determined by saturation effects caused by pump depletion, and thus the pumping geometry, such accurate control over its longitudinal variation is not possible. For this reason here we study the evolution of a pulse in an amplifier with an experimentally realistic profile that differs slightly in shape from the ideal profile, yet yields the same total pulse gain.

We consider the evolution of a pulse in an amplifier with distributed gain but constant dispersion and nonlinearity so that the situation corresponds to case (i) described in Section 7.4.2. We recall that the shape of the gain profile required for self-similar propagation in such a fibre is given by [Eq. (7.47)]:

$$g(z) = \frac{g_0}{1 - g_0 z}.$$

An experimentally realistic approximation to this, corresponding to counter-directional pumping, is an exponentially increasing profile of the form:

$$g\,(z) = g_0 \exp\,(z/z_a)\,, \tag{7.56}$$

where z_a determines the rate of increase. With the input pulse and fibre parameters the same as those used to generate Fig. 7.3(a), to ensure that the total pulse gain also remains the same ($\sim 10\,\mathrm{dB}$) we require $z_a = 5.44\,\mathrm{m}$. Fig. 7.6 shows the intensity profile and the chirp of the output pulse from the simulations with the gain profile given in Eq. (7.56) (solid curves), clearly in agreement with the theoretical predictions based on the exact gain profile (circles). Thus this suggests that the self-similar nature of these solutions is sufficiently robust to withstand amplification in an experimental situation where the longitudinal gain may deviate from the ideal profile.

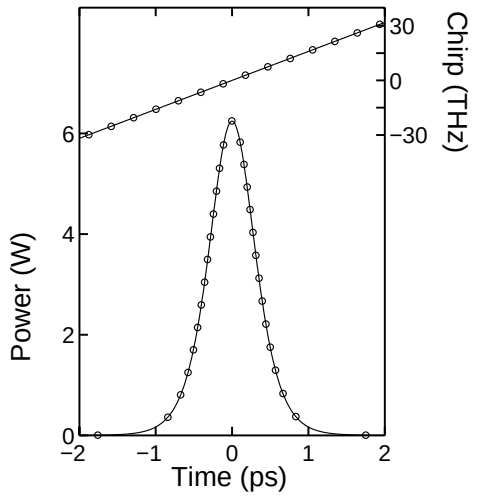

Figure 7.6: Intensity profile (left axis) and chirp (right axis) generated via amplification of the solitary wave solution with a gain profile given by Eq. (7.56) (solid curves) compared with the analytic solitary wave predictions for the exact gain profile (circles).

7.5.3 Evolution in an Amplifier with Higher Order Effects

Third Order Dispersion

As discussed in Chapter 3, although the basic form of the NLSE employed in this chapter [Eq. (7.1)] is remarkably successful in describing many of the features of pulse propagation in fibre amplifiers [4], it often needs to be extended to include higher order terms when the bandwidth of a pulse becomes large. Thus in this section we consider the effects of higher order dispersion and nonlinearity, independently, to establish whether the neglect of such terms in our theoretical analysis was justified. As in Section 7.5.1, in both cases we investigate the system described in Section 7.4.1 corresponding to propagation in an amplifier with distributed dispersion and nonlinearity, but constant gain, so that the solitary wave solution is given by Eqs. (7.43)–(7.46) with $\nu = 1$ and $\alpha < 0$. Again we choose the input pulse and fibre parameters to be the same as those used to generate Fig. 7.2(a).

The equation describing pulse propagation in a fibre including the effects of third order dispersion is [Eq. (3.7)]:

$$\mathrm{i}\frac{\partial \Psi}{\partial z} = \frac{\beta_2(z)}{2}\frac{\partial^2 \Psi}{\partial T^2} + \mathrm{i}\frac{\beta_3}{6}\frac{\partial^3 \Psi}{\partial T^3} - \gamma(z)\left|\Psi\right|^2\Psi + \mathrm{i}\frac{g\,(z)}{2}\Psi, \tag{7.57}$$

where we have assumed that the z-dependence of β_3 is negligible. With the choice of $\beta_3 = 0.1 \times 10^{-4}\,\mathrm{ps}^3\mathrm{m}^{-1}$, we obtain an output pulse of the form given in Fig. 7.7(a). Although there is still good agreement between the intensity profile of the simulated pulse (solid curves) and the solitary wave solution (circles), clearly the symmetry of the pulse profile and the linearity of the chirp have been destroyed. These intensity and phase distortions are well known consequences of propagation with higher order dispersion which arise due to the cubic spectral phase introduced by the third order dispersive term [4]. Consequently, we expect that for larger values of β_3, or alternatively, longer amplifier lengths, the pulses will become highly distorted so that the theoretical predictions will no longer be valid. However, these results show that the solitary pulses can endure a small amount of higher order dispersion and with the availability of dispersion flattened fibres to provide $\beta_3 \approx 0$ we expect that these solutions should be valid for a wide range of systems.

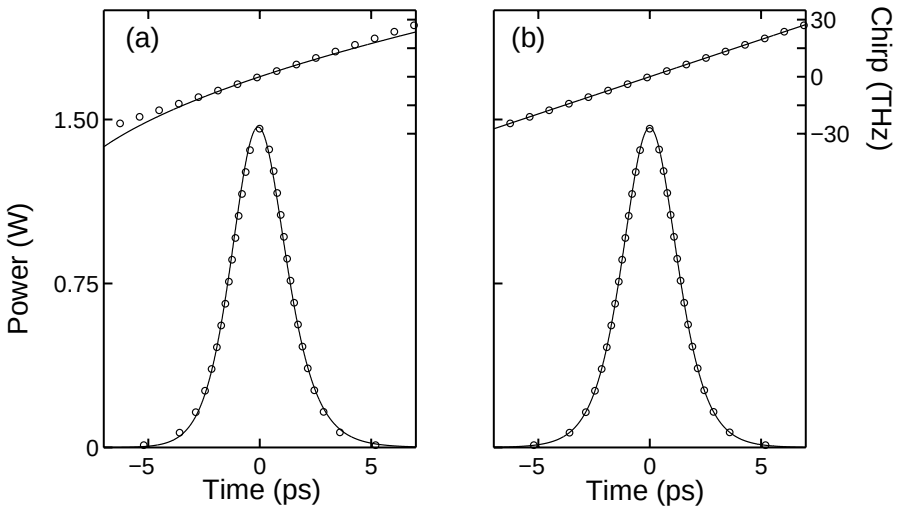

Figure 7.7: Intensity profiles (left axis) and chirps (right axis) of the output pulses generated under amplification with: (a) third order dispersion and (b) Raman gain. The numerical simulations (solid curves) are compared with the predicted self-similar solitary wave solutions (circles).

Delayed Nonlinear Response

In Section 3.10.2 it was noted that for pulses with bandwidths in excess of $1\,\mathrm{THz}$ it is possible for the Raman gain to amplify the low frequency components by transferring energy from the high frequency components of the same pulse. Modifying Eq. (3.54) to include the effects of longitudinally varying fibre parameters yields:

$$\mathrm{i}\frac{\partial \Psi}{\partial z} = \frac{\beta_2(z)}{2}\frac{\partial^2 \Psi}{\partial T^2} + \mathrm{i}\frac{g\ (z)}{2}\Psi - \gamma(z)\left(1 + \frac{\mathrm{i}}{\omega_0}\frac{\partial}{\partial T}\right)\Psi \int_0^\infty R(T')\left|\Psi\left(z, T - T'\right)\right|^2 \mathrm{d}T', \tag{7.58}$$

where again $R\left(T\right) = \left(1 - f_R\right)\delta\left(T\right) + f_R h_R\left(T\right)$. The output pulse from the simulations is plotted in Fig. 7.7(b) (solid curves) showing excellent agreement with the solitary wave solution (circles). As expected the simulated pulse has undergone a slight frequency shift. However, this was calculated to be $0.192\,\mathrm{MHz}$ (in the red direction) which, compared to the terahertz bandwidth of the pulse, is negligible. The slightness of the self-frequency shift seen here, relative to the soliton self-frequency shift [29], can be attributed to the fact that the pulse is chirped (which results in a spreading of the frequency components) so that internal pumping of the high frequency components to the low frequencies is less efficient. Although the effects of Raman gain also accumulate over the length of the fibre, the length required for the effects to become noticeable is

well beyond practical amplifier lengths. Thus these results illustrate the insensitivity of the solitary wave solutions to Raman gain, justifying the neglect of this effect in the theoretical analysis.

7.5.4 Evolution in an Experimentally Realistic Amplifier

Having considered each of the perturbative effects independently, in this section we now consider the evolution of a pulse in an amplifier with realistic experimental parameters under the influence of a combination of these effects. Again we return to the case of a pulse in an amplifier with distributed gain but constant dispersion and nonlinearity so that the situation corresponds to case (i) described in Section 7.4.2. Assuming an input pulse given by Eqs. (7.48) and (7.49), with $T_0 = 4\,\mathrm{ps}$ and $5\,\%$ random noise on the amplitude and phase, we investigate the propagation of pulses in an amplifier with the exponentially increasing gain profile as given in Section 7.5.2 [Eq. (7.56)] and including the effects of Raman gain. Explicitly, the amplifier parameters are: $\beta_2 = -0.024\,\mathrm{ps^2 m^{-1}}$, $\beta_3 = 0.1 \times 10^{-4}\,\mathrm{ps^3 m^{-1}}$, $\gamma = 5.6 \times 10^{-4}\,\mathrm{W^{-1} m^{-1}}$, $g_0 = 0.1\,\mathrm{m^{-1}}$ and $z_a = 6.36\,\mathrm{m^{-1}}$. Here z_a was chosen so that the total pulse gain is the same as that for the exact gain profile after $8\,\mathrm{m}$ of amplification. The simulated output

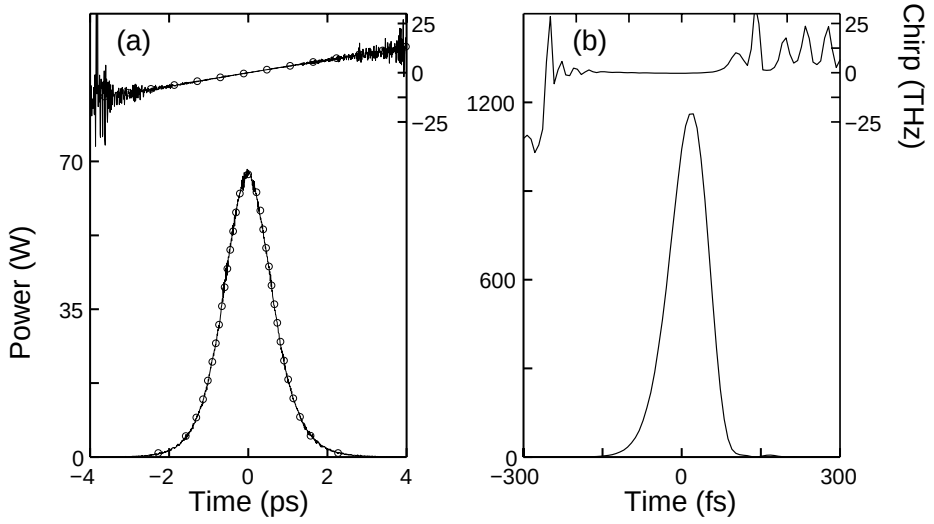

Figure 7.8: Intensity profile (left axis) and chirp (right axis) of the output pulse generated under amplification with experimentally realistic parameters and a combination of perturbative effects. The numerical simulations (solid curves) are compared with the predicted self-similar solitary wave solutions (circles). (b) The corresponding pulse after additional linear compression.

pulse is plotted in Fig. 7.8(a) (solid curves), showing excellent agreement with the theoretical predictions (circles). The corresponding pulse after additional linear compression is then given in Fig. 7.8(b) where the minimum pulse width is $85\,\mathrm{fs}$ (FWHM) so that $F_\mathrm{c} = 76$. The success of these results provides the final evidence of the robustness of these solutions to real experimental conditions.

7.5.5 Discussion

The results presented in this section have shown that the solitary wave solutions found for Eq. (7.1), in the case of anomalous dispersion, are relatively insensitive to perturbations from the ideal system. Thus in spite of the simple model on which the theory was based, the analytic solutions should provide an accurate description of pulse propagation in fibres and fibre amplifiers with distributed parameters. In addition, these simulations have highlighted areas where extra care needs to be taken when designing an experimental system such as the precise choice of the input chirp and the use of fibres and amplifiers with relatively flat dispersion slopes.

Chapter 8

Conclusion

In Part 1 of this thesis I have presented results of investigations of self-similar solutions for high intensity pulses propagating in optical fibres and optical fibre amplifiers.

The experimental and numerical results of Chapters 5 and 6 have demonstrated novel techniques for generating linearly chirped parabolic pulses which are well known self-similar solutions to the NLSE with gain. The experimental investigations of Chapter 5 to generate high energy parabolic pulses in a cascaded amplifier chain have shown that whilst it is indeed possible to generate output pulses in the early stages of the parabolic regime, the output energies are lower than expected. Numerical simulations have indicated that the main limitation to the system performance is the small gain bandwidths of the preamplifiers.

The numerical simulations presented in Chapter 6 then demonstrated that parabolic pulse formation was possible in a range of normal dispersion undoped microstructured fibre Raman amplifiers. The success of these results was attributed to the large gain bandwidth offered by the pure silica host and the ability to tailor the dispersion profile of a microstructured fibre to provide normal dispersion over a wide range of wavelengths. In addition, preliminary experimental results of parabolic pulse formation in a highly nonlinear microstructured were also reported. Despite being limited by our low output powers and our pulse diagnostic techniques, comparison with numerical simulations indicated that the pulses were nonetheless entering the early stages of

the parabolic regime, thus confirming the numerical predictions.

Finally, Chapter 7 presented the results of theoretical calculations to describe a new class of self-similar solutions which exist for the NLSE with distributed coefficients. It was shown that this class encloses a set of solitary wave solutions as well as a set of periodic “oscillatory” solutions which describe amplitude modulated light. The theoretical results have been verified numerically and additional simulations were conducted to established the stability of the solutions.

The work described in this part of the thesis has led to some important new results regarding self-similar pulse solutions in nonlinear optics. Due to the unique distortion-free propagation properties of self-similar pulses, it is expected that they will find wide ranging applications in the development of the next generation of ultrashort pulse sources. It is hoped that the results presented in this part of the thesis can contribute to this development.

Part II

Controlling Light Propagation in Periodic Materials

Chapter 9

Introduction

A considerable number of the major technological breakthroughs of our time have evolved out of the establishment of a deeper understanding of the properties of materials. Importantly, the significance of knowing a material's properties was a concept that was established even as far back as prehistoric times. Indeed, the transition of our ancestors from the Stone age through to the Iron age can be attributed to their increased recognition of the physical qualities of natural materials. However, motivated by the desire for more elaborate tools, eventually early engineers learned to do more than simply take what the Earth provided in the raw form. By manipulating the properties of naturally occurring materials it was quickly established that substances with even more desirable properties could be produced, with one of the earliest examples being bronze [68].

In the last century, our control over materials has become even more sophisticated and today our lives are surrounded by a whole host of artificial materials such as plastics, ceramics and metal alloys. In particular, more recently control of the electrical and optical properties of such materials has led to important revolutions in many fields such as semiconductor physics and optical telecommunications. Whilst some of these advancements have been associated with the invention of complex structures such as band gap crystals that can prohibit the propagation of light at certain frequencies [69], others have been as simple as optical fibres which can guide and manipulate the propagation of light (as described in Part 1 of this thesis).

In this second part of this thesis I will describe investigations to control the propagation of light in materials whose physical properties have been modulated in some way. Such materials are commonly referred to as metamaterials. In the investigations, two distinct types of modified materials will be considered which have both been shown to exhibit effects which strongly influence electromagnetic fields. The first are the exotic negative refractive index materials which have only recently been observed experimentally [70]. Such negative index materials are currently generating much interest because they exhibit a number of properties that differ considerably from those of positive index materials, and specifically for their ability to manipulate the speed of light. The second are two dimensional electrically poled nonlinear crystals [71]. These form a novel extension to the well known one dimensional photonic crystal structures and in particular, provide an attractive opportunity to achieve phase matching of multiple nonlinear processes. Despite the significant differences between the two materials, all of the investigations presented in the following chapters are focused towards the common theme of controlling and manipulating the propagation of light in modulated crystal structures. Thus it is expected that they will benefit many areas of optical technologies including the development of lasers, high speed computers and optical data storage devices.

9.1 Controlling the Speed of Light

It follows from the fundamental physical notion of causality and the theory of special relativity that information cannot be passed with a velocity exceeding that of light in a vacuum. However, it is well known that various velocities, such as the phase velocity v_p , can exceed c without violating special relativity because they do not represent velocities of signals, or information. Despite this, an enduring misconception is that the group velocity v_g of a light pulse cannot be faster than c, or equivalently negative, where the propagation is also considered to be superluminal [72]. Thus, in 1968 when Veselago proposed that a material with a negative refractive index will possess a negative group velocity [73], this sparked much debate into the validity of his work which still continues today [74, 75].

Due to the absence of naturally occurring negative index materials, until re-

cently there was little research that could be conducted to settle these arguments. However, in 1996 Pendry *et al.* proposed a simple periodic structure that could be used to observe a negative dielectric permittivity [76] and this was closely followed by subsequent work to construct a material with a negative magnetic permeability [77]. Consequently, it was not long before these results were combined to provide the first demonstration of a negative refractive index material [70]. As well as providing the vital component for the verification of Veselago's predictions this demonstration aroused considerable interest into the phenomena of negative refraction, and in particular, to the possibility of manipulating the speed of light. Thus, to date, not only have there been a number of demonstrations of superluminal light [78, 79], it has also been shown that these materials can exhibit slow light which has important implications for the design of optical traps [80].

9.2 Harmonic Frequency Generation

Coherent short wavelength sources have a wide range of applications in many areas of optical technology. In particular, such sources can increase the capacity of optical storage devices and can be used to fabricate and inspect nanostructures and high density integrated circuits [81]. Although the production of semiconductor lasers which operate at blue, or shorter, wavelengths has been achieved, this technology is still in the early stages of development [82]. An alternative approach, which avoids the expensive development of new materials, is to employ well established existing "cheap" lasers which operate at longer wavelengths and frequency double (or triple) their output radiation. To this end, highly nonlinear materials such as lithium niobate ($LiNbO_3$) and potassium titanyl phosphate (KTP) have been the subject of much attention as candidates for use in quasi-phase matched second harmonic generation (SHG) devices.

Since the first observation of SHG by Franken *et al.* in 1961 [83], interest in this field has grown considerably. As a result, much attention has been devoted to the development of highly efficient nonlinear crystals and the enhancement of harmonic processes. The primary limitation of efficient harmonic generation in nonlinear crystals has always been the material dispersion, which causes

the interacting fields to move out of phase. An important breakthrough in this area thus came in 1962 when Giordmaine [84] and Maker *et al.* [85] demonstrated that the efficiency of these processes could be dramatically improved by using the birefringence of the crystal to match the relative phase velocities of the propagating beams. However, later in the same year Armstrong *et al.* proposed the concept of quasi-phase matching in which the fields are periodically brought back into phase by modifying the crystal structure, and it is this technique that is most commonly employed today [86]. Although quasi-phase matching was originally conceived for the purpose of one dimensional geometries such as periodically poled lithium niobate (PPLN) [86, 87, 88], the concept has been extended to one dimensional aperiodic structures [89] and more recently, to two dimensional periodic patterns, with great success [71, 90].

9.3 Outline for Part 2

Chapter 10 introduces the basic structure of a photonic crystal and presents some of the theory used to describe the propagation of light in these crystals. In particular, this will include a model to describe SHG in a nonlinear photonic crystal.

In Chapter 11, numerical investigations of the properties of the guided modes in negative refractive index waveguides are described. By calculating the propagation characteristics of the guided modes a number of peculiar properties of the solutions will be revealed.

Chapter 12 presents experimental measurements of SHG in a two dimensional photonic crystal structure. To enhance the efficiency of the process a planar waveguide geometry is employed in the investigations. The performance of the waveguide is evaluated by determining the interaction properties of the fundamental and second harmonic fields.

In Chapter 13 a new type of two dimensional quasi-crystal structure based on a Penrose tiled pattern is investigated. The preliminary experiments involving SHG have indicated the dense nature of the reciprocal lattice space so that phase matching can occur almost continuously over a wide range of angles.

Finally, in Chapter 14 I will present the conclusions to Part 2 of this thesis.

Chapter 10

Controlling Light in Periodic Materials

10.1 Introduction

As discussed in the previous chapter, the second part of this thesis investigates the control and manipulation of light in modulated crystal structures. In order to understand the physical aspects of the various processes, this chapter introduces some of the basic properties of a crystalline structure and the equations which describe them.

This chapter begins with an introduction to the concept of a photonic crystal, on which the bulk of the investigations are based, and discusses the construction of such structures in one and two dimensions. After a brief description of the mathematical formalism which defines the crystal lattice and its representation in reciprocal lattice (or wavevector) space, the linear and nonlinear effects which influence the evolution of a propagating field will be described. To complement the discussion of these effects, the mathematical equations which define the fields under certain special conditions will also be presented with particular attention being paid to the phase matching considerations for fields interacting in nonlinear dispersive materials. Finally, as the bulk of the investigations considered in this part of thesis will focus on second harmonic generation (SHG) in nonlinear crystals, the development of a model to analyse the evolution of the propagating fields will be described.

10.2 Photonic Crystals

To understand how a material structure might be modified in order to manipulate the propagation of light within it, it is useful to make an analogy with electronic materials, such as ordinary semiconductor crystals. These crystals form a periodic lattice where the basic building blocks are atoms or molecules. Thus a semiconductor crystal will present a periodic potential to a propagating electron where the conduction properties will be dictated by the geometry of the structure. In particular, due to Bragg-like diffraction from the atoms, the lattice can introduce gaps into the energy spectrum of the electron so that electrons with energies within these gaps are forbidden to propagate.

An optical analogy to this effect is the material structure offered by photonic crystals, where the lattice is now constructed via a periodic modulation of a material's properties. Provided the modulation is sufficiently strong, scattering off the interfaces in a photonic crystal can produce many of the same phenomena for photons as the atomic potential does for electrons. Significantly, as photonic crystals are scalable to a wide range of dimensions these can be constructed with millimeter periodicity for microwave control, or with micron periodicity for infrared control. Photonic crystals can form the basis of a wide range of devices from dielectric mirrors to waveguides and are thus currently being exploited in many areas of optical technology [69].

10.2.1 One Dimensional Photonic Crystals

The simplest photonic crystal is a one dimensional Bragg grating structure of the type shown in Fig. 10.1. This consists of alternating semi-infinite layers of material with differing physical properties. In situations where the modulated property is the dielectric constant, such crystals have found use as dielectric mirrors and optical filters [1]. However, in this part of the thesis the majority of the investigations will consider the periodic modulation of the nonlinear coefficient, and in this arrangement these nonlinear photonic crystals can be used to phase match SHG in dispersive nonlinear media [86].

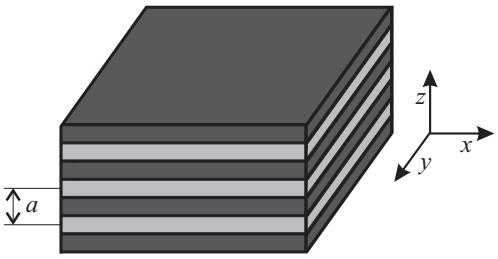

Figure 10.1: Sketch of a one dimensional photonic crystal.

10.2.2 Two Dimensional Photonic Crystals

A typical two dimensional photonic crystal is shown in Fig. 10.2. This is constructed based on a square lattice of columns where again the physical properties of the columns differ from that of the background media. These structures are periodic in a plane constructed along two of its axes and are homogeneous in the third. Thus the propagation effects observed in the z direction of a one dimensional crystal can now occur for propagation over the entire $x-y$ plane.

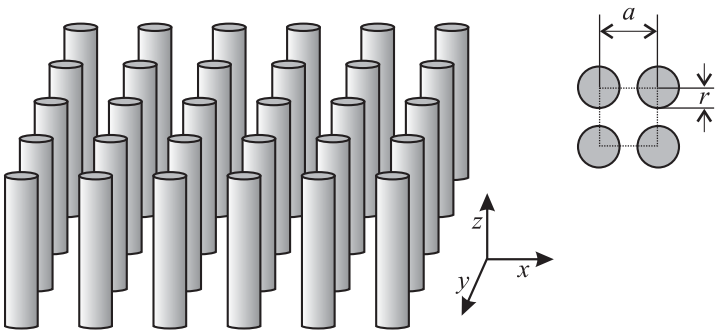

Figure 10.2: Sketch of a two dimensional photonic crystal. The right inset shows the square lattice from above together with the unit cell (dashed line).

10.2.3 Quasi-Crystals

An interesting extension to the defined subset of periodic photonic crystals described above are quasi-crystals. These structures have a quasi-periodic translational order and can be designed in either one dimension (Fibonacci sequences [91]) or two dimensions (Penrose tiles [92]). One dimensional quasi-crystals are very similar to the structure shown in Fig. 10.1 but with layers of

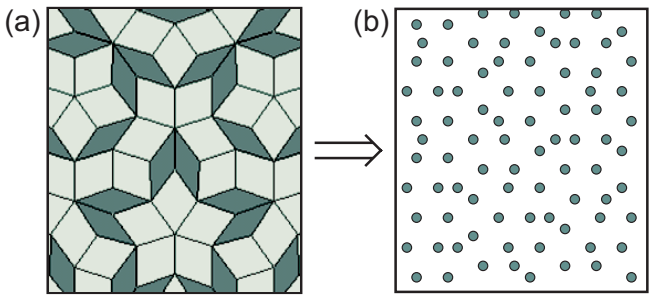

Figure 10.3: (a) A Penrose tile pattern that is constructed out of thick and thin rhombi. (b) An example of a two dimensional quasi-crystal (cross section in the $x - y$ plane) based on the structure in (a).

differing widths stacked aperiodically. However, in two dimensions the structures are usually constructed by placing a feature with a single basic shape (such as a cylinder as used in Fig. 10.2) at the vertices of a quasi-crystalline tiling pattern. An example of a two dimensional quasi-crystal based on a Penrose tile pattern, constructed out of thick and thin rhombi, is shown in Fig. 10.3. A significant feature of quasi-crystals is that they can possess higher, or even forbidden, rotational symmetries than periodic crystals and this has important consequences to their use in multiple harmonic generation processes, as will be demonstrated in Chapter 13.

10.3 Reciprocal Lattice Space and the Brillouin Zone

The photonic structures illustrated in Figs. 10.1–10.3 were shown in real, or lattice, space. However, an equally valid presentation of the crystal could have also been obtained through their structure in reciprocal lattice space. As the reciprocal lattice is the space inhabited by the wavevectors, it is this space that will be considered when establishing the phase matching conditions of the crystals in Chapters 12 and 13. The following analysis develops the mathematical representation of the reciprocal lattice vectors which define the reciprocal space.

If a function $f(\mathbf{r})$ is considered which is periodic on a lattice, then $f(\mathbf{r}) = f(\mathbf{r} + \mathbf{R})$ where the set of vectors $\mathbf{R}$ are the lattice vectors. Expanding $f(\mathbf{r})$ in terms of plane waves with various wave vectors $\mathbf{q}$ yields:

$$f(\mathbf{r}) = \int \mathrm{d}\mathbf{q} g(\mathbf{q}) \mathrm{e}^{\mathrm{i}\mathbf{q}\cdot\mathbf{r}}, \tag{10.1}$$

where $g(\mathbf{q})$ is the coefficient of the plane wave. It follows that the requirement $f(\mathbf{r}) = f(\mathbf{r}+\mathbf{R})$ implies:

$$f(\mathbf{r}+\mathbf{R}) = \int \mathrm{d}\mathbf{q} g(\mathbf{q}) \mathrm{e}^{\mathrm{i}\mathbf{q}\cdot\mathbf{r}} \mathrm{e}^{\mathrm{i}\mathbf{q}\cdot\mathbf{R}} = \int \mathrm{d}\mathbf{q} g(\mathbf{q}) \mathrm{e}^{\mathrm{i}\mathbf{q}\cdot\mathbf{r}}, \tag{10.2}$$

so that $\mathrm{e}^{\mathrm{i}\mathbf{q}\cdot\mathbf{R}} = 1$ or $\mathbf{q}\cdot\mathbf{R} = 2\pi N$, where N is an integer. Thus the vectors which satisfy this condition are the reciprocal lattice vectors and these are usually designated by the letter $\mathbf{G}$. Furthermore, as in general the analysis can be restricted to consider a discrete number of reciprocal lattice vectors, the integration in Eq. (10.1) can be replaced by a weighted sum so that:

$$f(\mathbf{r}) = \sum_{\mathbf{G}} f_{\mathbf{G}} \mathrm{e}^{\mathrm{i}\mathbf{G}\cdot\mathbf{r}}, \tag{10.3}$$

where $f_{\mathbf{G}}$ are the corresponding Fourier coefficients.

For a given set of lattice vectors $\mathbf{R}$ it is straight forward to calculate the reciprocal lattice vectors $\mathbf{G}$. As every lattice vector can be expressed in terms of a set of primitive lattice vectors $\mathbf{a}_1$ and $\mathbf{a}_2$ (which are the smallest vectors pointing from one lattice point to another), $\mathbf{R}$ can be written as: $\mathbf{R} = l\mathbf{a}_1 + m\mathbf{a}_2$. Likewise, the reciprocal lattice also has a set of primitive vectors $\mathbf{b}_i$ so that: $\mathbf{G} = l'\mathbf{b}_1 + m'\mathbf{b}_2$. Thus the reciprocal lattice vectors can be calculated simply by ensuring that they satisfy:

$$\mathbf{G}\cdot\mathbf{R} = (l\mathbf{a}_1 + m\mathbf{a}_2)\cdot(l'\mathbf{b}_1 + m'\mathbf{b}_2) = 2\pi N. \tag{10.4}$$

An important feature of the modes of a periodic structure is that the wavevectors $\mathbf{k}$ and $\mathbf{k}$+$\mathbf{G}$ represent the same mode. Because of this there is a redundancy in the labelling of the wavevectors and thus attention can be restricted to a reduced zone within the reciprocal space in which you cannot get from one part to another by simply adding any $\mathbf{G}$. This zone is called the Brillouin zone [69]. A more visual description of the Brillouin zone is to imagine highlighting the

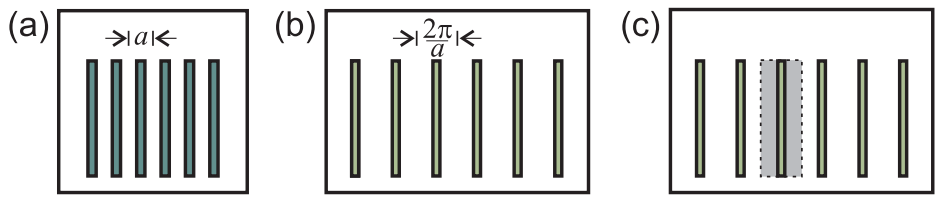

Figure 10.4: (a) Lattice space and (b) reciprocal space for a one dimensional photonic crystal. (c) The corresponding Brillouin zone (shaded region).

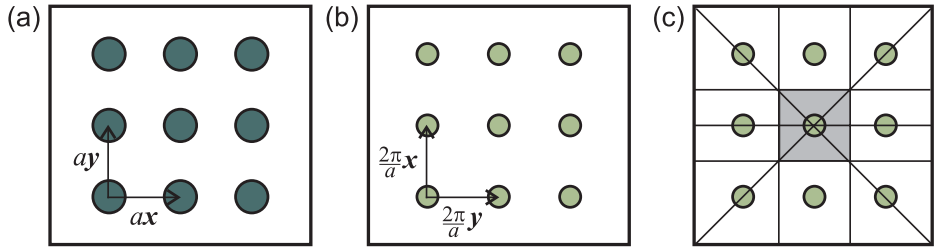

Figure 10.5: (a) Lattice space and (b) reciprocal space for a two dimensional photonic crystal. (c) The corresponding Brillouin zone (shaded region).

volume around a lattice point in the reciprocal space which is closer to that lattice point than any other. If the original lattice point is chosen to be the origin, then the highlighted region is the Brillouin zone. Examples of the (a) lattice space, (b) reciprocal space and (c) the corresponding Brillouin zone in one and two dimensional photonic crystals are illustrated in Figs. 10.4 and 10.5, respectively.

Unlike the periodic structures, the reciprocal lattice vectors of an aperiodic quasi-crystal densely fill all reciprocal space. However, it is often useful to choose a subset of basic reciprocal lattice vectors that correspond to the relatively intense spots in the diffraction pattern. This is illustrated in Fig. 10.6 which shows (a) the two dimensional quasi-crystal lattice together with (b) the corresponding diffraction pattern, where the radii of the spots are proportional to the magnitude of the related Fourier coefficients. Importantly, the diffraction pattern highlights the self-similar nature of these quasi-crystals in that the outer sets of reciprocal lattice vectors can be obtained by inflation of the inner sets [93]. In addition, although quasi-crystals do not possess a Brillouin zone, it is possible to construct an analogue called the pseudo-Jones zone which is defined by the lines bisecting the basic reciprocal lattice vectors [94]. For the crys-

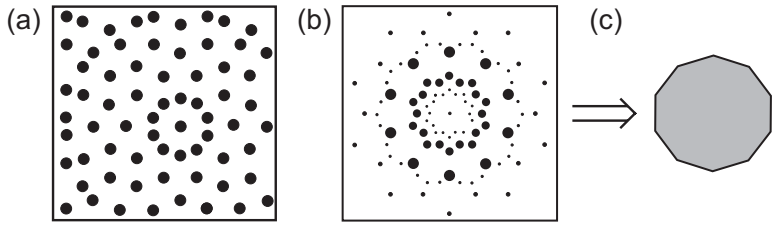

Figure 10.6: (a) Lattice space and (b) the corresponding diffraction pattern showing some of the larger Fourier coefficients for a two dimensional quasi-crystal. (c) The corresponding shape of the pseudo-Jones zone.

tal shown in Fig. 10.6(a), the corresponding shape of the pseudo-Jones zone is a decagon as sketched in (c).

10.3.1 Rotational Symmetry and the Irreducible Brillouin Zone

In addition to translational symmetries, photonic crystals can also possess rotational symmetries, as mentioned in Section 10.2.3. When there is rotational symmetry in the lattice the frequency bands $\omega(\mathbf{k})$ have additional redundancies within the Brillouin zone. Thus it is not necessary to consider every $\mathbf{k}$-point within the zone and the smallest area for which all $\omega(\mathbf{k})$ are not related by symmetry is called the irreducible Brillouin zone. As an example, Fig. 10.7 shows the Brillouin zone for the simple square lattice of Fig. 10.5 where the shaded triangular wedge is the irreducible Brillouin zone. Here the conventional notation for the points defining the irreducible zone is used [69].

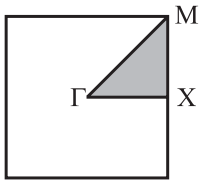

Figure 10.7: Brillouin zone for a two dimensional photonic crystal based on a square lattice where the shaded region is the irreducible zone.

10.4 Linear Effects in Crystals

In Section 3.4 the chromatic dispersion was described as the frequency dependence of the refractive index. In particular the Sellmeier equation which describes the material dispersion of the propagation medium was introduced. However, the exact form of this equation is in fact dependent on the nature of the material and differs quite considerably for crystal structures. For example this section considers the Sellmeier equation describing a congruently grown lithium niobate crystal of the type employed in Chapters 12 and 13. Lithium niobate is a uniaxial birefringent crystal and thus it is necessary to consider both the ordinary refractive index n^{o} (electric field polarised normal to the crystal axis) and the extraordinary refractive index n^{e} (electric field polarised

along the crystal axis) [1]. Furthermore, when intense light is incident on these crystals it can induce an optical change in the refractive index referred to as the photorefractive effect [95]. Although in some applications the photorefractive effect is welcome [38], in the investigations presented in this thesis it is not as it degrades the beam quality. However, by heating the crystal to temperatures above $\sim 100\,^{\circ}\mathrm{C}$, the photorefractive effect becomes self-annealing for infrared wavelengths and thus these deleterious effects can be avoided. However, this temperature change means that it is also important to consider the temperature dependence of the refractive indices. With these considerations, the form of the equation defining the refractive indices was previously found directly from experimental measurements, by Edwards and Lawrence [96], to be:

$$n^i(\lambda, T) = \sqrt{A_1^i + \frac{A_2^i + B_1^i f}{\lambda^2 - (A_3^i + B_2^i f)^2} + B_3 f - A_4^i \lambda^2}, \tag{10.5}$$

where $i = \mathrm{o}, \mathrm{e}$ corresponds to the ordinary and the extraordinary values, respectively, λ is in microns and

$$f = (T - 24.5\,^{\circ}\mathrm{C})(T + 570.82\,^{\circ}\mathrm{C}), \tag{10.6}$$

with T in degrees Celsius. The parameters A_j^i and B_k^i ($j = 1-4$, $k = 1-3$) were then calculated from fits to the experimental data and are given Table 10.1.

Ordinary Indices		Extraordinary Indices	
$A_1^{\mathrm{o}} = 4.9048$	$B_1^{\mathrm{o}} = 2.2314 \times 10^{-8}$	$A_1^{\mathrm{e}} = 4.5820$	$B_1^{\mathrm{e}} = 5.2716 \times 10^{-8}$
$A_2^{\mathrm{o}} = 0.11775$	$B_2^{\mathrm{o}} = -2.9671 \times 10^{-8}$	$A_2^{\mathrm{e}} = 0.09921$	$B_2^{\mathrm{e}} = -4.9143 \times 10^{-8}$
$A_3^{\mathrm{o}} = 0.21802$	$B_3^{\mathrm{o}} = 2.1429 \times 10^{-8}$	$A_3^{\mathrm{e}} = 0.21090$	$B_3^{\mathrm{e}} = 2.2971 \times 10^{-7}$
$A_4^{\mathrm{o}} = 0.027153$		$A_4^{\mathrm{e}} = 0.021940$	

Table 10.1: Physical parameters for calculation of the refractive index using Eq. (10.5).

With more recent attention being focused on quasi-phase matching processes where both beams are propagated along the extraordinary axis (see Section 10.8), it has been observed that Eq. (10.5) is not sufficiently accurate for predicting the linear properties of a crystal at longer wavelengths and / or elevated temperatures [97]. Owing to these observations, the equation for the extraordinary refractive index has since been revised by Jundt so that it is now described by [98]:

$$n^{\mathrm{e}}(\lambda, T) = \sqrt{A_1^{\mathrm{e}} + B_1^{\mathrm{e}} f + \frac{A_2^{\mathrm{e}} + B_2^{\mathrm{e}} f}{\lambda^2 - (A_3^{\mathrm{e}} + B_3^{\mathrm{e}} f)^2} + \frac{A_4^{\mathrm{e}} + B_4^{\mathrm{e}} f}{\lambda^2 - {A_5^{\mathrm{e}}}^2} - A_6^{\mathrm{e}} \lambda^2}, \tag{10.7}$$

Extraordinary Indices	
$A_1^{\mathrm{e}} = 5.35583$	$B_1^{\mathrm{e}} = 4.629 \times 10^{-7}$
$A_2^{\mathrm{e}} = 0.100473$	$B_2^{\mathrm{e}} = 3.862 \times 10^{-8}$
$A_3^{\mathrm{e}} = 0.20692$	$B_3^{\mathrm{e}} = -0.89 \times 10^{-8}$
$A_4^{\mathrm{e}} = 100$	$B_4^{\mathrm{e}} = 2.657 \times 10^{-5}$
$A_5^{\mathrm{e}} = 11.34927$	
$A_6^{\mathrm{e}} = 1.5334 \times 10^{-2}$	

Table 10.2: Physical parameters for calculation of the extraordinary refractive index using Eq. (10.7).

where the parameters A_j^i and B_k^i ($j = 1 - 6$, $k = 1 - 4$) are given in Table 10.2. Importantly, at present it is this equation that is most commonly used for calculating the refractive indices in lithium niobate.

While it is expected that there will also be a waveguide contribution to the chromatic dispersion (as for the case of fibre geometries), as this is highly dependent on the waveguide geometry it will not be discussed here.

10.5 Mathematical Description of Waveguides

In Chapter 9 it was briefly mentioned that a photonic crystal can be used as a waveguiding device to manipulate the propagation of light. Indeed, an example of this has already been demonstrated in Chapter 6 in the form of the microstructured fibres. As discussed in Section 3.2, an optical waveguide consists of a core in which the majority of the light is confined, surrounded by a cladding. The most common waveguide geometries are optical fibres (as considered in Part 1 of this thesis), channel waveguides and planar waveguides. Typically the refractive index is given by Eq. (3.1) and is higher in the core than in the cladding so that light coupled into the waveguide is confined to the core via total internal reflection. However, as Chapter 11 extends the definition of the refractive index to consider negative index materials, the dielectric permittivity and the magnetic permeability should now be expressed as:

$$\begin{aligned} \varepsilon &= \varepsilon_0 \varepsilon_i, \\ \mu &= \mu_0 \mu_i, \end{aligned} \tag{10.8}$$

where ($i = 2, 1$) in the core and cladding, respectively, and both ε_i and μ_i can take on negative values. Thus it is necessary to redefine the refractive index as:

$$n = \sqrt{\varepsilon\mu/\varepsilon_0\mu_0}. \tag{10.9}$$

Clearly, as $\mu = \mu_0$ for all nonmagnetic materials, in such cases this definition simply reduces to Eq. (3.1). The wavenumber of light in the medium is then expressed as:

$$k' = \omega\sqrt{\varepsilon\mu} = \omega n\sqrt{\varepsilon_0\mu_0} = kn, \tag{10.10}$$

where k is the wavenumber in a vacuum,

$$k = \omega/c. \tag{10.11}$$

The search for guided mode solutions of a waveguide begin with Maxwell's equations for a dielectric medium [3]:[1]

$$\nabla \times \tilde{\mathbf{E}} = -\frac{\partial \tilde{\mathbf{B}}}{\partial t}, \tag{10.12}$$

$$\nabla \times \tilde{\mathbf{H}} = \frac{\partial \tilde{\mathbf{D}}}{\partial t} + \tilde{\mathbf{J}}. \tag{10.13}$$

In media which contain no free currents such as those considered in this thesis, $\tilde{\mathbf{J}}$ can immediately be set to zero. Furthermore, as the formation of the guided modes is determined by the linear properties of the medium, it follows that:

$$\tilde{\mathbf{B}} = \mu\tilde{\mathbf{H}}, \tag{10.14}$$

$$\tilde{\mathbf{D}} = \varepsilon\tilde{\mathbf{E}}, \tag{10.15}$$

so that Maxwell's equations reduce to the form [99]:

$$\nabla \times \tilde{\mathbf{E}} = -\mu\frac{\partial \tilde{\mathbf{H}}}{\partial t}, \tag{10.16}$$

$$\nabla \times \tilde{\mathbf{H}} = \varepsilon\frac{\partial \tilde{\mathbf{E}}}{\partial t}. \tag{10.17}$$

Defining the electric $\tilde{\mathbf{E}}$ and magnetic $\tilde{\mathbf{H}}$ fields as:

$$\tilde{\mathbf{E}}(\mathbf{r}, t) = \mathbf{E}(\mathbf{r})\,\mathrm{e}^{-\mathrm{i}(\omega t - \beta z)}, \tag{10.18}$$

[1] It is important to note that in this part of the thesis tilde are used to denote fields that include the full temporal dependence, as illustrated in Eqs. (10.18) and (10.19).

$$\tilde{\mathbf{H}}(\mathbf{r},t) = \mathbf{H}(\mathbf{r})\,\mathrm{e}^{-\mathrm{i}(\omega t-\beta z)}, \tag{10.19}$$

it is easy to see how Eqs. (10.16) and (10.17) can be solved to obtain the mode profiles of the waveguides. However, it is important to note that these equations do not determine the fields completely and must be solved in conjunction with the boundary conditions of the respective problem.

Once Eqs. (10.16) and (10.17) have been solved for a given mode profile, the total power flowing in the direction of propagation through a surface S can be calculated via:

$$P = \int\int_S \left(\tilde{\mathbf{E}} \times \tilde{\mathbf{H}}\right) \cdot \mathbf{u}_z \mathrm{d}x\mathrm{d}y, \tag{10.20}$$

where $\mathbf{u}_z$ is the inward directed unit vector. Thus $\tilde{\mathbf{E}} \times \tilde{\mathbf{H}}$ represents the power flow density and it is useful to define:

$$\mathbf{S} = \tilde{\mathbf{E}} \times \tilde{\mathbf{H}}, \tag{10.21}$$

which is referred to as the Poynting vector.

10.6 Nonlinear Effects in Crystals

As discussed in Section 3.5, for intense electric fields the induced polarisation $\tilde{\mathbf{P}}$ no longer depends linearly on the incident field $\tilde{\mathbf{E}}$ and the relation must be extended to the more general expression [20]:

$$\tilde{\mathbf{P}} = \varepsilon_0 \left(\chi^{(1)} \cdot \tilde{\mathbf{E}} + \chi^{(2)} : \tilde{\mathbf{E}} + \chi^{(3)} \vdots \tilde{\mathbf{E}}\tilde{\mathbf{E}}\tilde{\mathbf{E}} + \cdots\right), \tag{10.22}$$

where the nonlinear response is assumed to be instantaneous, and again $\chi^{(j)}$ is the $(j+1)$ th rank susceptibility tensor. Although for fibres the second order susceptibility $\chi^{(2)}$ vanishes due to the inversion symmetry of silica glass, this is not the case for all crystal structures and thus it is now this term that gives rise to the lowest order nonlinear effects. In particular, it is the $\chi^{(2)}$ term that is responsible for second harmonic generation, whilst $\chi^{(3)}$ is responsible for third harmonic generation.

If the initial electric field is of the form:

$$\tilde{\mathbf{E}}(\mathbf{r},t) = \frac{1}{2}\hat{z}\left[E(\mathbf{r})\exp(-\mathrm{i}\omega t) + \mathrm{c.c.}\right], \tag{10.23}$$

where the light is assumed to be polarised along the z axis, then the second term of Eq. (10.22) is:

$$\tilde{\mathbf{P}}_2(\mathbf{r},t) = \varepsilon_0 \chi^{(2)} \tilde{\mathbf{E}}^2(\mathbf{r},t) = \varepsilon_0 \chi^{(2)}_{zzz} \hat{z} \left[E^2(\mathbf{r}) \exp(2\mathrm{i}\omega t) + \text{c.c.} \right]. \tag{10.24}$$

Thus if $\varepsilon_0 \chi^{(2)} \tilde{\mathbf{E}}^2$ is sufficiently large, then the fundamental field will generate a second harmonic field. The scale of the nonlinear effects in a crystal are controlled by the structure and the polarisation of the incident light. To quantify the performance of a crystal to generate second harmonic frequencies, the nonlinear coefficients $d_{ijk} = \chi^{(2)}_{ijk}/2$ can be introduced, where for SHG it is common to use the reduced notation such that:

$$\begin{bmatrix} P_x(2\omega) \\ P_y(2\omega) \\ P_z(2\omega) \end{bmatrix} = 2\varepsilon_0 \begin{bmatrix} d_{11} & d_{12} & d_{13} & d_{14} & d_{15} & d_{16} \\ d_{21} & d_{22} & d_{23} & d_{24} & d_{25} & d_{26} \\ d_{31} & d_{32} & d_{33} & d_{34} & d_{35} & d_{36} \end{bmatrix} \times \begin{bmatrix} E_x^2(\omega) \\ E_y^2(\omega) \\ E_z^2(\omega) \\ 2E_y(\omega) E_z(\omega) \\ 2E_x(\omega) E_z(\omega) \\ 2E_x(\omega) E_y(\omega) \end{bmatrix}. \tag{10.25}$$

It is clear from Eq. (10.25) that the sign of the nonlinear coefficients determines the sense of the polarisation, whilst the size determines the overall efficiency η of the process where:

$$\eta = \frac{P_{2\omega}}{P_{\omega}}. \tag{10.26}$$

10.7 Wave Equation in Nonlinear Crystals

This section presents a brief derivation of the wave equation to describe the propagation of light in a nonlinear optical medium. In particular, the considerations will be extended to describe SHG, as it is this process on which the experimental investigations of Chapters 12 and 13 are based.

The derivations begin with Maxwell's equations as given by their form in Eqs. (10.12) and (10.13). Again with the assumption of a material containing no free currents, so that $\tilde{\mathbf{J}} = 0$, and $\tilde{\mathbf{B}}$ given by Eq. (10.14), the material is now allowed to be nonlinear in the sense that $\tilde{\mathbf{D}}$ is related to $\tilde{\mathbf{E}}$ via:

$$\tilde{\mathbf{D}} = \varepsilon \tilde{\mathbf{E}} + \tilde{\mathbf{P}}^{\mathrm{NL}}, \tag{10.27}$$

where $\tilde{\mathbf{P}}^{\mathrm{NL}}$ depends nonlinearly on the strength of the electric field. Taking the curl of Eq. (10.12) and substituting the right hand side of Eq. (10.13) for $\nabla \times \tilde{\mathbf{B}}$ yields:

$$\nabla \times \nabla \times \tilde{\mathbf{E}} + \mu \frac{\partial^2}{\partial t^2} \tilde{\mathbf{D}} = 0. \tag{10.28}$$

Using Eq. (10.27) to eliminate $\tilde{\mathbf{D}}$, this can be expressed in terms of the fields $\tilde{\mathbf{E}}$ and $\tilde{\mathbf{P}}^{\mathrm{NL}}$ as:

$$\nabla \times \nabla \times \tilde{\mathbf{E}} + \varepsilon\mu \frac{\partial^2}{\partial t^2} \tilde{\mathbf{E}} = -\mu \frac{\partial^2}{\partial t^2} \tilde{\mathbf{P}}^{\mathrm{NL}}, \tag{10.29}$$

which is the most general form of the wave equation. However, in most cases of interest Eq. (10.29) can be simplified using the vector relation

$$\nabla \times \nabla \times \tilde{\mathbf{E}} = \nabla \left(\nabla \cdot \tilde{\mathbf{E}} \right) - \nabla^2 \tilde{\mathbf{E}}$$

as $\nabla \cdot \tilde{\mathbf{E}}$ is, in general, negligibly small. In such instances the wave equation becomes:

$$\nabla^2 \tilde{\mathbf{E}} - \varepsilon\mu \frac{\partial^2}{\partial t^2} \tilde{\mathbf{E}} = \mu \frac{\partial^2}{\partial t^2} \tilde{\mathbf{P}}^{\mathrm{NL}}. \tag{10.30}$$

Eq. (10.30) can now be extended to describe SHG in which two photons of frequency ω are converted to one of frequency 2ω. For simplicity, the polarisation and the direction of the propagating fundamental beam are assumed to be fixed so that a scalar relationship can be considered. Furthermore, with the additional assumption that the fields are polarised along the z axis, the tensor notation of the nonlinear susceptibility is dropped so that $\chi^{(2)} = \chi^{(2)}_{zzz}$. Expressing the total electric field within the nonlinear medium as,

$$\tilde{E}\left(\mathbf{r}, t\right) = \tilde{E}_{\omega}\left(\mathbf{r}, t\right) + \tilde{E}_{2\omega}\left(\mathbf{r}, t\right), \tag{10.31}$$

it can be assumed that each frequency component obeys Eq. (10.30) so that:

$$\nabla^2 \tilde{E}_j - \varepsilon_j \mu_j \frac{\partial^2}{\partial t^2} \tilde{E}_j = \mu_j \frac{\partial^2}{\partial t^2} \tilde{P}^{\mathrm{NL}}_j, \tag{10.32}$$

where $j = \omega, 2\omega$. The expressions for $\tilde{P}^{\mathrm{NL}}_j$ are then obtained from Eq. (10.24) as:

$$\tilde{P}^{\mathrm{NL}}_{\omega} = 2\varepsilon_0 \chi^{(2)} \tilde{E}_{2\omega} \tilde{E}^*_{\omega}, \tag{10.33}$$

$$\tilde{P}^{\mathrm{NL}}_{2\omega} = \varepsilon_0 \chi^{(2)} \tilde{E}^2_{\omega}. \tag{10.34}$$

For propagation in a conventional (positive index) medium, where $\mu = \mu_0$ and $n = \sqrt{\varepsilon/\varepsilon_0}$ [Eq. (3.1)], this yields the coupled SHG equations in their standard form as:

$$\nabla^2 \tilde{E}_{\omega} - \frac{n^2_{\omega}}{c^2} \frac{\partial^2}{\partial t^2} \tilde{E}_{\omega} = \frac{2}{c^2} \chi^{(2)} \frac{\partial^2}{\partial t^2} \left(\tilde{E}_{2\omega} \tilde{E}^*_{\omega} \right), \tag{10.35}$$

$$\nabla^2 \tilde{E}_{2\omega} - \frac{n_{2\omega}^2}{c^2}\frac{\partial^2}{\partial t^2}\tilde{E}_{2\omega} = \frac{1}{c^2}\chi^{(2)}\frac{\partial^2}{\partial t^2}\tilde{E}_{\omega}^2. \tag{10.36}$$

10.8 Phase Matching Harmonic Generation

As mentioned in Section 9.2, due to material dispersion, the nonlinear processes discussed in the previous sections require that the interacting fields be phase matched. To illustrate this, this section describes the physical considerations of the SHG process in more detail.

Second harmonic generation is a three photon process where: $\omega + \omega \rightarrow 2\omega$, so that the requirement of energy conservation is satisfied:

$$\hbar\omega + \hbar\omega = \hbar\left(2\omega\right). \tag{10.37}$$

Similarly, conservation of momentum for the photons yields:

$$\mathbf{k}_{\omega} + \mathbf{k}_{\omega} = \mathbf{k}_{2\omega}, \tag{10.38}$$

where $\mathbf{k}_i$ $(k_i = 2\pi n_i/\lambda_i)$ are the wavevectors, n_i are the refractive indices, λ_i are the wavelengths and $i = \omega, 2\omega$ for the fundamental and second harmonic fields, respectively. Rewriting Eq. (10.38) in one dimension as,

$$2\left(\frac{2\pi n_{\omega}}{\lambda_{\omega}}\right) = \frac{2\pi n_{2\omega}}{\lambda_{\omega}/2}, \tag{10.39}$$

it is clear that momentum is conserved if and only if $n_{\omega} = n_{2\omega}$. However, because of the wavelength dispersion, in general $n_{\omega} \neq n_{2\omega}$ and the fundamental and second harmonic waves periodically move in and out of phase as they propagate through the crystal. As a result, the intensity of the second harmonic wave also varies periodically and the period at which this occurs is twice the coherence length l_{c}, where [87]:

$$l_{\mathrm{c}} = \frac{\pi}{k_{2\omega} - 2k_{\omega}} = \frac{\lambda_{\omega}}{4\left(n_{2\omega} - n_{\omega}\right)}. \tag{10.40}$$

Thus after the waves have propagated one coherence length the energy of the second harmonic starts to return to the fundamental. This is demonstrated in Fig. 10.8 which shows the evolution of the second harmonic power where it can be seen that $P_{2\omega} = 0$ at $x = 2l_{\mathrm{c}}$ when there is no phase matching.

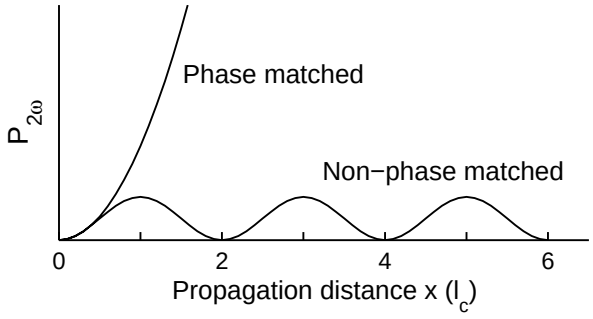

Figure 10.8: Evolution of the second harmonic power for phase matched and non-phase matched propagation.

The process of balancing the refractive indices at the different wavelengths is what is referred to as phase matching. This was first demonstrated in negative birefringent crystals by propagating the two beams at an angle to the optic axis within the crystal such that the condition $n_{\omega}^{\mathrm{o}} = n_{2\omega}^{\mathrm{e}}$ was satisfied [84, 85]. However, this technique is somewhat limited in that it is restricted to wavelengths where $n_{\omega}^{\mathrm{o}} = n_{2\omega}^{\mathrm{e}}$ and, because of the angular / polarisation restrictions, it is often unable to access the largest nonlinear coefficient of the crystal [see Eq. (10.25)] so that a smaller alternative coefficient may have to be employed, thus reducing the nonlinear conversion efficiency [87]. For example, while the largest nonlinear coefficient in lithium niobate is $d_{33} = 31.5\,\mathrm{pmV}^{-1}$, the largest nonlinear coefficient that can be accessed by a birefringent phase matched process is $d_{31} = -4.52\,\mathrm{pmV}^{-1}$, which is almost an order of magnitude smaller.

An alternative to birefringent phase matching is quasi-phase matching (QPM) and it is this technique that is employed in the experiments described in Chapters 12 and 13. Quasi-phase matching requires modification of the crystal structure by periodically reversing the spontaneous polarisation, which is equivalent to reversing the sign of the nonlinear coefficient. This in turn rephases the fundamental and generated second harmonic fields as they propagate through the crystal so that they remain in phase. Because the nonlinear susceptibility tensor $\chi^{(2)}$ is now periodic, it can be written as a Fourier series,

$$\chi^{(2)}\left(\mathbf{r}\right) = \sum_{n,m} \kappa_{n,m} \mathrm{e}^{\mathrm{i}\mathbf{G}_{n,m}\cdot\mathbf{r}}, \tag{10.41}$$

where $\kappa_{n,m}$ are the Fourier coefficients corresponding to the reciprocal lattice vectors $\mathbf{G}_{n,m}$ [Eq. (10.3)]. The phase matching condition then becomes:

$$\mathbf{k}_{2\omega} - 2\mathbf{k}_{\omega} = \mathbf{G}_{mn}. \tag{10.42}$$

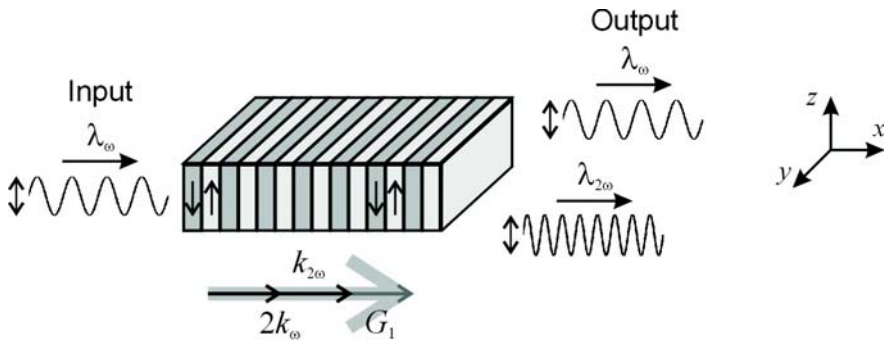

Figure 10.9: Schematic diagram of SHG in PPLN showing the periodic domain structure and the phase matching condition (below). The input and output fields are vertically polarised.

Importantly, it can be noted that the coupling strength of a phase matched process using a particular $\mathbf{G}_{n,m}$ is proportional to the corresponding coefficient $\kappa_{n,m}$, and if $\kappa_{n,m} = 0$ the interaction will not occur.

As a simple example, the one dimensional case of SHG in periodically poled lithium niobate (PPLN) is considered, as illustrated in Fig. 10.9. A schematic of the phase matching diagram, given below, shows that this process is collinear. Quasi-phase matching this process requires $G_1 = 2\pi/\Lambda$ where the grating period Λ, poled along the optic axis, is given by [87]:

$$\Lambda = 2l_c = \frac{\lambda_\omega}{2\left(n_{2\omega} - n_\omega\right)}. \tag{10.43}$$

To illustrate the success of this technique, the evolution of the second harmonic power $P_{2\omega}$ for poled (quasi-phase matched) and unpoled (non-phase matched) lithium niobate is presented in Fig. 10.10, clearly showing the increase in the

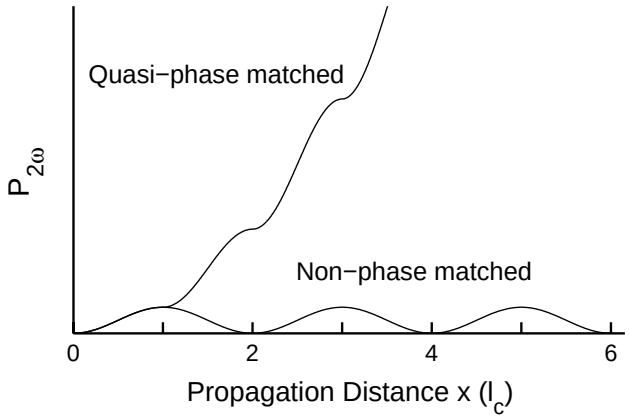

Figure 10.10: Evolution of the second harmonic power for quasi-phase matched and non-phase matched propagation.

efficiency for the quasi-phase matched process.

This example highlights the main attraction of using nonlinear photonic crystals in that, once the defining condition $\mathbf{G}$ has been established, the lattice structure can then be designed specifically to phase match the desired nonlinear interaction. In addition, by altering the shape of the poled regions the relative ratios of the Fourier coefficients can be adjusted such that some nonlinear interactions are stronger than others, and this is particularly important when one is considering using higher order reciprocal lattice vectors.

10.9 Modelling Second Harmonic Generation in Nonlinear Crystals

In this section, a numerical model to investigate SHG in nonlinear crystals will be described. This work was motivated by the previous observations of Broderick *et al.* that second harmonic generation could occur over a wide range of angles in two dimensional periodically poled structures [90]. It was hoped that this model would not only provide a means by which to compare the experimental results, but that it would also aid in the design of new crystal structures. The significant feature of this model is that, if it is to accurately describe two dimensional crystals, any restrictions on the propagation angle of the second harmonic beam must be avoided. Thus the following calculations will not make use of the usual paraxial approximation which assumes that the electric field varies slowly in the direction of propagation.

10.9.1 Preliminary Investigations

The initial approach to this problem was to consider the evolution of the fields in the frequency domain so that the system could be described by the Fourier transform of the coupled SHG equations (10.35) and (10.36) as:

$$\nabla^2 \tilde{E}_\omega(\mathbf{r},\omega) + \frac{n_\omega^2 \omega^2}{c^2}\tilde{E}_\omega(\mathbf{r},\omega) = \frac{2\omega^2}{c^2}\chi^{(2)}(\mathbf{r})\,\tilde{E}_{2\omega}(\mathbf{r},\omega)\,\tilde{E}_\omega^*(\mathbf{r},\omega), \tag{10.44}$$

$$\nabla^2 \tilde{E}_{2\omega}(\mathbf{r},\omega) + \frac{n_{2\omega}^2 (2\omega)^2}{c^2}\tilde{E}_{2\omega}(\mathbf{r},\omega) = \frac{(2\omega)^2}{c^2}\chi^{(2)}(\mathbf{r})\,\tilde{E}_\omega^2(\mathbf{r},\omega). \tag{10.45}$$

In this representation the total electric field is given by: $\tilde{E}(\mathbf{r},\omega) = \tilde{E}_{\omega}(\mathbf{r},\omega) + \tilde{E}_{2\omega}(\mathbf{r},\omega)$, where $\tilde{E}_i(\mathbf{r},\omega)$ is the Fourier transform of the field $\tilde{E}_i(\mathbf{r},t)$ [Eq. (10.23)], defined as:

$$\tilde{E}_i(\mathbf{r},\omega) = \frac{1}{\sqrt{2\pi}} \int_{-\infty}^{\infty} \tilde{E}_i(\mathbf{r},t) \exp(\mathrm{i}\omega t)\, \mathrm{d}t. \tag{10.46}$$

However, as for a particular process the frequencies of the electric fields are fixed, the ω dependence in Eqs. (10.44) and (10.45) can be dropped. In addition, to further simplify these preliminary investigations the analysis was based on the undepleted pump approximation so that knowledge of the fundamental field could be assumed over all space. Thus the investigations of the system could be reduced to solving the single equation:

$$\nabla^2 \tilde{E}_{2\omega}(\mathbf{r}) + \frac{n_{2\omega}^2 (2\omega)^2}{c^2} \tilde{E}_{2\omega}(\mathbf{r}) = \frac{(2\omega)^2}{c^2} \chi^{(2)}(\mathbf{r})\, \tilde{E}_{\omega}^2(\mathbf{r}). \tag{10.47}$$

In the formulation of the numerical problem, a two dimensional structure based on the coordinate system of Fig. 10.2 is considered. Thus it could be assumed that the fields extended infinitely in the z direction so that: $\tilde{E}_i(x,y,z) = \tilde{E}_i(x,y)$ and $\nabla^2 = \partial^2/\partial x^2 + \partial^2/\partial y^2$. By discretising the resulting fields over the $x-y$ plane, they could then be represented in the form of an $M \times N$ matrix where M is the x dimension and N is the y dimension. Solutions to equations of the form of Eq. (10.47) can usually be found by employing either finite difference or finite element techniques. However, as both these methods require the boundary conditions to be fixed in advance, to avoid placing any restrictions on the outgoing second harmonic field an absorbing layer was placed on the end of the grid and the field at the output was set to be: $\tilde{E}_{2\omega}(L_x, y) = 0$. In addition, after ensuring that the input Gaussian fundamental beam was sufficiently contained within the y direction, the fields at the y axis boundaries could also be set as: $\tilde{E}_{2\omega}(x,0) = \tilde{E}_{2\omega}(x,L_y) = 0$. A schematic diagram of the numerical construction which illustrates these conditions is shown in Fig. 10.11.

Unfortunately, none of the solutions to Eq. (10.47) obtained via either of these methods were found to be stable as they all depended strongly on the choice of the grid and system parameters.[2] Although the observed instabilities were initially attributed to an inadequate numerical technique, it has since been established that the problem in fact lies in the form of Eq. (10.47) itself. To un-

[2]These numerical investigations were conducted with the help of Dr K. Thomas from the department of Electronics and Computer Science (ECS).

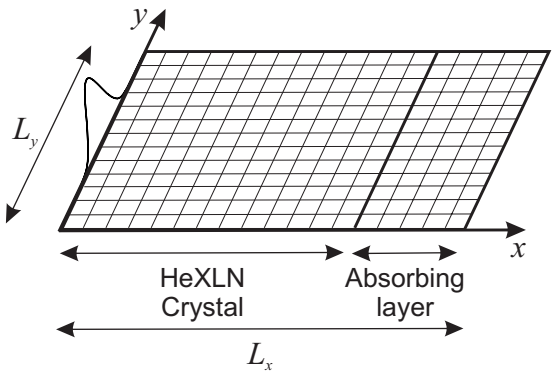

Figure 10.11: Schematic diagram showing the construction of the grid used to numerically model interactions in a two dimensional nonlinear crystal.

derstand why the solutions do not converge, it is useful to consider the finite difference representation and write the resulting system of linear equations in the conventional matrix form:

$$A\mathbf{x} = \mathbf{b}, \tag{10.48}$$

where A is an $N' \times N'$ matrix, $\mathbf{b}$ is a vector of the given data and $\mathbf{x}$ is the vector of the N' unknown field values. As for a two dimensional system the matrix describing the field must be unwrapped into a single column vector, for the purposes of this demonstration, a reduced problem in one dimension is considered so that: $\tilde{E}_i(x,y) = \tilde{E}_i(x)$, $\nabla^2 = \partial^2/\partial x^2$ and $N' = M$. Eq. (10.47) can then be rewritten in the form:

$$\frac{1}{h^2}\left[\tilde{E}_{2\omega}\Big|_{m+1} - 2\,\tilde{E}_{2\omega}\Big|_{m} + \tilde{E}_{2\omega}\Big|_{m-1}\right] + \alpha^2\,\tilde{E}_{2\omega}\Big|_{m} = \frac{(2\omega)^2}{c^2}\left[\chi^{(2)}\,\tilde{E}^2_{\omega}\Big|_{m}\right], \tag{10.49}$$

where $\alpha^2 = n^2_{2\omega}\,(2\omega)^2/c^2$, h is the size of the x grid and the difference formula refers to the grid point $x = mh$. It follows from Eq. (10.49) that:

$$A = \begin{pmatrix} \frac{-2}{h^2}+\alpha^2 & \frac{1}{h^2} & 0 & 0 & \dots & 0 \\ \frac{1}{h^2} & \frac{-2}{h^2}+\alpha^2 & \frac{1}{h^2} & 0 & \dots & 0 \\ 0 & \frac{1}{h^2} & \frac{-2}{h^2}+\alpha^2 & \frac{1}{h^2} & \dots & 0 \\ \vdots & & & \ddots & & \vdots \\ & & & & \ddots & \\ 0 & \dots & \dots & 0 & \frac{1}{h^2} & \frac{-2}{h^2}+\alpha^2 \end{pmatrix}.$$

The condition for the convergence of the system given by Eq. (10.48) is that the matrix A is strictly diagonally dominant, in that for each row the magnitude

of the diagonal element must be larger than the sum of the moduli of the off-diagonal elements [100],

$$|A_{ll}| > \sum_{m \neq l} |A_{lm}| \,, \qquad \forall l. \tag{10.50}$$

Thus as $\alpha^2 > 0$, it is clear that for this problem the condition is not satisfied and the solutions will not converge.

10.9.2 Finite Difference Model for SHG

Following the results of the preliminary investigations, the next step was to consider a revised problem where the fields include the full time dependence. Although this modified problem now involves an additional variable, the incorporation of the time dependence should force the stability of the solutions [101]. Owing to the inclusion of the extra temporal dimension, the investigations in this section will be restricted to problems with only one spatial dimension. However, a brief discussion on the possible extension to two spatial dimensions will be included as a final remark.

Solutions in One Dimension

Again the investigations begin by considering the case of an undepleted pump so that in one spatial dimension the system is simply described by Eq. (10.36) as:

$$\frac{\partial^2}{\partial x^2}\tilde{E}_{2\omega}\left(x,t\right) - \frac{n_{2\omega}^2}{c^2}\frac{\partial^2}{\partial t^2}\tilde{E}_{2\omega}\left(x,t\right) = \frac{1}{c^2}\chi^{(2)}\left(x\right)\frac{\partial^2}{\partial t^2}\tilde{E}_{\omega}^2\left(x,t\right). \tag{10.51}$$

With the fields now discretised in the sense of x and t, so that they can be represented as an $M \times N$ matrix where M is the x dimension and N is the t dimension, the explicit form of the finite difference representation of Eq. (10.51) is written as [102]:

$$\begin{aligned} \tilde{E}_{2\omega}\,|_m^{n+1} &= 2\left(1-p^2\right)\tilde{E}_{2\omega}\,|_m^n + p^2\left[\tilde{E}_{2\omega}\,|_{m+1}^n + \tilde{E}_{2\omega}\,|_{m-1}^n\right] \\ &- \tilde{E}_{2\omega}\,|_m^{n-1} - \frac{k^2}{n_{2\omega}^2}\chi^{(2)}\left.\frac{\partial^2\tilde{E}_{\omega}^2}{\partial t^2}\right|_m^n, \qquad m,n \in \mathbb{Z}. \end{aligned} \tag{10.52}$$

Here $p = kc/hn_{2\omega}$, h and k are the grid sizes in the distance and time coordinates, respectively, and the difference formula refers to the grid point $x = mh$,

$t = nk$. As the determination of the field at $t = (n+1)k$ requires that the fields at the two previous time steps are known, to further simplify the problem, propagation of the fundamental field is started well before the front face of the crystal so that the first two temporal second harmonic fields can be set to zero. In addition, the time of the propagation is restricted so that neither of the fields reach the end of the crystal and thus: $\tilde{E}_\omega(L_x, t) = 0$ and $\tilde{E}_{2\omega}(L_x, t) = 0$.

In order to test the solutions to Eq. (10.52), the first step is to consider a perfectly phase matched system so that: $n_{2\omega} = n_\omega = n$ and the nonlinear susceptibility is a constant: $\chi^{(2)}(x) = \chi^{(2)}(0)$. In this instance, theory predicts that for a continuous wave (CW) pump beam the evolution of the second harmonic power is given by [87]:

$$P_{2\omega}(x) = \frac{2\omega^2 d_{\text{eff}}^2 P_\omega^2}{n^3 c^3 \varepsilon_0 A} x^2, \tag{10.53}$$

where A is the mode area and

$$d_{\text{eff}} = \kappa_{n,m} d_{ij}, \tag{10.54}$$

is the effective nonlinear coefficient. Fig. 10.12 shows the evolution of the quasi-CW fundamental field (top) and the generated second harmonic field (bottom) for two snap shots in time, where (a) $t = 3\,\text{ps}$ and (b) $t = 6\,\text{ps}$, for: $n = 2.14236$, $\lambda = 1.536\,\mu\text{m}$ and $\chi^{(2)} = 33 \times 10^{-6}\,\mu\text{mV}^{-1}$. Comparing the second harmonic fields with the predictions of Eq. (10.53) (dashed curve) clearly, in the

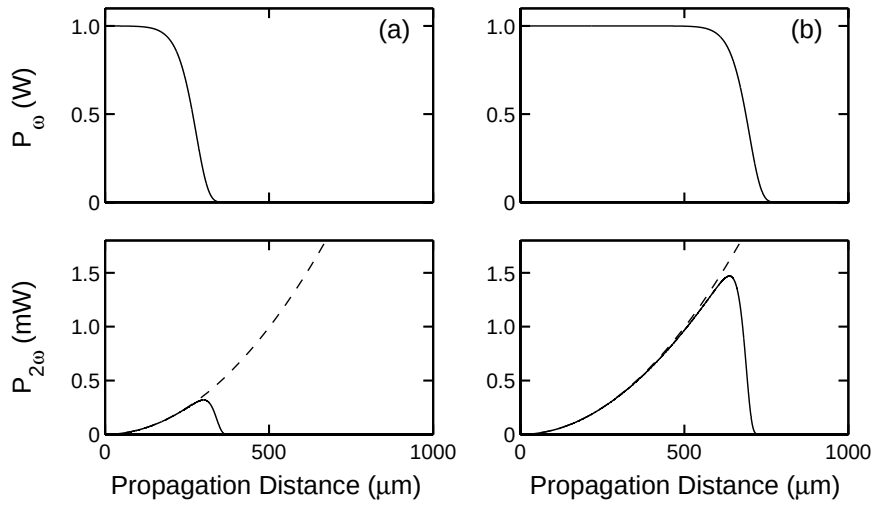

Figure 10.12: Evolution of the fundamental field (top) and the second harmonic field (bottom) for the case of perfect phase matching and assuming no pump depletion. The panels illustrate two snap shots in time where (a) $t = 3\,\text{ps}$ and (b) $t = 6\,\text{ps}$, and the dashed curves are the theoretical prediction for the evolution of $P_{2\omega}$ from Eq. (10.53).

first half of the crystal where the field has become essentially CW, the agreement is excellent. The slight deviation in the latter stages of the crystal [see Fig. 10.12(b)] can be attributed to the initial ramping up of the fundamental field.

Once satisfied that the program was generating the second harmonic field correctly, the next step was to consider the case where $n_{2\omega} \neq n_{\omega}$ so that a periodic $\chi^{(2)}(x)$ was required to quasi-phase match the process. Fig. 10.13(a) shows the evolution of the second harmonic field, at $t = 6\,\mathrm{ps}$, generated from the same fundamental field as shown in Fig. 10.12(b), but now with: $n_{\omega} = 2.14236$, $n_{2\omega} = 2.18450$, $\lambda = 1.536\,\mu\mathrm{m}$ and a nonlinear susceptibility with a magnitude: $\left|\chi^{(2)}(x)\right| = 33 \times 10^{-6}\,\mu\mathrm{mV}^{-1}$ and period: $\Lambda = 18.22\,\mu\mathrm{m}$ [Eq. (10.43)]. On comparing the evolution of the second harmonic with the theoretical prediction calculated for the previous case of perfect phase matching (see Fig. 10.12(b) - dashed curve), it can be seen that, as expected, the quasi-phase matched power grows at a slower rate. However, in this calculation it has been assumed that the same nonlinear coefficient is available for use in both cases. In lithium niobate crystals this is in fact not the case and, whilst the quasi-phase matched process uses the largest nonlinear coefficient d_{33}, the perfect phase matched case uses $d_{31} \simeq d_{33}/7$. The efficiency of a quasi-phase matched process relative to perfect phase matching can thus be calculated as $(d_{33}/d_{31})^2(2/\pi)^2 \approx 20$. Accounting for this correction yields the dotted curve, also in Fig. 10.13(a), which is in excellent agreement with the SHG evolution in the first half of the crystal. In addition, the close up of the initial stages of the evolution in the crystal

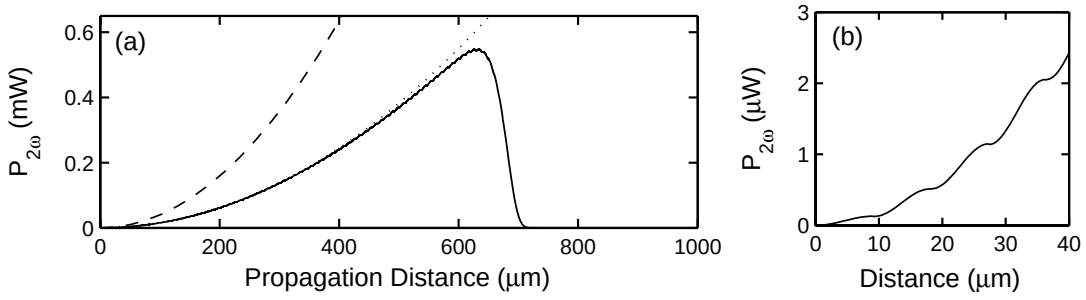

Figure 10.13: (a) Evolution of the second harmonic field for the case of quasi-phase matching together with the theoretical prediction from Eq. (10.53) for perfect phase matching (dashed curve) and the corrected predictions for quasi-phase matching (dotted curve). (b) Close up of the second harmonic evolution showing the periodic nature of the generation.

shown in Fig. 10.13(b) confirms that the second harmonic field is indeed being generated at the correct period, which provides further verification of the accuracy of the model.

Up to this point the analysis has been restricted to solving systems where the effects of pump depletion can be neglected [Eqs. (10.47) and (10.51)]. Although, because of its simplicity, it is this approach that is typically employed in theoretical studies of SHG, it soon breaks down in the limits of high conversion efficiencies. Thus ultimately the coupled equations need to be considered to describe the evolution of both the second harmonic and the fundamental field within the crystal. Rewriting Eqs. (10.35) and (10.36) in one spatial dimension yields:

$$\frac{\partial^2}{\partial x^2}\tilde{E}_{2\omega}\left(x,t\right)-\frac{n_{2\omega}^2}{c^2}\frac{\partial^2}{\partial t^2}\tilde{E}_{2\omega}\left(x,t\right)=\frac{1}{c^2}\chi^{(2)}\left(x\right)\frac{\partial^2}{\partial t^2}\left[\tilde{E}_{\omega}\left(x,t\right)\right]^2, \tag{10.55}$$

$$\frac{\partial^2}{\partial x^2}\tilde{E}_{\omega}\left(x,t\right)-\frac{n_{\omega}^2}{c^2}\frac{\partial^2}{\partial t^2}\tilde{E}_{\omega}\left(x,t\right)=\frac{2}{c^2}\chi^{(2)}\left(x\right)\frac{\partial^2}{\partial t^2}\left[\tilde{E}_{2\omega}\left(x,t\right)\tilde{E}_{\omega}^{*}\left(x,t\right)\right]. \tag{10.56}$$

The explicit forms of the finite difference representations of Eqs. (10.55) and (10.56) at $x=mh$ and $t=nk$ are [102]:

$$\begin{aligned}\tilde{E}_{2\omega}\mid_m^{n+1} &= 2\left(1-p^2\right)\tilde{E}_{2\omega}\mid_m^n+p^2\left[\tilde{E}_{2\omega}\mid_{m+1}^n+\tilde{E}_{2\omega}\mid_{m-1}^n\right]-\tilde{E}_{2\omega}\mid_m^{n-1}\\ &- \frac{1}{n_{2\omega}^2}\chi^{(2)}\mid_m^n\left[\tilde{E}_{\omega}^2\mid_m^{n+1}-2\tilde{E}_{\omega}^2\mid_m^n+\tilde{E}_{\omega}^2\mid_m^{n-1}\right],\end{aligned} \tag{10.57}$$

$$\begin{aligned}\tilde{E}_{\omega}\mid_m^{n+1} &= 2\left(1-r^2\right)\tilde{E}_{\omega}\mid_m^n+r^2\left[\tilde{E}_{\omega}\mid_{m+1}^n+\tilde{E}_{\omega}\mid_{m-1}^n\right]-\tilde{E}_{\omega}\mid_m^{n-1}\\ &- \frac{2}{n_{\omega}^2}\chi^{(2)}\mid_m^n\left[\tilde{E}_{2\omega}\tilde{E}_{\omega}^{*}\mid_m^{n+1}-2\tilde{E}_{2\omega}\tilde{E}_{\omega}^{*}\mid_m^n+\tilde{E}_{2\omega}\tilde{E}_{\omega}^{*}\mid_m^{n-1}\right],\\ &\quad m,n\in\mathbb{Z},\end{aligned} \tag{10.58}$$

where $p=kc/hn_{2\omega}$ and $r=kc/hn_{\omega}$. The significant feature of considering the effects of pump depletion is that, unlike Eq. (10.52), Eqs. (10.57) and (10.58) involve undetermined source terms in the $t=(n+1)k$ step. Thus, in order to solve these equations an iterative (predictor-corrector) method is employed where the fields at the earlier time step $t=nk$ are used as the initial guess of the fields at the following step. This procedure is then executed repeatedly, updating the guess of the fields at $t=(n+1)k$ at each step, until the algorithm converges.

Again, to test the solutions to Eqs. (10.57) and (10.57) the first step is to consider the case of perfect phase matching and set: $n_{2\omega}=n_{\omega}=2.14236$, $\lambda=1.536\,\mu\mathrm{m}$

and $\chi^{(2)} = 33 \times 10^{-6}\,\mu\mathrm{mV}^{-1}$. Fig. 10.14 plots the evolution of both the quasi-CW fundamental field (top) and the second harmonic field (bottom) inside the crystal for two snap shots in time where (a) $t = 3\,\mathrm{ps}$ and (b) $t = 6\,\mathrm{ps}$. From these it is clear that by comparing the second harmonic field with the theoretical predictions of Eq. (10.53), the fundamental power has been sufficiently reduced to slow down the rate of generation of the second harmonic. Although the reduction in this rate is quite large, this can be attributed to the effects being exaggerated by the initial ramping up of the fundamental field which is substantiated by the change in the shape of the leading edge of the beams from Fig. 10.12 to Fig. 10.14. As a means of verifying the accuracy of this model, the evolution of the energy has been calculated showing that, at any given time, the fields satisfy the requirement of energy conservation [3]:

$$U_{\mathrm{tot}} = \int I_\omega \mathrm{d}x + \int I_{2\omega}\mathrm{d}x = \frac{2n_\omega}{Z_0}\int |\tilde{E}_\omega|^2\mathrm{d}x + \frac{2n_{2\omega}}{Z_0}\int |\tilde{E}_{2\omega}|^2\mathrm{d}x, \qquad (10.59)$$

where $Z_0 = 377\,\Omega$ is the vacuum impedance and the total energy U_{tot} can be calculated from the known input field.

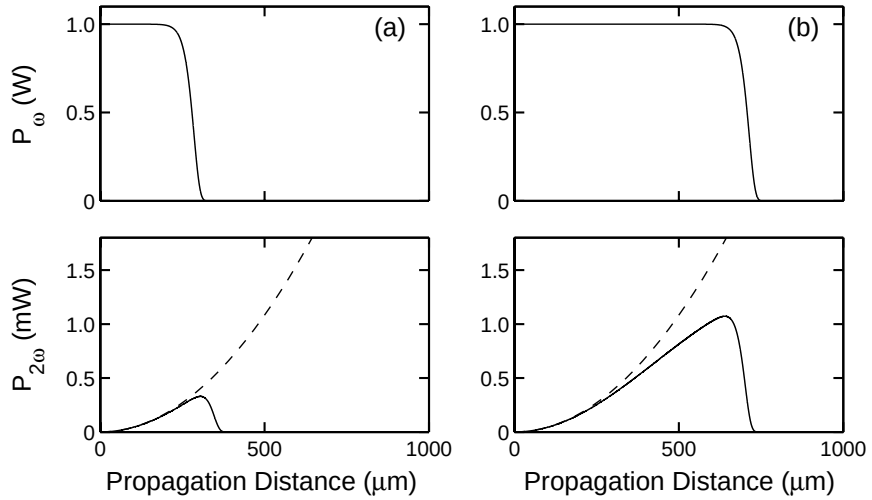

Figure 10.14: Evolution of the fundamental field (top) and the second harmonic field (bottom) for the case of perfect phase matching and including the effects of pump depletion. The panels illustrate two snap shots in time where (a) $t = 3\,\mathrm{ps}$ and (b) $t = 6\,\mathrm{ps}$, and the dashed curves are the theoretical prediction from Eq. (10.53) for the case of perfect phase matching and no pump depletion.

Finally, this model is used to investigate a quasi-phase matched second harmonic process where the fundamental input is pulsed. To this end, the injection of a $145\,\mathrm{pJ}$, $180\,\mathrm{fs}$ (FWHM) Gaussian fundamental pulse at $\lambda = 2\,\mu\mathrm{m}$ into

a PPLN crystal is simulated, with: $n_\omega = 2.12988$, $n_{2\omega} = 2.16406$, $\left|\chi^{(2)}(x)\right| = 33 \times 10^{-6}\,\mu\mathrm{mV}^{-1}$, $\Lambda = 29.2521\,\mu\mathrm{m}$ and $L = 400\,\mu\mathrm{m}$. It is worth noting that for a Gaussian input pulse, Eq. (10.51) predicts that the second harmonic pulse will also have a Gaussian profile with a FWHM width $\Delta T_0^{2\omega} = \Delta T_0^{\omega}/\sqrt{2}$. The output second harmonic pulse is shown in Fig. 10.15 and this has an energy of $9.4\,\mathrm{pJ}$ and a width of $128\,\mathrm{fs}$ (FWHM). For comparison, the circles show a Gaussian fit to the intensity profile. The good agreement between the simulated pulse and the fit is supported by calculation of the ratio: $\Delta T_0^{2\omega}/\Delta T_0^{\omega} = 0.711$, which is close to the predicted value of ~ 0.707. Although the conversion efficiency of this process appears quite low, this can be attributed to the phase mismatch due to the broad bandwidth associated with the short input fundamental pulse [103]. Thus these results can be expected to be a valid representation of SHG with a pulsed fundamental beam.

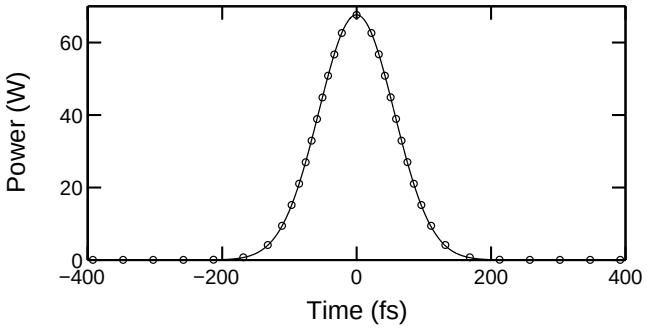

Figure 10.15: The output pulse from a quasi-phase matched SHG process with a pulsed fundamental beam, together with a Gaussian fit.

Comment on Solutions in Two Dimensions

As discussed earlier, the primary motivation for developing this model was to investigate harmonic generation in two dimensional nonlinear crystals. However, due to the resolution required to ensure that the phase of the second harmonic field is generated correctly, and thus that phase matching occurs, even in one dimension this problem quickly approaches the limits of the memory size of typical desktop computers.[3] Thus in order to consider two dimensional

[3]It is for this reason that the crystal lengths have been restricted to $1\,\mathrm{mm}$ in the simulations of Figs. 10.12 and 10.13.

problems, access to a computational device with a much larger memory capacity will need to be obtained.

Chapter 11

1D Negative Refractive Index Materials

11.1 Introduction

In this chapter the properties of the guided modes in one dimensional negative refractive index waveguides are investigated. This analysis was motivated by previous calculations performed by Shadrivov *et al.* for negative index planar waveguides [80]. The chapter begins with a discussion of negative refractive index materials, before describing existing fabrication techniques. By calculating possible guided mode solutions of both channel waveguides and optical fibres, a number of peculiar properties of negative index core waveguides will be revealed. Particular attention is paid to the manipulation of the velocities of the propagating modes.

11.2 Negative Refractive Index Materials

Negative index materials offer a unique possibility to extend the experimental domain and investigate novel physical phenomena. Such materials, which possess simultaneously negative values of the dielectric permittivity ε and magnetic permeability μ, were initially investigated theoretically by Veselago in 1968 where he concluded that they would have dramatically different prop-

agation characteristics to conventional materials [73]. In particular, these negative index materials can exhibit extraordinary properties such as negative refraction, antiparallel group and phase velocities (backwards waves) and negative energy fluxes (radiation tension). Despite the physical significance of his analysis, the results appeared to be of limited practical application due to the absence of naturally occurring negative index materials. However, motivated by earlier investigations [76, 77], in 2000 the first negative index material was demonstrated by Smith *et al.* in the form of a composite material consisting of periodic regions of negative ε and negative μ [70].

To date, the only experimental investigations of negative refraction phenomena have been reported in the microwave regime where the fabrication of such composite materials is possible [70, 104]. These experiments have confirmed that the electromagnetic waves behave as predicted by the theory. It is, however, unlikely that these composite materials will scale to optical frequencies and instead photonic crystals have often been suggested as an alternative to extend the effects of negative refraction into the optical regime [105]. Indeed, in 2000 Notomi performed a detailed theoretical and numerical investigation of light propagation in photonic crystals and showed that as the effective refractive index is determined by the photonic band structure, it can in fact be less than unity or even negative [106]. Although these photonic crystals may have positive ε and μ throughout, they have nonetheless been shown to exhibit similar anomalous light behavior to the composite negative ε and μ materials [107]. Recently a dielectric photonic crystal based on an array of aluminum rods in air was shown to exhibit negative refraction [108] and despite the fact that this experiment was still conducted in the microwave regime, by using electrical poling techniques [109] it should be possible to fabricate more complex structures that may scale to the optical regime.

11.2.1 Fabrication

In the microwave regime, a negative refractive index material can be fabricated by constructing a periodic array of interspaced regions of negative permittivity ε and permeability μ. The concept of a negative ε material is well established in the context of plasmons [110]. Here the ideal dielectric response of a plasma

is given by:

$$\varepsilon_i(\omega) = 1 - \frac{\omega_{p,i}^2}{\omega^2}, \tag{11.1}$$

where $\omega_{p,i}$ is the electronic plasma frequency and again ($i = 2, 1$) in the core and cladding, respectively. Clearly, when $\omega < \omega_{p,i}$, then ε_i takes on negative values. To date, the most common plasmon structure employed in negative ε experiments consists of very thin metallic wires arranged in a periodic lattice such as a simple cubic lattice shown in Fig. 11.1. Significantly, as the plasma frequency depends on the width and length of the wires, these structures can be tailored to exhibit $\omega_{p,i}$ at microwave or lower frequencies [76].

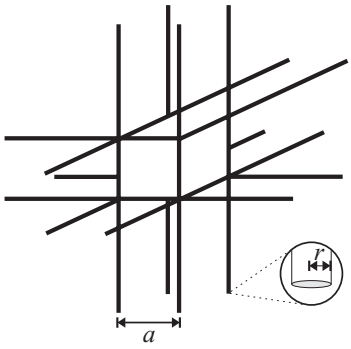

Figure 11.1: Schematic of a material structure which can exhibit a negative ε at microwave frequencies. The periodic array is composed of thin metallic wires arranged in a simple cubic lattice.

In contrast to the negative ε materials which have long been known to occur in both gaseous and solid state plasmas, until recently there were no known negative μ materials. However, in 1999 Pendry *et al.* [77] demonstrated a structure whose properties mimicked those of a magnetic plasma so that they exhibited effective permeabilities which where not accessible in naturally occurring materials. This structure consisted of a sequence of flat split ring disks comprising of two thin sheets of metal, as illustrated in Fig. 11.2. Analogous to the electronic plasma, the magnetic response of μ can be expressed as:

$$\mu_i(\omega) = 1 - \frac{F\omega^2}{\omega^2 - \omega_{0,i}^2}, \tag{11.2}$$

where $\omega_{0,i}$ is the magnetic resonance frequency and F is a constant dependent on the material structure. Significantly, it was a combination of this split ring lattice with the wire lattice of Fig. 11.1 which led to the first demonstration of a composite medium with simultaneously negative ε and μ by Smith *et al.* [70].

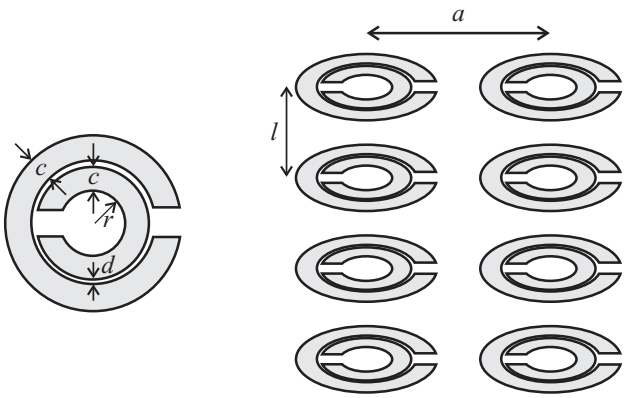

Figure 11.2: Schematic of a material structure which can exhibit a negative μ at microwave frequencies. Each split ring is comprised of two thin metal sheets and is stacked in a periodic structure as shown.

As mentioned previously, although it is possible to modulate the optical properties of a crystal periodically by means of the electronic poling technique,[1] to date such photonic crystals have only been shown to have an effective negative refractive index. However, as the techniques involved in the fabrication processes are improved, it can be expected that this technology could be combined with that of the composite materials to obtain negative ε negative μ materials in the optical wavelength regime.

11.3 Channel Waveguides

In this section, the guided mode solutions for a channel waveguide with a negative index (negative ε and μ) core are calculated. By investigating the properties of the modes, it will be shown that these differ considerably from the guided modes of a conventional positive index waveguide. Typical features of these waveguides include the absence of the fundamental mode, possible double degeneracy of modes and backwards propagating waves with negative energy flux.

[1] This will be discussed in more detail in Chapter 12.

11.3.1 Guided Mode Solutions

Similar to the geometry of an optical fibre [Section 3.2], a channel waveguide consists of a square (or rectangular) core surrounded by a cladding which differs in its refractive index. The calculations presented here consider a symmetric channel waveguide with the geometry and parameters given in Fig. 11.3. The dielectric permittivity and the magnetic permeability in the cladding ($i = 1$) and the core ($i = 2$) are related to their vacuum values via Eq. (10.8). In the analysis, the cladding is assumed to have a positive index with both ε_1 and μ_1 positive, and the core is set to have ε_2 and μ_2 negative. The guided modes will be stationary solutions to Maxwell's equations of the form,

$$\tilde{\mathbf{E}}(x, y, z, t) = \mathbf{E}(x, y)\, \mathrm{e}^{-\mathrm{i}(\omega t - \beta z)}, \tag{11.3}$$

$$\tilde{\mathbf{H}}(x, y, z, t) = \mathbf{H}(x, y)\, \mathrm{e}^{-\mathrm{i}(\omega t - \beta z)}, \tag{11.4}$$

where ω is the angular frequency of the field, β is the propagation constant and $\mathbf{E}(x, y)$ and $\mathbf{H}(x, y)$ are the spatially localised transverse mode profiles of the electric and magnetic fields, respectively.

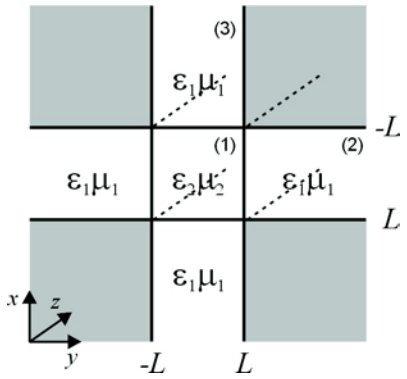

Figure 11.3: Channel waveguide geometry and parameters.

The analysis of the system given in Fig. 11.3 follows Marcatili's method for two dimensional optical waveguides [111]. Although more complicated methods allow for a more rigorous description of the mode properties (e.g., Kumar's method [99]), this method should nevertheless be sufficient to obtain a qualitative understanding of the mode characteristics. The electric field is chosen to be polarised in the x direction (i.e., the E^x_{pq} modes), with E_x and H_y as the principal field components. Here p and q are integers which correspond to the

number of peaks of the optical power in the x and y directions, respectively. Substituting Eqs. (11.3) and (11.4) into Maxwell's equations [Eqs. (10.16) and (10.17)] it follows that the wave equation in this representation is:

$$\frac{\partial^2 H_y}{\partial x^2} + \frac{\partial^2 H_y}{\partial y^2} + \left(k^2 \varepsilon_i \mu_i - \beta\right) H_y = 0, \tag{11.5}$$

and the remaining field representations are related to H_y via,

$$\begin{aligned} H_x &= 0 \\ H_z &= \frac{-\mathrm{i}}{\beta}\frac{\partial H_y}{\partial y} \\ E_x &= \frac{\omega \mu_0 \mu_i}{\beta} H_y + \frac{1}{\omega \varepsilon_0 \varepsilon_i \beta}\frac{\partial^2 H_y}{\partial x^2} \\ E_y &= \frac{1}{\omega \varepsilon \beta}\frac{\partial^2 H_y}{\partial x \partial y} \\ E_z &= \frac{-\mathrm{i}}{\omega \varepsilon}\frac{\partial H_y}{\partial x}. \end{aligned} \tag{11.6}$$

Marcatili's method is based on the assumption that the electric and magnetic fields are confined to the core so that they decay exponentially in the cladding and are negligible in the shaded regions of Fig. 11.3. In addition, since the waveguide shown in this figure is symmetric with respect to the x and y axes, the analysis can be restricted to only consider regions (1)–(3). With these considerations, the electric field distributions in the three regions can be expressed as:

$$H_y = \begin{cases} A\cos\left(k_x x - \phi\right)\cos\left(k_y y - \psi\right) & \text{region (1)} \\ A\cos\left(k_x L - \phi\right)\mathrm{e}^{-\gamma_x (x-L)}\cos\left(k_y y - \psi\right) & \text{region (2)} \\ A\cos\left(k_x x - \phi\right)\mathrm{e}^{-\gamma_y (y-L)}\cos\left(k_y L - \psi\right) & \text{region (3),} \end{cases} \tag{11.7}$$

where the constant A is related to the power carried by the mode [Eq. (10.20)]. Here k_x, k_y, γ_x and γ_y are related by:

$$\begin{aligned} -k_x^2 - k_y^2 + k^2 \varepsilon_2 \mu_2 - \beta^2 = 0 \qquad & \text{region (1)} \\ \gamma_x^2 - k_y^2 + k^2 \varepsilon_1 \mu_1 - \beta^2 = 0 \qquad & \text{region (2)} \\ -k_x^2 + \gamma_y^2 + k^2 \varepsilon_1 \mu_1 - \beta^2 = 0 \qquad & \text{region (3),} \end{aligned} \tag{11.8}$$

and the optical phases ϕ and ψ are,

$$\begin{aligned} \phi &= (p-1)\tfrac{\pi}{2} \qquad (p = 1, 2, \ldots) \\ \psi &= (q-1)\tfrac{\pi}{2} \qquad (q = 1, 2, \ldots). \end{aligned} \tag{11.9}$$

Applying the boundary condition that the field components E_z and H_z should be continuous at $x = L$ and $y = L$, respectively, the following dispersion relations are obtained:

$$\gamma_x L = \frac{\varepsilon_1}{\varepsilon_2} k_x L \tan\left(k_x L - (p-1)\frac{\pi}{2}\right), \tag{11.10}$$

$$\gamma_y L = k_y L \tan\left(k_y L - (q-1)\frac{\pi}{2}\right). \tag{11.11}$$

Rearranging Eqs. (11.8) so that γ_x and γ_y are expressed in terms of ε, μ and the transverse wavenumbers, k_x and k_y, yields:

$$\gamma_x^2 = \frac{\omega^2}{c^2}\left(\varepsilon_2\mu_2 - \varepsilon_1\mu_1\right) - k_x^2, \tag{11.12}$$

$$\gamma_y^2 = \frac{\omega^2}{c^2}\left(\varepsilon_2\mu_2 - \varepsilon_1\mu_1\right) - k_y^2. \tag{11.13}$$

The propagation constant β can then be calculated from,

$$\beta^2 = \frac{\omega^2}{c^2}\varepsilon_2\mu_2 - \left(k_x^2 + k_y^2\right). \tag{11.14}$$

The dispersion relations of Eqs. (11.10) and (11.11) can be solved together with Eqs. (11.12) and (11.13) using standard graphical techniques (see Ref. [99]). Previous analysis of negative index planar waveguides has shown that it is possible to obtain solutions where the transverse wavenumber k becomes purely imaginary [80]. These "slow wave" solutions occur when β exceeds a critical value and have been likened to surface waves in metal films [112]. Thus the parameter planes $(k_x L, \gamma_x L)$ and $(k_y L, \gamma_y L)$ can be extended to include imaginary values of k_x and k_y by defining: $\kappa_x = \mathrm{i}k_x$ and $\kappa_y = \mathrm{i}k_y$. Fig. 11.4 shows typical solutions for the x and y components of the field with: $\varepsilon_1 = 0.8$, $\mu_1 = 0.41$, $\varepsilon_2 = -2.3$, $\mu_2 = -2.2$ and $\omega/2\pi = 4.4\,\mathrm{GHz}$.[2] The solid lines are the right hand sides of Eqs. (11.10) and (11.11) and the dashed lines are obtained from the right hand sides of Eqs. (11.12) and (11.13). Here the 3 dashed lines correspond to waveguides with the widths: (1) $L = 0.1\,\mathrm{cm}$, (2) $L = 0.4\,\mathrm{cm}$ and (3) $L = 1.4\,\mathrm{cm}$.

The points of intersection indicate the existence of guided modes. From these intersections, six different solutions can be constructed and, to illustrate this, examples of typical mode profiles can be seen in Fig. 11.5. The possible $H^y_{2,1}$

[2] These parameters where chosen based on realistic values of $\omega_{p,i}$, $\omega_{0,i}$ and F [70, 80].

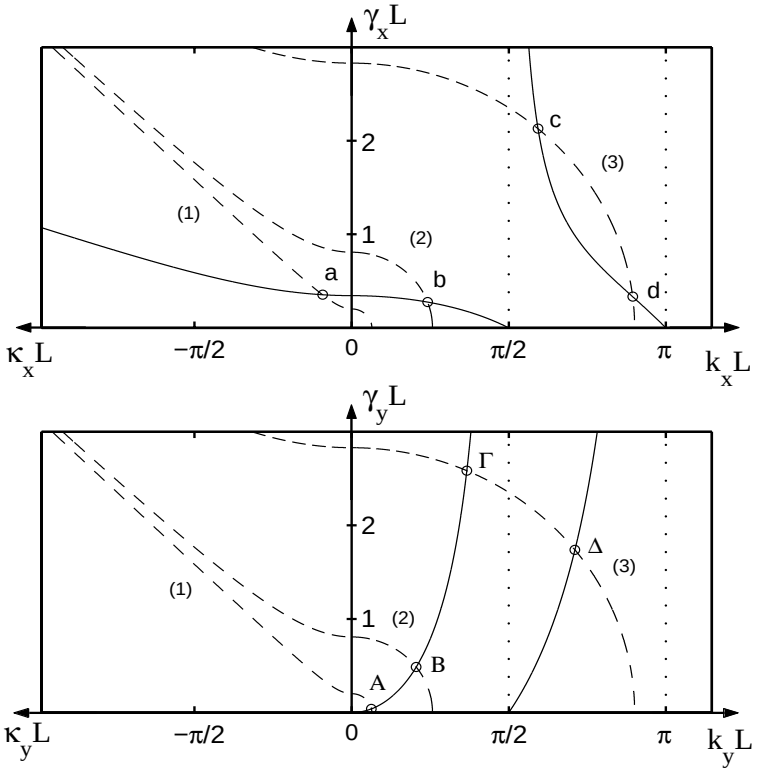

Figure 11.4: Typical solutions for the x (top) and y (bottom) components of the guided modes of a negative index channel waveguide. The solid lines are the right hand sides of Eqs. (11.10) and (11.11) and the dashed lines are obtained from the right hand sides of Eqs. (11.12) and (11.13).

modes are plotted in the top row where the (a, A) mode has an imaginary k_x but real k_y and the (b, B) mode has both k_x and k_y real. The middle row shows the strongly (c, Γ) and weakly (d, Γ) localised $H^y_{3,1}$ modes. Similarly, the bottom row shows the strongly (c, Δ) and weakly (d, Δ) localised $H^y_{3,2}$ modes, although in this instance the weakly localised mode has an imaginary β so that it decays exponentially as it propagates in z. It is worth noting that a similar analysis for the E^y_{pq} mode (electric field polarised in the y direction) leads to H_x solutions with forms such as those shown in Fig. 11.4, but with the x and y components interchanged. In addition, as the solutions in Fig. 11.4 are still functions of L, it is clear that similar solutions will be found for rectangular guides.

Figs. 11.4 and 11.5 illustrate some of the important properties of negative index channel waveguides. Firstly, the guided modes can only be supported in high-index waveguides (i.e., $\varepsilon_2\mu_2 > \varepsilon_1\mu_1$). This is in contrast to negative index

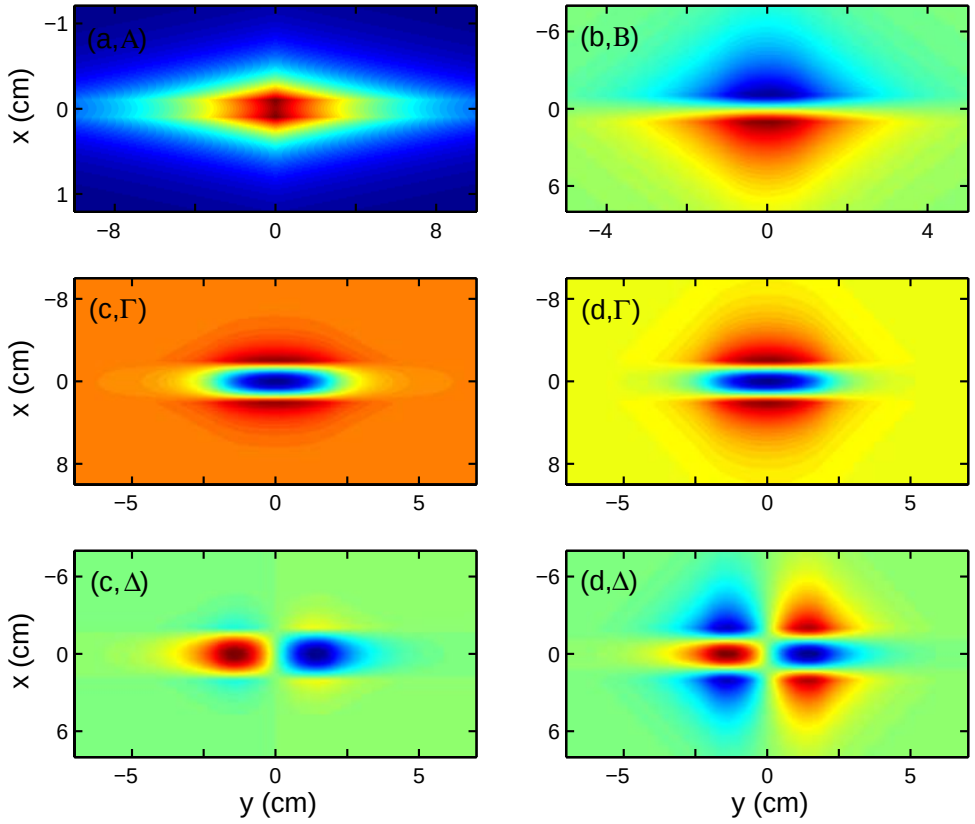

Figure 11.5: Examples of the mode profiles for the solutions in Fig. 11.4. Top row: $H^y_{2,1}$ solutions corresponding to intersections (a,A) and (b,B). Middle row: $H^y_{3,1}$ solutions corresponding to intersections (c,Γ) and (d,Γ). Bottom row: $H^y_{3,2}$ solutions corresponding to intersections (c,Δ) and (d,Δ).

slab waveguides [80] and is a consequence of the dispersion relations of the y component of the field. In addition, as the dispersion relations do not allow for an imaginary k_y, only the x component of the field can exhibit surface wave effects. Secondly, however, in accordance with the observations in negative index planar waveguides it is again found that the conventional hierarchy of the fast modes disappears. In particular, (i) for $p = 0$ the right hand side of Eq. (11.10) is negative so that the fundamental $H^y_{1,1}$ mode does not exist; (ii) for a given width L, solutions of $\gamma_x L$ associated with the first order $H^y_{2,1}$ mode only exist for a particular range of ω greater than a critical value; (iii) for modes greater than $H^y_{2,1}$, as the $\gamma_x L$ solutions in Fig. 11.4 decrease monotonically with $k_x L$ at different rates, there are two possible solutions to Eq. (11.10) so that two modes with the same number of nodes (i.e., degenerate modes) can coexist in a waveguide, as illustrated by the solution pairs: (c,Γ), (d,Γ) and (c,Δ), (d,Δ).

11.3.2 Propagation Characteristics of the Guided Modes

To investigate the frequency dispersion of the guided waves it is necessary to consider the frequency dependence of both ε_i and μ_i in Eq. (11.14). Although the specific form of the refractive index of a photonic crystal depends of the band structure [106], in this analysis the forms for the composite negative index material, as given in Eqs. (11.1) and (11.2), will be used. Based on earlier analysis the defining parameters are chosen to be: $\omega_{p,2}/2\pi = 10\,\mathrm{GHz}$, $\omega_{0,2}/2\pi = 4\,\mathrm{GHz}$ and $F = 0.56$ [70, 80]. In this case, the region of simultaneously negative ε_2 and μ_2 ranges from $4\,\mathrm{GHz}$ to $6\,\mathrm{GHz}$. The values of $\omega_{p,1}/2\pi = 2\,\mathrm{GHz}$ and $\omega_{0,1}/2\pi = 1\,\mathrm{GHz}$ were then chosen so that ε_1 and μ_1 are always positive and $\varepsilon_2\mu_2 > \varepsilon_1\mu_1$ in this range. Examples of dispersion curves for the modes of Fig. 11.5 are plotted in the top curves of Fig. 11.6. These curves correspond to the solutions: (a) (a,A) with $L = 0.1\,\mathrm{cm}$, (b) (b,B) with $L = 1\,\mathrm{cm}$ (i.e., the

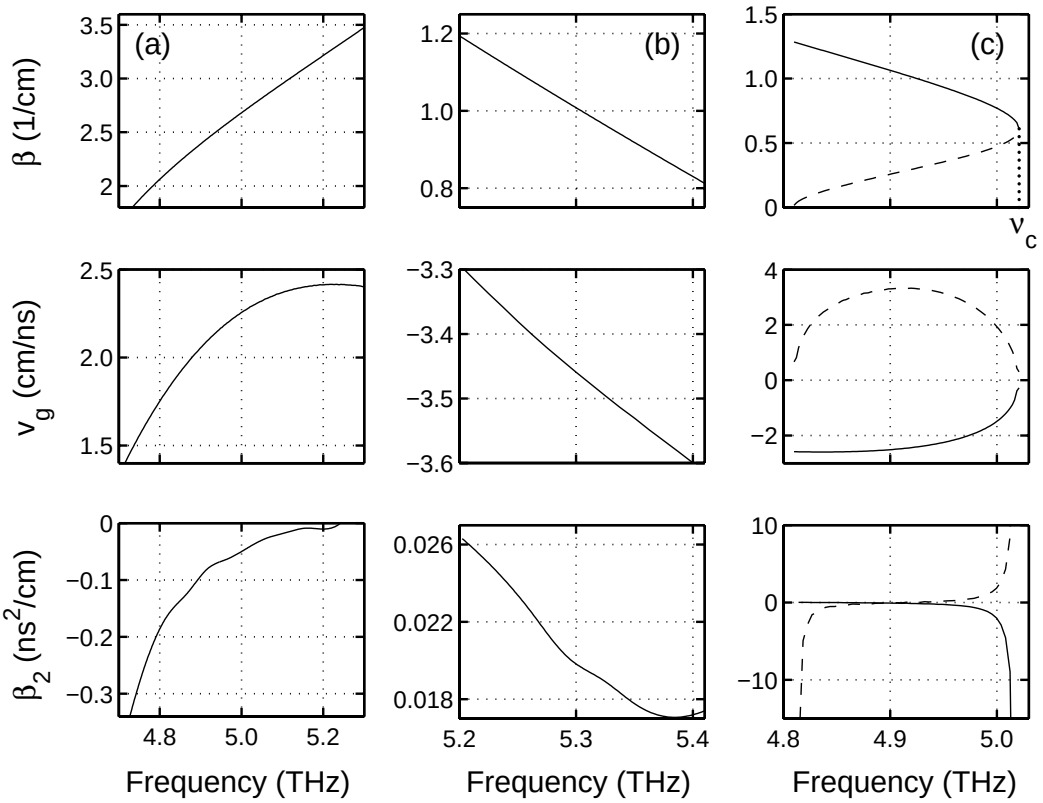

Figure 11.6: Top: propagation constants β, middle: group velocities v_g and bottom: group velocity dispersion parameters β_2. These solutions correspond to the modes: (a) (a,A), (b) (b,B), and (c) (c,Γ) and (d,Γ) of Fig. 11.5 where in (c) the solid and dashed lines correspond to the strongly (c,Γ) and weakly (d,Γ) localised modes, respectively.

two $H^y_{2,1}$ solutions), and (c) (c,Γ) and (d,Γ) with $L = 2\,\mathrm{cm}$ (i.e., the degenerate $H^y_{3,1}$ solutions) where the solid line corresponds to the strongly localised mode and the dashed line is the weakly localised mode. From this it is seen that of the two solutions offered by each designated mode type, one has a dispersion curve with a positive slope and the other a negative slope. Significantly, as $v_g = 1/\beta_1 = \mathrm{d}\omega/\mathrm{d}\beta$ [Eq. (3.17)], this implies that the sign of the group velocities will also be different and thus each mode can support both forward and backwards propagating waves [113]. This is confirmed in the middle curves of Fig. 11.6 where v_g is plotted explicitly for each of the modes. For the case of the $H^y_{2,1}$ modes it is the non-surface wave which has a negative v_g, and for the $H^y_{3,1}$ modes it is the tightly confined mode. In addition, it can also be seen that for the case of the degenerate modes, as the frequency is increased the two solutions for β converge until they reach a cutoff frequency ν_c associated with their intersection.[3] As a result, this convergence of the two solutions means that as the frequency approaches ν_c, v_g approaches zero so that the propagating mode will be slowed considerably. Thus this waveguide offers a convenient method for generating "fast" light ($v_g < 0$), "slow" light ($v_g \ll c$) and perhaps to even trap light ($v_g = 0$). The possibility to slow or trap light has many potential applications such as optical data storage, optical memories and quantum computing. Furthermore, as the light-matter interaction is enhanced for low v_g, slow light can be used to observe nonlinear processes such as harmonic generation and four-wave mixing in even weakly nonlinear materials [114].

The group velocity dispersion (GVD) of the guided modes as calculated via: $\beta_2 = \mathrm{d}^2\beta/\mathrm{d}\omega^2$ [Eq. (3.16)] is then plotted for each of the modes in the bottom curves of Fig. 11.6. In all cases the GVD parameter is quite large, particularly for the degenerate modes where the frequency approaches ν_c (the region of low v_g), and can be either anomalous [(a,A) and (c,Γ)] or normal [(b,B) and (d,Γ)]. Such large dispersion is typical behavior of the GVD at the band edges of photonic crystals [115] and for these particular modes, the dispersion can be around 9 orders of magnitude larger than that of conventional materials such as silica fibres ($20\,\mathrm{ps^2km^{-1}}$). This makes these waveguides idea for dispersion management and particularly for use in integrated circuits where short device lengths are favoured. In addition, by exploiting the reduced non-

[3] Although the strongly localised mode exists for frequencies below those plotted here, the weakly localised mode does not as the right hand side of Eq. (11.10) crosses the x axis.

linear threshold / large GVD combination it should be possible to investigate nonlinear effects such as optical soliton formation (see Section 3.8.1).

The energy flux of the guided (degenerate) modes in Fig. 11.6(c), which is characterised by the z component of the Poynting vector [Eq. (10.21)], has also been calculated. Since for backwards waves the Poynting vector and the wavevector point in opposite directions, it is expected that the energy flux of the modes will also have opposite signs [73]. The total power flux through the core and cladding regions of the waveguide are calculated as,

$$P_{core} = \int\int_{core} S_z \mathrm{d}x\mathrm{d}y, \qquad P_{clad} = \int\int_{clad} S_z \mathrm{d}x\mathrm{d}y. \tag{11.15}$$

For both modes the power flux inside the core is opposite to that in the cladding (see middle row of Fig. 11.5). However, on calculating the total normalised energy flux defined as:

$$P = \frac{P_{core} + P_{clad}}{|P_{core}| + |P_{clad}|}, \tag{11.16}$$

Fig. 11.7 shows that total energy flows in a positive direction for the weakly localised mode and a negative direction for the strongly localised mode, in agreement with the signs of v_g. It is worth noting that by definition, $|P| < 1$ and $P \to 1$ as the mode becomes poorly confined and $P \to -1$ as the mode becomes tightly confined. The significant feature of this result is that as the solutions converge at ν_c, the energy fluxes inside and outside the guide exactly cancel so that the total energy flux vanishes. Importantly, in their analysis for a negative index planar waveguide, Shadrivov *et al.* showed that at $P = 0$ the energy flowed in a double-vortex structure so that most of the energy remained localised inside the wave packet [80]. Thus as the energy flux goes to zero, the guided modes do not disintegrate and an analogous result for the modes of a channel waveguide can be expected.

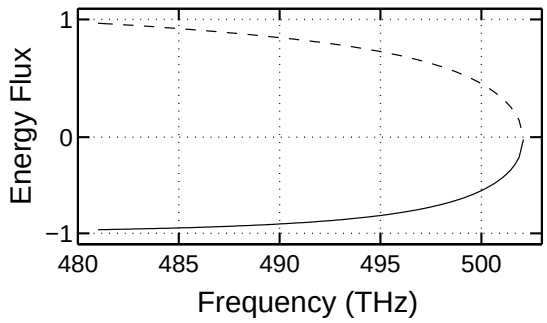

Figure 11.7: Normalised energy flux as calculated for the $H^y_{3,1}$ solutions of Fig. 11.6(c).

In Figs. 11.6 and 11.7 the dispersion and energy flux of typical modes have been examined as functions of the frequency. Alternatively, it is also useful to consider the dependence of the mode properties on the waveguide width L. Fig. 11.8 shows (a) the propagation constant and (b) the normalised energy flux for the $H^y_{3,1}$ modes at a fixed frequency, $\omega/2\pi = 5\,\mathrm{GHz}$, where again the solid line corresponds to the strongly localised mode (c, Γ) and the dashed line is the weakly localised mode (d, Γ). As expected, these have similar forms to the previous curves for varying frequency except that this time the two solutions converge as L is decreased until they reach a cutoff length L_c. Thus these results suggest that the propagating mode can be slowed simply by adiabatically decreasing the waveguide width. Furthermore, by decreasing the width to the critical length L_c it should be possible to stop the light completely. Thus it is expected that a simple waveguide structure such as that shown in the inset of Fig. 11.8 should act as an optical trap, where the frequency of light that can be trapped is determined by the range of the waveguide width.

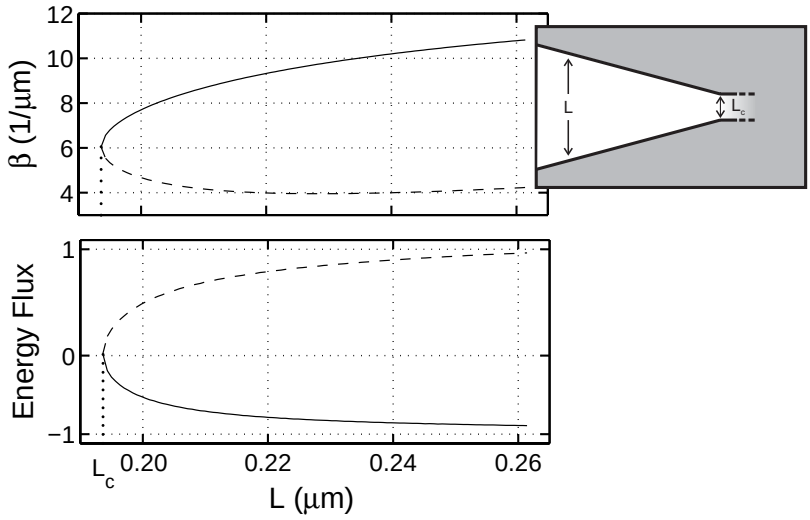

Figure 11.8: (a) Propagation constant and (b) normalised energy flux of the $H^y_{3,1}$ solutions from Fig. 11.6(c) as functions of the waveguide width L. The solid and dashed lines correspond to the strongly (c, Γ) and weakly (d, Γ) localised modes, respectively. Inset: design for an optical trap.

11.4 Fibre Modes

The previous section has shown that the guided mode solutions of a channel waveguide with a negative index core possess a number of properties that differed from those of a conventional positive index waveguide. In this section, similar analysis is conducted to investigate the properties of the guided modes of an optical fibre with a negative index (negative ε and μ) core. It will be shown that in contrast to the channel waveguides, negative index core fibres exhibit similar guiding characteristics to conventional fibres.

11.4.1 Wave Theory of Step-Index Fibres

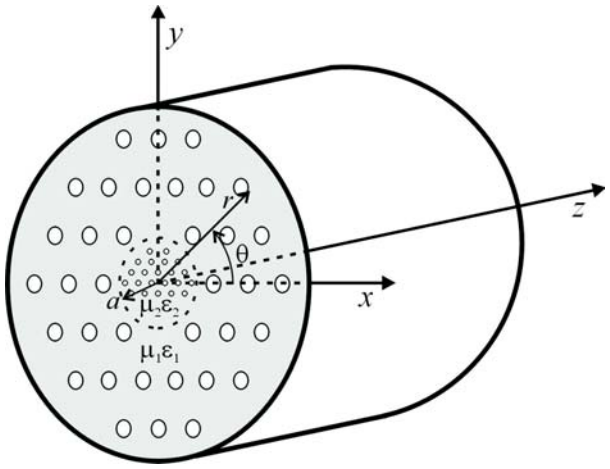

Figure 11.9: Waveguide structure and parameters of an optical fibre.

The analysis is based on the wave theory of step-index fibres [99]. Although, this approach ignores the complex refractive index profile of the negative index fibre, it should nevertheless be sufficient to obtain a qualitative understanding of the allowed modes. The analysis considers an axially symmetric fibre with the geometry and parameters given in Fig. 11.9. Here, the fibre has been illustrated as having a periodic cross sectional structure similar to that of the microstructured fibres described in Section 6.2.1, however, the mathematical analysis will be kept general so that it could equally apply to any fibre structure. In particular, if the fibre presented in Fig. 11.9 is to exhibit regions of negative refractive index then the “air hole” regions, at least in the core, are in fact likely to be regions of differing material. In this figure, the core, with a

radius a, and the cladding are defined by regions of differing hole diameter d and hole-to-hole spacing Λ. Again, it is assumed that the cladding has a positive index ($\varepsilon_1 > 0$ and $\mu_1 > 0$) and the core has a negative index ($\varepsilon_2 < 0$ and $\mu_2 < 0$). In cylindrical coordinates, the guided modes in an optical fibre are expressed as:

$$\tilde{\mathbf{E}}(r,\theta,z,t) = \mathbf{E}(r,\theta)\,\mathrm{e}^{-\mathrm{i}(\omega t-\beta z)}, \tag{11.17}$$

$$\tilde{\mathbf{H}}(r,\theta,z,t) = \mathbf{H}(r,\theta)\,\mathrm{e}^{-\mathrm{i}(\omega t-\beta z)}. \tag{11.18}$$

Substituting Eqs. (11.17) and (11.18) into Maxwell's equations [Eqs. (10.16) and (10.17)], the well known wave equations are obtained as:

$$\frac{\partial^2 E_z}{\partial r^2} + \frac{1}{r}\frac{\partial E_z}{\partial r} + \frac{1}{r^2}\frac{\partial^2 E_z}{\partial \theta^2} + \left[k^2\varepsilon_i\mu_i - \beta^2\right]E_z = 0, \tag{11.19}$$

$$\frac{\partial^2 H_z}{\partial r^2} + \frac{1}{r}\frac{\partial H_z}{\partial r} + \frac{1}{r^2}\frac{\partial^2 H_z}{\partial \theta^2} + \left[k^2\varepsilon_i\mu_i - \beta^2\right]H_z = 0, \tag{11.20}$$

with the transverse fields related to E_z and H_z as follows:

$$\begin{aligned}
E_r &= -\frac{\mathrm{i}}{[k^2\varepsilon_i\mu_i - \beta^2]}\left(\beta\frac{\partial E_z}{\partial r} + \frac{\omega\mu}{r}\frac{\partial H_z}{\partial \theta}\right)\\
E_\theta &= -\frac{\mathrm{i}}{[k^2\varepsilon_i\mu_i - \beta^2]}\left(\frac{\beta}{r}\frac{\partial E_z}{\partial \theta} - \omega\mu\frac{\partial H_z}{\partial r}\right)\\
H_r &= -\frac{\mathrm{i}}{[k^2\varepsilon_i\mu_i - \beta^2]}\left(\beta\frac{\partial H_z}{\partial r} - \frac{\omega\varepsilon}{r}\frac{\partial E_z}{\partial \theta}\right)\\
H_\theta &= -\frac{\mathrm{i}}{[k^2\varepsilon_i\mu_i - \beta^2]}\left(\frac{\beta}{r}\frac{\partial H_z}{\partial \theta} + \omega\varepsilon\frac{\partial E_z}{\partial r}\right).
\end{aligned} \tag{11.21}$$

11.4.2 TE and TM modes

The analysis begins by considering the TE modes ($E_z = 0$) for which the wave equation is:

$$\frac{\partial^2 H_z}{\partial r^2} + \frac{1}{r}\frac{\partial H_z}{\partial r} + \left[k^2\varepsilon_i\mu_i - \beta^2 - \frac{n^2}{r^2}\right]H_z = 0, \tag{11.22}$$

where n is an integer and the related fields can be found via:

$$E_r = \frac{-\mathrm{i}\omega\mu}{(k^2\varepsilon_i\mu_i - \beta^2)}\frac{1}{r}\frac{\partial H_z}{\partial \theta}, \qquad E_\theta = \frac{\mathrm{i}\omega\mu}{(k^2\varepsilon_i\mu_i - \beta^2)}\frac{\partial H_z}{\partial r}, \tag{11.23}$$

$$H_r = \frac{-\mathrm{i}\beta}{(k^2\varepsilon_i\mu_i - \beta^2)}\frac{\partial H_z}{\partial r}, \qquad H_\theta = \frac{-\mathrm{i}\beta}{(k^2\varepsilon_i\mu_i - \beta^2)}\frac{1}{r}\frac{\partial H_z}{\partial \theta}. \tag{11.24}$$

Due to the cylindrical symmetry of the fibre, the magnetic field H_z in the core and the cladding can be expressed as:

$$H_z = \left\{ \begin{array}{l} g\left(r\right) \\ h\left(r\right) \end{array} \right\} \cos\left(n\theta + \psi\right) \qquad \begin{array}{l} (0 \leq r \leq a) \\ (r > a). \end{array} \tag{11.25}$$

Applying the boundary condition that the tangential field components H_z and H_θ should be continuous at $r = a$, it follows that:

$$g(a) = h(a),$$

$$\frac{\mathrm{i}\beta}{k^2\varepsilon_2\mu_2 - \beta^2}\frac{n}{a}g(a)\sin\left(n\theta + \psi\right) = \frac{\mathrm{i}\beta}{k^2\varepsilon_1\mu_1 - \beta^2}\frac{n}{a}h(a)\sin\left(n\theta + \psi\right). \tag{11.26}$$

As $\mu_2\varepsilon_2 \neq \mu_1\varepsilon_1$, for the bottom equation to hold for all angles θ, n must equal zero which is referred to as the azimuthal condition. Thus $\partial H_z/\partial\theta = 0$ which when substituted into the appropriate components of Eqs. (11.23) and (11.24) yields: $E_r = H_\theta = 0$. Combining these results, the wave equation for the TE modes reduces to:

$$\frac{\partial^2 H_z}{\partial r^2} + \frac{1}{r}\frac{\partial H_z}{\partial r} + \left[k^2\varepsilon_i\mu_i - \beta^2\right]H_z = 0, \tag{11.27}$$

together with:

$$E_\theta = \frac{\mathrm{i}\omega\mu_0\mu_i}{(k^2\varepsilon_i\mu_i - \beta^2)}\frac{\partial H_z}{\partial r}, \qquad H_r = \frac{-\mathrm{i}\beta}{(k^2\varepsilon_i\mu_i - \beta^2)}\frac{\partial H_z}{\partial r}. \tag{11.28}$$

Defining the wavenumbers in the core and cladding along the transversal direction as:

$$\kappa = \sqrt{k^2\varepsilon_2\mu_2 - \beta^2} \quad \text{and} \quad \sigma = \sqrt{\beta^2 - k^2\varepsilon_1\mu_1}, \tag{11.29}$$

the wave equation in the core $[H_z = g(r)]$ can be written as:

$$\frac{\partial^2 g}{\partial r^2} + \frac{1}{r}\frac{\partial g}{\partial r} + \kappa g = 0, \tag{11.30}$$

and in the cladding $[H_z = h(r)]$:

$$\frac{\partial^2 h}{\partial r^2} + \frac{1}{r}\frac{\partial h}{\partial r} - \sigma h = 0. \tag{11.31}$$

As $\varepsilon_i\mu_i > 0$ in both the core and the cladding, Eqs. (11.30) and (11.31) have an identical form to the wave equations found for a positive index core fibre and thus, by analogy, the solution for the H_z mode is:

$$H_z = \left\{ \begin{array}{ll} AJ_0\left(\kappa r\right) & (0 \leq r \leq a) \\ BK_0\left(\sigma r\right) & (r > a). \end{array} \right. \tag{11.32}$$

Applying the boundary conditions for H_z and E_θ at $r = a$:

$$AJ_0(\kappa a) = BK_0(\sigma a),$$
$$\mu_0\mu_2\frac{A}{\kappa}J_0'(\kappa a) = -\mu_0\mu_1\frac{B}{\sigma}K_0'(\sigma a), \tag{11.33}$$

yields the dispersion relation as:

$$\mu_2\frac{J_1(u)}{uJ_0(u)} = -\mu_1\frac{K_1(w)}{wK_0(w)}, \tag{11.34}$$

where

$$u = a\kappa = a\sqrt{k^2\varepsilon_2\mu_2 - \beta^2} \quad \text{and} \quad w = a\sigma = a\sqrt{\beta^2 - k^2\varepsilon_1\mu_1}. \tag{11.35}$$

Finally, it is noted that the transverse wavenumbers u and w are related via:

$$u^2 + w^2 = k^2(\varepsilon_2\mu_2 - \varepsilon_1\mu_1)a^2 = v^2, \tag{11.36}$$

where v is referred to as the normalised frequency. Thus, once v is given, u and w can be found from Eqs. (11.34) and (11.36) and the electromagnetic fields for the TE modes are completely determined. The explicit forms of the electric and magnetic fields can be summarised as:

$$E_r = E_z = H_\theta = 0, \tag{11.37}$$

$$\begin{aligned}
\text{(a) core } (0 \le r \le a): E_\theta &= -\mathrm{i}\omega\mu_0\mu_2\frac{a}{u}AJ_1\left(\frac{u}{a}r\right) \\
H_r &= \mathrm{i}\beta\frac{a}{u}AJ_1\left(\frac{u}{a}r\right) \\
H_z &= AJ_0\left(\frac{u}{a}r\right), \qquad (11.38)\\
\text{(b) cladding } (r > a): E_\theta &= \mathrm{i}\omega\mu_0\mu_1\frac{a}{w}\frac{J_0(u)}{K_0(w)}AK_1\left(\frac{w}{a}r\right) \\
H_r &= -\mathrm{i}\beta\frac{a}{w}\frac{J_0(u)}{K_0(w)}AK_1\left(\frac{w}{a}r\right) \\
H_z &= \frac{J_0(u)}{K_0(w)}AK_0\left(\frac{w}{a}r\right), \qquad (11.39)
\end{aligned}$$

and again the constant A is related to the mode power [Eq. (11.7)].

Applying the same procedure for the TM modes ($H_z = 0$), it follows that the dispersion relation is:

$$\varepsilon_2\frac{J_1(u)}{uJ_0(u)} = -\varepsilon_1\frac{K_1(w)}{wK_0(w)}, \tag{11.40}$$

and the electromagnetic fields are given by:

$$E_\theta = H_z = H_r = 0, \tag{11.41}$$

$$\begin{aligned}
\text{(a) core } (0 \le r \le a): E_r &= \mathrm{i}\beta\frac{a}{u}AJ_1\left(\frac{u}{a}r\right) \\
E_z &= AJ_0\left(\frac{u}{a}r\right) \\
H_\theta &= \mathrm{i}\omega\varepsilon_0\varepsilon_2\frac{a}{u}AJ_1\left(\frac{u}{a}r\right), \qquad (11.42) \\
\text{(b) cladding } (r > a): E_r &= -\mathrm{i}\beta\frac{a}{w}\frac{J_0(u)}{K_0(w)}AK_1\left(\frac{w}{a}r\right) \\
E_z &= \frac{J_0(u)}{K_0(w)}AK_0\left(\frac{w}{a}r\right) \\
H_z &= -\mathrm{i}\omega\varepsilon_0\varepsilon_1\frac{a}{w}\frac{J_0(u)}{K_0(w)}AK_1\left(\frac{w}{a}r\right). \qquad (11.43)
\end{aligned}$$

The propagation constant β of the fibre can be calculated by solving the dispersion equations [Eq. (11.34) or Eq. (11.40)] under the condition $u^2 + w^2 = v^2$, using similar graphical techniques to those employed for the case of the channel waveguides (see Ref. [99]). Fig. 11.10 shows typical dispersion relations for the (a) TE modes and (b) TM modes of a fibre with: $\varepsilon_1 = 1.46$, $\mu_1 = 1$, $\varepsilon_2 = -1.7$, $\mu_2 = -0.9$, $a = 2\,\mu\mathrm{m}$ and $v = 10$.[4] The similarity in the appearance of these two figures can be explained by noting that the dispersion relations only differ by the ratios $\mu_1/\mu_2 = -1.11$ and $\varepsilon_1/\varepsilon_2 = -0.86$, and in both cases the mode boundaries are defined by the zero crossings of J_0 and J_1 (dotted lines). For comparison, Fig. 11.10(c) shows an example of the dispersion relations for a fibre with identical parameters but a positive index core ($\varepsilon_2 = 1.7$ and $\mu_2 = 0.9$). Significantly, it can be seen that the allowed modes of the negative index guide exist in the forbidden regions of the positive index guide. Thus the negative guide permits modes at lower frequencies than the cutoff frequency for the positive index guide. Furthermore, in accordance with the observations of a channel guide, it can also be seen that for a given core radius a, solutions of the first order mode of a negative index fibre only exist for a particular range of v. Possible solutions for the first order TE mode of the negative guide are shown in Figs. 11.10(d) and (e).[5] These figures illustrate solutions in

[4] The parameters were chosen so that n^2 $(= \varepsilon\mu)$ and a are close to that of a standard silica fibre [4].

[5] The discontinuity in Fig. 11.10(e) is due to a discontinuity in $K_0(w)$.

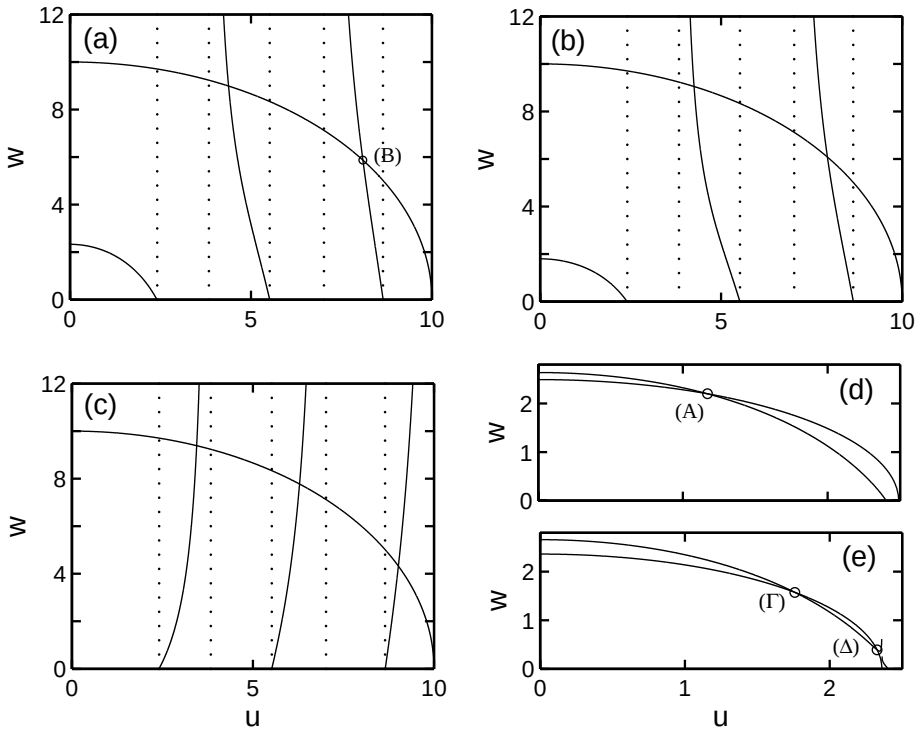

Figure 11.10: $u - w$ relationships for (a) TE and (b) TM modes with a negative index core. (c) TE modes with a positive index core and (d)-(e) first order TE modes for a negative index core.

two different regimes: (i) in (d) $v = 2.5$ and only one possible solution exists, and (ii) in (e) $v = 2.36$ and two solutions can exist. Although this property of degenerate modes (i.e., two modes with the same number of nodes coexisting in the guide) was also established for the negative index channel guides, unlike the situation here, those existed for the higher order modes.

Examples of typical profiles for the TE modes are shown in Fig. 11.11 where $B_r = \mu H_r$ is plotted [Eq. (10.14)], which is continuous in r. These correspond to the solutions marked in Fig. 11.10. Here A is a first order mode, B is a third order mode and Γ and Δ are the tightly and weakly confined degenerate first order modes, respectively. It is worth noting that as the appearance of the TM modes are similar to the TE modes but with H_r interchanged for E_r, examples of the TM solutions will not be plotted here. The interesting feature of these plots is that modes A, and to a lesser extent Γ, have the appearance of surface waves. Such surface waves were also found for the case of negative index channel guides and they also appeared in a region where propagating modes were forbidden for positive guides.

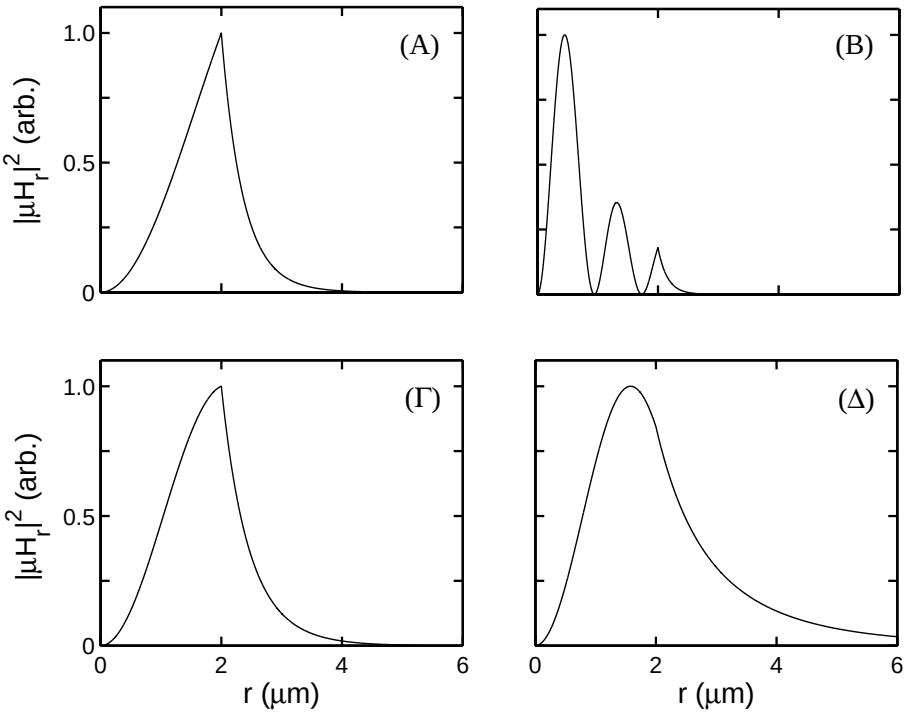

Figure 11.11: TE mode profiles corresponding to the marked solutions in Fig. 11.10 where A is a first order mode, B is a third order mode and Γ and Δ are degenerate first order modes.

Figs. 11.10 and 11.11 have illustrated a number of important properties of the negative index fibre modes which are similar to those of the negative index channel waveguide modes. Such similarities are not unexpected due to similarities in the geometries. In additional, it has also been established that, like the negative index channel guides, these fibres can only support propagating modes in a high-index waveguide (i.e., $\varepsilon_2\mu_2 > \varepsilon_1\mu_1$).

It now remains to investigate the frequency dispersion of the guided modes. Clearly, as the composite material described in Section 11.2.1 is not practical for a fibre geometry, it is not possible to use the forms of the permittivity and permeability as given in Section 11.3. Thus the following analysis will simply assume that $\varepsilon_i(\omega)$ and $\mu_i(\omega)$ are constant over the frequency range being investigated. This is a reasonable assumption as for the frequencies considered in Fig. 11.6, $\varepsilon_i(\omega)$ and $\mu_i(\omega)$ varied by less than 2%. The dispersion curves for modes A, B and Δ, as found from Eqs. (11.34) and (11.35), are plotted in Figs. 11.12(a), (b) and (c), respectively. Again, the group velocity, $v_g = \mathrm{d}\omega/\mathrm{d}\beta$, and the GVD, $\beta_2 = \mathrm{d}^2\beta/\mathrm{d}\omega^2$ (middle and bottom curves, respectively) are also calculated. From the curves for the first two modes it is clear that these exhibit

dispersion characteristics similar to those of standard positive index fibres and in particular, in both cases the slope of β is positive so that the group velocities are also positive. However, one difference is that the GVD parameter of the first order mode is 3 orders of magnitude larger than a conventional fibre ($20 \times 10^{-3}\,\mathrm{ps^2 m^{-1}}$). Significantly, from the curves for the third mode it can be noticed that although the group velocity of the mode Δ is still positive, this does in fact exhibit "fast" light as for the lower frequency range $v_g > c$ ($c = 300\,\mu\mathrm{m\,ps^{-1}}$).

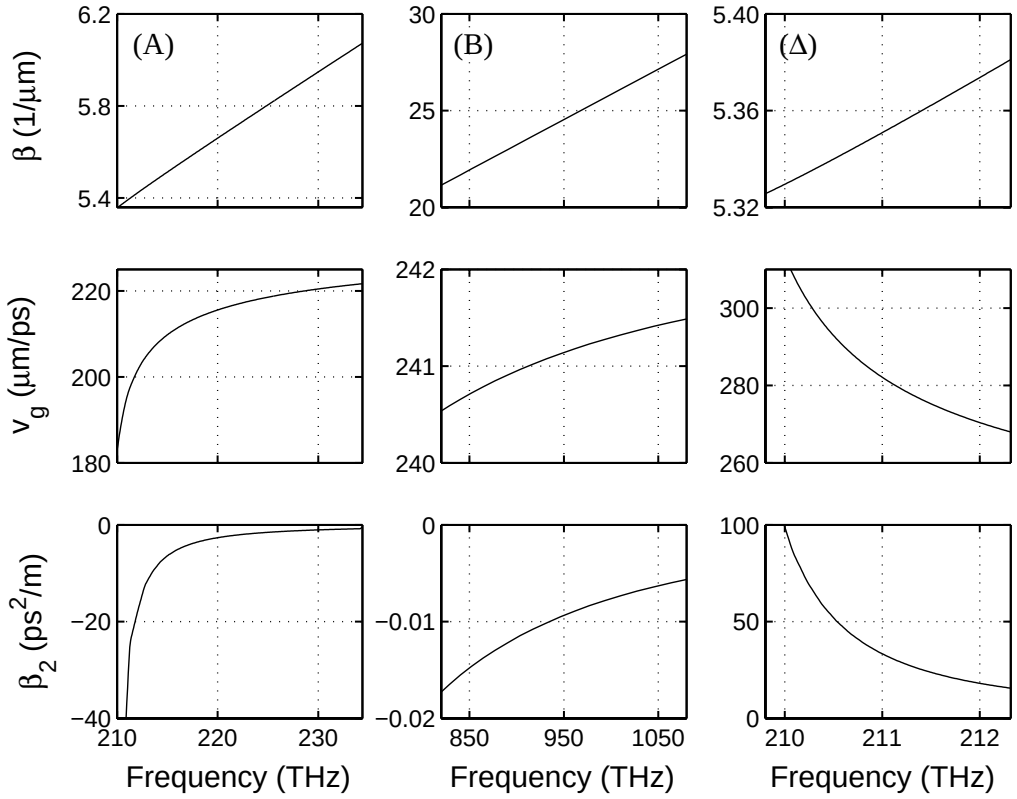

Figure 11.12: Dispersion curves for the TE mode profiles given in Fig. 11.11.

Again, these results have indicated the ability of the negative index waveguides to manipulate the propagation characteristics of the guided modes. Importantly, although it has been shown that these negative index fibres can support fast light, in all cases $v_g > 0$ and furthermore, there was no evidence of them supporting slow ($v_g \to 0$) light. Thus for these reasons the normalised power flow will not be calculated here as, for all the modes represented in Fig. 11.12, it will simply fall in the range $0 < P < 1$ [Eq. (11.16)].

11.4.3 Hybrid modes

The following analysis will now consider the case of the hybrid modes where both the axial electromagnetic field components E_z and H_z are non-zero. In such instances, $\partial E_z/\partial r$ and $\partial H_z/\partial\theta$ (or $\partial E_z/\partial\theta$ and $\partial H_z/\partial r$) should have the same θ dependencies. Taking this into consideration, using Eq. (11.32) the z-components of the electric field can be written as [116]:

$$E_z = \begin{cases} AJ_n\left(\frac{u}{a}r\right)\cos\left(n\theta+\phi\right) & (0 \le r \le a) \\ CK_n\left(\frac{w}{a}r\right)\cos\left(n\theta+\phi\right) & (r > a), \end{cases} \tag{11.44}$$

$$H_z = \begin{cases} BJ_n\left(\frac{u}{a}r\right)\sin\left(n\theta+\phi\right) & (0 \le r \le a) \\ DK_n\left(\frac{w}{a}r\right)\sin\left(n\theta+\phi\right) & (r > a), \end{cases} \tag{11.45}$$

where u and w are still given by Eq. (11.35). Substituting Eqs. (11.44) and (11.45) into Eq. (11.21), it follows that the transverse components are,
(a) core $(0 \le r \le a)$:

$$\begin{aligned} E_r &= -\frac{\mathrm{i}a^2}{u^2}\left[A\beta\frac{u}{a}J_n'\left(\frac{u}{a}r\right) + B\omega\mu_0\mu_2\frac{n}{r}J_n\left(\frac{u}{a}r\right)\right]\cos\left(n\theta+\phi\right) \\ E_\theta &= -\frac{\mathrm{i}a^2}{u^2}\left[-A\beta\frac{n}{r}J_n\left(\frac{u}{a}r\right) - B\omega\mu_0\mu_2\frac{u}{a}J_n'\left(\frac{u}{a}r\right)\right]\sin\left(n\theta+\phi\right) \\ H_r &= -\frac{\mathrm{i}a^2}{u^2}\left[A\omega\varepsilon_0\varepsilon_2\frac{n}{r}J_n\left(\frac{u}{a}r\right) + B\beta\frac{u}{a}J_n'\left(\frac{u}{a}r\right)\right]\sin\left(n\theta+\phi\right) \\ H_\theta &= -\frac{\mathrm{i}a^2}{u^2}\left[A\omega\varepsilon_0\varepsilon_2\frac{u}{a}J_n'\left(\frac{u}{a}r\right) + B\beta\frac{n}{r}J_n\left(\frac{u}{a}r\right)\right]\cos\left(n\theta+\phi\right), \end{aligned} \tag{11.46}$$

(b) cladding $(r > a)$:

$$\begin{aligned} E_r &= \frac{\mathrm{i}a^2}{w^2}\left[C\beta\frac{w}{a}K_n'\left(\frac{w}{a}r\right) + D\omega\mu_0\mu_1\frac{n}{r}K_n\left(\frac{w}{a}r\right)\right]\cos\left(n\theta+\phi\right) \\ E_\theta &= \frac{\mathrm{i}a^2}{w^2}\left[-C\beta\frac{n}{r}K_n\left(\frac{w}{a}r\right) - D\omega\mu_0\mu_1\frac{w}{a}K_n'\left(\frac{w}{a}r\right)\right]\sin\left(n\theta+\phi\right) \\ H_r &= \frac{\mathrm{i}a^2}{w^2}\left[C\omega\varepsilon_0\varepsilon_1\frac{n}{r}K_n\left(\frac{w}{a}r\right) + D\beta\frac{w}{a}K_n'\left(\frac{w}{a}r\right)\right]\sin\left(n\theta+\phi\right) \\ H_\theta &= \frac{\mathrm{i}a^2}{w^2}\left[C\omega\varepsilon_0\varepsilon_1\frac{w}{a}K_n'\left(\frac{w}{a}r\right) + D\beta\frac{n}{r}K_n\left(\frac{w}{a}r\right)\right]\cos\left(n\theta+\phi\right). \end{aligned} \tag{11.47}$$

Continuity of the tangential components (E_z, E_θ, H_z and H_θ) at the boundary $r = a$ yields, for the E fields:

$$\begin{aligned} AJ_n\left(u\right) &= CK_n\left(w\right), \qquad (11.48) \\ \frac{an\beta}{u^2}AJ_n\left(u\right) + \frac{a\omega}{u}\mu_0\mu_2BJ_n'\left(u\right) &= -\frac{an\beta}{w^2}CK_n\left(w\right) - \frac{a\omega}{w}\mu_0\mu_1DK_n'\left(w\right), \end{aligned}$$

and for the H fields:

$$\begin{aligned} BJ_n(u) &= DK_n(w), \qquad (11.49)\\ -\frac{a\omega}{u}\varepsilon_0\varepsilon_2 AJ_n'(u) - \frac{an\beta}{u^2}BJ_n(u) &= \frac{a\omega}{w}\varepsilon_0\varepsilon_1 CK_n'(w) + \frac{an\beta}{w^2}DK_n(w). \end{aligned}$$

For these four equations to be consistent the determinant of the coefficients must vanish and this gives the dispersion relation as:

$$\begin{aligned} &\left(\mu_0\mu_1\frac{K_n'(w)}{wK_n(w)} + \mu_0\mu_2\frac{J_n'(u)}{uJ_n(u)}\right)\left(\varepsilon_0\varepsilon_1\frac{K_n'(w)}{wK_n(w)} + \varepsilon_0\varepsilon_2\frac{J_n'(u)}{uJ_n(u)}\right)\\ &\qquad = n^2\left(\frac{1}{u^2}+\frac{1}{w^2}\right)\left(\frac{\varepsilon_0\varepsilon_2\mu_0\mu_2}{u^2} + \frac{\varepsilon_0\varepsilon_1\mu_0\mu_1}{w^2}\right). \qquad (11.50) \end{aligned}$$

As for the TE and TM modes, the propagation constant β of the hybrid modes is calculated by solving Eq. (11.50) together with the $u-w$ relation of Eq. (11.35). In addition, using the continuity equations the constants B, C and D can be written in terms of the usual amplitude coefficient A as:

$$\begin{aligned} C &= A\frac{J_n(u)}{K_n(w)},\\ D &= B\frac{J_n(u)}{K_n(w)},\\ B &= -\frac{n\beta A}{\omega}\frac{\left[\frac{1}{u^2}+\frac{1}{w^2}\right]}{\left[\frac{J_n'(u)}{uJ_n(u)}+\frac{K_n'(w)}{wK_n(w)}\right]}. \qquad (11.51) \end{aligned}$$

Unlike the analysis for the TE and TM modes of Section 11.4.2, the dispersion relation for the hybrid mode cannot be solved exactly via simple graphical techniques. Instead to solve Eq. (11.50) it is necessary to employ Newton's method which states that after $m+1$ iterations,

$$\beta_{m+1} = \beta_m - \frac{F(\beta_m)}{F'(\beta_m)}, \qquad (m = 0, 1, 2, 3, \ldots), \qquad (11.52)$$

where β_0 is the initial guess for β and F is the differentiable function,

$$\begin{aligned} F(\beta_m) &= \left(\frac{\mu_0\mu_1 K_n'(w_m)}{w_m K_n(w_m)} + \frac{\mu_0\mu_2 J_n'(u_m)}{u_m J_n(u_m)}\right)\left(\frac{\varepsilon_0\varepsilon_1 K_n'(w_m)}{w_m K_n(w_m)} + \frac{\varepsilon_0\varepsilon_2 J_n'(u_m)}{u_m J_n(u_m)}\right)\\ &- n^2\left(\frac{1}{u_m^2}+\frac{1}{w_m^2}\right)\left(\frac{\varepsilon_0\varepsilon_2\mu_0\mu_2}{u_m^2} + \frac{\varepsilon_0\varepsilon_1\mu_0\mu_1}{w_m^2}\right), \qquad (11.53) \end{aligned}$$

which depends on the current estimate of β_m through u_m and w_m. Calculation of Eq. (11.52) is then repeated until the required accuracy of β is reached. However, in order for the solution to converge the initial guess for β must be quite

accurate. Thus to obtain a first approximation for β_0 the dispersion relation is rewritten as:

$$w = \left[\frac{\left(\mu_0\mu_1 \frac{K_n'(w')}{w'K_n(w')} + \mu_0\mu_2 \frac{J_n'(u)}{uJ_n(u)}\right)\left(\varepsilon_0\varepsilon_1 \frac{K_n'(w')}{w'K_n(w')} + \varepsilon_0\varepsilon_2 \frac{J_n'(u)}{uJ_n(u)}\right)}{n^2\left(\frac{\varepsilon_0\varepsilon_2\mu_0\mu_2}{u^2} + \frac{\varepsilon_0\varepsilon_1\mu_0\mu_1}{w'^2}\right)} - \frac{1}{u^2} \right]^{-1/2}, \tag{11.54}$$

where,

$$w' = \sqrt{v^2 - u^2}, \tag{11.55}$$

so that the graphical method of Section 11.4.2 can again be used to plot u vs w curves.

Fig. 11.13 shows the $u - w$ curves for: $\varepsilon_1 = 1.46$, $\mu_1 = 1$, $\varepsilon_2 = -1.7$, $\mu_2 = -0.9$, $a = 2\,\mu$m, $v = 10$ and $n = 1$. From these curves it can be seen that there exists two solutions within the boundaries of the allowed modes. By analogy with the solutions found for a conventional positive index core fibre, these solutions can be designated as EH and HE modes, where the EH solutions appear to the immediate left of the mode boundaries (dotted lines) and the HE solutions appear to the right. The three solutions found here give: (a) $\beta = 2.334\,\mu$m, (b) $\beta = 2.320\,\mu$m and (c) $\beta = 2.317\,\mu$m. Using these as the initial guesses for β, Newton's method then yields: (a) $\beta = 2.336\,\mu$m, (b) $\beta = 2.321\,\mu$m and $\beta = 2.318\,\mu$m. The corresponding mode profiles at $\theta = 0$ are plotted in Fig. 11.14 via $D_r = \varepsilon E_r$, which is continuous in r. These clearly illustrate the differences between the EH and HE modes.

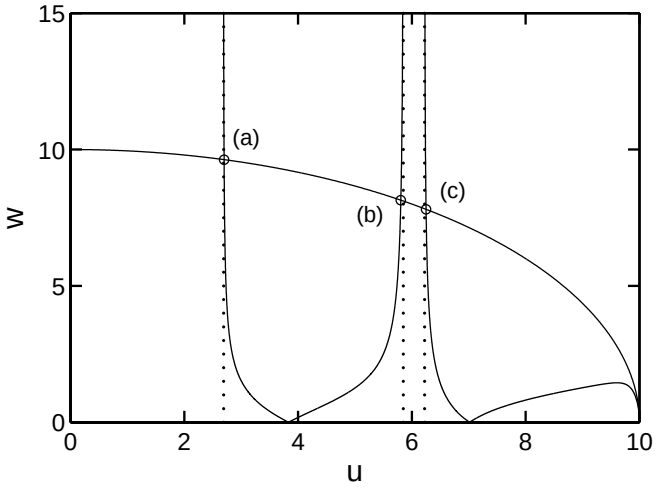

Figure 11.13: $u - w$ relationship for hybrid modes in a negative index core fibre with $n = 1$.

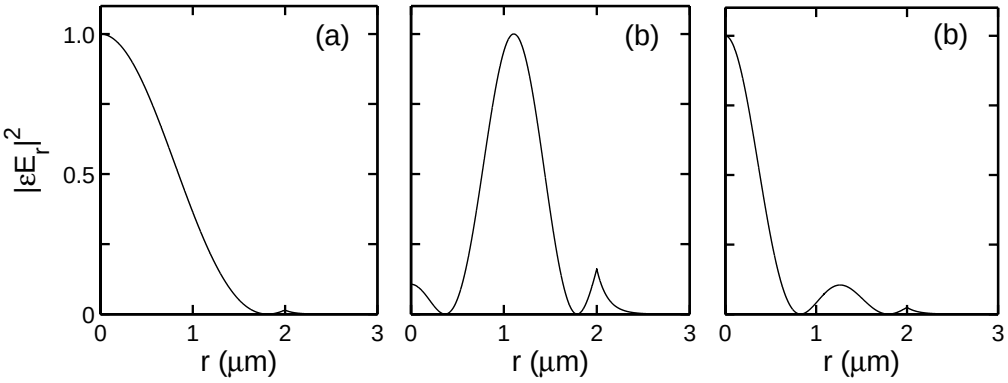

Figure 11.14: Hybrid mode profiles, at $\theta = 0$, corresponding to the marked solutions in Fig. 11.13 where (a) is a the first HE mode, (b) is the first EH mode and (c) is the second HE mode.

The dispersion curves for these modes, as found from Eqs. (11.35) and (11.50), are plotted in Fig. 11.15. Interestingly, despite the difference in the mode profiles, the frequency dispersion of the first EH mode and the second HE mode (and even the first HE mode) are very similar. In addition, it can also be noticed that the shapes of these curves are remarkably similar to the dispersion

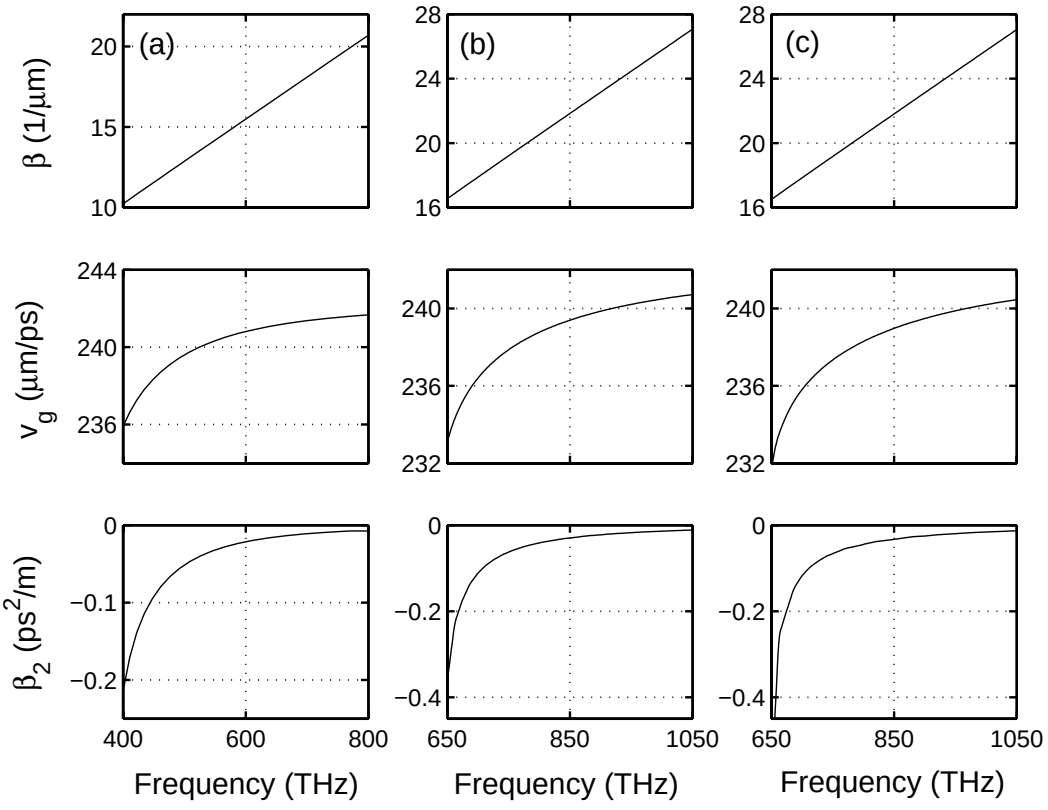

Figure 11.15: Dispersion curves for the hybrid mode profiles of Fig. 11.14.

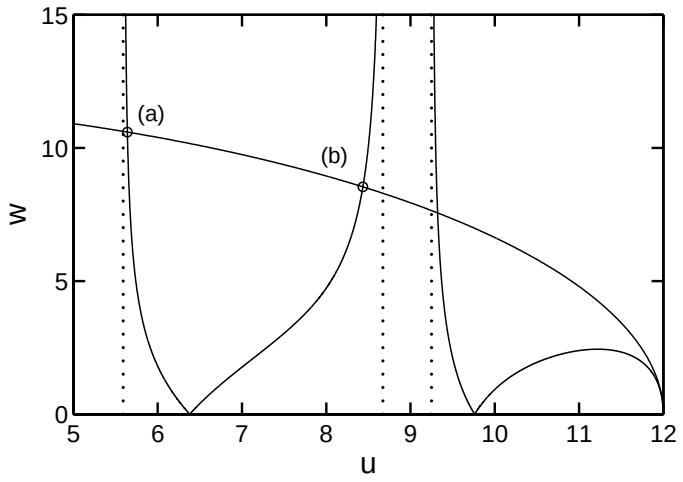

Figure 11.16: $u - w$ relationship for hybrid modes in a negative index core fibre with $n = 3$.

profiles of the TE modes and in particular, all of the modes exhibit a positive v_g. However, in contrast to the TE modes, it is clear that none of the modes represented here exhibit fast light and that all of the GVD parameters are of a similar order of magnitude to values obtained in positive index fibres.

Finally, the properties of some higher order modes (i.e., $n > 1$) are also investigated. Fig. 11.16 shows the $u - w$ curves for: $\varepsilon_1 = 1.46$, $\mu_1 = 1$, $\varepsilon_2 = -1.7$, $\mu_2 = -0.9$, $a = 2\,\mu$m, $v = 10$ and $n = 3$. Due to the similarity in the dispersion curves of the first EH mode and the second HE mode, only the first (a) HE and (b) EH modes are considered here. The propagation constants obtained using Newton's method are: (a) $\beta = 28.07\,\mu$m and (b) $\beta = 27.75\,\mu$m, and the corresponding mode profiles at $\theta = 0$ are plotted in Fig. 11.17. Calculating

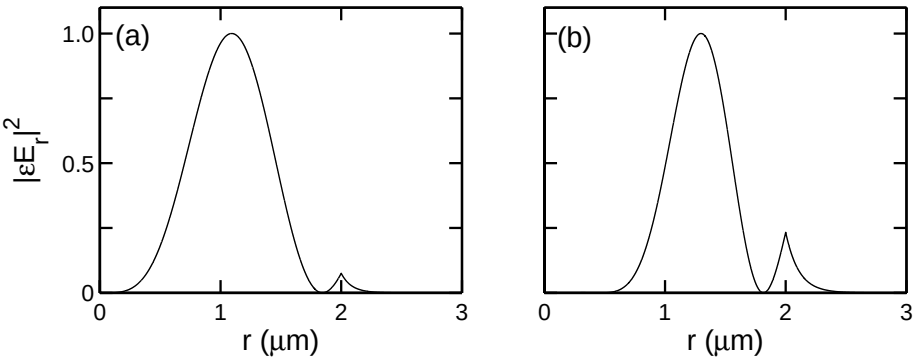

Figure 11.17: Hybrid mode profiles, at $\theta = 0$, corresponding to the marked solutions in Fig. 11.16 where (a) is the first HE mode and (b) is the first EH mode.

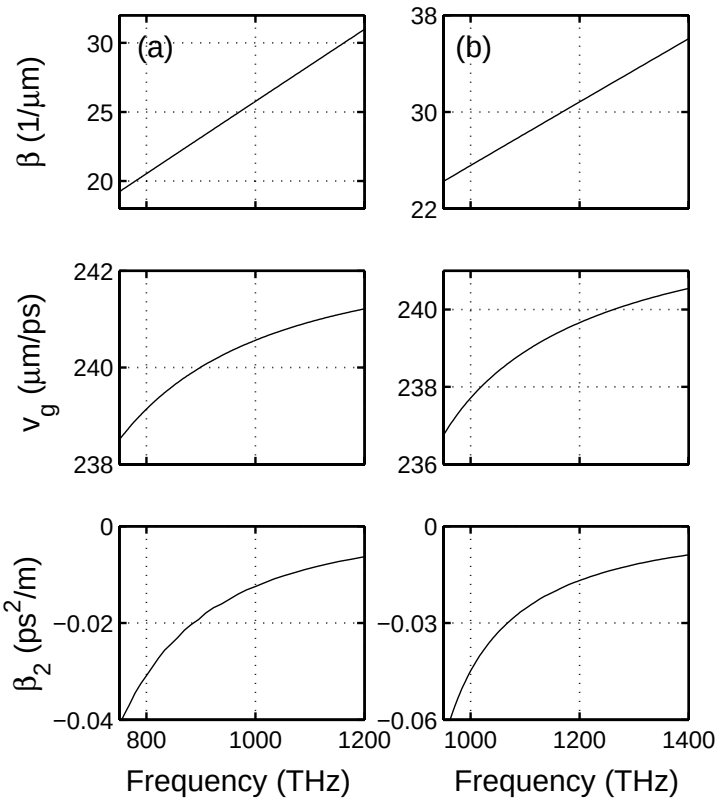

Figure 11.18: Dispersion curves for the hybrid mode profiles of Fig. 11.17.

the frequency dispersion of these modes they are found to exhibit dispersion characteristics similar to those of the $n = 1$ modes, and hence also of the standard positive index fibres. Significantly, a further reduction in the order of magnitude of the GVD parameter can also be noticed which, by comparing Figs. 11.12, 11.15 and 11.18, is in accordance with the trend that the GVD decreases for increasing mode order. Thus it appears that it is the lowest order modes that exhibit the most unusual dispersion characteristics.

11.5 Coupling Between Guided Modes

If negative refractive index waveguides are to find practical application in optical systems it is necessary to establish ways in which to couple light into them. Thus this section calculates the coupling coefficients between guided modes of adjacent parallel waveguides with both positive and negative indices in the core. In particular, the analysis is based on the guided mode solutions of nega-

tive index channel waveguides which were shown to permit both forward and backward propagating waves.

11.5.1 Formulation of the Problem

The analysis considers the case of two symmetric channel waveguides, as illustrated in Fig. 11.19. The refractive index distributions for the two guides in the absence of coupling are:

$$n_p^2 = \begin{cases} \varepsilon_p \mu_p & x \pm x_0 \in [-L, L], y \in [-L, L] \\ \varepsilon_1 \mu_1 & x \pm x_0 \in [-L_m, -L) \cup (L, L_m], y \in [-L_m, -L) \cup (L, L_m], \end{cases} \tag{11.56}$$

where $p = a, b$ ($-x_0$ corresponds to $p = a$) and $2L$ and $2L_m$ are the widths of the waveguides and the bulk material, respectively. The combined refractive index profile is then given by:

$$n_p^2(x, y) + \Delta n_p^2(x, y) = n^2(x, y), \tag{11.57}$$

where Δn_p^2 are the perturbations to the refractive index of the waveguide due to the neighbouring guide. The transverse electromagnetic field distributions for a particular mode of waveguide p alone are denoted $E_t^{(p)}$ and $H_t^{(p)}$, and the propagation constant is β_p.

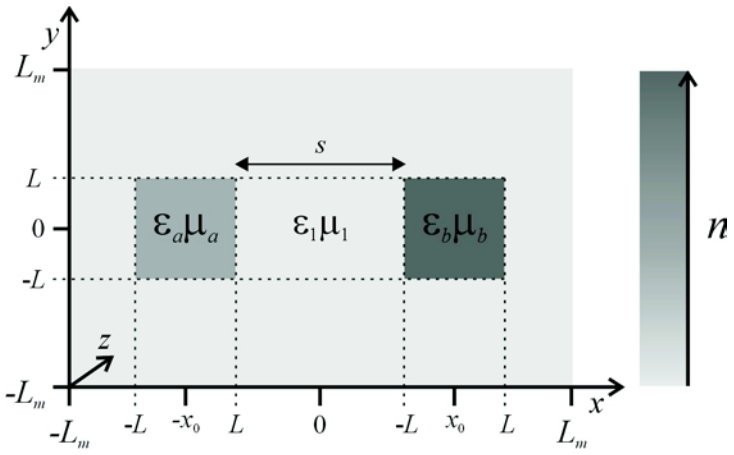

Figure 11.19: Double channel waveguide geometry and parameters.

The first step to deriving the coupled mode equations is to restrict attention to situations where each individual waveguide only supports one guided mode,

and to assume that the field in the coupled guide structure can be approximated by a linear combination of the unperturbed fields as:

$$E_t(x,y,z) = A(z)E_t^{(a)}(x,y) + B(z)E_t^{(b)}(x,y), \tag{11.58}$$

and

$$H_t(x,y,z) = A(z)H_t^{(a)}(x,y) + B(z)H_t^{(b)}(x,y), \tag{11.59}$$

where $A(z)$ and $B(z)$ express the z-dependence of the individual guided modes [117]. However, this approximation is only valid in situations where the coupling between the modes is weak which typically requires that the guides are well separated and also that they are not too dissimilar. Although it is easy to satisfy the requirement that the guides are well separated, clearly when considering coupling between positive and negative index guides the similarity condition of the guides will be violated. Thus before the standard coupled mode theory can be applied to this problem, the validity of the approximation of Eqs. (11.58) and (11.59) must first be established. To this end, the first step is to consider solving for the exact electromagnetic field distribution of a coupled mode system where one guide has a positive index and the other a negative index. Provided the calculated solution has an intensity profile which is similar in appearance to the sum of the two unperturbed fields, it is reasonable to expect that the superposition approximation will be valid.

To solve for the exact field distribution of a coupled mode system a numerical technique known as the Shooting Method is employed [118]. The validity of this technique has long been established in the field of Quantum mechanics for determining the wave function of particles trapped in a system of square

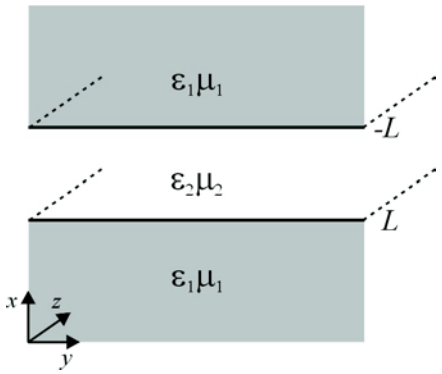

Figure 11.20: Planar waveguide geometry and parameters.

wells [119]. As the coupling between modes of two channel guides is a two dimensional problem, and is thus very computationally intensive, here the analysis is restricted to consider the reduced problem of coupling between modes in adjacent slab waveguides. As mentioned in Section 11.1, the mode solutions to the problem of a single negative refractive index slab waveguide have been found previously by Shadrivov *et al.* [80]. From Maxwell's equations [Eqs. (10.16) and (10.17)] it follows that, for a waveguide geometry as given in Fig. 11.20, the E_y component of the TE modes is described by:

$$\frac{\partial^2 \tilde{E}_y}{\partial z^2} + \frac{\partial^2 \tilde{E}_y}{\partial x^2} + \omega^2 \varepsilon \mu \tilde{E}_y - \frac{1}{\mu}\frac{\partial \mu}{\partial x}\frac{\partial \tilde{E}_y}{\partial x} = 0. \tag{11.60}$$

Expressing the electric field distribution as [99]:

$$E_y = \begin{cases} A\cos(\kappa L - \phi)\,\mathrm{e}^{-\sigma(x-L)} & (x > L) \\ A\cos(\kappa x - \phi) & (-L \le x \le L) \\ A\cos(\kappa L - \phi)\,\mathrm{e}^{\sigma(x+L)} & (x < -L), \end{cases} \tag{11.61}$$

where κ and σ are given in Eq. (11.29), and following the analysis outlined in Section 11.3, it is easy to show that continuity of the E_y and H_z components of the field at $x = \pm L$ yield the dispersion relation as:

$$\tan\left(\kappa L - \frac{m\pi}{2}\right) = \frac{\mu_2 \sigma}{\mu_1 \kappa}, \tag{11.62}$$

where m is an integer. The guided mode solutions can then be found by solving the Eqs. (11.29) and (11.62) using the same graphical technique as employed for the channel waveguides [Section 11.3.1]. An example of a typical mode profile obtained for: $\omega/2\pi = 5.29\,\mathrm{GHz}$, $\varepsilon_1 = 0.86$, $\mu_1 = 0.44$, $\varepsilon_2 = -0.75$,

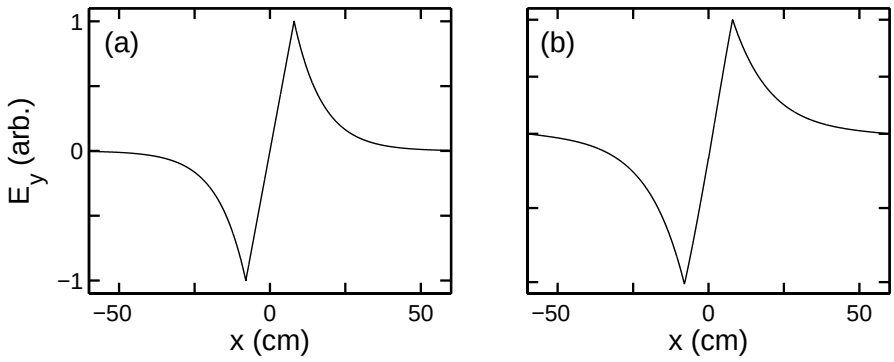

Figure 11.21: Example of a mode profile for a negative refractive index slab guide where (a) is calculated using Eq. (11.61) and (b) is found via the Shooting method.

$\mu_2 = -0.51$ and $L = 8\,\mathrm{cm}$ is shown in Fig. 11.21(a), where the propagation constant is calculated to be: $\beta = 68.48\,\mathrm{m}^{-1}$.

The numerical analysis to find the exact field distribution begins by rewriting Eq. (11.60) using the form of the electric field: $\tilde{E}_y(x,z) = E_y(x)\,\mathrm{e}^{-\mathrm{i}(\omega t - \beta z)}$ to obtain:

$$\frac{\mathrm{d}^2 E_y}{\mathrm{d}x^2} = \left(\beta^2 - \omega^2\varepsilon\mu\right) E_y + \frac{1}{\mu}\frac{\mathrm{d}\mu}{\mathrm{d}x}\frac{\mathrm{d}E_y}{\mathrm{d}x}. \tag{11.63}$$

This system has the natural boundary conditions $E_y(\pm\infty) = 0$, where infinity is taken to be some value of x sufficiently far from the edge of the guide. Eq. (11.63) can then be expressed as a coupled first order system:

$$\mathbf{X}' = \begin{pmatrix} 0 & 1 \\ \beta^2 - \omega^2\varepsilon\mu & \frac{1}{\mu}\frac{\mathrm{d}\mu}{\mathrm{d}x} \end{pmatrix} \mathbf{X}, \tag{11.64}$$

where $\mathbf{X} = (\mathrm{X}_1\ \mathrm{X}_2)^T = (E_y\ \mathrm{d}E_y/\mathrm{d}x)^T$ together with the boundary conditions $\mathrm{X}_1(-\infty) = 0$ and $\mathrm{X}_2(-\infty) = \alpha$. Here α is the estimate of the initial slope of the electric field, which should be close to but not equal to zero. The Shooting method is then implemented as follows.

(1). Make an initial guess of the propagation constant β_i.
(2). Solve the system of differential equations [Eq. (11.64)] using a fourth order Runge-Kutta scheme [118].
(3). Compare the solution of $\mathrm{X}_1(\infty)$ with the known value: $E_y(\infty) = 0$.
(4). If $\mathrm{X}_1(\infty) = 0$ to within the required tolerance, then $\beta = \beta_i$. If not, adjust the value of β_i (either bigger or smaller) and go back to step (2).

To illustrate this technique it is used to solve for the mode solution plotted in Fig. 11.21(a). With an initial guess of $\alpha = -1 \times 10^{-7}$, following steps (1)–(4) yields a propagation constant of $\beta = 68.12\,\mathrm{m}^{-1}$, which is in good agreement with that obtained using the graphical technique. Consequently, the mode profile found via the Shooting method, as shown in Fig. 11.21(b), is also in good agreement with that of Eq. (11.61).

This method is now used to solve for a coupled slab waveguide system as illustrated in Fig. 11.22. With: $\alpha = -1 \times 10^{-7}$, $\varepsilon_1 = 0.86$, $\mu_1 = 0.44$, $\varepsilon_a = -0.75$, $\mu_a = -0.51$, $\varepsilon_b = 0.90$, $\mu_b = 0.44$, $L = 8\,\mathrm{cm}$ and a waveguide separation of $s = 72\,\mathrm{cm}$, the propagation constant is found to be $\beta = 68.47\,\mathrm{m}^{-1}$. The E_y mode

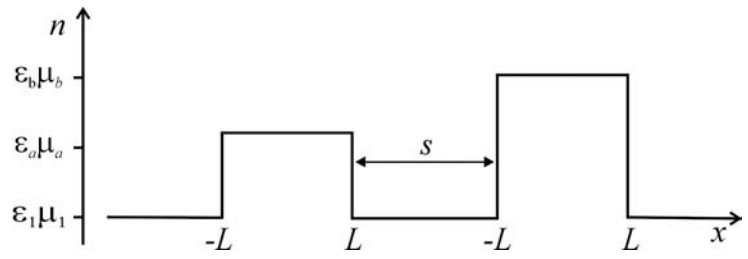

Figure 11.22: Double slab waveguide geometry and parameters.

profile is then plotted in Fig. 11.23(a). The bottom curve shows a close up of the profile in the region of the negative guide which is very similar to that found for the single negative index guide [Fig. 11.21]. Comparing this with a linear combination of the mode solutions for the two individual guides shown in Fig. 11.23(b) it is clear that, with an appropriate choice of the coefficients A and B, the mode profiles appear very similar. Thus despite the large dissimilarity in the refractive indices of the two guides the approximations of Eqs. (11.58) and (11.59) are nevertheless still valid.

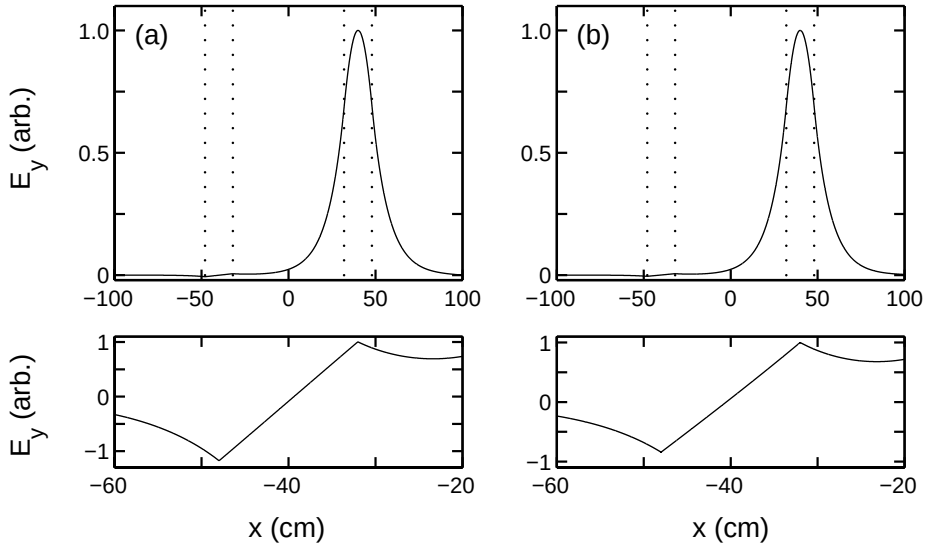

Figure 11.23: Top: mode profiles of the double slab waveguide of Fig. 11.22 obtained via (a) the Shooting method and (b) a linear combination of the mode solutions of the individual guides with $A = 1$ and $B = 20$. Bottom: close up of the profile in the region of the negative guide. Dotted lines are the waveguide boundaries.

11.5.2 Coupled Mode Theory

The coupled mode theory considered in the following was developed by Hardy and Streifer [117]. Their derivation is based on solutions to Maxwell's equations [Eqs. (10.16) and (10.17)] where the effect of a neighbouring guide can be considered as a perturbation to the refractive index profile, as given by Eq. (11.57). The coupled mode equations can then be written as:

$$\frac{\mathrm{d}A}{\mathrm{d}z} = \mathrm{i}\gamma^{(a)}A + \mathrm{i}\kappa_{ab}B, \tag{11.65}$$

$$\frac{\mathrm{d}B}{\mathrm{d}z} = \mathrm{i}\gamma^{(b)}B + \mathrm{i}\kappa_{ba}A, \tag{11.66}$$

where $\gamma^{(a)}$ and $\gamma^{(b)}$ represent corrections to the propagation constants β_a and β_b, respectively, and κ_{ab} and κ_{ba} are the coupling coefficients.

The equations (11.65) and (11.66) follow from the orthogonality condition of the modes which, for a material with $\mu = \mu_0$ over $x, y \in (-\infty, \infty)$, is given as [14]:

$$\int_{-\infty}^{\infty}\int_{-\infty}^{\infty} E_t^{(l)} E_t^{(m)} \mathrm{d}x\mathrm{d}y = \frac{2\omega\mu_0}{\beta_m}\delta_{l,m}. \tag{11.67}$$

However, if negative index waveguides, where $\mu \neq \mu_0$ over $x, y \in (-\infty, \infty)$, are to be considered, Eq. (11.67) must be modified as:

$$\int_{-\infty}^{\infty}\int_{-\infty}^{\infty} \frac{E_t^{(l)} E_t^{(m)}}{\mu} \mathrm{d}x\mathrm{d}y = \frac{2\omega}{\beta_m}\delta_{l,m}. \tag{11.68}$$

Although this will not alter the forms of Eqs. (11.65) and (11.66), it does have to be accounted for in the coefficients $\gamma^{(a)}$, $\gamma^{(b)}$, κ_{ab} and κ_{ba}.

Defining the waveguide overlap as [120]:

$$C_{pq} = \hat{z} \cdot \int_{-\infty}^{\infty}\int_{-\infty}^{\infty} \left[E^{(p)} \times H^{(q)\,*} + E^{(q)\,*} \times H^{(p)}\right] \mathrm{d}x\mathrm{d}y, \tag{11.69}$$

the modes are normalised such that:

$$C_{aa} = C_{bb} = 1. \tag{11.70}$$

By analogy with the analysis of Hardy and Streifer, the modified propagation constants can be written as:

$$\gamma^{(a)} = \beta^{(a)} + \left[\tilde{\kappa}_{aa} - C_{ab}\tilde{\kappa}_{ba} + C_{ab}C_{ba}\left(\beta^{(a)} - \beta^{(b)}\right)\right]/(1 - C_{ab}C_{ba}), \tag{11.71}$$

$$\gamma^{(b)} = \beta^{(b)} + \left[\tilde{\kappa}_{bb} - C_{ba}\tilde{\kappa}_{ab} + C_{ab}C_{ba}\left(\beta^{(b)} - \beta^{(a)}\right)\right]/(1 - C_{ab}C_{ba}), \tag{11.72}$$

and the coupling coefficients:

$$\kappa_{ab} = \left[\tilde{\kappa}_{ab} + C_{ab}\left(\beta^{(a)} - \beta^{(b)} - \tilde{\kappa}_{bb}\right)\right]/(1 - C_{ab}C_{ba}), \tag{11.73}$$

$$\kappa_{ba} = \left[\tilde{\kappa}_{ba} + C_{ba}\left(\beta^{(b)} - \beta^{(a)} - \tilde{\kappa}_{aa}\right)\right]/(1 - C_{ab}C_{ba}). \tag{11.74}$$

Using Eq. (11.68), the constants $\tilde{\kappa}_{pq}$ appearing in Eqs. (11.71)–(11.74), which depend on the perturbations to the individual guides, can be expressed in a modified form as:

$$\tilde{\kappa}_{pq} = \alpha_p \int_{-\infty}^{\infty}\int_{-\infty}^{\infty} \Delta n^{2\,(p)}\left[E_t^{(p)} \cdot E_t^{(p)} - \frac{\varepsilon^{(q)}}{\varepsilon} E_z^{(p)} E_z^{(p)}\right] \mathrm{d}x\mathrm{d}y, \tag{11.75}$$

where the coefficient,

$$\alpha_l = \frac{k^2/2\beta_l}{\int\int \left(E_t^{(l)}\right)^2 \mathrm{d}x\mathrm{d}y}. \tag{11.76}$$

Clearly, when $\mu = \mu_0$ Eq. (11.67) can be used to reduce Eq. (11.75) to the form given in Ref. [117]. It is important to note that, in contrast to what is often claimed in the literature, in general $\kappa_{ab} \neq \kappa_{ba}^*$ [14]. Although the complex conjugate relationship for the coupling coefficients follows from power conservation considerations, as it ignores cross terms between the two waveguide fields it is only valid for lossless identical guides.

To calculate the power flow between the waveguides it is assumed that at $z = 0$, all of the power is in guide b and Eqs. (11.65) and (11.66) are solved subject to the initial conditions $A(0) = 0$ and $B(0) = B_0$. In a lossless system this yields:

$$B(z) = B_0\left[\cos(\xi z) + \frac{\mathrm{i}\Delta}{\xi}\sin(\xi z)\right]\mathrm{e}^{\mathrm{i}\phi z}, \tag{11.77}$$

$$A(z) = B_0\frac{\mathrm{i}\kappa_{ab}}{\xi}\sin(\xi z)\,\mathrm{e}^{\mathrm{i}\phi z}, \tag{11.78}$$

where

$$\begin{aligned} \phi &= \left[\gamma^{(a)} + \gamma^{(b)}\right]/2, \\ \Delta &= \left[\gamma^{(b)} - \gamma^{(a)}\right]/2, \end{aligned} \tag{11.79}$$

and

$$\xi = \sqrt{\Delta^2 + \kappa_{ab}\kappa_{ba}}. \tag{11.80}$$

From the equation for the average power flowing in z [Eq. (10.20)], it follows that:

$$P_z = \frac{1}{4}|B_0|^2 \left\{1 + \frac{\kappa_{ab}}{\xi^2}\left[(\kappa_{ab} - \kappa_{ba}) + \Delta\left(C_{ab} + C_{ba}\right)\right]\sin^2(\xi z)\right\}. \tag{11.81}$$

In Eq. (11.81), the coefficient of the term $\sin^2(\xi z)$ is a measure of the power conservation and thus should be negligibly small,

$$\epsilon = \frac{\kappa_{ab}}{\xi^2}\left[(\kappa_{ab} - \kappa_{ba}) + \Delta\left(C_{ab} + C_{ba}\right)\right] \approx 0. \tag{11.82}$$

Consequently, to ensure that the weak coupling condition is satisfied so that power will be conserved, in the following section the waveguide separation s is chosen so that ϵ is sufficiently small that the maximum variation in P_z is less than 1%.

11.5.3 Calculating the Mode Coupling

The calculations begin by considering the coupling between the lowest order $H^y_{2,1}$ mode of a negative index guide, with a real k_x (e.g., mode (b,B) in Fig. 11.5), with a first order $H^y_{1,1}$ mode of a positive index guide. With the system parameters: $\omega/2\pi = 5.29\,\mathrm{GHz}$, $\varepsilon_1 = 0.86$, $\mu_1 = 0.44$, $\varepsilon_a = -0.97$, $\mu_a = -0.51$, $\varepsilon_b = 0.90$, $\mu_b = 0.44$ and $L = 3\,\mathrm{cm}$, the propagation constants of the modes for the individual guides are found to be: $\beta_a = 65.600\,\mathrm{m}^{-1}$ and $\beta_b = 65.525\,\mathrm{m}^{-1}$. To ensure power conservation, the separation between the guides is chosen to be: $s = 30\,\mathrm{cm}$. To illustrate the qualitative features of the coupled mode profile, the system is plotted with $A = B = 1$ [in Eq. (11.59)] in Fig. 11.24(a).

Under these conditions, Eqs. (11.71) and (11.74) yield the modified propagation constants: $\gamma^{(a)} = 65.601\,\mathrm{m}^{-1}$ and $\gamma^{(b)} = 66.532\,\mathrm{m}^{-1}$ and the coupling coefficients: $\kappa_{ab} = 0.015\,\mathrm{m}^{-1}$ and $\kappa_{ba} = 0.100\,\mathrm{m}^{-1}$. In both cases the coupling coefficient is quite small so that the power transfer between the modes will also be small. This is illustrated in Fig. 11.24(b) where the evolution of the coefficients of the mode fields $A(z)$ and $B(z)$ are plotted assuming that all of the power is initially in the positive index guide b [Eqs. (11.77) and (11.78)]. Furthermore, also from Fig. 11.24(b) it can be seen that the rate at which the power is transferred between the modes is slow and again this can be attributed to the small coupling efficiency through the value ξ which for these modes is only

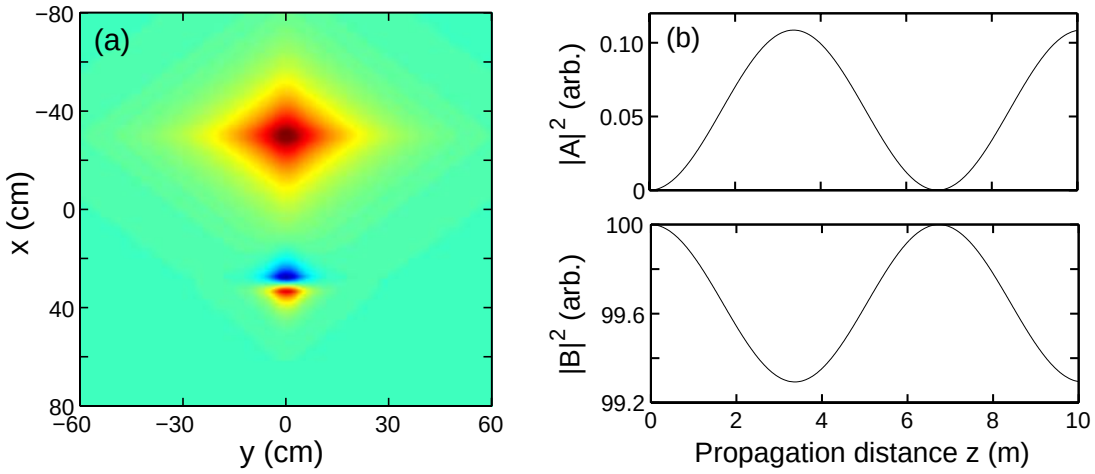

Figure 11.24: (a) The coupled mode profile for the $H^y_{2,1}$ mode of a negative index guide (k_x real) and the $H^y_{1,1}$ of a positive index guide with $A = B = 1$. (b) Evolution of the coefficients A and B.

$\xi = 0.467$ [Eq. (11.80)]. Significantly, however, although the power transfer rate appears to be too slow for practical waveguide lengths, as these waves are in the microwave regime (and not the optical), these distances are not unreasonable.

Although the small efficiencies calculated here can be partially attributed to the fact that the coupling is occurring between modes of a different order, more significantly, as it was seen in Fig. 11.6, in a negative index guide the $H^y_{2,1}$ mode with real k_x is in fact a backwards propagating mode. Consequently, despite the small efficiencies, these results have nevertheless shown that light can be coupled from a forwards propagating mode in a positive index guide to a backwards propagating mode in a negative index guide. In addition, the coupling coefficients between the $H^y_{2,1}$ mode with an imaginary k_x and a $H^y_{1,1}$ mode of a positive index guide have also been calculated. However, in this instance the coupling was found to be negligibly small.

The next step was to calculate the coupling coefficients between the higher order $H^y_{3,1}$ modes (e.g., modes (c, Γ) and (d, Γ) in Fig. 11.5), with a first order $H^y_{1,1}$ mode of a positive index guide. It should be recalled that the $H^y_{3,1}$ mode of a negative index guide was a degenerate mode where the strongly localised modes are backwards propagating waves, whilst the weakly localised modes are forward propagating waves. Thus these calculations will enable us to determine the relative coupling strengths of the two different types of mode.

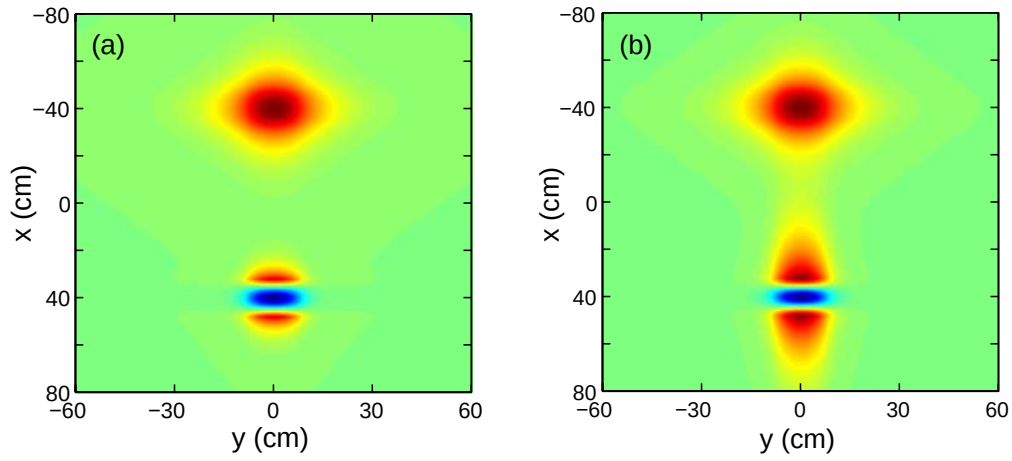

Figure 11.25: Coupled mode profiles for the $H^y_{3,1}$ modes of a negative index guide and the $H^y_{1,1}$ of a positive index guide with $A = B = 1$, where (a) is the strongly localised $H^y_{3,1}$ mode and (b) is the weakly localised $H^y_{3,1}$ mode.

Using the same system parameters as above, but increasing the waveguide width to $L = 8\,\mathrm{cm}$, to ensure power conservation the separation between the guides is increased to $s = 40\,\mathrm{cm}$. The propagation constants of the modes are then found to be: $\beta_a = 69.070\,\mathrm{m}^{-1}$ for the strongly localised $H^y_{3,1}$ mode, $\beta_a = 66.358\,\mathrm{m}^{-1}$ for the weakly localised $H^y_{3,1}$ mode, and $\beta_b = 67.701\,\mathrm{m}^{-1}$ for the $H^y_{1,1}$ mode. The mode profiles of the coupled systems with $A = B = 1$ are plotted in Fig. 11.24, where the mode in guide a is (a) the strongly localised mode and (b) the weakly localised mode.

Calculating the coupling coefficients for these two systems yields: (a) $\kappa_{ab} =$

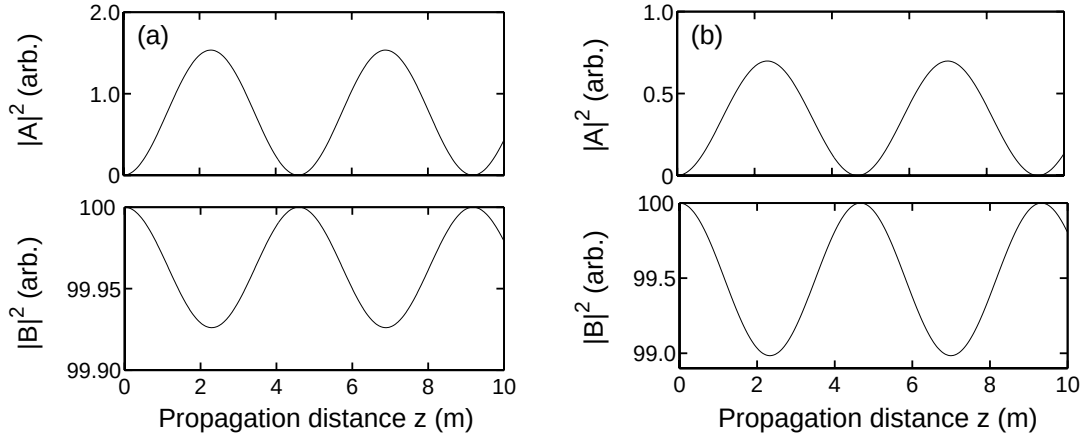

Figure 11.26: Evolution of the coefficients A and B for coupling between the $H^y_{3,1}$ modes and the $H^y_{1,1}$ mode, where (a) is the strongly localised mode and (b) is the weakly localised mode.

$0.002\,\mathrm{m}^{-1}$, $\kappa_{ba} = 0.001\,\mathrm{m}^{-1}$ and (b) $\kappa_{ab} = 0.099\,\mathrm{m}^{-1}$, $\kappa_{ba} = 0.039\,\mathrm{m}^{-1}$. On comparing the relative sizes of κ_{ab} and κ_{ba} for the two systems, these results indicate that light propagating in a positive index guide is more likely to be coupled into a forward propagating wave than a backwards propagating wave. Calculation of the corresponding modified propagation constants: (a) $\gamma^{(a)} = 69.070\,\mathrm{m}^{-1}$, $\gamma^{(b)} = 67.7012\,\mathrm{m}^{-1}$ and (b) $\gamma^{(a)} = 66.360\,\mathrm{m}^{-1}$, $\gamma^{(b)} = 67.698\,\mathrm{m}^{-1}$ then yields the evolution of the mode coefficients $A(z)$ and $B(z)$ and these are shown in Fig. 11.26. Interestingly, despite the difference in the coupling coefficients and the modified propagation constants, the two systems yield similar values of ξ: (a) $\xi = 0.684\,\mathrm{m}^{-1}$ and (b) $\xi = 0.674\,\mathrm{m}^{-1}$, so that in both cases the rate at which the power is transferred between the modes is also similar. In addition, in both cases the power transfer rate has increased slightly from the previous case of coupling between the $H^y_{2,1}$ mode and the $H^y_{1,1}$ mode.

The results above have indicated that light in a positive index guide is more likely to be coupled into a forward propagating wave than a backward propagating wave. Thus it may in fact be more efficient to couple light into a backwards propagating mode after first coupling it into a forwards propagating mode of a negative index guide. To this end, the final calculations consider the coupling between the degenerate forward and backward propagating waves of the $H^y_{3,1}$ modes in two identical negative index waveguides. Choosing the system parameters as: $\omega/2\pi = 5.287\,\mathrm{GHz}$, $\varepsilon_1 = 0.86$, $\mu_1 = 0.44$, $\varepsilon_a = \varepsilon_b = -0.97$,

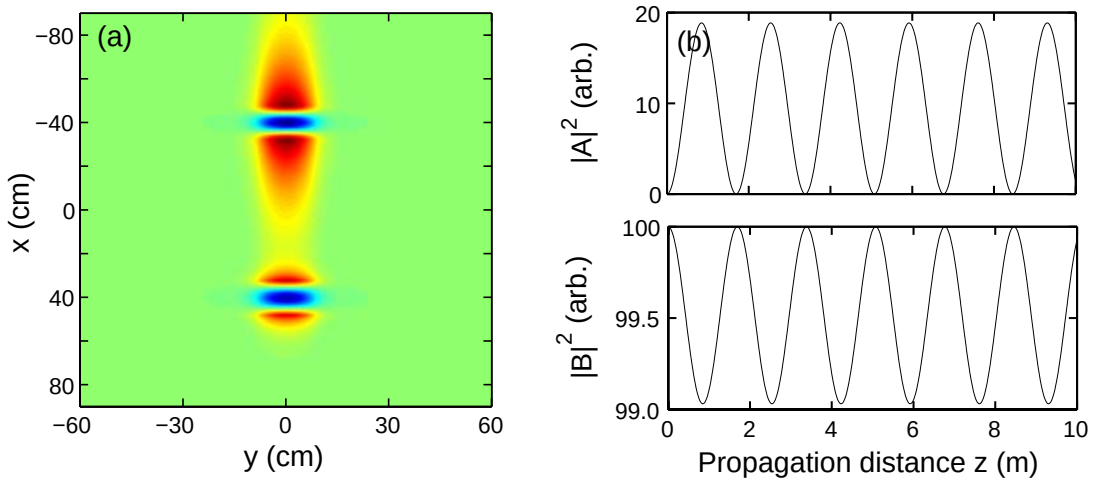

Figure 11.27: (a) The coupled mode profile for the two $H^y_{3,1}$ modes of a negative index guide with $A = B = 1$. (b) Evolution of the coefficients A and B calculated via Eqs. (11.77) and (11.78).

$\mu_a = \mu_b = -0.51$, $L = 8\,\mathrm{cm}$ and $s = 40\,\mathrm{cm}$, the propagation constants of the modes are found to be: $\beta_a = 69.726\,\mathrm{m}^{-1}$ and $\beta_b = 66.098\,\mathrm{m}^{-1}$. The mode profile of the coupled system with $A = B = 1$ is plotted in Fig. 11.27(a).

This system yields the coupling coefficients: $\kappa_{ab} = 0.807\,\mathrm{m}^{-1}$ and $\kappa_{ba} = 0.041\,\mathrm{m}^{-1}$ which, as it would be hoped, are an order of magnitude larger than the coupling coefficients between modes of a positive and a negative index guide. Furthermore, it follows from the calculation of the modified propagation constants: $\gamma^{(a)} = 69.717\,\mathrm{m}^{-1}$ and $\gamma^{(b)} = 66.021\,\mathrm{m}^{-1}$, that $\xi = 1.857$. Thus the rate of power transfer between the two modes is also more efficient than before and this is illustrated in Fig. 11.27(b) where the evolution of $A(z)$ and $B(z)$ have been plotted over the same propagation length ($10\,\mathrm{m}$) as considered for the systems with guides of differing signs of the refractive indices. An interesting feature of this result is that it suggests that once light has been coupled into a negative index guide which permits degenerate modes with differing signs of v_g, it should be possible to excite a cyclic coupling with a second adjacent identical guide between the forwards and backwards propagating modes. This is illustrated in Fig. 11.28 which shows how the light could be trapped between the guides.

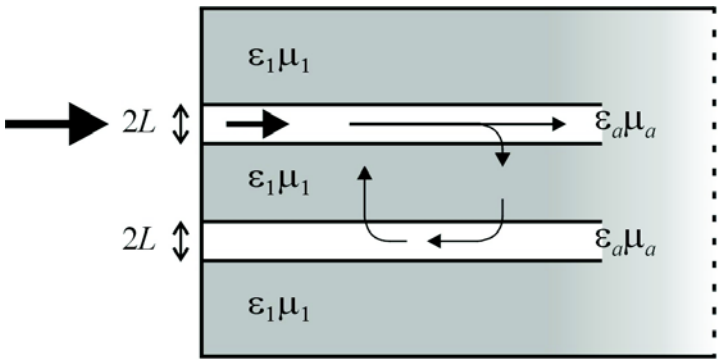

Figure 11.28: Coupling between forwards and backwards propagating waves in identical adjacent negative index waveguides.

11.6 Discussion

The results of this chapter have demonstrated a number of unusual properties of negative index core waveguides that differ considerably from those of

conventional waveguides. Significantly, however, whilst the propagation characteristics of the negative index channel waveguide modes were shown to exhibit exotic effects such as low or negative group velocity, the negative index fibres did not. Nevertheless, under certain conditions the modes of a negative index fibre have still been shown to exhibit extremely large GVD and also to support "fast light" ($v_g > c$). Finally, the results of the mode coupling analysis have shown that it is possible to couple light into both forwards and backwards propagating modes of a negative index waveguide.

Chapter 12

2D HeXLN Planar Buried Waveguides

12.1 Introduction

This chapter describes experiments to investigate efficient second harmonic generation in a two dimensional periodic photonic crystal based on a hexagonal lattice in lithium niobate (HeXLN). To enhance the conversion efficiency of the harmonic process a planar waveguide geometry is employed. After a brief description of the design requirements and fabrication procedures of the device, the efficiency of the second harmonic process is analysed via the interaction properties of the waveguide.

12.2 2D Photonic Crystals

Since the development of one dimensional nonlinear crystals to phase match second harmonic generation (SHG), devices such as periodically poled lithium niobate (PPLN) have generated considerable interest amongst research groups around the world [97, 121, 122, 123]. Following on the success of these one dimensional structures, in 1998 Berger set about investigating the possibility of realising two dimensional crystals [71]. The results of his theoretical analysis showed that SHG could indeed occur over multiple angles in the plane

of the crystal. Since this observation, SHG in HeXLN has been experimentally demonstrated here at the ORC by Broderick *et al.* with internal conversion efficiencies as high as 80% [90]. In addition, this work has recently been extended to observe multiple harmonic generation, demonstrating the possibility of simultaneous phase matching in multiple directions, and the efficiencies of these processes with respect to the operating temperature and wavelength have been examined [124]. However, despite their success, all of these experiments were performed in bulk crystals so that in general they suffered from relatively low conversion efficiencies, particularly for the higher harmonics.

12.2.1 Phase Matching in HeXLN

The hexagonal domain pattern for the two dimensional HeXLN structure is shown in Fig. 12.1. For a lattice with a period a and the basis vectors $\mathbf{a}_1 = a(1,0)$ and $\mathbf{a}_2 = a(1/2, \sqrt{3}/2)$, the corresponding reciprocal lattice vectors are: $\mathbf{G}_{n,m} = n\mathbf{b_1} + m\mathbf{b_2}$ [Section 10.3]. Here $\mathbf{b}_1$ and $\mathbf{b}_2$ are the basis vectors for the reciprocal space, which is another hexagonal lattice rotated by 90° with respect to the real space, with a period of $4\pi/\left(\sqrt{3}a\right)$, as illustrated by the first Brillouin zone shown on the right hand side of Fig. 12.1. From these sketches it can be seen that the possibilities of quasi-phase matching are six fold degenerate (due to the symmetry of the triangular lattice).

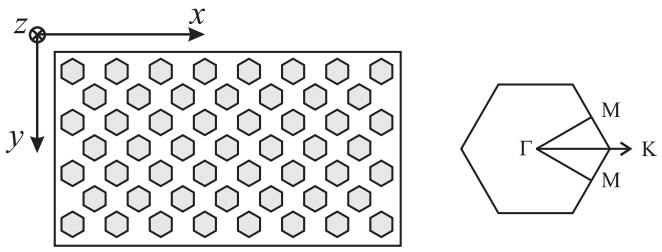

Figure 12.1: Structure of the hexagonal domain pattern of the poled lithium niobate in the $x-y$ plane, together with the first Brillouin zone.

The complete reciprocal lattice structure of Fig. 12.1 is then plotted in Fig. 12.2. Overlaid on this figure are two examples of quasi-phase matched processes.[1] The first is the fundamental process which involves the shortest possible recip-

[1] Note that in this figure the phase matching processes are not represented to scale as typically $|k_\omega| >> |a|$.

rocal lattice vector $G_{0,1}$. The second is a higher order process which involves a momentum transfer that is in fact $\sqrt{3}$ times greater than the fundamental process. Such a momentum transfer is not possible in a one dimensional structure and thus this shows that these two dimensional structures also open up new quasi-phase matching orders. It is worth noting that the two dimensional quasi-phase matching order can be labelled with two integer coordinates given in the $(\mathbf{G}_1, \mathbf{G}_2)$ basis of the reciprocal lattice. In Fig. 12.2, the two processes that are represented are of orders $[1, 0]$ and $[1, 1]$.

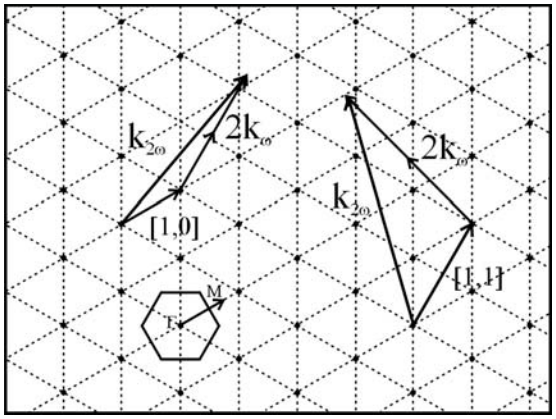

Figure 12.2: Reciprocal lattice of a HeXLN structure showing two possible quasi-phase matched processes.

12.2.2 Fabrication

The two dimensional nonlinear photonic crystals used in our experiments were hexagonally poled by Dr C. Gawith, Dr K. Gallo and Mr L. Ming using a technique similar to that applied to pole PPLN [109]. In this technique, an electric field is applied to macroscopic regions of the crystal to invert the spontaneous electric polarisation $\mathbf{P}_\mathrm{s}$. The resulting effect is to create ferroelectric domains in which the direction of $\mathbf{P}_\mathrm{s}$ differs from that of the adjacent domain. A schematic diagram of the electric poling process can be seen in Fig. 12.3. This process was conducted at room temperature on a z-cut $500\,\mu\mathrm{m}$ thick congruent lithium niobate crystal. Firstly, the hexagonal array is defined photolithographically on a thin layer of photoresist on the $-z$ face.

The mask used in the photolithography was the same as that used for the earlier HeXLN experiments described in Ref. [90], and so was designed for SHG

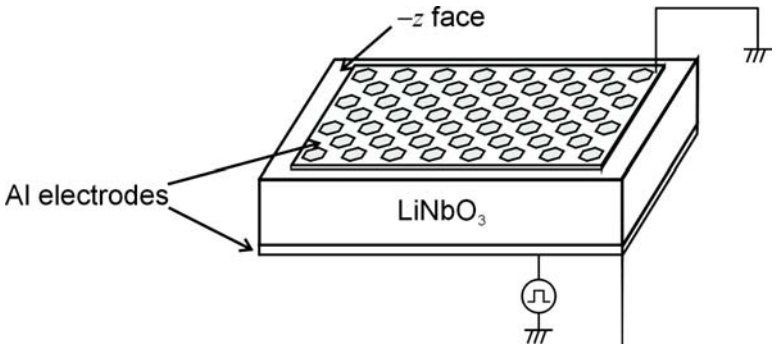

Figure 12.3: Schematic diagram of electric poling for domain inversion in lithium niobate.

in a bulk sample. With a $1.536\,\mu\mathrm{m}$ fundamental beam (propagating along the x axis) quasi-phase matched through the $G_{1,0}$ reciprocal lattice vector, at $120\,^{\circ}\mathrm{C}$ the required spatial period was: $\Lambda = 18.05\,\mu\mathrm{m}$. This was aligned carefully so that the $x-y$ orientation of the hexagonal structure coincided with the crystals natural preferred domain wall orientation. For lithium niobate, which has trigonal atomic symmetry (crystal class $3m$), the tendency is for the domain walls to form parallel to the y axis and at $\pm 60\,^{\circ}$.

A conductive gel is then applied to both faces of the crystal to act as electrodes over which the electric field is applied. In order to invert the spontaneous electric polarisation of lithium niobate at room temperature, an electric field exceeding the coercive field $\left(E_{\mathrm{c}} = 21\,\mathrm{kVmm}^{-1}\right)$ is required and thus the photoresist must be sufficiently thick to block the applied field in the hexagonal regions. Finally, the photoresist is removed using an acetone bath.

Fig. 12.4 shows the resulting hexagonal domain pattern of the poled lithium

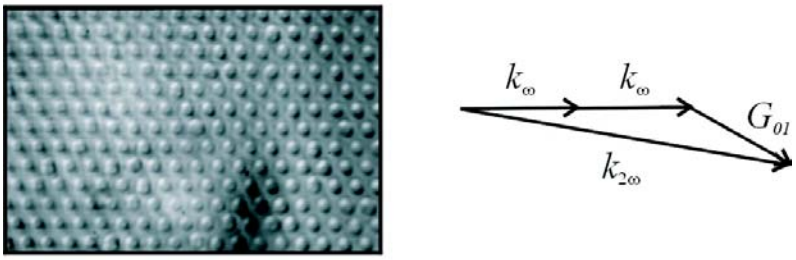

Figure 12.4: Photograph showing the structure of the hexagonal domain pattern of the poled lithium niobate crystal, in the $x-y$ plane, together with the wavevectors involved in the [1,0] order SHG process.

niobate crystal, in the $x-y$ plane, together with the wavevectors involved in the first order [1,0] SHG process. In this sample, which is typical of the HeXLN crystals used in our experiments, the hexagons constitute $\sim 30\,\%$ of the total area. We note that the clarity of the hexagonal structure of the crystal is reduced from that often displayed in the literature due to the fact that this sample was not etched. The reason for this is because of the close proximity of the waveguide to the surface of the crystal and thus it is likely that etching would affect its guiding properties.

12.3 Planar Waveguides

As seen in Section 11.5.1, a planar waveguide is characterised by three semi-infinite layers of differing refractive indices with respect to one direction (see Fig. 12.5). In our investigations the significant feature of the planar geometry is that it preserves all the benefits of the two dimensional structure, whilst providing tighter mode confinement. Thus the intensities and the modal overlap of the interacting fundamental and second harmonic fields are enhanced. Although the top layer (n_1) can simply be the air outside the crystal, in order to symmetrise the mode profile of the guided fields the waveguide within the bulk HeXLN crystal is buried.

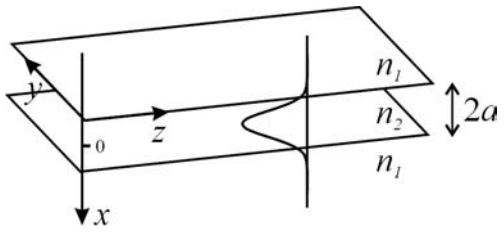

Figure 12.5: Diagram of a basic three-layer planar waveguide.

In our experiments the fundamental beam was launched into the waveguide in the TM configuration (see Section 12.4). The solutions for the TE modes of a negative index slab waveguide have already been presented in Section 11.5.1 and similarly the TM modes can be obtained via equivalent analysis. However, as we are now dealing with a positive index material, we can return to the original definition of n ($=\sqrt{\varepsilon/\varepsilon_0}$) as given by Eq. (3.1). It then follows from

Maxwell's equations [Eqs. (10.16) and (10.17)] that (for the coordinate system given in Fig. 12.5) the H_y component of the TM modes is described by:

$$\frac{\partial^2 H_y}{\partial x^2} + \frac{\partial^2 H_y}{\partial z^2} + k^2 n^2 H_y - \frac{1}{\varepsilon}\frac{\partial \varepsilon}{\partial z}\frac{\partial H_y}{\partial z} = 0. \tag{12.1}$$

Assuming a symmetric waveguide ($n_1 = n_3$), the magnetic field distribution can be expressed as:

$$H_y = \begin{cases} A\cos(\kappa a - \phi)\,\mathrm{e}^{-\sigma(z-a)} & (z > a) \\ A\cos(\kappa z - \phi) & (-a \le z \le a) \\ A\cos(\kappa a - \phi)\,\mathrm{e}^{\sigma(z+a)} & (z < -a), \end{cases} \tag{12.2}$$

where κ and σ are now written as:

$$\kappa = \sqrt{k^2 n_2^2 - \beta^2} \quad \text{and} \quad \sigma = \sqrt{\beta^2 - k^2 n_1^2}. \tag{12.3}$$

Applying the boundary conditions that H_y and E_x should be continuous at $z = \pm a$, the dispersion relation is obtained as:

$$\tan\left(\kappa a - \frac{m\pi}{2}\right) = \frac{\varepsilon_2 \sigma}{\varepsilon_1 \kappa}, \tag{12.4}$$

where m is an integer. Solving Eqs. (12.3) and (12.4) using the graphical technique of Section 11.3.1 yields the guided modes and an example of a typical profile is plotted in Fig. 12.6. This solution corresponds to the fundamental TM_0 mode with the waveguide parameters: $n_1 = 2.130$, $n_2 = 2.158$ and $a = 2\,\mu\mathrm{m}$, calculated for a wavelength of $\lambda = 1.536\,\mu\mathrm{m}$.

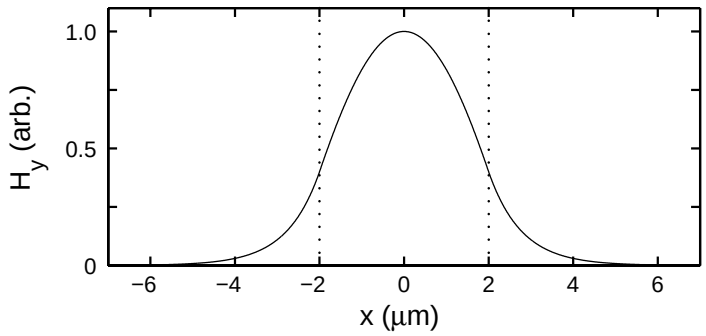

Figure 12.6: Example of a fundamental mode profile for a TM slab guide.

12.3.1 Fabrication

The planar buried waveguide was fabricated by Dr K. Gallo using a process of annealed proton exchange followed by reverse-proton exchange [125]. The

initial proton exchange involves immersion of the sample in molten benzoic acid at a temperature of $160\,^{\circ}\mathrm{C}$. During this process H^+ ions are exchanged with Li^+ ions in the crystal, resulting in a thin proton-rich layer with a higher extraordinary refractive index. The sample is then annealed in air at $328\,^{\circ}\mathrm{C}$ so that the protons diffuse deeper into the substrate yielding an annealed-proton-exchanged (APE) waveguide with a graded index profile that has a maximum at the surface of the crystal. To impose symmetry to the waveguide, reverse-proton exchange via immersion in a lithium-rich melt ($LiNO_3$:KNO_3:$NaNO_3$) is then performed again at $328\,^{\circ}\mathrm{C}$. This process removes protons from the surface which in turn acts to move the peak of the refractive index profile into the crystal. The resulting structure and refractive index profile of the crystal are shown in Fig. 12.7, together with the profile of the surface waveguide before the reverse exchange.

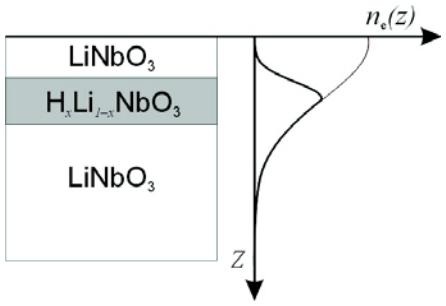

Figure 12.7: Cross section of the HeXLN crystal in the $x-z$ plane. The right hand side shows the extraordinary index profile of the buried waveguide (thick line), together with the profile of the surface waveguide before the reverse proton exchange (thin line).

12.4 Experimental Setup

A schematic diagram of the experimental setup to observe harmonic generation in a planar HeXLN waveguide is shown in Fig. 12.8. The pulse source used in our experiments is the all fibre amplifier chain described in Section 6.4.1. This produces $5\,\mathrm{ns}$ pulses at $1.536\,\mu\mathrm{m}$ and the repetition rate is adjustable between $1-500\,\mathrm{kHz}$ so that peak powers of up to $\sim 20\,\mathrm{kW}$ can be achieved. The HeXLN crystal was housed in a computer-driven oven where the temperature could be controlled via the direction of the current through a $\sim 3\,\mathrm{cm}$

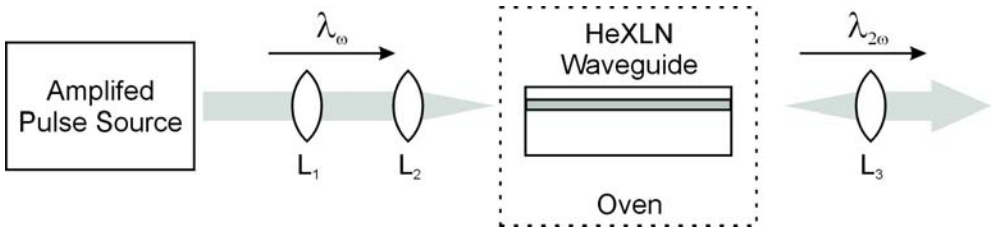

Figure 12.8: Schematic diagram of the experimental setup used to observe harmonic generation in a planar HeXLN waveguide. L_1 is the cylindrical lens and L_2 and L_3 are spherical lenses.

long Peltier element.[2] However, as the Peltier was considerably longer than the length of a typical HeXLN crystal ($\sim 1\,\mathrm{cm}$), due to the large diffraction of the exiting fields in the z direction, it was necessary to place the sample on a copper coupling block whose base was the same size as the Peltier, but with a top face whose x length was the same as the crystal's. This enabled the output coupling lens to be placed close enough to the exit face of the crystal so that all of the generated second harmonic could be collected. A sketch of the oven design is shown in Fig. 12.9. To avoid the photorefractive effects discussed in Section 10.4, we ensured that the oven was maintained at a temperature above $\sim 100\,^{\circ}\mathrm{C}$ when light was incident on the crystal.

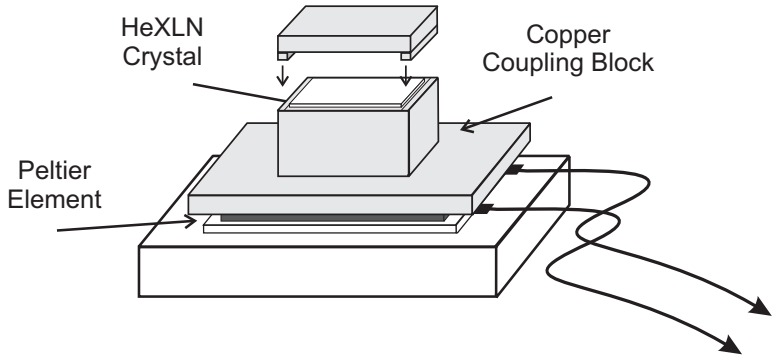

Figure 12.9: Sketch of the Peltier oven design.

To assist with the coupling of the fundamental beam into the waveguide the oven setup was then mounted on a series of adjustable stages (x, y, z and a rotational stage θ). Efficient coupling into a planar waveguide requires a beam with a narrow waist in the z direction but with a broad waist in the y direction so that the diffraction effects in this direction are minimised. To achieve this the beam was first shaped into an ellipse using a cylindrical lens (focal length: $f =$

[2]This oven was designed by Dr R. Bratfalean.

Figure 12.10: Intensity profile of the TM_0 mode at $1.536\,\mu\mathrm{m}$ at the output of the waveguide.

$20\,\mathrm{cm}$) before focusing through a spherical lens ($10\times$ objective). This resulted in a spot size of $5.6\,\mu\mathrm{m} \times 80\,\mu\mathrm{m}$ (FWHM) at the input face of the waveguide. An image of the intensity profile of the TM_0 mode at $1.536\,\mu\mathrm{m}$, at the output of the waveguide, can be seen in Fig. 12.10.

Using this geometry a coupling efficiency of 36% into the waveguide was obtained and significant generation of the second, third and fourth harmonics (red, green and blue light) was achieved as shown in Fig. 12.11.

Figure 12.11: Output from the HeXLN planar waveguide showing the generated second, third and fourth harmonics (red, green and blue light).

12.5 SHG in a HeXLN Planar Waveguide

Information on both the linear and nonlinear properties of HeXLN waveguides can be obtained by studying the quadratic response of the waveguide. This can be achieved by varying a number of parameters such as the infrared pump power, the temperature, the wavelength of the fundamental beam and the incident angle. In these preliminary experiments the variation of the generated second harmonic power with the operating temperature and input fundamental power are considered.

The HeXLN crystal used in these experiments was similar to that shown in Fig. 12.4 with an x length of $14\,\mathrm{mm}$. A typical temperature tuning curve for the output second harmonic power of our waveguide is plotted in Fig. 12.12. This curve was obtained using an automated system which takes a single measurement of the fundamental and second harmonic powers at each temperature

step. The most noticeable anomalies of this curve are the large oscillations in the second harmonic power we scanned through the temperature. Although it is possible that these oscillations are due to a lack of averaging of the second harmonic power measurement, the fact that they occur with a regular spacing suggests that they are actually a real feature of the crystal. A possible explanation for these oscillations is that the quality of the polished ends of this crystal were so good, the waveguide could act as a cavity. Indeed, on calculating the average spacing of these fringes we have in fact found that they are the same as that expected between the fringes of a Fabry-Perot resonator with a length and refractive index equal to those of our waveguide. However, this particular sample was unfortunately broken before this effect could be investigated any further.

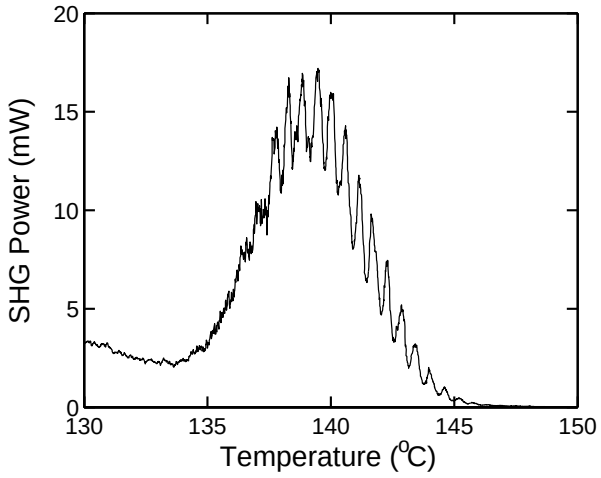

Figure 12.12: Average second harmonic power at the output of the waveguide as a function of temperature obtained with the Peltier oven design.

A further irregularity of this tuning curve is that it is asymmetric. This asymmetry can be attributed to the thermal expansion of the copper coupling block used in our oven design which led to a vertical displacement of the input beam with respect to the waveguide as the temperature was varied. Thus we can observe that the peak at $138\,^{\circ}\mathrm{C}$ corresponds to SHG in the waveguide, whilst the low temperature shoulder corresponds to some of the fundamental beam being coupled into the bulk and the rapid decay at higher temperatures is due to coupling into the air. As a result, we expect that the measured temperature tuning bandwidth of $5.2\,^{\circ}\mathrm{C}$ underestimates the true bandwidth of the interaction.

After reoptimising the coupling of the fundamental beam into the waveguide, our next step was to consider the variation of the second harmonic power with the input pump power. A plot of the internal second harmonic conversion efficiency: $\eta_{\mathrm{SHG}}^{\mathrm{int}} = P_{2\omega}^{\mathrm{OUT}}/P_{\omega}^{\mathrm{IN}}$, is shown in Fig. 12.13. Here $P_{2\omega}^{\mathrm{OUT}}$ and P_{ω}^{IN} are the average powers of the second harmonic at the output and the fundamental at the input, respectively. Although the peak power of the pulses can be adjusted by changing the repetition rate at which the laser diode is modulated, the level of amplified spontaneous emission (ASE) is higher for low repetition rates as there is a longer time between the pulses for it to be amplified by the stored energy. Thus to avoid spurious effects due to ASE, the repetition rate of the source was fixed to be $1\,\mathrm{kHz}$ and the peak power of the pulses was adjusted externally using a combination of a half-wave plate and a polarising beam splitter.

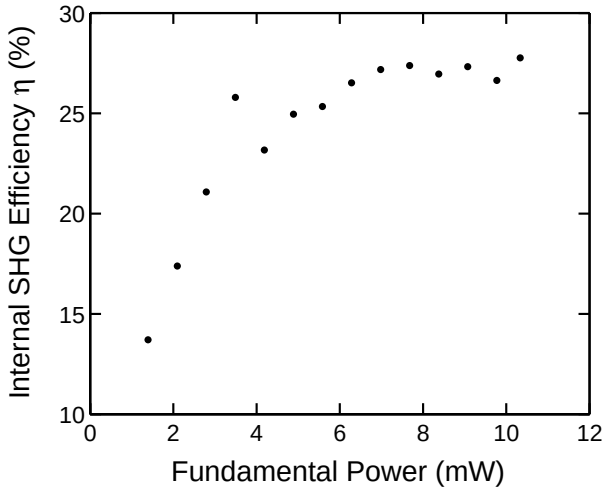

Figure 12.13: SHG internal efficiency as a function of the average input fundamental power coupled into the waveguide obtained with the Peltier oven design.

These results show that as we increase the average power of the fundamental beam at the input, the conversion efficiency approaches an asymptotic limit. Although this curve is in qualitative agreement with results obtained in the high conversion limit, the saturation effects occur at a much lower efficiency than expected [126]. Initially it was thought that this reduced efficiency could be due to the fact that the middle of the exit face ($+x$ face) of the crystal was damaged, thus forcing us to use a region off centre where we expect the poling to be less effective. However, after re-cutting and polishing the damaged end we found that there was no significant increase in the efficiency. Thus a more

rigorous investigation was needed to establish the limitations to the conversion efficiency and this will discussed in the following section.

12.6 Characterisation of HeXLN Waveguides

Following the success of the preliminary experiments presented in Section 12.5, in this section we describe the improvements made to the oven and present the subsequent results. The performance of this modified system is analysed via calculation of the conversion efficiencies.

12.6.1 Modified Experimental Setup

As we saw in Fig. 12.12, the thermal expansion of the copper block affected the coupling into the waveguide which led to inherent errors in our measurements. Thus as a solution to this problem a new oven was designed that employed a flat resistor to heat a thin copper plate suspended via an aluminium stand.[3] A sketch of this new oven is shown in Fig. 12.14. Although this oven did not allow for such accurate control of the temperature, the advantage of using a resistor is that these can be purchased for a large range of lengths, thus eliminating the need for the copper coupling block. The suspension design then allowed for closer placement of the focusing lenses, enhancing the coupling efficiency both into and out of the waveguide. Thus it was expected that this new design should produce a more accurate description of the tem-

[3]This oven was designed by Dr R. Bratfalean and Dr K. Gallo.

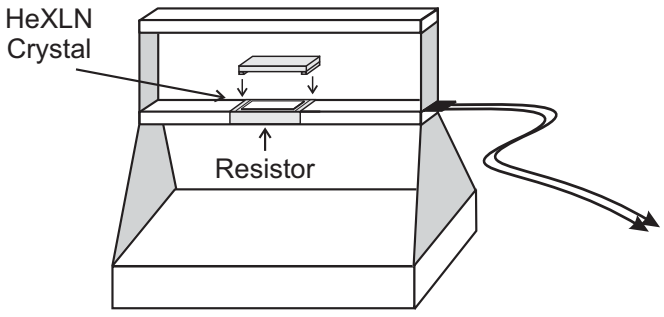

Figure 12.14: Sketch of the resistor oven design.

perature tuning at the extreme temperatures as well as yielding larger second harmonic output powers.

12.6.2 Interaction Properties of the HeXLN Waveguide

Using the oven described in the above section, our first step was to repeat the temperature tuning curve of Fig. 12.12 in attempt to obtain a more accurate description of the bandwidth of the waveguide. Unlike our previous results, this time the curve was measured manually, optimising the coupling and averaging over the powers at each step. The new tuning curve is plotted in Fig. 12.15. From this we see that the temperature curve is now quite symmetric indicating the success of the new oven design. In addition, the measured temperature bandwidth is $19.5\,^{\circ}\mathrm{C}$ so that it is much larger than that previously obtained in Fig. 12.12.

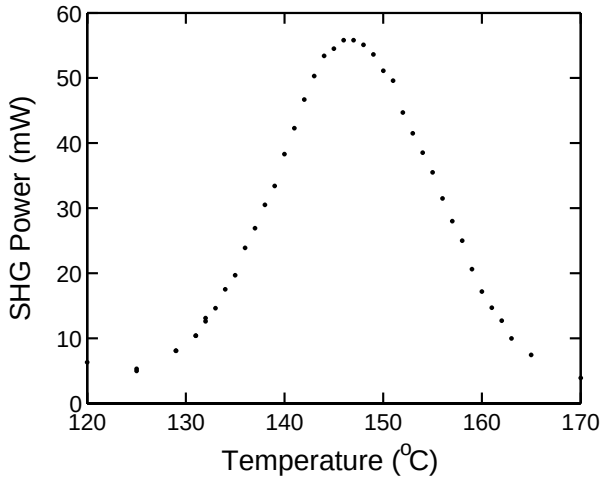

Figure 12.15: Average second harmonic power at the output of the waveguide, as a function of temperature, obtained with the resistor oven design.

Our next task was to establish why the second harmonic conversion efficiencies obtained in Section 12.5 were lower than expected. Firstly we note that, as mentioned in Section 12.2.2, the period of our crystal was designed for optimum collinear conversion of a $1.536\,\mu\mathrm{m}$ fundamental field to the second harmonic in bulk HeXLN at a temperature of $120\,^{\circ}\mathrm{C}$. Thus, as the dispersion properties of the waveguide differ slightly from those of the bulk [Section 12.3], we will need to align the fundamental beam slightly off the x-axis in order to em-

ploy the $G_{1,0}$ reciprocal lattice vector.

For our waveguide experiments we found that the maximum SHG efficiencies in fact occurred at a higher operating temperature of $147.5\,^{\circ}\mathrm{C}$. Significantly, however, at this temperature we observed that the guided wave interaction $\mathrm{TM}_0(\omega) \rightarrow \mathrm{TM}_0(2\omega)$ appeared at relatively high internal incidence angles ($\theta_\omega \sim 6^\circ$ relative to the x-axis) thus implying that a higher order reciprocal lattice vector was being employed. From this we could determine that this interaction was in fact being phase matched via the $G_{1,1}$ lattice vector. Interestingly, we also noticed a second interaction which did occur at a smaller angle ($\theta_\omega \sim 3^\circ$) so that it was being phase matched by the $G_{1,0}$ lattice vector, and this was determined to be the $\mathrm{TM}_0(\omega) \rightarrow \mathrm{TM}_1(2\omega)$ interaction. Thus we could conclude that the waveguide was multimodal. The observed low efficiencies can then be explained by noting that because the $\mathrm{TM}_0(\omega) \rightarrow \mathrm{TM}_1(2\omega)$ interaction yielded the larger conversion efficiencies (due to the lower non-collinearity and reciprocal lattice vector order), it was this process that we had been using in our measurement processes of Section 12.5. However, as the overlap between these two modes is smaller than between two fundamental modes, the relative expected efficiency should be less. Nevertheless, due to the larger SHG efficiencies, we still chose to use the latter process to further investigate the properties of the waveguide.

With a better understanding of the processes occurring in the waveguide, we optimised the setup for the $\mathrm{TM}_0(\omega) \rightarrow \mathrm{TM}_1(2\omega)$ interaction for the purpose of evaluating the intrinsic efficiency. Fig. 12.16 shows the evolution of the external second harmonic average power $P_{2\omega}^{\mathrm{OUT}}$ as a function of the average input pump power P_{ω}^{IN} (circles).

To calculate the quadratic efficiency of our waveguide we use the standard coupled mode equations (assuming no spatial walk-off or propagation losses) in a quasi-stationary approximation [14]:

$$\frac{\mathrm{d}A_\omega}{\mathrm{d}x} = -\mathrm{i}\frac{\kappa}{2} A_{2\omega} A_\omega^*, \tag{12.5}$$

$$\frac{\mathrm{d}A_{2\omega}}{\mathrm{d}x} = -\mathrm{i}\frac{\kappa}{2} A_\omega^2, \tag{12.6}$$

where here κ is the nonlinear coupling coefficient and the mode amplitudes A_i ($i = \omega, 2\omega$) are in units of $\mathrm{W}^{1/2}$. After accounting for the coupling losses and

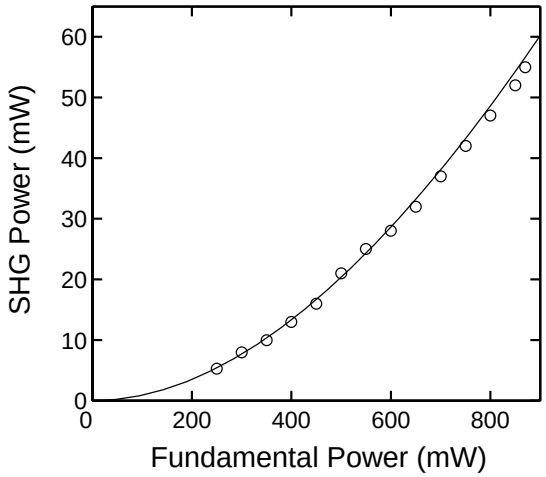

Figure 12.16: Evolution of the external second harmonic average power (of the TM_1 mode) as a function of the average input pump power (circles). The solid curve is a numerical fit obtained from the coupled mode equations with $\eta = 0.05\%\,\mathrm{W}^{-1}\mathrm{cm}^{-2}$.

the pulsed nature of the pump beam, the numerical fit given in Fig. 12.16 (solid curve) was obtained from Eqs. (12.5) and (12.6) by adjusting κ. An estimate of the normalised quadratic efficiency could then be obtained simply via κ^2 as $\eta_{\mathrm{nor}} = 0.05\%\,\mathrm{W}^{-1}\mathrm{cm}^{-2}$ [125].

For a full-nonlinearity preserving waveguide, the expected quadratic efficiency is given by [87]:

$$\eta_{\mathrm{nor}} = 2\sqrt{\frac{\mu_0}{\varepsilon_0}}\left(\frac{3d_{33}^2}{\pi^2}\right)\frac{\omega^2}{{n_\omega^{\mathrm{eff}}}^2 n_{2\omega}^{\mathrm{eff}}}\frac{1}{w}\frac{\int E_\omega^2(z)\,E_{2\omega}(z)\,\mathrm{d}z}{\left(\int E_\omega^2(z)\,\mathrm{d}z\right)^2\int E_{2\omega}(z)\,\mathrm{d}z}, \tag{12.7}$$

where w is the average beam width along y. In this equation the mode profiles E_i and effective indices $n_i^{\mathrm{eff}} = \beta_i/k_i$ are calculated for the index profile:

$$n(z) = n_{\mathrm{LiNbO_3}} + \begin{cases} \Delta n \exp\left[-(z-z_0)^2/z_1\right] & z \geq z_0 \\ \Delta n \exp\left[-(z-z_0)^2/z_2^2\right] & z < z_0 \end{cases}, \tag{12.8}$$

where the defining parameters are estimated from the waveguide to be:

$$z_0 = 1.6\,\mu\mathrm{m}, \quad z_1 = 1.3\,\mu\mathrm{m}, \quad z_2 = 1.3\,\mu\mathrm{m},$$

$$\Delta n\,(1536\,\mathrm{nm}) = 0.022, \quad \Delta n\,(768\,\mathrm{nm}) = 0.028,$$

and $n_{\mathrm{LiNbO_3}}$ is given by the Sellmeier equations [Section 10.4]. With $d_{33} = 27\,\mathrm{pmV}^{-1}$ and $w = 100\,\mu\mathrm{m}$, the expected efficiency was calculated to be $\eta_{\mathrm{nor}} = 0.09\%\,\mathrm{W}^{-1}\mathrm{cm}^{-2}$. Thus this is in reasonable agreement (same order of magnitude) with our measured efficiency.

12.6.3 Discussion

The results of this section have highlighted two key features of the device design that have limited the efficiency of the second harmonic process. The first is that the waveguide is multimodal so that interactions can occur between modes with a small overlap, which clearly have reduced efficiencies. The second is that the poling pattern of the HeXLN structure needs to be optimised for the collinear interaction in the waveguide which requires an accurate knowledge of the refractive index profile of the structure. Once this has been established, the spatial period Λ required to phase match this process can then be calculated. It is expected that by optimising the phase matching of the $\mathrm{TM}_0(\omega) \rightarrow \mathrm{TM}_0(2\omega)$ interaction, it should be possible to increase the quadratic efficiencies in the HeXLN waveguides to approach the theoretical value of $\eta_{\mathrm{nor}} = 2.7\%\,\mathrm{W}^{-1}\mathrm{cm}^{-2}$, predicted by Eq. (12.7).

Chapter 13

2D Quasi-Photonic Crystals

In the previous chapter, a two dimensional nonlinear hexagonally poled lithium niobate (HeXLN) crystal was used to demonstrate phase matching for second harmonic generation (SHG) and higher order harmonic processes. In this chapter these investigations are extended to consider phase matching in a two dimensional quasi-crystal based on a Penrose tile pattern. The discussions begin with a brief introduction to quasi-crystals and their use in harmonic generation. After describing the design and fabrication requirements, the preliminary experimental results to investigate SHG in a Penrose tile quasi-crystal are presented. These results have not only enabled characterisation of the Fourier space but they have also demonstrated the numerous possibilities for phase matching SHG processes, emphasising the dense nature of the reciprocal lattice space.

13.1 Quasi-Crystals for Harmonic Generation

In 1984, whilst investigating the diffraction properties of AlMn metal alloys, Shechtman *et al.* made the first experimental observation of a quasi-crystalline structure [127]. Since then, there have been numerous studies on the properties of quasi-crystals in many other physical systems such as dielectric and nonlinear structures. In particular, recently there has been considerable interest in quasi-phase matching harmonic processes in one dimensional lattices based on Fibonacci sequences [89, 91, 128].

The benefits of using quasi-crystals over more conventional periodic structures can immediately be seen by considering the problem of simultaneously phase matching two nonlinear processes in one dimension. Since the only free parameter in a periodically poled lithium niobate (PPLN) structure is the domain period a (see Section 10.2.1), simultaneous collinear phase matching of multiple processes is, in general, not possible as phase mismatches are rarely integer multiples of a constant. However, as a Fibonacci sequence is constructed via the tiling of two lattice constants, a and b, this provides the necessary extra degree of freedom.

An alternative approach to the problem of simultaneously phase matching multiple nonlinear processes is to move to two dimensions whilst retaining periodicity in the pattern. In this instance, the additional degree of freedom arises from the fact that the reciprocal lattice vector is now a linear combination of two orthogonal vectors (see Section 10.3). Indeed, this was the approach taken in the previous chapter which considered harmonic generation in a two dimensional HeXLN crystal. With this in mind, a natural extension to the multiple phase matching problem, which should provide even more flexibility to the design of the structures, is to combine the aperiodicity of the Fibonacci type patterns with the two dimensionality of the HeXLN structures in the form of a two dimensional quasi-crystal. It is worth noting that, although these quasi-crystals are expected to be worse for single interactions such as SHG, they should be better for multiple harmonic generation than strictly periodic crystals due to the greater density of reciprocal lattice vectors.

13.2 Two Dimensional Quasi-Crystals

The principal two dimensional aperiodic patterns are Penrose tiles [129]. These patterns are constructed out of a set of basic shapes that tile the plane only aperiodically and are characterised by long range order[1] and “forbidden” rotational symmetries. Significantly, these patterns do not have any translational symmetries.

[1] A structure is said to have long range order if the precise location of all lattice points can be calculated once the location of two lattice points are known.

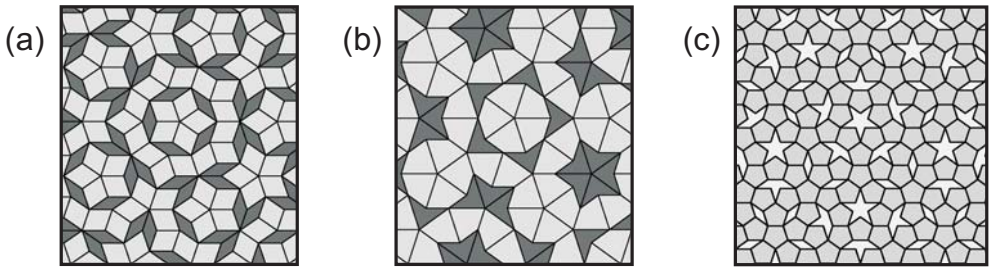

Figure 13.1: Examples of Penrose tile patterns constructed from (a) two rhombi, (b) kites and darts and (c) pentacles.

The classic Penrose tile consists of two rhombi of equal length sides but with different angles (as already seen in Fig 10.3). However, there are an infinite number of possible tilings and a sample of these are illustrated in Fig. 13.1.

13.2.1 Design Criteria

The first step to designing a two dimensional quasi-crystal is to decide on an appropriate Penrose tile pattern. Although all Penrose tiles have roughly the same properties, for the purpose of simplifying the fabrication process it is useful to choose a pattern with an even distribution of lattice points. For this reason the crystals used in the following experiments are designed based on the classic double rhombi Penrose tile of Fig. 13.1(a).

The second step in the design process is to optimise the crystal for phase matching SHG at the desired wavelength and temperature. This involves choosing the correct lattice period, deciding where in the lattice to put the poled regions (e.g., face centred or body centred) and the number of poled regions required per unit cell. Finally, it is necessary to decide on the size of the poled region and this is chosen such that it maximises the relevant Fourier coefficient of the desired harmonic interaction.

13.2.2 Fabrication

The lithographic mask used to define the Penrose tile was designed specifically for collinear quasi-phase matched SHG (aligned along the x axis) of a $1.536\,\mu\mathrm{m}$ fundamental beam at $140\,^{\circ}\mathrm{C}$. To ensure maximum efficiency, the pattern was

arranged so that the Fourier coefficient with the largest magnitude was used in the phase matching process. For a nonlinear lithium niobate crystal, with the poled regions placed at the vertices of the Penrose pattern (i.e., face centred), these requirements translate to rhombi with sides of length $18.999\,\mu\mathrm{m}$. Due to the trigonal atomic symmetry of lithium niobate [Section 12.2.2], the natural shape for the poled regions are hexagons. It should be noted that the dimensions of the hexagons on the mask were reduced with respect to the final desired domain size to account for domain broadening beyond the electrodes during the poling process. A schematic diagram of an expanded view of the mask design used in the fabrication process is shown in Fig. 13.2, together with the corresponding pattern in Fourier space. In particular, the five fold symmetry of the Fourier space, which is forbidden in a periodic crystal, can clearly be seen.

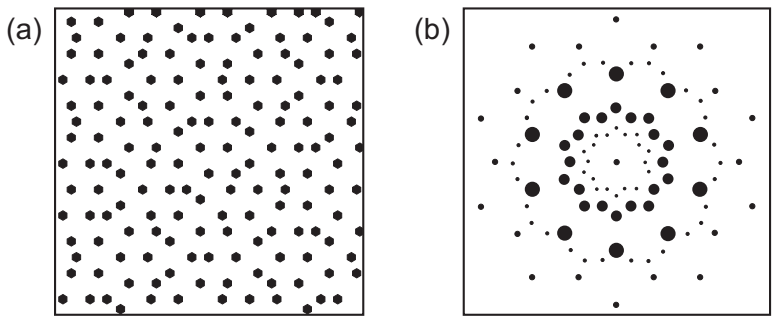

Figure 13.2: Schematic diagrams of the (a) mask design and (b) Fourier space, showing only the larger Fourier coefficients, for the Penrose tile domain pattern.

The two dimensional quasi-crystals used in our experiments were hexagonally poled by Dr K. Gallo. The fabrication procedure for the Penrose pattern was the same as that used for the HeXLN crystal described in Section 12.2.2, namely electric field poling [109]. However, in contrast to the HeXLN case where the mask consisted of a single bulk pattern, in the hope of minimising the poling errors this time the mask was designed to pattern 5 identical regions of size $1\,\mathrm{mm} \times 20\,\mathrm{mm}$ on each sample. In all the poled samples the Penrose patterns were found to be uniform across the whole structure and were faithfully reproduced throughout the crystal depth, thus confirming the validity of this technique for fabricating two dimensional quasi-crystals. The resulting tile pattern is shown in Fig. 13.3, as revealed by a light etch in HF acid. In this sample the hexagons have a thickness of $8.7\,\mu\mathrm{m}$ (between opposite corners)

and constitute $\sim 25\,\%$ of the total patterned area. These images clearly illustrate the long range orientational order and the quasi-periodic translational order of the structure.

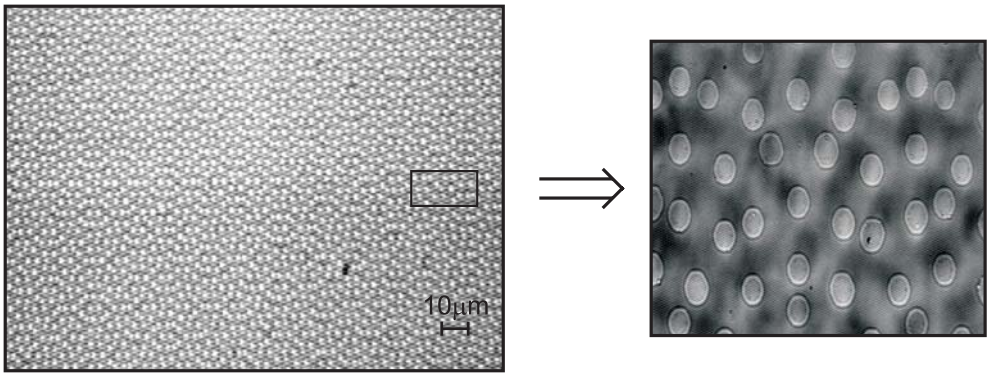

Figure 13.3: Photographs of the structure of the Penrose tile domain pattern of the poled lithium niobate crystal in the $x - y$ plane.

13.2.3 Phase Matching in a Quasi-Crystal

The precise diffraction pattern for the Fourier space, as calculated for the mask design given in Fig. 13.2(a), is shown in Fig. 13.4. Here Fig. 13.4(a) shows the collinear second harmonic process for which the crystal was designed. To illustrate the dense nature of the Fourier space, Fig. 13.4(b) then shows a second possible phase matched process that is not collinear. However, as well as being highly noncollinear, this second process employs a reciprocal lattice

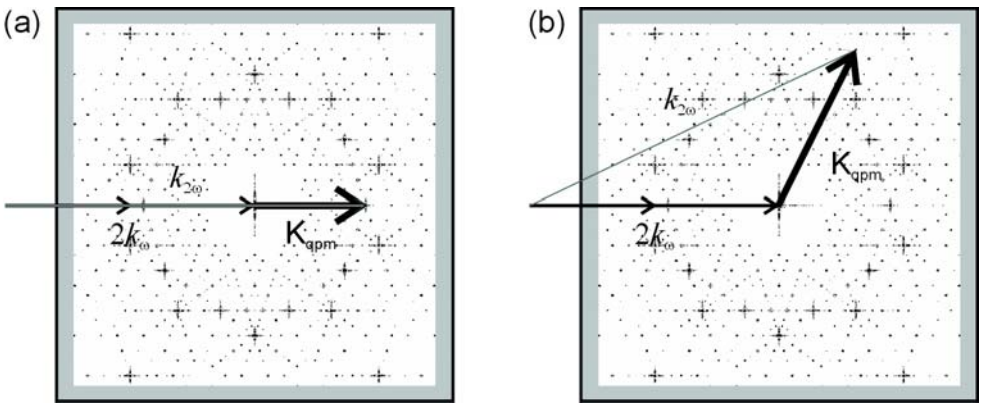

Figure 13.4: Calculated diffraction pattern for the Penrose tile quasi-crystal together with two possible phase matching conditions where (a) is the collinear case and (b) is a noncollinear case.

vector with a much smaller Fourier coefficient and so is unlikely to be seen. The significance of the density of the Fourier space can be further emphasised through the observation that even small adjustments in the angle of the propagating fundamental beam, with respect to the crystal axis, will provide a large number of additional phase matching conditions.

13.3 Experimental Setup

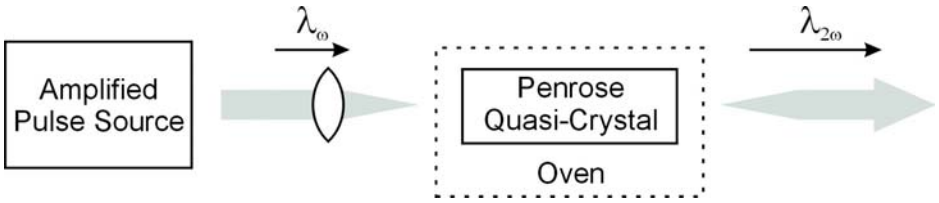

Figure 13.5: Schematic diagram of the experimental setup used to observe harmonic generation in a Penrose tiled quasi-crystal.

A schematic diagram of the experimental setup to observe harmonic generation in the Penrose tile quasi-crystal is shown in Fig. 13.5. This setup is similar to that used to investigate harmonic generation in a two dimensional HeXLN crystal. The significant difference, however, is that in the HeXLN experiments we employed a planar waveguide geometry to enhance the efficiency of the nonlinear interaction, whereas here we simply consider harmonic generation in the bulk sample. Thus coupling into the crystal was achieved by using a single spherical lens (focal length: $f = 13\,\mathrm{cm}$) from which we could obtain a minimum focused spot diameter of $40\,\mu\mathrm{m}$ (FWHM) in the centre of the crystal.

The pulse source used in our experiments was the same all fibre amplifier chain used in the HeXLN experiments, as described in Section 6.4.1. As before, to avoid photorefractive effects it was necessary to heat the sample to a temperature elevated above $\sim 100\,^{\circ}\mathrm{C}$. Because in this experiment we are considering nonlinear interactions in the bulk, the diffraction effects are less significant than those of the waveguide setup. Thus the Penrose quasi-crystal could be housed in the computer-driven Peltier oven, described in Section 12.4, but without the coupling block shown in Fig. 12.9. A typical example of the output from the Penrose tile quasi-crystal is given in Fig. 13.6 showing significant generation of both the second (red) and third (green) harmonics.

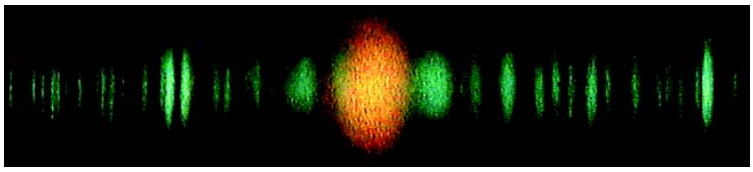

Figure 13.6: Output from the Penrose tile quasi-crystal showing the generated second (red) and third (green) harmonics.

13.4 Second Harmonic Generation in a Quasi-Crystal

This section presents the preliminary experimental results to investigate second harmonic generation in a two dimensional Penrose tile quasi-crystal. By investigating the phase matched interactions, the Fourier space has been characterised and the efficiency of the crystal established.

13.4.1 Temperature and Wavelength Tuning

We begin our investigations of the properties of the Penrose tiled quasi-crystal by measuring the interaction bandwidth for which information can be obtained by either measuring the second harmonic power as a function of temperature or wavelength. The Penrose tiled quasi-crystal used in these experiments was similar to that shown in Fig. 13.3. We start by considering the temperature tuning of the second harmonic power. For this measurement, the fun-

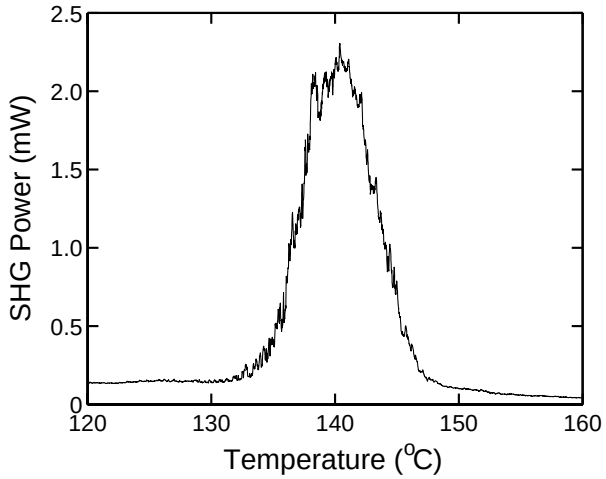

Figure 13.7: Average second harmonic power at the output of the Penrose tiled quasi-crystal as a function of temperature.

damental pump source was operated at a repetition rate of $100\,\mathrm{kHz}$ to produce $5\,\mathrm{ns}$ pulses with an average power of $200\,\mathrm{mW}$ incident on the crystal. With the fundamental beam gently focused into the crystal, the incident power was sufficiently low to ensure that we were in the low conversion regime. The crystal was then aligned with respect to the incident beam to obtain phase matching for the brightest single second harmonic spot at $140\,^{\circ}\mathrm{C}$. The resulting temperature tuning curve is plotted in Fig. 13.7 and this has a FWHM of $7.3\,^{\circ}\mathrm{C}$. Significantly, the distinctly non-sinc shape of this curve, which we would expect for a collinear interaction [3], suggests that the interaction we are investigating is in fact noncollinear [124]. Indeed, using the relation for the predicted intensity of the second harmonic field:

$$I_{2\omega} \propto \frac{\sin^2(\Delta k L/2)}{(\Delta k L/2)^2}, \tag{13.1}$$

where $\Delta k = 2k_{\omega} - k_{2\omega}$ and L is the length of the crystal, we have calculated that the expected bandwidth for a corresponding collinear interaction in PPLN is $3.6\,^{\circ}\mathrm{C}$, which is under half our measured width, also impling a noncollinear interaction. However, before investigating this any further, we first measured the second harmonic power as a function of wavelength using the same geometry.

For these measurements the fundamental pump source was again operated at a repetition rate of $100\,\mathrm{kHz}$. However, as the available power from the source is wavelength dependent, this time we used an external attenuator (consist-

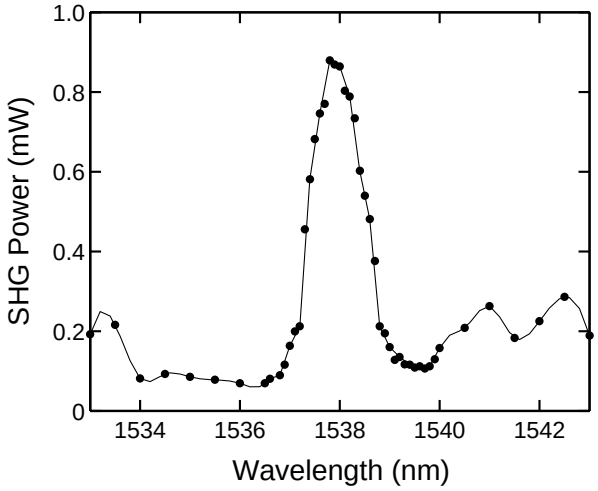

Figure 13.8: Average second harmonic power at the output of the Penrose tiled quasi-crystal as a function of wavelength.

ing of a half-wave plate and a polarising beam splitter combination) to ensure that the average power incident on the crystal remained constant at $150\,\mathrm{mW}$. The resulting wavelength tuning curve is presented in Fig. 13.8 with a FWHM of $1.39\,\mathrm{nm}$. Again, using Eq. (13.1) the expected bandwidth for a collinear interaction was calculated to be $0.55\,\mathrm{nm}$, providing further evidence of the non-collinearity of our interaction. We note that the tuning peaks seen on the edges of this curve correspond to additional phase matching processes occurring simultaneously, and thus can be attributed to the dense nature of the reciprocal lattice vectors.

13.4.2 Efficiency Measurements

In the interest of obtaining a better understanding of the interactions occurring in the crystal, our next step was to measure the maximum attainable conversion efficiency to the second harmonic power. For this measurement, the setup was optimised to provide $480\,\mathrm{mW}$ average power at a repetition rate of $100\,\mathrm{kW}$, corresponding to a fundamental peak power of $960\,\mathrm{W}$. With the coupling adjusted for maximum focusing to the smallest spot size, the crystal was aligned with respect to the incident beam to obtain the optimum phase matching at $140\,^{\circ}\mathrm{C}$. In this configuration we achieved a second harmonic peak power of $15.7\,\mathrm{W}$, which corresponds to an external conversion efficiency of 1.63%. For a collinear interaction, the expected internal conversion efficiency can be calculated via:

$$\eta_{\mathrm{int}} = \tanh\left(GL\right), \tag{13.2}$$

where L is the interaction length and

$$G = \sqrt{\frac{2\omega^2}{\varepsilon_0 c^3}\frac{d_{\mathrm{eff}}^2}{n^3} I_\omega(0)}. \tag{13.3}$$

Here $I_\omega(0)$ is the input fundamental intensity, $n \approx n_\omega \approx n_{2\omega}$ and d_{eff} is the effective nonlinear coefficient which is proportional to the size of the Fourier coefficient [Eq. (10.54)]. Assuming that the interaction corresponds to that depicted in Fig. 13.4(a), where the peak has a Fourier coefficient of 0.1053, and taking into account the Fresnel reflections at the input and output faces of the crystal, Eq. (13.2) predicts an external efficiency of $\sim 27\%$. Significantly this is considerably larger (by an order of magnitude) than our measured value and

thus to establish the reason for this discrepancy a more careful investigation of the setup was required.

Our first step was to establish the collinearity of the interaction and this was achieved by measuring the angle between the pump beam and its back reflection from the front face of the crystal, which for a perfectly collinear case should be zero. In doing this we noticed that there was actually a significant angle between the normal of the crystal and the propagating fundamental beam. Furthermore, by rotating the crystal back through the normal we found that there was an identical spot on the other side at a corresponding negative angle. Thus it was clear that at this temperature the crystal was not phase matching the collinear process illustrated in Fig. 13.4(a), and that a higher order reciprocal lattice vector was in fact being employed. As a result, the mask design was rechecked and it was found that there was an error in the Penrose pattern such that the sides of the rhombi were in fact $17.818\,\mu\mathrm{m}$, that is $1.172\,\mu\mathrm{m}$ shorter than the calculated value [Section 13.2.2]. Thus in order to establish the phase matching processes that we were observing in our crystal it was necessary to characterise the Fourier space of our crystal.

So that we could make use of the expected symmetrical nature of the Fourier space (see Fig. 13.4), we began our characterisation process by realigning the crystal so that the fundamental beam was perpendicular to the input face. By scanning through the temperature range $100 - 160\,^{\circ}\mathrm{C}$ we could then observe a number of SHG interactions which were phase matched in this geometry and these processes were associated with the appearance of two second harmonic spots symmetric about the output fundamental, as illustrated in Fig. 13.9. The two brightest sets of spots occurred at $105\,^{\circ}\mathrm{C}$ and $148\,^{\circ}\mathrm{C}$ and it was the set at $148\,^{\circ}\mathrm{C}$ that we chose to use for our further investigations of the Fourier space.

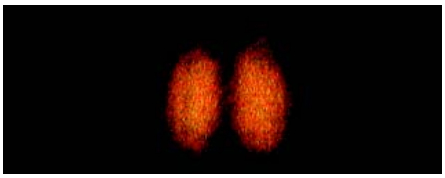

Figure 13.9: Output from the Penrose tile quasi-crystal with the fundamental beam perpendicular to the crystal face showing the two symmetric second harmonic spots.

To determine the phase matching processes occurring in this configuration we

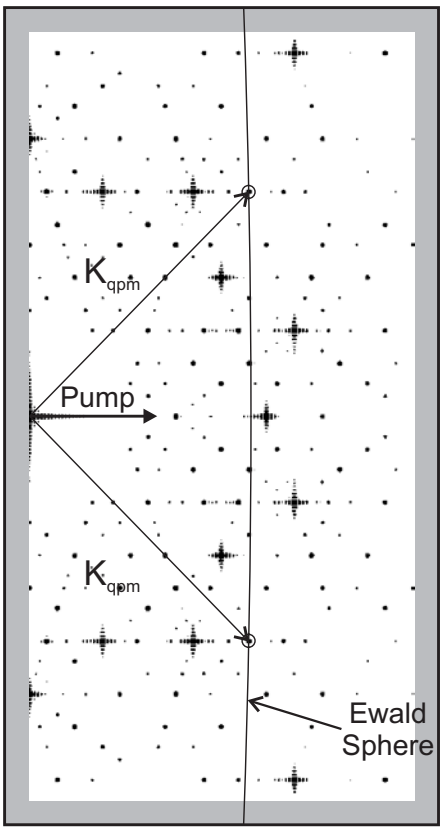

Figure 13.10: Fourier space overlaid with the Ewald sphere showing phase matching for the symmetric second harmonic spots at $148\,^{\circ}\mathrm{C}$.

first recalculated the diffraction pattern for the Penrose tile pattern for rhombi with sides of length $17.818\,\mu\mathrm{m}$ at $148\,^{\circ}\mathrm{C}$. The recalculated diffraction pattern is shown in Fig. 13.10 together with the Ewald sphere construction [71]. Although the Ewald sphere was initially defined for investigating x-ray diffraction problems, it is also extremely useful for understanding two dimensional quasi-phase matching processes. Here the sphere is constructed such that its centre is located $-2k_{\omega}$ away from the origin of the reciprocal lattice with a radius of $k_{2\omega}$. The relevant reciprocal lattice vectors and the corresponding Fourier coefficients for the allowed phase matched processes can then be determined from the peaks which are located on the Ewald sphere as indicated on the figure. For these two spots the Fourier coefficients were calculated to be 0.019 which is an order of magnitude smaller than the Fourier coefficient for the collinear interaction. By measuring the external angles of the pump and the second harmonic beams for the spots in Fig. 13.9 we could confirm that these were in fact being generated via the interactions represented in Fig. 13.10.

Spot	Pump Ang.	SHG Ang.	Spot	Pump Ang.	SHG Ang.
1	$0.167°$	$2.624°$	22	$-21°$	$-19.421°$
2	$0.167°$	$-2.290°$	23	$-24.333°$	$-25.438°$
3	$-1.5°$	$-2.684°$	24	$2.167°$	$3.238°$
4	$-2°$	$-6.054°$	25	$2.75°$	$6.504°$
5	$-2°$	$-12.483°$	26	$2.75°$	$13.306°$
6	$-3°$	$-9.179°$	27	$3.583°$	$9.932°$
7	$-5.5°$	$-5.838°$	28	$6.083°$	$6.658°$
8	$-6.5°$	$-2.222°$	29	$7°$	$2.005°$
9	$-6.5°$	$0.381°$	30	$8°$	$10.232°$
10	$-7.75°$	$-9.700°$	31	$8.583°$	$5.428°$
11	$-8.167°$	$-4.922°$	32	$11.333°$	$14.937°$
12	$-10.833°$	$-13.482°$	33	$11.333°$	$2.538°$
13	$-10.833°$	$-4.208°$	34	$11.75°$	$9.867°$
14	$-11.167°$	$-9.104°$	35	$12.583°$	$12.222°$
15	$-12°$	$-11.774°$	36	$13°$	$15.705°$
16	$-12°$	$-14.930°$	37	$15.333°$	$18.274°$
17	$-14.75°$	$-17.421°$	38	$15.333°$	$19.510°$
18	$-14.75°$	$-18.725°$	39	$16.583°$	$12.473°$
19	$-16.083°$	$-11.917°$	40	$18.583°$	$15.991°$
20	$-17.833°$	$-15.038°$	41	$18.583°$	$21.535°$
21	$-17.833°$	$-20.842°$			

Table 13.1: Angular measurements for the SHG interactions in a Penrose tile quasi-crystal.

To establish a more complete characterisation of the Fourier space, our next step was to measure the angular dependence of the second harmonic processes. For this measurement we simply rotated the crystal with respect to the pump beam so that phase matching via different reciprocal lattice vectors could be observed. As above, by measuring the external angles of the fundamental and second harmonic beams the corresponding Fourier peaks which were responsible for the particular interaction could be determined. Using an average pump power of $\sim 260\,\mathrm{mW}$, and rotating the crystal through an angular range of $\pm 25°$, we observed 41 phase matched SHG processes. For reference, the measured angles are given explicitly in Table 13.1, where both

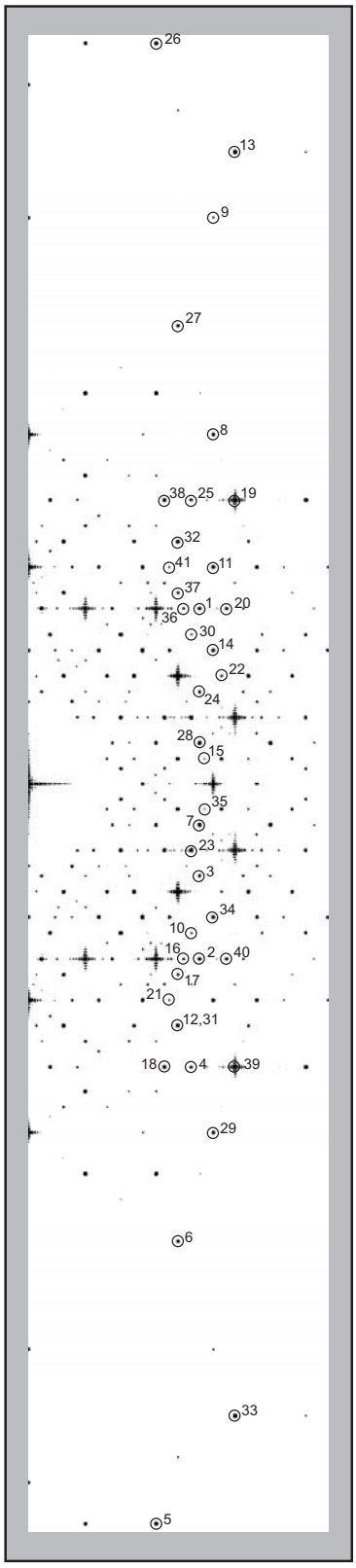

Figure 13.11: Fourier space showing the corresponding Fourier peaks for the measured second harmonic spots given in Table 13.1.

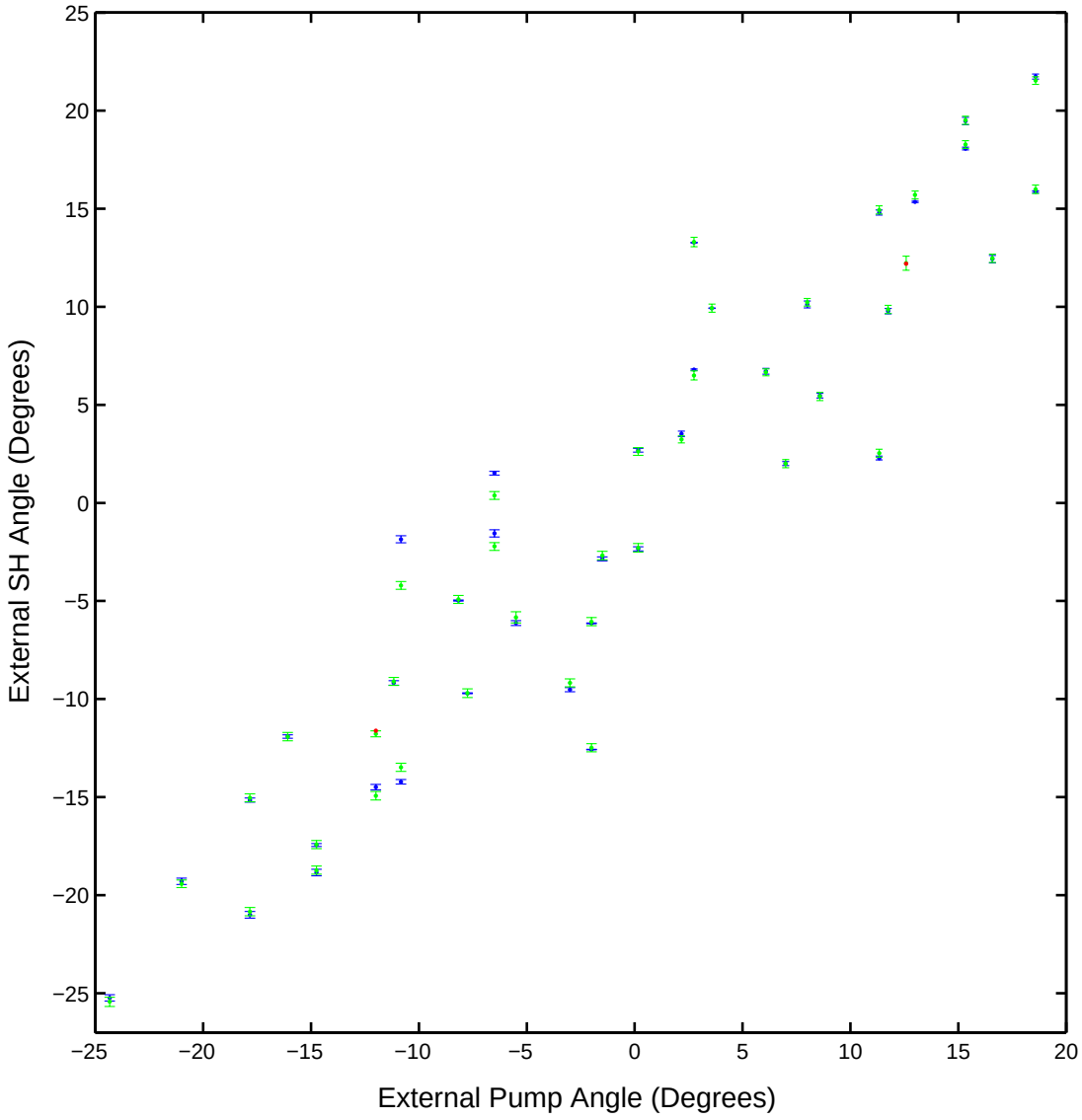

Figure 13.12: External second harmonic angle as a function of the external pump angle where 0° corresponds to propagation along the crystal axis. The green spots correspond to the experimental measurements and the blue to the theoretical predictions.

the pump and second harmonic angles are given with respect to the normal of the crystal. The corresponding Fourier peaks are then labelled in Fig. 13.11.

This data is summarised in Fig. 13.12 where the external second harmonic angle is plotted as a function of the external pump angle, and 0° corresponds to propagation along the crystal axis. In this figure the green and blue spots correspond to the experimental measurements and theoretical predictions obtained from the Fourier space of Fig. 13.11, respectively. We note that the two red spots which appear at symmetric angles about 0° correspond to situa-

tions where, for the measured pump angle, no Fourier peaks lay exactly on the Ewald sphere. Unfortunately we have not been able to establish the reason for this discrepancy. However, by choosing the Fourier peak closest to the sphere it is clear that we can still obtain a reasonable match to the measured output second harmonic angle so that it is likely that this can be attributed to experimental error. Thus these results have demonstrated an excellent agreement between the experimental and theoretical angles over the majority of interactions, including those corresponding to higher order reciprocal lattice vectors, indicating the high quality of the crystal.

Having satisfied ourselves that the diffraction patterns illustrated in Figs. 13.10 and 13.11 are indeed accurate representations of the Fourier space of the Penrose tile quasi-crystal, our final task was to recalculate the expected efficiency for the original single spot interaction. Again, by measuring the external angles of the fundamental and the second harmonic beams we could determine that the Fourier peak which was phase matching this process was the same Fourier peak as used in the interaction which generated spot 28 in Fig. 13.11 and this has a Fourier coefficient of 0.026. Thus using this value in Eq. (13.2) the expected external conversion efficiency is now only 2.06%, which is in reasonable agreement with our measured value of 1.63%.

13.4.3 Discussion

The results presented in this section have provided the first preliminary demonstration of second harmonic generation in a two dimensional quasi-crystal. By analysing the interaction processes occurring in the crystal, we have established that the main limitation to our conversion efficiencies is the inability to phase match the collinear interaction illustrated in Fig. 13.4(a), which involves the largest Fourier peak. This was due to an error in the mask design which resulted in a reduced phase matching period. Although in theory it should be possible to access this particular interaction by simply considering a process involving different wavelengths, we have calculated that the required wavelength of the fundamental pump is $\sim 1.2\,\mu\mathrm{m}$, which is well outside the tuning range of our source.[2] Thus in order to utilise this particular interaction ge-

[2]The exact wavelength will depend on the choice of operating temperature.

ometry, we would first need to redesign our lithographic mask for the correct dimensions.

Despite the small observed conversion efficiencies, this crystal has nevertheless highlighted one of the most important features of a two dimensional quasi-crystal which is the dense nature of the reciprocal lattice space. This increased density of the reciprocal lattice vectors should provide greater flexibility to phase matching processes in many novel devices, particularly for situations where multiple nonlinear interactions are required.

Chapter 14

Conclusion

In Part 2 of this thesis I have numerically and experimentally investigated the control and manipulation of light propagating in novel crystal structures.

The results of numerical calculations used to analyse the guided mode solutions of one dimensional negative refractive index waveguides, presented in Chapter 11, have demonstrated a number of unusual properties that differ considerably from those of conventional waveguides. Typical features of these waveguides include anomalies in the appearance of the mode orders, double degeneracy of modes, superluminal propagation speeds as well as extraordinarily large group velocity dispersion. Calculation of the coupling coefficients between modes of positive and negative index waveguides has shown that it is possible to couple light into these structures.

The experimental investigations of Chapter 12 provided the first demonstration of second harmonic generation in a HeXLN buried planar waveguide. By analysing the interaction between the guided fields it was established that the waveguide was in fact multimodal. The low conversion efficiencies measured for the second harmonic process were attributed to an incorrect phase matching period in the waveguide, which led to the interaction occurring between modes of differing order.

Finally, the measurements presented in Chapter 13 also provided another first by demonstrating second harmonic generation in a two dimensional quasicrystal based on a Penrose tile pattern. Despite the low observed conversion efficiencies, which were due to an error in the mask design, these are neverthe-

less in good agreement with the expected efficiencies obtained via a Fourier analysis of the crystal. These results have illustrated numerous possibilities for phase matching SHG processes, emphasising the dense nature of the reciprocal lattice space and the flexibility of such crystals for use in novel devices based on multiple nonlinear interactions.

The work presented in this part of the thesis has demonstrated many new concepts which can be employed to control and manipulate the propagation of light in modulated crystal structures. Although many of these results are preliminary, they represent a number of “firsts” in their respective technological areas and thus they should provide a basis on which to develop more refined devices. It is hoped that the results presented in this second part of the thesis will not only spark interest as novel curiosities, but also that they will benefit many areas of optical technologies.

Part III

Applications and Future Directions

Chapter 15

Introduction

The results presented in the proceeding chapters have demonstrated a number of important new results regarding the control and manipulation of light in optical devices. In particular, in Part 1 I investigated self-similar pulse solutions which offer unique distortion free propagation so that the pulses can be amplified to high powers and compressed to ultrashort durations. Then in Part 2 I considered novel crystal structures which can be used to control the speed of light or to generate new, shorter, wavelengths via harmonic conversion processes.

As mentioned in Chapter 1, it is hoped that an improved understanding of the processes described in the first two parts of this thesis can be combined to aid with the design of more efficient devices. Indeed, to some extent I have already demonstrated this within the body of the thesis. For example, in Chapter 6 the experiment to generate parabolic pulses in a highly nonlinear microstructured fibre via Raman amplification was seeded using an optical parametric oscillator (OPO) based on a periodically poled lithium niobate (PPLN) crystal specifically because this type of source could provide a signal beam at wavelengths tunable under the Raman gain curve. Then in Chapter 11 the investigations of the guided mode solutions for a fibre with a negative index core were based on a structure with a periodic cross section similar to that of the conventional air filled microstructured fibres.

In this final part of the thesis I will describe a novel oscillator design that combines many of the interesting features of the earlier results to produce an effi-

cient, widely tunable short pulse source. Although to date the widest tuning ranges are still obtained in OPOs based on periodically poled crystals [130], recently some attention has been focused on wavelength tuning in fibre based sources [131]. However, to overcome restrictions in their tunability both these source designs have typically required continuous cavity modifications such as changing the grating period of the crystal and/or the cavity length. For this reason the device described in the following chapter combines both the large wavelength conversion obtained via frequency doubling in PPLN with the tunability of fibre loops based on the Raman frequency shift. Due to the flexibility of this oscillator design, it is expected to find wide application in many areas of short pulse technologies.

To conclude this thesis, the final chapter in this part will discuss suggestions for future research directions.

Chapter 16

Widely Tunable Self-Similar Oscillator

16.1 Introduction

In this chapter a numerical model of a widely tunable oscillator, that operates in the wavelength range of $1\,\mu\mathrm{m} \rightarrow 2\,\mu\mathrm{m}$, will be investigated. This oscillator combines the large wavelength conversion obtained via frequency doubling in solid state periodically poled lithium niobate (PPLN) devices with the tunability of fibre loops based on the Raman frequency shift, and thus contains some of the important results obtained in the first two parts of this thesis. Significantly, it will be shown that despite the wide range of devices used in the system the pulses evolve self-similarly in each stage of the oscillator, maintaining a hyperbolic secant form, whilst their peak power and width scale according to the device mechanism.

16.2 Oscillator Model

The oscillator is simulated based on the schematic diagram given in Fig. 16.1. The seed pulses are first Raman shifted from $1.5\,\mu\mathrm{m}$ to $2\,\mu\mathrm{m}$ before being frequency doubled via quasi-phase matched second harmonic generation (SHG) back down to $1\,\mu\mathrm{m}$. After the pulses undergo regeneration in an amplifier/

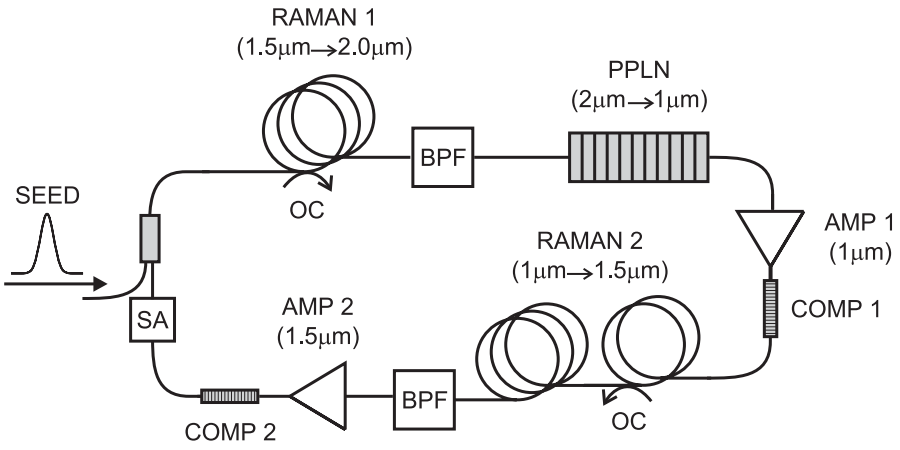

Figure 16.1: Schematic diagram of the oscillator model.

compressor combination they are then Raman shifted back up to $1.5\,\mu\mathrm{m}$ where again they are amplified and compressed before being relaunched into the first Raman shifting stage. To ensure pulse stability in the oscillator, a saturable absorber with a power dependent transmission characteristic is included. This ensures that the pulse energy does not become too great so that the correct Raman shifts are maintained and is particularly important for the first Raman stage as the efficiency of the subsequent PPLN stage is highly dependent on the input wavelength. The resulting system can then be tailored to provide soliton pulses potentially at any wavelength within the range $1\,\mu\mathrm{m} - 2\,\mu\mathrm{m}$ simply by placing an output coupler at the required length along either of the Raman shifting fibres.

16.3 Numerical Model and Device Parameters

16.3.1 Propagation Equations

Modelling of the pulse evolution in the oscillator of Fig. 16.1 can be considered in two parts, one for the fibre stages and one for the PPLN stage. Propagation in the fibre stages can be described by an equation which combines the generalised forms of the nonlinear Schrödinger equations (NLSE) presented in

Section 3.10:

$$\begin{aligned} \mathrm{i}\frac{\partial}{\partial z}\Psi &= \frac{\beta_2(\omega_0)}{2}\frac{\partial^2}{\partial T^2}\Psi - \gamma(\omega_0)\left(1+\frac{\mathrm{i}}{\omega_0}\frac{\partial}{\partial T}\right)\Psi\int_0^\infty R(T')\left|\Psi(z,T-T')\right|^2\mathrm{d}T' \\ &+ \frac{\mathrm{i}}{2\sqrt{2\pi}}\int_{-\infty}^{\infty}\alpha(\omega)\,\tilde{\Psi}\exp(-\mathrm{i}\omega T)\,\mathrm{d}\omega. \end{aligned} \tag{16.1}$$

The important feature of this equation is the inclusion of the frequency dependence of the fibre parameters. This is essential because of the large $0.5\,\mu\mathrm{m}$ wavelength shifts of the pulses in the Raman stages. As the dispersion and nonlinearity profiles vary relatively slowly with frequency, in these terms the frequency dependence is simply accounted for by updating their values for the central frequency of the pulse ω_0 at each propagation step. However, as both the loss ($\alpha < 0$) and gain ($\alpha > 0$) profiles exhibit strong peaks, it is necessary to include the full frequency dependence of these parameters [4]. It should be noted that in the Raman term, $R(T)$ is the usual nonlinear response function expressed in the form: $R(T) = (1-f_R)\delta(T) + f_R h_R(T)$ [Section 3.10.2]. This equation can be solved using a combination of the techniques described in Section 3.10.

The PPLN section of the system is modelled using the coupled equations for SHG as given in Section 10.9.2:

$$\frac{\partial^2}{\partial z^2}\mathbf{\Psi}_{2\omega} - \frac{n_{2\omega}^2}{c^2}\frac{\partial^2}{\partial T^2}\mathbf{\Psi}_{2\omega} = \frac{1}{c^2}\chi^{(2)}(z)\,\frac{\partial^2}{\partial T^2}\left(\mathbf{\Psi}_{\omega}\right)^2, \tag{16.2}$$

$$\frac{\partial^2}{\partial z^2}\mathbf{\Psi}_{\omega} - \frac{n_{\omega}^2}{c^2}\frac{\partial^2}{\partial T^2}\mathbf{\Psi}_{\omega} = \frac{2}{c^2}\chi^{(2)}(z)\,\frac{\partial^2}{\partial T^2}\left(\mathbf{\Psi}_{2\omega}\mathbf{\Psi}_{\omega}^*\right). \tag{16.3}$$

Here the fields $\mathbf{\Psi}_m$ are related to the slowly varying amplitude in Eq. (16.1) via: $\mathbf{\Psi}_m = \Psi_m \exp\left[\mathrm{i}\left(k_m z - mT\right)\right]$, and $m = \omega, 2\omega$ for the fundamental and second harmonic fields, respectively. Again n_m are the refractive indices, $k_m = 2\pi n_m/\lambda_m$ are the wavenumbers, and the equations are solved using the finite difference technique also described in Section 10.9.2.

16.3.2 Device Parameters

The specific design of the oscillator was chosen so that it could take advantage of the efficient rare-earth doped fibre amplifiers at $\sim 1\,\mu\mathrm{m}$ (Yb^{3+}:doped) and $\sim 1.5\,\mu\mathrm{m}$ (Er^{3+}:doped). To obtain the large frequency shifts, small core highly nonlinear microstructured fibres are used for the Raman shifting stages. In

particular, the use of a microstructured fibre for the second Raman stage is necessary as their dispersion properties can be tailored such that they exhibit anomalous dispersion over the entire $1\,\mu\mathrm{m} - 1.5\,\mu\mathrm{m}$ wavelength range. Furthermore, due to the strong OH-absorption peak in the loss profile of silica fibres that appears at $1.37\,\mu\mathrm{m}$ (see Ref. [4] and Fig. 16.2), a two stage Raman shift was found to be more efficient in this section.

For each of the fibre stages the parameters used in the simulations are based on realistic experimental values [12, 132, 133]. As mentioned above, due to the large $0.5\,\mu\mathrm{m}$ wavelength shifts of the pulses in the Raman stages, it is essential to include the frequency dependence of the fibre parameters. For the nonlinearity parameter, this simply requires calculating $\gamma = n_2\omega_0/cA_{\mathrm{eff}}$ at each propagation step. However, for the dispersion, loss and gain terms the explicit forms of the parameter profiles need to be considered. The dispersion and gain profiles for a standard SMF geometry have already been given in Chapter 3 and it is these that are used for the amplifier stages. For the microstructured fibre stages, although the exact form of the fibre parameters will depend on the specific structural design, here the calculations are simply based on the shape of the dispersion and loss profiles for a pure silica fibre, but with some slight modifications. In particular, for the second Raman stage the zero dispersion wavelength needs to be shifted so that the fibres exhibit anomalous dispersion over the entire wavelength range. Also, as the losses are greater in a microstructured fibre than in a standard SMF, the magnitude of the loss profile (as given in Ref. [4]) needs to be increased. The modified forms of the

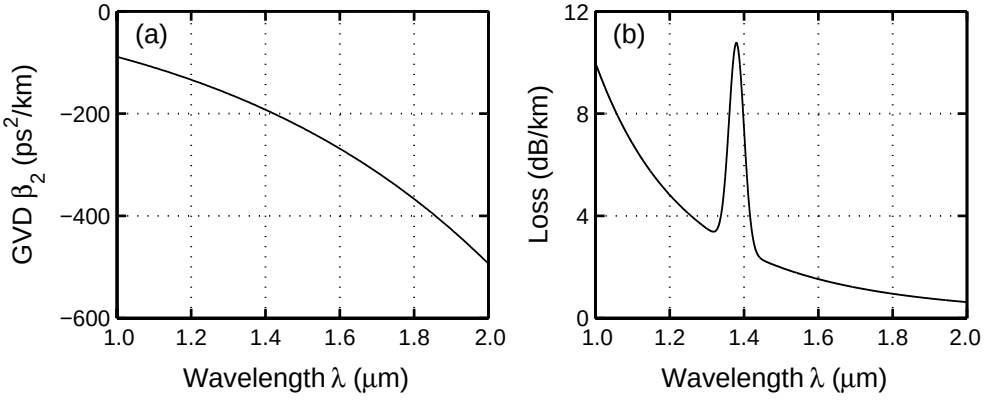

Figure 16.2: (a) Dispersion shifted profile for the second Raman shifting stage and (b) the loss profile used for both the microstructured fibre stages.

dispersion and loss profiles used in the simulations can be seen in Fig. 16.2. For convenience, the relevant parameters are given explicitly in Table 16.1.

	RAMAN 1	AMP 1	COMP 1	RAMAN 2	AMP 2	COMP 2
L (m)	85	3.9	2.2	45,50	2.45	1.15
β_2 ($\mathrm{ps}^2\,\mathrm{km}^{-1}$)	silica	20	-31	DS silica	20	-31
A_{eff} ($\mu\mathrm{m}^2$)	13	35	0	8,5	23	0
α (m^{-1})	silica	1	0	silica	0.3	0

Table 16.1: Device parameters for the fibre stages.

For the PPLN stage of the oscillator the crystal length was chosen to be $400\,\mu\mathrm{m}$ so that, whilst it is typical of that employed in real experimental configurations [134], it is not too long that it results in impractical computation times. Assuming an operating temperature of $T = 120\,^{\circ}\mathrm{C}$ (to avoid photorefractive effects), the grating period for a $2\,\mu\mathrm{m} \rightarrow 1\,\mu\mathrm{m}$ process is $\Lambda = 29.3\,\mu\mathrm{m}$. The refractive indices in Eqs. (16.2) and (16.3) are then calculated at each cycle for the exact wavelength of the pulse exiting the first Raman stage. Typical conversion efficiencies for this process are or the order of $\sim 8\,\%$. The low efficiency of this process is consistent with experimental observations [12] and, as discussed in Section 10.9.2, can be attributed to the phase mismatch due to the broad bandwidth associated with the short input fundamental pulse.

Finally, the saturation energy E_{sat} of the saturable absorber is chosen to be that of the input pulse energy with a power dependent transmission characteristic, as mentioned in Section 16.2.

16.4 Simulations Results

The oscillator is assumed to be initially seeded with $312\,\mathrm{pJ}$, $350\,\mathrm{fs}$ (FWHM) hyperbolic secant pulses, typical of those generated via compression of the output from an Er^{3+}:doped fibre laser (such as that described in Section 6.4.1). The evolution of the pulses in the oscillator at $1.5\,\mu\mathrm{m}$ is shown in Fig. 16.3. Despite the slight variation in the pulse shape, especially near the peak, this figure illustrates the ability of the oscillator to produce a consistent output of uniform pulses.

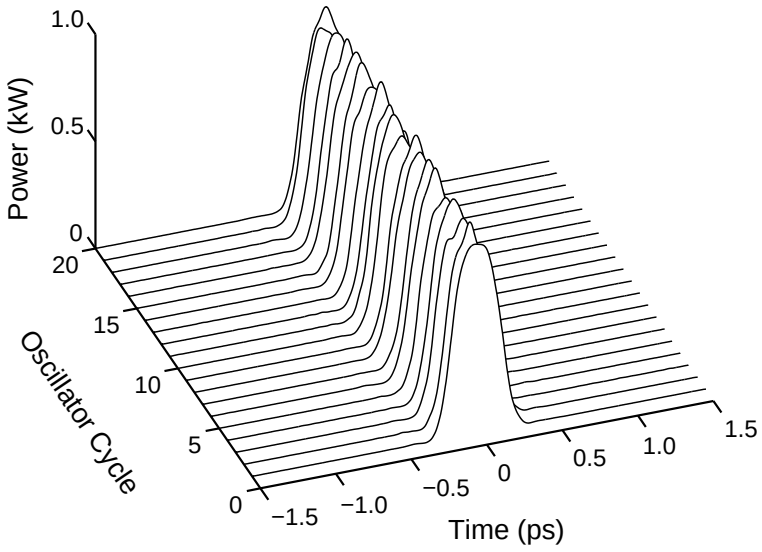

Figure 16.3: Evolution of the pulses in the oscillator at $1.5\,\mu\mathrm{m}$ over 20 cycles.

The stability of the oscillator is then confirmed in Fig. 16.4 which shows the evolution of the (a) FWHM width and (b) peak power of the pulses also at $1.5\,\mu\mathrm{m}$. Significantly, it is clear that after each loop the pulses have returned to a form where their parameters are consistent with those of the seed pulse. It is important to note that in Figs. 16.3 and 16.4 the number of oscillator cycles is only restricted to 20 cycles due to the long computation time, particularly for the PPLN stage.

Examples of the pulse profiles and chirps at the output of each stage of the oscillator system are then plotted in Fig. 16.5, together with the original seed

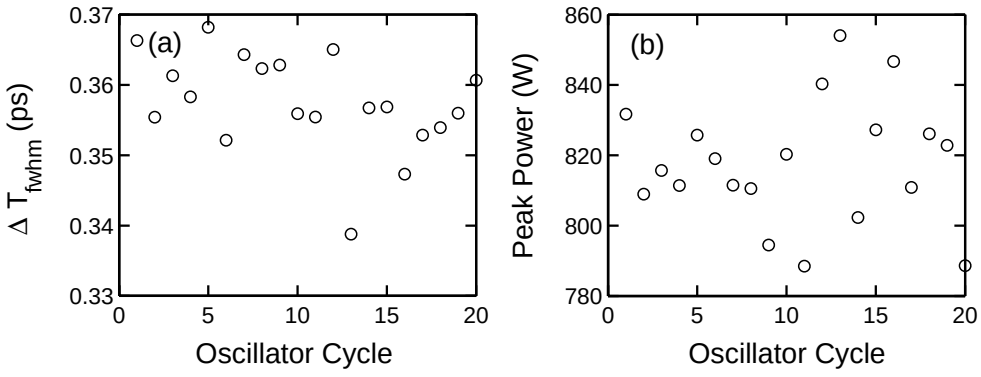

Figure 16.4: Evolution of the (a) FWHM width and (b) peak power of the pulses at $1.5\,\mu\mathrm{m}$.

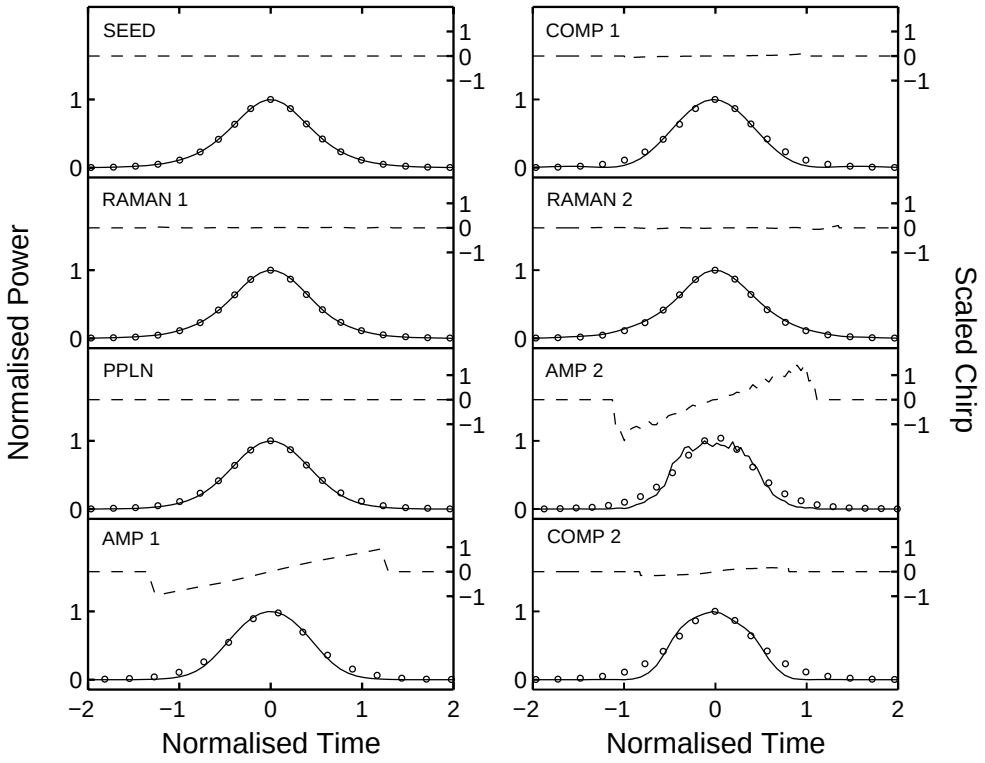

Figure 16.5: Pulse profiles (left axes) and chirps (right axes) of the output pulses after each stage of the oscillator, together the seed pulse. The pulse profiles have been normalised in power and time so that they have a peak intensity and FWHM width of 1. The circles are hyperbolic secant fits.

pulse. To allow for easy comparison between the pulses they have been normalised in power and time with their physical parameters given explicitly in Table 16.2. Significantly, by comparing the shape of the intensity profiles it can be seen that the functional form of the pulse remains essentially unchanged after each stage of the oscillator. This is particularly obvious in the early stages of the loop before it is necessary for the pulses to undergo significant regeneration to compensate for the large losses experienced in the second Raman stage. However, despite the slightly noisy appearance of the pulses after this second regeneration stage, in all cases the pulses exhibit a reasonable agreement with

	RAMAN 1	PPLN	AMP 1	COMP 1	RAMAN 2	AMP 2	COMP 2
ΔT (fs)	180	130	1900	150	240	1400	360
P_0 (W)	760	70	240	3150	530	230	820
E (pJ)	150	10	480	480	160	310	310

Table 16.2: Average pulse parameters after each oscillator stage.

the hyperbolic secant fits to the intensity profiles (circles). In addition, it can also be noticed that in most cases the pulses have a flat phase with only the amplified pulses possessing a significant chirp. Importantly, as it has been shown in the first part of this thesis, the development of a linear chirp is often associated with self-similar evolution and furthermore, ensures efficient compression of the pulses with minimal pulse distortions. Thus it appears that the evolution of the pulses in the oscillator is, in a sense, self-similar.

To understand the self-similar nature of the pulses in this system, the evolution of the pulses in the individual stages are considered. In the Raman stages, to obtain the large frequency shifts a shifting mechanism based on the break up of high power pulses into multiple fundamental solitons, at different Stokes frequencies, is employed. These solitons then propagate under the influence of the soliton self-frequency shift, which is clearly a self-similar process. The final pulse is then obtained simply by placing a bandpass filter of the desired wavelength at the output of the fibre.

In the amplifier stages, as only moderate amplification is required, the evolution occurs in a regime where the nonlinear effects are still small so that dispersion dominates the pulse propagation. Significantly, self-similar analysis of the evolution of pulses in an amplifier has shown that in the early stages of the propagation, where the dispersion does indeed dominate, intermediate asymptotic solutions exist which will maintain their initial form whilst developing a linear chirp [135]. For a hyperbolic secant input pulse the form of the solutions are:

$$\Psi(z,T) = \sqrt{\frac{P_0}{\Gamma(z)}}\mathrm{sech}\left(\frac{T}{T_0\Gamma(z)}\right)\exp\left(\frac{G(z)}{2}\right)\exp\left[\mathrm{i}\Phi(z,T)\right], \tag{16.4}$$

where

$$\Phi(z,T)=\phi_0+\frac{\beta_2}{2T_0^2}\int_0^z\frac{1}{\Gamma^2(z')}\mathrm{d}z'+\gamma P_0\int_0^z\frac{\exp\left[G(z')\right]}{\Gamma(z')}\mathrm{d}z'-\frac{T^2}{2\beta_2\Gamma(z)}\frac{\mathrm{d}\Gamma(z)}{\mathrm{d}z}. \tag{16.5}$$

Here the evolution of the pulse width, peak power and chirp are determined by the amplifier parameters through:

$$G(z) = \int_0^z g(z')\mathrm{d}z', \tag{16.6}$$

and

$$\begin{aligned}\Gamma(z) &= \sqrt{1+\lambda^2 z^2} + \frac{\delta\left(\lambda^2 z^2 - 1\right)}{\sqrt{1+\lambda^2 z^2}} \int_0^z \frac{z' \exp\left[G(z')\right]}{\left(1+\lambda^2 z'^2\right)^{3/2}} \mathrm{d}z' \\ &- \frac{\delta z}{\sqrt{1+\lambda^2 z^2}} \int_0^z \frac{\left(\lambda^2 z'^2 - 1\right) \exp\left[G(z')\right]}{\left(1+\lambda^2 z'^2\right)^{3/2}} \mathrm{d}z', \end{aligned} \tag{16.7}$$

where $\lambda = 2\left|\beta_2\right| / \pi T_0^2$ and $\delta = 4\gamma\beta_2 P_0 / \pi^2 T_0^2$.

Fig. 16.6 compares typical output pulses from the two amplifier stages with Eqs. (16.4)–(16.7). Despite the noise on the output pulse from the second Er^{3+}: doped amplifier stage, both these pulses and their chirps are in good agreement with the theoretical predictions (circles). Thus it can be concluded that the pulses in the amplifier stages are also evolving self-similarly, maintaining their hyperbolic secant form. An important feature of the self-similarity of these pulses is that because of the linearity of the developed chirps, the output pulses from the amplifier stages can be compressed via a simple linear compressor (as described in Section 5.3.3) to yield transform limited pulses that will also retain an approximate hyperbolic secant profile.

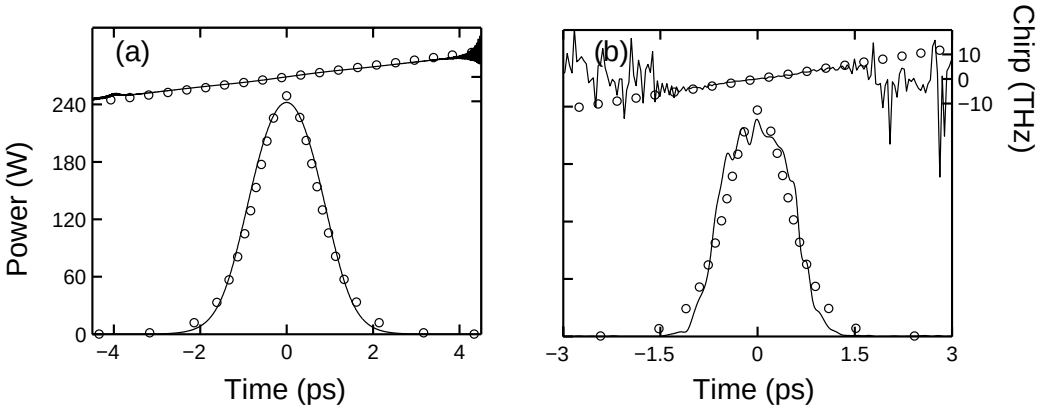

Figure 16.6: Examples of the output intensities (left axes) and chirps (right axes) from (a) the Yb^{3+} amplifier stage and (b) the Er^{3+} amplifier stage of the oscillator (solid lines). The circles are the theoretical predictions for the intermediate asymptotic solutions.

The final stage to consider is the pulse evolution in the PPLN crystal. As it can be seen from Eqs. (16.2) and (16.3), the form of the SHG pulse is determined by the fundamental so that this will again be generated to have an approximate hyperbolic secant form but with a reduced width: $\Delta T_{2\omega} \sim \Delta T_\omega / \sqrt{2}$,[1] as

[1]This is exact for a Gaussian pulse with the assumption of an undepleted pump.

discussed in Section 10.9.2.

Thus these results have shown that the pulses evolve self-similarly in all stages of the oscillator with their peak powers and widths scaling according to the device mechanism. At this point it is important to emphasise that the self-similar nature does not apply to the system as a whole, but only in the individual stages. However, significantly, in all stages the self-similar propagation evolves to a pulse with a hyperbolic secant form so that there is an overall quasi-self-similar nature of the system.

16.4.1 Extension to Higher Energies

As a final test of the stability of this oscillator, a modified system is considered where the oscillating pulses have higher energies than the previous system. Importantly, this will establish the ability of the pulses to withstand deleterious distortions associated with high energy propagation, and thus reinforce the self-similar nature of the oscillator.

	RAMAN 1	AMP 1	COMP 1	RAMAN 2	AMP 2	COMP 2
L (m)	45	3.75	2	5,50	2.2	1
β_2 ($\mathrm{ps^2\,km^{-1}}$)	silica	20	-31	DS silica	20	-31
A_{eff} ($\mu\mathrm{m}^2$)	13	35	0	8,5	23	0
α (m^{-1})	silica	1	0	silica	0.5	0

Table 16.3: Modified device parameters for the fibre stages.

The modified system parameters are given explicitly in Table 16.3. In this system the oscillator is now assumed to be seeded with a $380\,\mathrm{pJ}$, $350\,\mathrm{fs}$ (FWHM) hyperbolic secant pulse. The output pulses and chirps after each stage of the oscillator are plotted in Fig. 16.7 where again, for comparison purposes, they have been normalised in power and time. The corresponding pulse parameters are given in Table 16.4. Clearly, despite the overall increase of the pulse energies and peak powers in the system, these pulses have a very similar appearance to those of the previous system as seen in Fig. 16.5. Additional confirmation of the self-similar nature of this modified system is again provided by the good agreement with the hyperbolic secant fits to the intensity profiles (circles). Thus it is reasonable to expect that these pulses are evolving in a similar

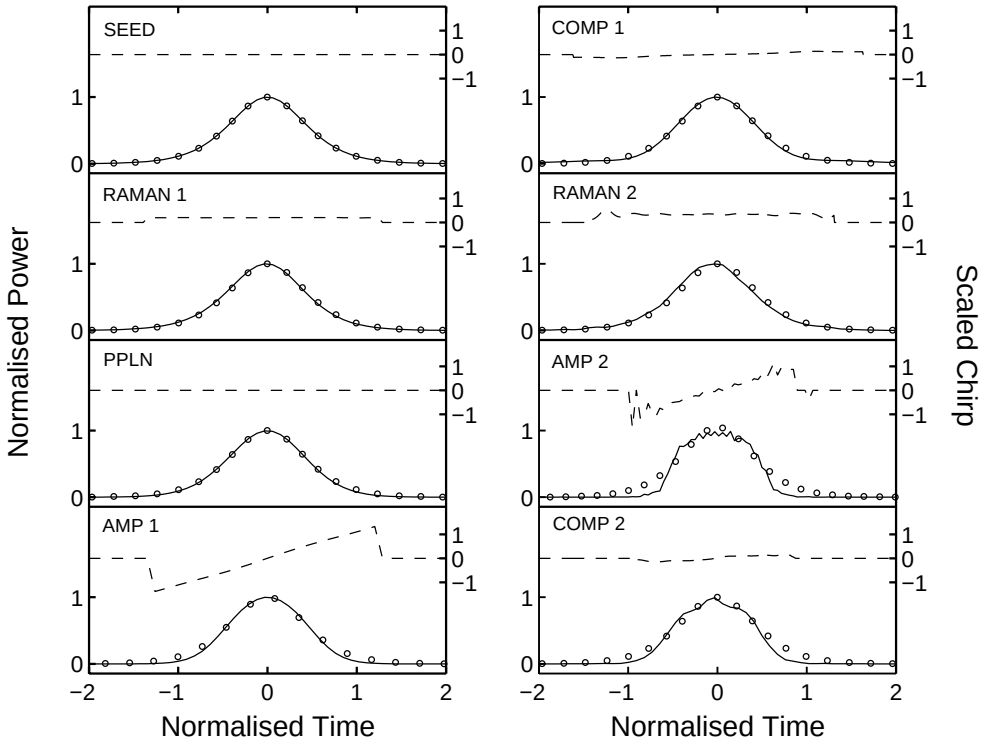

Figure 16.7: Pulse profiles (left axes) and chirps (right axes) of the output pulses after each stage of the modified oscillator, together the seed pulse. The pulse profiles have been normalised in power and time so that they have a peak intensity and FWHM width of 1. The circles are hyperbolic secant fits.

manner to those of the previous system.

Finally, to demonstrate the stability of this modified system, Fig. 16.8 plots the evolution of the (a) FWHM width and (b) peak power at $1.5\,\mu\mathrm{m}$, as a function of the oscillator cycle. Again, it is clear that after each loop the pulses have returned to a form where their parameters are consistent with those of the seed pulse.

	RAMAN 1	PPLN	AMP 1	COMP 1	RAMAN 2	AMP 2	COMP 2
ΔT (fs)	146	107	2273	150	309	1226	342
P_0 (W)	1020	130	270	3640	350	270	1110
E (pJ)	170	15	630	630	130	380	380

Table 16.4: Average pulse parameters after each oscillator stage for the modified system.

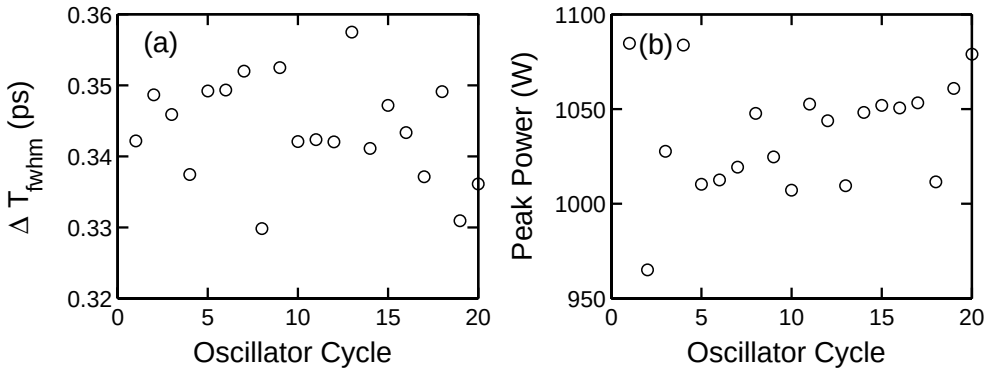

Figure 16.8: Evolution of the (a) FWHM width and (b) peak power of the pulses at $1.5\,\mu\mathrm{m}$ in a higher energy oscillator.

16.5 Discussion

The results presented in this chapter have demonstrated a self-similar oscillator, tunable over the wavelength range $1\,\mu\mathrm{m} - 2\,\mu\mathrm{m}$, which is capable of producing hyperbolic secant pulses with peak powers of the order of a kilowatt and sub-picosecond widths. Significantly, this oscillator has illustrated how the various technologies described in the earlier parts of this thesis can be combined to produce a novel short pulse source. In addition, it has also been shown that with careful choice of the device parameters it is possible to scale this oscillator to a system with higher pulse energies. Thus it is expected that this oscillator could be tailored to yield a wide range of pulse widths and peak powers depending on the system requirements.

Chapter 17

Future Directions

The work carried out in this thesis has identified many areas of research worthy of further study.

The results presented in Part 1 to demonstrate high intensity self-similar pulse solutions in optical fibres have left considerable scope for development and could potentially spark many new directions for future research. In particular, although the experimental demonstrations described in Chapters 5 and 6 have indicated the early stages of parabolic pulse evolution, there is still plenty of room for optimisation of the systems. As the main limiting feature of both these experiments has been attributed to a lack of suitable fibres, most of the recent efforts have been focused on developing new fibre designs.

Owing to the success of the theoretical and numerical investigations described in Chapter 7, the next step in this project will be to conduct experiments to provide the ultimate verification of these solutions. Because of the wide range of fibres, pulse sources and pulse shaping techniques that are available within the ORC it is likely that the experiments will be conducted here. Significantly, in all likely experiments involving self-similar evolution it is highly important that the measured pulses can be accurately characterised not only to allow for rigorous comparisons with the predicted solutions, but also to aid in the optimisation of the systems. Thus it would be beneficial if parallel work was carried out to improve the available pulse diagnostic techniques and this will involve developing FROG pulse measurement devices optimised for the appropriate wavelengths and design criteria of the experimental setups.

The investigations into the use of novel crystal structures to control and manipulate the propagation of light, described in Part 2, have also exposed numerous possible directions for further research. Although there are no immediate plans to conduct any experiments involving the negative refractive index guides discussed in Chapter 11, it is hoped that as the technologies involved in the fabrication processes of these structures are advanced, this is something that could be considered in the future. In contrast to this, the two dimensional nonlinear structures used for harmonic frequency generation in Chapters 12 and 13 are still currently under considerable investigation in the pursuit of improving the efficiency of the devices. Once this has been achieved, future tasks will involve using these devices to investigate novel physical phenomena, such as spatial solitons, as well as seeing them incorporated into practical integrated systems.

In addition to considering the future directions of the individual projects, as discussed in Chapter 15, there is also the option to exploit the combined knowledge of the various technologies to design and develop more efficient devices. To this end it would be desirable to construct a single device which is based on the different structures investigated in the two parts of this thesis (i.e., fibres and modulated crystals). In the context of this thesis, ultimately this would be in the form of the self-similar oscillator described in Chapter 16. However, there are numerous other design possibilities for novel devices based on these structures and thus it is hoped that the results presented in this thesis will contribute to their development.

Appendix A

Calculation of Spectral Phase in the Transform Limit

The notion of a "transform-limited" pulse is widely used in ultrafast optics to refer to a pulse whose temporal duration is the shortest possible, given the available spectral width. In this Appendix, the precise form of the spectral phase which corresponds to this condition will be determined.

Given the complex spectral amplitude: $\tilde{\Psi}(\nu) = \tilde{A}(\nu) \exp\left[\mathrm{i}\tilde{\Phi}(\nu)\right]$, where $\tilde{A}(\nu) = |\tilde{\Psi}(\nu)|$, the analysis is based on the search for the form of the spectral phase $\tilde{\Phi}(\nu)$ such that the temporal duration of the pulse is minimised. Here the RMS width is considered so that:

$$\Delta\tau = \left[\left\langle t^2 \right\rangle - \langle t \rangle^2\right]^{1/2}, \tag{A.1}$$

where

$$\langle t^n \rangle = \frac{\int_{-\infty}^{\infty} t^n \left|\Psi(z,t)\right|^2 \mathrm{d}t}{\int_{-\infty}^{\infty} \left|\Psi(z,t)\right|^2 \mathrm{d}t}. \tag{A.2}$$

From Parseval's theorem [136],

$$\int_{-\infty}^{\infty} \left|\Psi(z,t)\right|^2 \mathrm{d}t = \int_{-\infty}^{\infty} \left|\tilde{\Psi}(z,\nu)\right|^2 \mathrm{d}\nu = U, \tag{A.3}$$

so that the denominator in Eq. (A.2) is simply the pulse energy U.

From the definitions of the Fourier transform,

$$\tilde{\Psi}(\nu) = \int_{-\infty}^{\infty} \Psi(t)\, \mathrm{e}^{\mathrm{i}2\pi\nu t} \mathrm{d}t, \tag{A.4}$$

and its inverse transform,

$$\Psi(t) = \int_{-\infty}^{\infty} \tilde{\Psi}(\nu)\, \mathrm{e}^{-\mathrm{i}2\pi\nu t} \mathrm{d}\nu, \tag{A.5}$$

it follows that

$$\frac{\mathrm{d}\tilde{\Psi}(\nu)}{\mathrm{d}\nu} = \mathrm{i}2\pi \int_{-\infty}^{\infty} t\Psi(t)\, \mathrm{e}^{\mathrm{i}2\pi\nu t} \mathrm{d}t, \tag{A.6}$$

and thus

$$t\Psi(t) = \frac{-\mathrm{i}}{2\pi} \left[\int_{-\infty}^{\infty} \frac{\mathrm{d}\tilde{\Psi}(\nu)}{\mathrm{d}\nu} \mathrm{e}^{-\mathrm{i}2\pi\nu t} \mathrm{d}\nu \right]. \tag{A.7}$$

Using Eqs. (A.6) and (A.7), $\langle t^2 \rangle$ is related to $\tilde{\Psi}(\nu)$ through:

$$\begin{aligned}
\langle t^2 \rangle &= \frac{1}{U} \int_{-\infty}^{\infty} t^2 \left|\Psi(t)\right|^2 \mathrm{d}t \\
&= \frac{1}{U} \int_{-\infty}^{\infty} \left[t\Psi(t)\right] \left[t\Psi^*(t)\right] \mathrm{d}t \\
&= \frac{-\mathrm{i}}{2\pi U} \int_{-\infty}^{\infty} \left[\int_{-\infty}^{\infty} \frac{\mathrm{d}\tilde{\Psi}(\nu)}{\mathrm{d}\nu} \mathrm{e}^{-\mathrm{i}2\pi\nu t} \mathrm{d}\nu \right] t\Psi^*(t)\, \mathrm{d}t \\
&= \frac{-\mathrm{i}}{2\pi U} \int_{-\infty}^{\infty} \frac{\mathrm{d}\tilde{\Psi}(\nu)}{\mathrm{d}\nu} \left[\int_{-\infty}^{\infty} t\Psi(t)\, \mathrm{e}^{\mathrm{i}2\pi\nu t} \mathrm{d}t \right]^* \mathrm{d}\nu \\
&= \frac{1}{(2\pi)^2 U} \int_{-\infty}^{\infty} \frac{\mathrm{d}\tilde{\Psi}(\nu)}{\mathrm{d}\nu} \frac{\mathrm{d}\tilde{\Psi}^*(\nu)}{\mathrm{d}\nu} \mathrm{d}\nu, \\
&= \frac{1}{(2\pi)^2 U} \int_{-\infty}^{\infty} \left| \frac{\mathrm{d}\tilde{\Psi}(\nu)}{\mathrm{d}\nu} \right|^2 \mathrm{d}\nu.
\end{aligned}$$

Similarly, the relationship between $\langle t \rangle$ and $\tilde{\Psi}(\nu)$ is:

$$\begin{aligned}
\langle t \rangle &= \frac{1}{U} \int_{-\infty}^{\infty} t \left|\Psi(t)\right|^2 \mathrm{d}t \\
&= \frac{1}{U} \int_{-\infty}^{\infty} t\Psi(t)\, \Psi^*(t)\, \mathrm{d}t \\
&= \frac{-\mathrm{i}}{2\pi U} \int_{-\infty}^{\infty} \left[\int_{-\infty}^{\infty} \frac{\mathrm{d}\tilde{\Psi}(\nu)}{\mathrm{d}\nu} \mathrm{e}^{-\mathrm{i}2\pi\nu t} \mathrm{d}\nu \right] \Psi^*(t)\, \mathrm{d}t \\
&= \frac{-\mathrm{i}}{2\pi U} \int_{-\infty}^{\infty} \frac{\mathrm{d}\tilde{\Psi}(\nu)}{\mathrm{d}\nu} \left[\int_{-\infty}^{\infty} \Psi(t)\, \mathrm{e}^{\mathrm{i}2\pi\nu t} \mathrm{d}t \right]^* \mathrm{d}\nu \\
&= \frac{-\mathrm{i}}{2\pi U} \int_{-\infty}^{\infty} \frac{\mathrm{d}\tilde{\Psi}(\nu)}{\mathrm{d}\nu} \tilde{\Psi}^*(\nu)\, \mathrm{d}\nu.
\end{aligned}$$

However, by writing the field $\tilde{\Psi}(\nu)$ in terms of its amplitude and phase, then

clearly,

$$\begin{aligned}\frac{\mathrm{d}\tilde{\Psi}(\nu)}{\mathrm{d}\nu} &= \frac{\mathrm{d}}{\mathrm{d}\nu}\left[\tilde{A}(\nu)\,\mathrm{e}^{\mathrm{i}\tilde{\Phi}(\nu)}\right], \\ &= \left[\frac{\mathrm{d}\tilde{A}}{\mathrm{d}\nu} + \mathrm{i}\tilde{A}\frac{\mathrm{d}\tilde{\Phi}}{\mathrm{d}\nu}\right]\mathrm{e}^{\mathrm{i}\tilde{\Phi}(\nu)},\end{aligned}$$

which yields,

$$\begin{aligned}\left\langle t^2\right\rangle &= \frac{1}{(2\pi)^2 U}\int_{-\infty}^{\infty}\left|\frac{\mathrm{d}\tilde{A}}{\mathrm{d}\nu} + \mathrm{i}\tilde{A}\frac{\mathrm{d}\tilde{\Phi}}{\mathrm{d}\nu}\right|^2 \mathrm{d}\nu, \\ &= \frac{1}{(2\pi)^2 U}\left\{\int_{-\infty}^{\infty}\left(\frac{\mathrm{d}\tilde{A}}{\mathrm{d}\nu}\right)^2 \mathrm{d}\nu + \int_{-\infty}^{\infty}\tilde{A}^2\left(\frac{\mathrm{d}\tilde{\Phi}}{\mathrm{d}\nu}\right)^2 \mathrm{d}\nu\right\}, \qquad \text{(A.8)}\end{aligned}$$

and

$$\begin{aligned}\langle t\rangle &= \frac{-\mathrm{i}}{2\pi U}\int_{-\infty}^{\infty}\left[\frac{\mathrm{d}\tilde{A}}{\mathrm{d}\nu} + \mathrm{i}\tilde{A}\frac{\mathrm{d}\tilde{\Phi}}{\mathrm{d}\nu}\right]\mathrm{e}^{\mathrm{i}\tilde{\Phi}(\nu)}\tilde{A}\mathrm{e}^{-\mathrm{i}\tilde{\Phi}}\mathrm{d}\nu \\ &= \frac{-\mathrm{i}}{2\pi U}\int_{-\infty}^{\infty}\left[\tilde{A}\frac{\mathrm{d}\tilde{A}}{\mathrm{d}\nu} + \mathrm{i}\tilde{A}^2\frac{\mathrm{d}\tilde{\Phi}}{\mathrm{d}\nu}\right]\mathrm{d}\nu \\ &= \frac{-\mathrm{i}}{2\pi U}\left.\frac{\tilde{A}^2(\nu)}{2}\right|_{-\infty}^{\infty} + \frac{1}{2\pi}\int_{-\infty}^{\infty}\tilde{A}^2\frac{\mathrm{d}\tilde{\Phi}}{\mathrm{d}\nu}\mathrm{d}\nu \\ &= \frac{1}{2\pi U}\int_{-\infty}^{\infty}\tilde{A}^2\frac{\mathrm{d}\tilde{\Phi}}{\mathrm{d}\nu}\mathrm{d}\nu. \qquad \text{(A.9)}\end{aligned}$$

Combining Eqs. (A.8) and (A.9) in Eq. (A.1) , the RMS width is obtained as

$$\Delta\tau = \left[\begin{array}{c}\frac{1}{(2\pi)^2 U}\left\{\int_{-\infty}^{\infty}\left(\frac{\mathrm{d}\tilde{A}}{\mathrm{d}\nu}\right)^2\mathrm{d}\nu + \int_{-\infty}^{\infty}\tilde{A}^2\left(\frac{\mathrm{d}\tilde{\Phi}}{\mathrm{d}\nu}\right)^2\mathrm{d}\nu\right\} \\ -\frac{1}{(2\pi U)^2}\left\{\int_{-\infty}^{\infty}\tilde{A}^2\left(\frac{\mathrm{d}\tilde{\Phi}}{\mathrm{d}\nu}\right)\mathrm{d}\nu\right\}^2\end{array}\right]^{1/2}. \qquad \text{(A.10)}$$

Using a variational approach it can be shown that this expression is minimised when

$$\frac{\mathrm{d}\tilde{\Phi}}{\mathrm{d}\nu} = \text{const}, \qquad \text{(A.11)}$$

which implies that the transform limited pulse duration,

$$\Delta\tau_{\mathrm{TL}} = \frac{1}{2\pi\sqrt{U}}\left[\int_{-\infty}^{\infty}\left(\frac{\mathrm{d}\tilde{A}}{\mathrm{d}\nu}\right)^2\mathrm{d}\nu\right]^{1/2}, \qquad \text{(A.12)}$$

corresponds to a constant group delay [Eq. (3.11)]. In fact, since the only effect of this constant in the time domain is to introduce a shift in the temporal

position of the pulse, without loss of generality, this constant can be set equal to zero. Thus the physical interpretation that the minimum pulse duration is associated with a flat spectral phase is obtained.

Appendix B

Optical Wave Breaking

For a high intensity pulse propagating in an optical fibre the NLSE suggests that nonlinear effects should dominate over dispersive effects, at least during the initial stages of evolution. However, as it was seen in Section 3.9, the effects of GVD are sufficiently large that they cannot simply be treated as a perturbation to the dominant nonlinear evolution, because large nonlinearities lead to a large SPM-induced frequency chirp across the pulse. Hence even weak dispersive effects lead to significant pulse shaping. For a normal dispersion fibre, a high intensity pulse broadens into a rectangular pulse with a linear chirp across its entire width and self-steepened edges (see Fig. B.1). At these

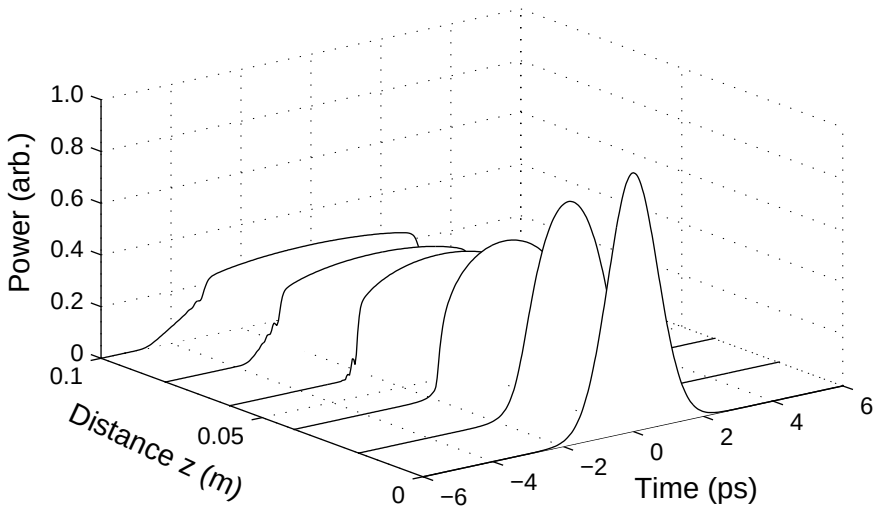

Figure B.1: Evolution of a high intensity Gaussian pulse, in the normal dispersion regime, to show the effects of optical wave breaking on an initially unchirped pulse.

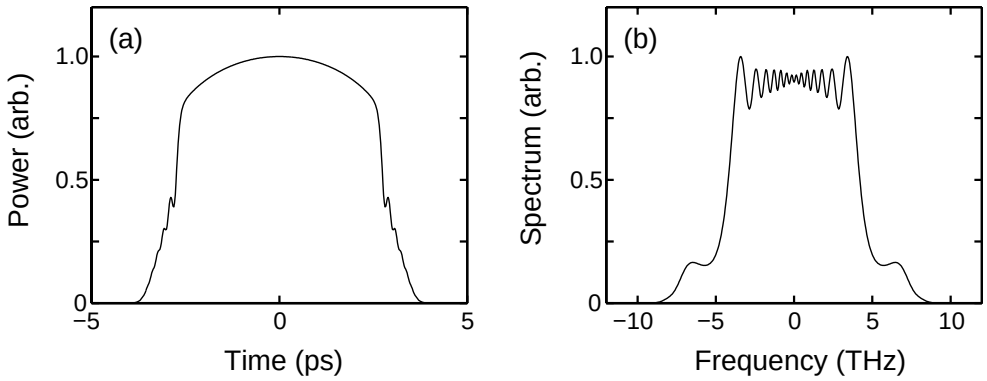

Figure B.2: Temporal profile and spectrum of pulse from Fig. B.1, at $z = 0.8\,\mathrm{m}$. The spectral side lobes and the temporal fine structure near the pulse edges are manifestations of optical wave breaking.

sharp edges the second derivative in the NLSE becomes large and as a result the pulse develops oscillations on its edges. It was first suggested by Tomlinson *et al.* [137] that this phenomenon should be termed optical wave breaking because of its similarity to the breaking of water waves.

The physical origin of these temporal oscillations stems from the chirp becoming a nonmonotonic function in time, which implies that the inner, high intensity, parts of the pulse expand more rapidly than the outer, low intensity, parts. Here the red (blue) shifted light near the leading (trailing) edge travels faster and overtakes the unshifted light in the front (end) tail of the pulse. The leading and trailing edges of the pulse then contain light of different frequencies whose interference results in the temporal oscillations seen near the pulse edges. In the frequency domain this process represents itself in the form of spectral side lobes consisting of the new frequency components. These effects can be clearly seen in Fig. B.2, where (a) shows the oscillations on the temporal profile and (b) shows the side lobes on the corresponding spectrum.

In the anomalous dispersion regime, pulse propagation is dominated by soliton propagation. However, even for high intensity propagation of non-soliton type pulses, optical wave breaking does not occur in the anomalous dispersion regime. In this regime the red (blue) shifted part of the pulse cannot overtake the faster (slower) moving tail and the energy in the pulse tails spreads. As a consequence, there is no interference of the frequency components and the pulse simply develops pedestals.

Appendix C

Publications

Papers in Refereed Journals:

1. A. C. Peacock and N. G. R. Broderick, *Guided modes in channel waveguides with a negative index of refraction,* Opt. Express, 11(20):2502-2510, 2003.

2. V. I. Kruglov, A. C. Peacock, and J. D. Harvey, *Exact self-similar solutions of the generalized nonlinear Schrödinger equation with distributed coefficients,* Phys. Rev. Lett., 90(11):113902, 2003.

3. A. C. Peacock, N. G. R. Broderick, and T. M. Monro, *Numerical study of parabolic pulse generation in microstructured fibre Raman amplifiers,* Opt. Commun., 218:167-172, 2003.

4. K. Gallo, R. T. Bratfalean, A. C. Peacock, N. G. R. Broderick, C. B. E. Gawith, L. Ming, P. G. R. Smith, and D. J. Richardson, *Second-harmonic generation in hexagonally-poled lithium niobate slab waveguides,* Electron. Lett., 39(1):75-76, 2002.

Papers in Preparation::

1. V. I. Kruglov, A. C. Peacock, and J. D. Harvey, *Exact self-similar solutions of the generalized nonlinear Schrödinger equation with distributed coefficients,* in preparation for submission to Phys. Rev. E, 2004.

2. R. T. Bratfalean, A. C. Peacock, N. G. R. Broderick, K. Gallo and R. Llewyn, *Harmonic generation in a two dimensional nonlinear quasicrystal*, in preparation for submission to Opt. Lett., 2004.

3. A.C. Peacock, A. Malinowski, N. G. R. Broderick, J. H. V. Price, K. Furusawa and D. J. Richardson, *Parabolic pulse generation in a high gain fibre amplifier chain*, in preparation for submission to Phys. Rev. A, 2004.

4. A. C. Peacock and N. G. R. Broderick, *Numerical model for a widely tunable self-similar oscillator*, in preparation for submission to Opt. Commun., 2004.

Refereed Conference Proceedings:

1. A. C. Peacock and N. G. R. Broderick, *Numerical model for a widely tunable self-similar oscillator*, "NLGW," MC16, March 29-31, 2004.

2. R. T. Bratfalean, N. G. R. Broderick, K. Gallo, and A. C. Peacock, *Frequency conversion in a nonlinear photonic quasi-crystal*, "NLGW," MB8, March 29-31, 2004.

3. N. G. R. Broderick, R. T. Bratfalean, K. Gallo, and A. C. Peacock, *Nonlinear photonic crystals in lithium niobate*, "LEOS summer topicals," TuA1.1 (Invited), July 14-16, 2003.

4. J. D. Harvey, A. C. Peacock, and V. I. Kruglov, *Analytic solutions of the nonlinear Schrödinger equation with distributed coefficients*, "LEOS," pg:319, Nov 10-14, 2002.

5. A. C. Peacock, N. G. R. Broderick, and T. M. Monro, *Numerical study of parabolic pulse generation in microstructured fibre Raman amplifiers*, "NLGW," NLTuD10-1, Sept 1-4, 2002.

6. K. Gallo, R. T. Bratfalean, A. C. Peacock, N. G. R. Broderick, C. B. E. Gawith, L. Ming, P. G. R. Smith, and D. J. Richardson, *Quadratic interactions in a hexagonally poled lithium niobate buried waveguide*, "NLGW," NLWC5, Sept 1-4, 2002.

7. J. D. Harvey, A. C. Peacock, and V. I. Kruglov, *Exact soliton solution of the nonlinear Schrödinger equation with distributed gain and anomalous group velocity dispersion*, "ACOFT," July 8-11, 2002.

Bibliography

[1] E. Hecht. *Optics*. Addison-Wesley Publishing Company, 2nd edition, 1987.

[2] J. S. Russell. Report on waves. Technical report, 14th (1844) meeting of the British Association for the Advancement of Science, 1845.

[3] R. W. Boyd. *Nonlinear Optics*. Academic Press, 1992.

[4] G. P. Agrawal. *Nonlinear Fiber Optics*. Academic Press, 2nd edition, 1995.

[5] G. P. Agrawal. Amplification of ultrashort solitons in erbium-doped fiber amplifiers. *IEEE Photon. Technol. Lett.*, 2(12):875–877, 1990.

[6] D. Anderson, M. Desaix, M. Lisak, and M. L. Quiroga-Teixeiro. Wave breaking in nonlinear-optical fibers. *J. Opt. Soc. Am. B*, 9(8):1358–1361, 1992.

[7] C. Paré and P.-A. Bélanger. Optical solitary waves in the presence of a Lorentzian gain line: Limitations of the Ginzburg-Landau model. *Opt. Commun.*, 145:385–392, 1998.

[8] A. C. Peacock, R. J. Kruhlak, J. D. Harvey, and J. M. Dudley. Solitary pulse propagation in high gain optical fiber amplifiers with normal group velocity dispersion. *Opt. Commun.*, 206:171–177, 2002.

[9] D. Anderson, M. Desaix, M. Karlsson, M. Lisak, and M. L. Quiroga-Teixeiro. Wave-breaking-free pulses in nonlinear-optical fibers. *J. Opt. Soc. Am. B*, 10(7):1185–1190, 1993.

[10] M. J. Ablowitz and H. Segur. *Solitons and the inverse scattering transform*. Society for Industrial and Applied Mathematics, 1981.

[11] P. J. Olver. *Applications of Lie Groups to Differential Equations*. Springer-Verlag, 2nd edition, 1993.

[12] M. E. Fermann, V. I. Kruglov, B. C. Thomsen, J. M. Dudley, and J. D. Harvey. Self-similar propagation and amplification of parabolic pulses in optical fibers. *Phys. Rev. Lett.*, 84(26):6010–6013, 2000.

[13] V. I. Kruglov, A. C. Peacock, J. M. Dudley, and J. D. Harvey. Self-similar propagation of high-power parabolic pulses in optical fiber amplifiers. *Opt. Lett.*, 25(24):1753–1755, 2000.

[14] A. Yariv. *Optical Electronics in Modern Communications*. Oxford University Press, 5th edition, 1997.

[15] R. Trebino, K. W. Delong, D. N. Fittinghoff, J. N. Sweetser, M. A. Krumbügel, and B. A. Richman. Measuring ultrashort laser pulses in the time-frequency domain using frequency-resolved optical gating. *Rev. Sci. Instrum.*, 68(9):3277–3295, 1997.

[16] M. Born and E. Wolf. *Principles of Optics*. Pergamon Press, 6th edition, 1990.

[17] I. Malitson. Interspecimen comparison of the refractive index of fused silica. *J. Opt. Soc. Am.*, 55:1205, 1965.

[18] K. E. Oughstun and H. Xiao. Failure of the quasimonochromatic approximation for ultrashort pulse propagation in a dispersive, attenuative medium. *Phys. Rev. Lett.*, 78(4):642–645, 1997.

[19] G. P. Agrawal. *Fiber-Optic Communication Systems*. John Wiley & Sons, 2nd edition, 1997.

[20] L. Mandel and E. Wolf. *Optical coherence and quantum optics*. Cambridge University Press, Cambridge, 1995.

[21] B. Deutsch and Th. Pfeiffer. Chromatic dispersion of erbium-doped silica fibres. *Electron. Lett.*, 28(3):303–305, 1992.

[22] R. Paschotta, J. Nilsson, A. C. Tropper, and D. C. Hanna. Ytterbium-doped fiber amplifiers. *IEEE J. Quantum Electron.*, 33(7):1049–1056, 1997.

[23] G. V. Grigoryan, I. T. Lima, Jr., T. Yu, V. S. Grigoryan, and C. R. Menyuk. Using colour to understand light transmission. *Optics and Photonics News*, 11(8):44–50, 2000.

[24] C. S. Gardener, J. M. Green, M. D. Kruskal, and R. M. Miura. Method for solving the Korteweg-deVries equation. *Phys. Rev. Lett.*, 19(19):1095–1097, 1967.

[25] R. K. Dodd, J. C. Eilbeck, J. D. Gibbon, and H. C. Morris. *Solitons and Nonlinear Wave Equations*. Academic Press, New York, 1984.

[26] P.-A. Bélanger, L. Gagnon, and C. Paré. Solitary pulses in an amplified nonlinear dispersive medium. *Opt. Lett.*, 14(17):943–945, 1989.

[27] N. R. Pereira and L. Stenflo. Nonlinear Schrödinger equation including growth and damping. *Phys. Fluids*, 20(10):1733–1734, 1977.

[28] S. Chi, C.-W. Chang, and S. Wen. Femtosecond soliton propagation in erbium-doped fibre amplifiers: The equivalence of two different models. *Opt. Commun.*, 106:193–196, 1994.

[29] J. P. Gordon. Theory of the soliton self-frequency shift. *Opt. Lett.*, 11(10):662–664, 1986.

[30] K. J. Blow and D. Wood. Theoretical description of transient stimulated Raman scattering in optical fibers. *IEEE J. Quantum Electron.*, 25(12):2665–2673, 1989.

[31] R. H. Stolen, J. P. Gordon, W. J. Tomlinson, and H. A. Haus. Raman response function of silica-core fibers. *J. Opt. Soc. Am. B*, 6(6):1159–1166, 1989.

[32] F. Vanholsbeeck. Personal Communication, 2000.

[33] G. I. Barenblatt. *Scaling, Self-Similarity, and Intermediate Asymptotics*. Cambridge University Press, Cambridge, 1996.

[34] A. A. Afanas'ev, V. I. Kruglov, B. A. Samson, R. Jakyte, and V. M. Volkov. Self-action of counterpropagating axially symmetric light beams in a transparent cubic-nonlinearity medium. *J. Mod. Opt.*, 38(6):1189–1202, 1991.

[35] S. An and J. E. Sipe. Universality in the dynamics of phase grating formation in optical fibers. *Opt. Lett.*, 16(19):1478–1480, 1991.

[36] K. Drühl, R. G. Wenzel, and J. L. Carlsten. Observation of solitons in stimulated Raman scattering. *Phys. Rev. Lett.*, 51(13):1171–1174, 1983.

[37] C. R. Menyuk, D. Levi, and P. Winternitz. Self-similarity in transient stimulated Raman scattering. *Phys. Rev. Lett.*, 69(21):3048–3051, 1992.

[38] T. M. Monro, P. D. Miller, L. Poladian, and C. M. de Sterke. Self-similar evolution of self-written waveguides. *Opt. Lett.*, 23(4):268–270, 1998.

[39] K. Tamura and M. Nakazawa. Pulse compression by nonlinear pulse evolution with reduced optical wave breaking in erbium-doped fiber amplifiers. *Opt. Lett.*, 21(1):68–70, 1996.

[40] V. I. Kruglov, A. C. Peacock, J. D. Harvey, and J. M. Dudley. Self-similar propagation of parabolic pulses in normal-dispersion fiber amplifiers. *J. Opt. Soc. Am. B*, 19(3):461–469, 2002.

[41] A. C. Peacock. Self-similar amplification and propagation of parabolic pulses in optical fibres. Master's thesis, The University of Auckland, 2001.

[42] M. E. Fermann, A. Galvanauskas, M. L. Stock, K. K. Wong, D. Harter, and L. Goldberg. Ultrawide tunable erbium soliton fiber laser amplified in ytterbium-doped fiber. *Opt. Lett.*, 24(20):1428–1430, 1999.

[43] B. Desthieux, R. I. Laming, and D. N. Payne. 111 kW (0.5 mJ) pulse amplification at 1.5 μm using a gated cascade of 3 erbium-doped fiber amplifiers. *Appl. Phys. Lett.*, 63(5):586–588, 1993.

[44] J. H. V. Price. *The development of high power, pulse fiber laser systems and their applications*. PhD thesis, Optoelectronics Research Centre, 2003.

[45] K. Tamura, E. P. Ippen, H. A. Haus, and L. E. Nelson. 77-fs pulse generation from a stretched-pulse mode-locked all-fiber ring laser. *Opt. Lett.*, 18(13):1080–1082, 1993.

[46] K. W. DeLong, R. Trebino, J. Hunter, and W. E. White. Frequency-resolved optical gating with the use of second-harmonic generation. *J. Opt. Soc. Am. B*, 11(11):2206–2215, 1994.

[47] S. Namiki and Y. Emori. Ultrabroad-band Raman amplifiers pumped and gain-equalized by wavelength-division-multiplexed high-power laser diodes. *J. Sel. Topics in Quant. Electron.*, 7(1):3–16, 2001.

[48] M. Kuznetsov. Design of widely tunable semiconductor 3-branch lasers. *J. Lightwave Technol.*, 12(12):2100–2106, 1994.

[49] A. M. Melo, J. L. S. Lima, R. S. de Oliveira, and A. S. B. Sombra. Photonic time-division multiplexing (OTDM) using ultrashort picosecond pulses in a terahertz optical asymmetric demultiplexer (TOAD). *Opt. Commun.*, 205:299–312, 2002.

[50] G. R. Williams, M. Vaziri, K. H. Ahn, B. C. Barnett, M. N. Islam, K. O. Hill, and B. Malo. Soliton logic gate using low-birefringence fiber in a nonlinear loop mirror. *Opt. Lett.*, 20(16):1671–1673, 1995.

[51] C. Finot, G. Millot, C. Billet, and J. M. Dudley. Experimental generation of parabolic pulses via Raman amplification. *Opt. Express*, 11(13):1547–1552, 2003.

[52] Z.Yusoff, J. H. Lee, W. Belardi, T. M. Monro, P. C. Teh, and D. J. Richardson. Raman effects in a highly nonlinear holey fiber: Amplification and modulation. *Opt. Lett.*, 27(6):424–426, 2002.

[53] M. Ho, K. Uesaka, M. Marhic, Y. Akasaka, and L. G. Kazovsky. 200-nm-bandwidth fiber optical amplifier combining parametric and Raman gain. *J. Lightwave Technol.*, 19(7):977–981, 2001.

[54] K. Furusawa. *Development of rare-earth doped microstructured optical fibres*. PhD thesis, University of Southampton, 2003.

[55] T. M. Monro, N. G. R. Broderick, and D. J. Richardson. Exploring the optical properties of holey fibres. Conference Proceedings: Nato *Summer School on Nanoscale Linear and Nonlinear Optics*, July 2000.

[56] J. A. Nelder and R. Mead. A simplex method for function minimization. *Comput. J.*, 7(4):308–313, 1965.

[57] D. N. Fittinghoff, K. W. DeLong, R. Trebino, and C. L. Ladera. Noise sensitivity in frequency-resolved optical-gating measurements of ultrashort pulses. *J. Opt. Soc. Am. B*, 12(10):1955–1967, 1995.

[58] K. O. Hill and G. Meltz. Fiber Bragg gratings technology fundamentals and overview. *J. Lightwave Technol.*, 15(8):1263–1276, 1997.

[59] W. A. Watson, M. V. O'Connor, P. S. Lloyd, D. P. Shepherd, D. C. Hanna, C. B. E. Gawith, L. Ming, P. G. R. Smith, and O. Balachninaite. Extended operation of synchronously pumped optical parametric oscillators to longer idler wavelengths. *Opt. Lett.*, 27(23):2106–2108, 2002.

[60] D. Taverner, D. J. Richardson, L. Dong, J. E. Caplen, K. Williams, and R. V. Penty. 158–mJ pulses from a single-transverse-mode, large-mode-area erbium-doped fiber amplifier. *Opt. Lett.*, 22(6):378–380, 1997.

[61] K. Furusawa. Personal communication. 2003.

[62] I. Cristiani, P. Franco, M. Midrio, and M. Romagnoli. Pulse generation and propagation beyond the limit of soliton spectral resonances. *Opt. Commun.*, 146:241–244, 1998.

[63] S. V. Chernikov, E. M. Dianov, D. J. Richardson, and D. N. Paye. Soliton pulse-compression in dispersion-decreasing fiber. *Opt. Lett.*, 18(7):476–478, 1993.

[64] J. D. Moores. Nonlinear compression of chirped solitary waves with and without phase modulation. *Opt. Lett.*, 21(8):555–557, 1996.

[65] M. Abramowitz and I. Stegun. *Handbook of Mathematical Functions*. Dover Publications, 1964.

[66] S. S. Santos. On the Galilean transformations and the stationary frame of reference for electromagnetic waves. *Phys. Essays*, 10(3):466–473, 1997.

[67] V. A. Bogatyrev, M. M. Bubnov, E. M. Dianov, A. S. Kurkov, P. V. Mamyshev, A. M. Prokhorov, S. D. Rumyantsev, V. A. Semenov, S. L. Semenov, A. A. Sysoliatin, S. V. Chernikov, A. N. Gur'yanov, G. G. Devyatykh, and S. I. Miroshnichenko. A single-mode fiber with chromatic dispersion varying along the length. *J. Lightwave Technol.*, 9(5):561–565, 1991.

[68] *The World Book encyclopedia*. World Book, Inc., 1991.

[69] J. D. Joannopoulos, R. D. Meade, and J. N. Winn. *Photonic Crystals : molding the flow of light*. Princeton University Press, 1995.

[70] D. R. Smith, W. J. Padilla, D. C. Vier, S. C. Nemat-Nasser, and S. Schultz. Composite medium with simultaneously negative permeability and permittivity. *Phys. Rev. Lett.*, 84(18):4184–4187, 2000.

[71] V. Berger. Nonlinear photonic crystals. *Phys. Rev. Lett.*, 81(19):4136–4139, 1998.

[72] M. S. Bigelow, N. N. Lepeshkin, and R. W. Boyd. Superluminal and slow light propagation in a room-temperature solid. *Science*, 301:200–202, 2003.

[73] V. G. Veselago. The electrodynamics of substances with simultaneously negative values of ϵ and μ. *Sov. Phys. Usp.*, 10(4):509–514, 1968.

[74] P. M. Valanju, R. M. Walser, and A. P. Valanju. Wave refraction in negative-index media: Always positive and very inhomogeneous. *Phys. Rev. Lett.*, 88(18):187401, 2002.

[75] S. Foteinopoulou, E. N. Economou, and C. M. Soukoulis. Refraction in media with a negative refractive index. *Phys. Rev. Lett.*, 90(10):107402, 2003.

[76] J. B. Pendry, A. J. Holden, W. J. Stewart, and I. Youngs. Extremely low frequency plasmons in metallic mesostructures. *Phys. Rev. Lett.*, 76(25):4773–4776, 1996.

[77] J. B. Pendry, A. J. Holden, D. J. Robbins, and W. J. Stewart. Magnetism from conductors and enhanced nonlinear phenomena. *IEEE Trans. Microwave Theory Tech.*, 47(11):2075–2084, 1999.

[78] J. Marangos. Faster than a speeding photon. *Nature*, 406:243–244, 2000.

[79] L. J. Wang, A. Kuzmich, and A. Dogariu. Gain-assisted superluminal light propagation. *Nature*, 406:277–2279, 2000.

[80] I. V. Shadrivov, A. A. Sukhorukov, and Y. S. Kivshar. Guided modes in negative-refractive-index waveguides. *Phys. Rev. E*, 67:057602, 2003.

[81] E. J. Lerner. Race is on to develop blue-green diode lasers. *Laser Focus World*, April 1998.

[82] I. Suemune, K. Nakanishi, Y. Fujii, Y. Kuroda, M. Fujimoto, and M. Yamanishi. Photopumped ZnSe/ZnSSe blue semiconductor-lasers and a theoretical calculation of the optical gain. *J. Cryst. Growth*, 117(1–4):1068–1072, 1992.

[83] P. A. Franken, A. E. Hill, C. W. Peters, and G. Weinreich. Generation of optical harmonics. *Phys. Rev. Lett.*, 7(4):118–119, 1961.

[84] J. A. Giordmaine. Mixing of light beams in crystals. *Phys. Rev. Lett.*, 8(1):19–20, 1962.

[85] P. D. Maker, R. W. Terhune, M. Nisenoff, and C. M. Savage. Effects of dispersion and focusing on the production of optical harmonics. *Phys. Rev. Lett.*, 8(1):21–22, 1962.

[86] J. A. Armstrong, N. Bloembergen, J. Ducuing, and P. S. Pershan. Interactions between light waves in a nonlinear dielectric. *Phys. Rev.*, 127(6):1918–1939, 1962.

[87] M. Houé and P. D. Townsend. An introduction to methods of periodic poling for second-harmonic generation. *J. Phys. D: Appl. Phys.*, 28:1747–1763, 1995.

[88] R. L. Byer. Quasi-phasematched nonlinear interactions and devices. *J. Nonlinear Opt. Phys. and Mat.*, 6(4):549–592, 1997.

[89] Y. Zhu and N. Ming. Second-harmonic generation in a Fibonacci optical lattice and the dispersive effect of the refractive index. *Phys. Rev. B*, 42(6):3676–3679, 1990.

[90] N. G. R. Broderick, G. W. Ross, H. L. Offerhaus, D. J. Richardson, and D. C. Hanna. Hexagonally poled lithium niobate: A two dimensional nonlinear photonic crystal. *Phys. Rev. Lett.*, 84(19):4345–4348, 2000.

[91] S. Zhu, Y. Zhu, Y. Qin, H. Wang, C. Ge, and N. Ming. Experimental realization of second harmonic generation in a Fibonacci optical superlattice of $LiTaO_3$. *Phys. Rev. Lett.*, 78(14):2752–2755, 1997.

[92] N. Wand, H. Chen, and K. H. Kuo. Two-dimensional quasi-crystal with eightfold rotational symmetry. *Phys. Rev. Lett.*, 59(9):1010–1013, 1987.

[93] K. Niizeki. A classification of quasilattices in two dimensions into mutual local-derivability classes. *J. Alloys Compd.*, 342(1-2):213–216, 2002.

[94] M. A. Kaliteevski, S. Brand, R. A. Abram, T. F. Krauss, R. DeLa Rue, and P. Millar. Two dimensional Penrose-tiled photonic quasicrystals: From diffraction pattern to band structure. *Nanotechnology*, 11:274–280, 2000.

[95] A. Ashkin, G. D. Boyd, J. M. Dziedzic, R. G. Smith, A. A. Ballman, J. J. Levinstein, and K. Nassau. Optically-induced refractive index inhomogeneities in $LiNbO_3$ and $LiTbO_3$. *Appl. Phys. Lett.*, 9(1):72–74, 1966.

[96] G. J. Edwards and M. Lawrence. A temperature-dependent dispersion-equation for congruently grown lithium-niobate. *Opt. Quantum. Elect.*, 16(4):373–375, 1984.

[97] L. E. Myers, G. D. Miller, R. C. Eckardt, M. M. Fejer, R. L. Byer, and W. R. Bosenberg. Quasi-phase-matched 1.064-μm-pumped optical parametric oscillator in bulk periodically poled $LiNbO_3$. *Opt. Lett.*, 20(1):52–54, 1995.

[98] D. H. Jundt. Temperature-dependent Sellmeier equation of the index of refraction, n_e, in congruent lithium niobate. *Opt. Lett.*, 22(20):1553–1554, 1997.

[99] K. Okamoto. *Fundamentals of optical waveguides.* Academic Press, 2000.

[100] K. W. Morton and D. F. Mayers. *Numerical Solution of Partial Differential Equations.* Cambridge University Press, 1994.

[101] M. J. Steel. Personal communication.

[102] A. R. Mitchell. *Computational Methods in Partial Differential Equations*. John Wiley & Sons, 1976.

[103] K. Mori, Y. Tamaki, M. Obara, and K. Midorikawa. Second-harmonic generation of femtosecond high-intensity Ti:sapphire laser pulses. *J. Appl. Phys.*, 83(6):2915–2919, 1998.

[104] R. A. Shelby, D. R. Smith, S. C. Nemat-Nasser, and S. Schultz. Microwave transmission through a two-dimensional, isotropic left-handed metamaterial. *Appl. Phys. Lett.*, 78(4):489–491, 2001.

[105] R. A. Shelby, D. R. Smith, and S. Schultz. Experimental verification of a negative index of refraction. *Science*, 292:77–79, 2001.

[106] M. Notomi. Theory of light propagation in strongly modulated photonic crystals: Refractionlike behavior in the vicinity of the photonic band gap. *Phys. Rev. B*, 62(16):10696, 2000.

[107] C. Luo, S. G. Johnson, J. D. Joannopoulos, and J. B. Pendry. All-angle negative refraction without negative effective index. *Phys. Rev. B*, 65:201104, 2002.

[108] E. Cubukcu, K. Aydin, E. Ozbay, S. Forteinopoulou, and C. M. Soukoulis. Electromagnetic waves: Negative refraction by photonic crystals. *Nature*, 423:604–605, 2003.

[109] M. Yamada, N. Nada, M. Saitoh, and K. Watanade. First-order quasi-phase matched $LiNbO_3$ waveguide periodically poled by applying an external field for efficient blue second-harmonic generation. *Appl. Phys. Lett.*, 62(5):435–436, 1993.

[110] É. A. Kaner and V. G. Skobov. Electromagnetic waves in metals in a magnetic field. *Sov. Phys. Usp.*, 9:480–503, 1967.

[111] E. A. Marcatili. Dielectric rectangular waveguide and directional coupler for integrated optics. *Bell Syst. Tech. J.*, 48(7):2071–2102, 1969.

[112] G. I. Stegeman, J. J. Burke, , and T. Tamir. Surface-polaritonlike waves guided by thin, lossy metal films. *Opt. Lett.*, 8(7):383–385, 1983.

[113] S. Ramo, J. R. Whinnery, and T. Van Duzer. *Fields and waves in communication electronics.* John Wiley & Sons, 1965.

[114] J. E. Heebner, R. W. Boyd, and Q-H. Park. SCISSOR solitons and other novel propagation effects in microresonator-modified waveguides. *J. Opt. Soc. Am. B*, 8(4):722–731, 2002.

[115] M. Notomi, K. Yamada, A. Shinya, J. Takahashi, C. Takahashi, and I. Yokohama. Extremely large group-velocity dispersion of line-defect waveguides in photonic crystal slabs. *Phys. Rev. Lett.*, 87(25):253902, 2001.

[116] E. Snitzer. Cylindrical dielectric waveguide modes. *J. Opt. Soc. Am.*, 51(5):491–498, 1961.

[117] A. Hardy and W. Streifer. Coupled mode theory of parallel waveguides. *J. Lightwave Technol.*, 3(5):1135–1146, 1985.

[118] W. H. Press. *Numerical recipes in C++: The art of scientific computing*. Cambridge University Press, 2002.

[119] P. Harrison. *Quantum wells, wires, and dots: Theoretical and computational physics*. John Wiley, 1999.

[120] W. Streifer, M. Osiński, and A. Hardy. Reformulation of the coupled-mode theory of multiwaveguide systems. *J. Lightwave Technol.*, 5(1):1–4, 1987.

[121] B. Boulanger, J. P. Fève, G. Marnier, C. Bonnin, P. Villeval, and J. J. Zondy. Absolute measurement of quadratic nonlinearities from phase-matched second-harmonic generation in a single KTP crystal cut as a sphere. *J. Opt. Soc. Am. B*, 14(6):1380–1386, 1997.

[122] M. Mizuuchi and K. Yamamoto. Waveguide second-harmonic generation device with broadened flat quasi-phase-matching response by use of a grating structure with located phase shifts. *Opt. Lett.*, 23(24):1880–1882, 1998.

[123] C. B. E. Gawith, D. P. Shepherd, J. A. Abernethy, D. C. Hanna, G. W. Ross, and P. G. R. Smith. Second-harmonic generation in a direct-bonded periodically poled $LiNbO_3$ buried waveguide. *Opt. Lett.*, 24(7):481–483, 1999.

[124] N. G. R. Broderick, R. T. Bratfalean, T. M. Monro, D. J. Richardson, and C. M. de Sterke. Temperature and wavelength tuning of 2nd, 3rd and 4th harmonic generation in a two dimensional hexagonally poled nonlinear crystal. *J. Opt. Soc. Am. B*, 19(9):2263–2272, 2002.

[125] K. R. Parameswaran, R. K. Route, J. R. Kurz, R. V. Roussev, M. M. Fejer, and M. Fujimura. Highly efficient second-harmonic generation in buried waveguides formed by annealed and reverse proton-exchange in periodically poled lithium niobate. *Opt. Lett.*, 27(3):179–181, 2002.

[126] R. L. Byer. *Nonlinear Optics edited by P. G. Harper and B. S. Wherrett*, chapter 2, pages 47–160. Academic Press, 1977.

[127] D. Shechtman, I. Blech, D. Gratias, and J. W. Cahn. Metallic phase with long-range orientational order and no translational symmetry. *Phys. Rev. Lett.*, 53(20):1951–1954, 1984.

[128] X. Yang and Y. Liu. Properties of the peaks of second harmonic light through Fibonacci-class ferroelectric domains. *Eur. Phys. J. B*, 15:625–631, 2000.

[129] R. Penrose. The role of aesthetics in pure and applied mathematical research. *Bull. Inst. Math. Appl.*, 10:266–271, 1974.

[130] M. J. McCarthy, S. D. Butterworth, and D. C. Hanna. High-power widely-tunable picosecond pulses from an all-solid-state synchronously-pumped optical parametric oscillator. *Opt. Commun.*, 102:297–303, 1993.

[131] H. Chen, M. Leblanc, and G. W. Schinn. Gain enhanced L-band optical fiber amplifiers and tunable fiber lasers with erbium-doped fibers. *Opt. Commun.*, 216:119–125, 2003.

[132] P. G. Bollond, L. P. Barry, J. M. Dudley, R. Leonhardt, and J. D. Harvey. Characterization of nonlinear switching in a figure-of-eight fiber laser using frequency-resolved optical gating. *IEEE Photon. Technol. Lett.*, 10(3):343–345, 1998.

[133] T. M. Monro and D. J. Richardson. Holey optical fibres: Fundamental properties and device applications. *C. R. Physique*, 4:175–186, 2003.

[134] A. Galvanauskas, M. A. Arbore, M. M. Fejer, M. E. Fermann, and D. Harter. Fiber-laser-based femtosecond parametric generator in bulk periodically poled $LiNbO_3$. *Opt. Lett.*, 22(2):105–107, 1997.

[135] J. D. Harvey, V. I. Kruglov, and A. C. Peacock. Intermediate self-similar dynamics of solitary waves in optical fibres and fibre amplifiers. *Proceedings for the Australian Conference on Optical Fibre Technology*, (TuC1-5), 2003.

[136] S. M. Tan. *Linear Systems Course Notes*. The University of Auckland, 1999.

[137] W. J. Tomlinson, R. H. Stolen, and A. M. Johnson. Optical wave breaking of pulses in nonlinear optical fibres. *Opt. Lett.*, 10(9):457–459, 1985.